

FLOW AND SKIN FRICTION OVER NATURAL ROUGH BEDS

by

Christopher Paola

B.S., Lehigh University (1976)

M.Sc., University of Reading (1977)

Submitted to the Department of Earth and Planetary Sciences,  
Massachusetts Institute of Technology, and to the Department  
of Geology and Geophysics, Woods Hole Oceanographic  
Institution, on February 16, 1983, in partial fulfillment of  
the requirements for the Degree of

DOCTOR OF SCIENCE

at the

MASSACHUSETTS INSTITUTE OF TECHNOLOGY

and the

WOODS HOLE OCEANOGRAPHIC INSTITUTION

February, 1983

© Massachusetts Institute of Technology 1983

Signature of Author: \_\_\_\_\_  
Joint Program in Oceanography,  
Massachusetts Institute of Technology and  
Woods Hole Oceanographic Institution

Certified by: \_\_\_\_\_ Thesis Supervisor

Certified by: \_\_\_\_\_ Thesis Supervisor

Accepted by: \_\_\_\_\_  
Chairman, Joint Committee for Marine  
Geology and Geophysics

Lindgren

JUN 15 1983

Lindgren

MASSACHUSETTS INSTITUTE OF TECHNOLOGY  
WANT TO DRAWN FROM LIBRARIES

# FLOW AND SKIN FRICTION OVER NATURAL ROUGH BEDS

by

Christopher Paola

Submitted to the Department of Earth and Planetary Sciences, Massachusetts Institute of Technology, and to the Department of Geology and Geophysics, Woods Hole Oceanographic Institution, on February 16, 1983, in partial fulfillment of the requirements for the Degree of Doctor of Science in Oceanography

## ABSTRACT

When a boundary layer develops over a bed that is hydrodynamically rough at a length scale or scales larger than the grain size (a macrorough bed), as is usually the case where bed forms are present, it is necessary to distinguish among total boundary shear stress and its components, form drag and spatially averaged skin friction. It is known that the mean-velocity field reflects the composite boundary shear stress. Above about one roughness height above the tops of the roughness elements, the velocity does not vary horizontally. Its vertical profile is semilogarithmic and scales with the total friction velocity  $u_*^t$  and total roughness length  $z_{ot}$ . This region is here called the integrated logarithmic layer (ILL). Below the ILL the velocity varies horizontally in response to the irregular boundary; this region is called the surface layer.

In the first of two sets of experiments reported here, skin-friction measurements were made with an array of flush-mounted hot films at four points on the stoss slope of one of a field of two-dimensional immobile current ripples. Total boundary shear stress was also measured, as were mean-velocity profiles in the ILL and the surface layer. The ILL behaves as described above. Although surface-layer velocity profiles are semilogarithmic, their semilogarithmic slope is not proportional to the local skin-friction velocity, so they do not locally obey the law of the wall. Rather, the velocity field can be decomposed into a spatially averaged rotational component and a local inviscid perturbation. The measured skin-friction field is consistent

with a simple model for sediment transport over the bed forms except near reattachment, where the fluctuating skin friction is important. The data are also consistent with the drag-partition theories of Einstein and Barbarossa (1952) and Engelund (1966). Normalized skin-friction spectra do not vary with streamwise position but do vary with Reynolds number; skin-friction probability density functions show significant increases in skewness and kurtosis near reattachment but do not vary strongly with Reynolds number.

In the second set of experiments the skin-friction vector field was measured around isolated hemispheres, with model sedimentary tails one and four obstacle heights long and without tails. The measured skin-friction fields are not consistent with deposition along the obstacle-flow centerline downstream of reattachment, which occurs about two obstacle heights downstream of the trailing edge of the hemisphere. This applies for local bed-load erosion and deposition and for general deflation of the bed, and is not substantially altered by the presence of either tail. Measurements were also made of skin friction, total boundary shear stress and ILL velocity profiles over  $h, B$ -rough arrays of hemispheres with and without tails four roughness heights long, at two areal densities. The skin-friction field in the denser array is significantly distorted from that around an isolated element. The measured skin friction in both arrays is significantly greater than that given by a drag-partition formula proposed by Wooding et al. (1973). The roughness length  $z_{0t}$  for both densities is not changed by addition of the tails.

Thesis supervisors: Dr. John B. Southard

Title: Associate Professor of Earth and Planetary  
Sciences

Dr. Giselher Gust

Title: Associate Professor of Marine Science,  
University of South Florida

## ACKNOWLEDGEMENTS

It is a pleasure to thank Giselher Gust and John Southard for the guidance they have given me over the past five years. The science described in this dissertation falls in the common ground between fluid physics and sedimentary geology. Although both GG and JS are strongly interdisciplinary scientists, each has contributed to my education and to this work from his own perspective; broadly, GG from physics and JS from sedimentology. I am grateful to them both for their willingness to cooperate, without which this dissertation could not even have been begun.

I thank Giselher Gust for providing most of the direct supervision of the work described here, for patiently teaching me a great deal about physical and experimental science, and for generously providing much of the equipment and technical support necessary for the completion of the experiments. All the digital data processing was done at his laboratory at the University of South Florida, much of it by B. Allen Patrick, for whose enthusiasm, skill, and generous hospitality I am extremely grateful.

I thank John Southard for his guidance and advice during my graduate career, and particularly for providing a stimulating research environment in which I was exposed to a wide range of problems related to physical sedimentology. I have learned a great deal from him, both directly and by example. Much of whatever clarity of expression this dissertation possesses reflects his influence.

I am grateful to Bill Grant, Mark Wimbush, and Charley Hollister, all members of my thesis committee, for careful and constructive readings of the manuscript, and to Dave Johnson for chairing the defense. In addition, I thank them all for many enlightening discussions during my time in the Joint Program. I particularly wish to thank Dave Johnson for helping me find my way, and Yogi Agrawal for generously sharing home and insight over the past two years.

I thank Donna Hall for carefully drafting many of the figures, John Annese for technical help generously given at several stages of the work, and Judith Stein for deftly untangling our project's allotment of red tape.

My graduate career has been enhanced considerably by lively and diverse discussions with my fellow students. In particular, I thank Kevin Bohacs and Bill Corea for helping me get started; Roger Kuhnle and Peter Vrolijk, who worked with me on the experiments, for their enthusiasm and ingenuity; Steve and Ann Swift for their patience and kind hospitality; Doug Walker, for his superb "get-it-donedness";

and Peter Wilcock for his good-natured insight and uncommon sense. I thank them all for their friendship and for sharing their understanding with me.

I thank Kathy, Hope, Mark, Jim, and Mary Lee for their love and support, particularly during the past year.

I thank Barb Russell for her love and support throughout the most difficult stages of my graduate career.

Finally, there is a debt of gratitude that I wish to record but can never repay; it is to my family. My father Nicholas, my mother Mary, and my sister Suzanne have helped me more than they can ever know. The name on the title page is also theirs, and if the work within is worthy of that I will be well satisfied. This dissertation is dedicated to them.

Financial support. I received fellowship support from the National Science Foundation for three years, and early stages of this project were supported by NSF grant OCE 77-20437. Most of the work was done under Office of Naval Research contract number N00014-80-C-0273.

Contents	Page
Acknowledgements.....	4
List of Figures.....	9
List of Tables.....	14
Chapter 1. Introduction.....	15
1.1. General.....	15
1.2. Experimental methods.....	36
1.21. General.....	36
1.22. The flume.....	36
1.23. Thermal anemometry.....	40
1.24. Data processing.....	54
Chapter 2. Flow and skin friction over two-dimensional current ripples.....	59
2.1. Introduction.....	59
2.11. Internal boundary layers.....	62
2.12. Application of IBL theory to flow over macrorough beds.....	66
2.2. Experimental methods.....	78
2.3. Results: mean quantities.....	95
2.31. Skin friction.....	95
2.32. Velocity.....	99
2.4. Results: fluctuating quantities.....	123
2.41. Root-mean-square intensity.....	123
2.42. Spectra.....	133
2.43. Probability density functions.....	144
2.5. Discussion.....	155
2.51. Why is the local response inviscid?.....	155

	Page
2.52. Comparison of the results with drag-partition theories.....	166
2.53. Application to sediment-transport calculations.....	171
2.54. Implications for bed-form dynamics and classification.....	178
2.6. Conclusions.....	187
Chapter 3. Flow and skin friction over three-dimensional macrorough beds.....	189
3.1. Introduction.....	189
3.2. Experimental methods.....	206
3.3. Results: isolated elements.....	238
3.31. Direction.....	238
3.32. Mean skin-friction magnitude.....	245
3.33. RMS skin friction.....	257
3.34. Horizontal divergence.....	268
3.4. Results: full fields.....	280
3.41. Skin friction.....	280
3.42. Velocity profiles.....	286
3.5. Discussion.....	298
3.51. Obstacle-trapped bed forms.....	298
3.52. Skin-friction patterns in relation to overall flow resistance.....	305
3.53. Application of the full-field results to natural conditions.....	308
3.6. Conclusions.....	323

	Page
4. References.....	325
Appendix A. Symbols.....	334
Appendix B. Computer programs.....	339
Biographical sketch.....	347



## List of Figures:

Figure		Page
1.1	Sketches of smooth, rough, and macrorough flows	19
1.2	General Cartesian coordinate system (x,y,z) and corresponding velocity components (u,v,w).	21
1.3	General features of a bed form and its associated flow field.	31
1.4	The flume in which all the experiments were done.	37
1.5	Schematic section of flow and the thermal boundary layer about a hot wire.	41
1.6	Simplified diagram of the circuitry for a constant-temperature thermal anemometer.	45
1.7	Schematic diagram of flow and the thermal boundary layer over a flush-mounted hot film.	50
1.8	The instrument chain used for recording digital data.	55
2.1	Simplified diagram of an internal boundary layer developing at a smooth-to-rough transition ( $z_{o2} > z_{o1}$ ).	63
2.2	An internal boundary layer model for the velocity field over bed forms of large aspect ratio ( $O(100)$ ), after Smith and McLean (1977).	69
2.3	The idealized two-part semilogarithmic form of the spatially averaged mean-velocity profile in macrorough flows possessing an equilibrium sublayer.	73
2.4	The TSI hot-wire sensor used to measure velocity in the two-dimensional ripple experiment.	81
2.5	Hot-wire calibration curves for each of the three runs in which velocity measurements were made.	83
2.6	(A) Photograph and (B) section of the hot-film array used to measure skin friction in the two-dimensional ripple experiment.	87

Figure	Page
2.7	Calibration curves for the skin-friction array shown in figure 2.6. 90
2.8	Comparison of the output voltage of a hot film mounted on a rubber substrate that is flat (squares) and curved normal to the direction of flow (circles) for different values of flow speed given in arbitrary units (the range of speeds is about 3 - 40 cm/s). 93
2.9	Mean values measured with the skin-friction array shown in figure 2.6, nondimensionalized with $u_*^t$ , as a function of $R^*$ and sensor position. 97
2.10	Sketch of the curvilinear vertical coordinate $\zeta$ in comparison with the rectilinear coordinate $y$ . 101
2.11	Mean-velocity profiles measured over two-dimensional ripples, nondimensionalized with the total friction velocity $u_*^t$ . 103
2.12	Mean-velocity profiles measured over two-dimensional ripples, nondimensionalized with the local skin-friction velocity $u_*^s$ , for skin-friction measuring positions 1 (A), 2 (B) and 3 (C). 107
2.13	Sketch of the velocity field given by first-order potential theory for flow over a sinusoidal bed. 115
2.14	Measured dimensional velocity profiles (open symbols) compared with the results (filled symbols) of adding a first-order inviscid solution to the profile measured at position 2. 119
2.15	The rms value $\sigma_\tau$ of the fluctuating skin friction as a function of $R^*$ and sensor position, in dimensional form (dynes/cm <sup>2</sup> ) and nondimensionalized with the total bottom stress $\tau_{ot}$ . 125
2.16	Relative fluctuation intensity $\sigma_\tau/\tau_{os}$ of skin friction measured over two-dimensional ripples as a function of sensor position and $R^*$ . 128
2.17	Relative fluctuation intensity $\sigma_\tau/\tau_{os}$ of skin friction as a function of bulk Reynolds number $Du/\nu$ for smooth flow. 130

Figure	Page	
2.18	Power spectral density $\phi$ of the skin friction, normalized by the total variance of the signal $\sigma_\tau^2$ , as a function of frequency $f$ . The data shown were measured at the crest (1) and near reattachment (3).	135
2.19	Nondimensional skin-friction spectra measured on two-dimensional ripples and in smooth flow.	141
2.20	Skin-friction probability density functions for all sensor positions and roughness Reynolds numbers.	145
2.21	Mean-velocity profiles measured by Zilker (1976) at different streamwise positions over a sinusoidal bed (open symbols) compared with the results (filled symbols) of adding a first-order inviscid solution to the profile measured at $x/L = 0.8$ .	161
2.22	Profiles of Reynolds shear stress obtained by Zilker (1976) at different streamwise positions over a sinusoidal bed.	163
2.23	Calculated skin-friction-velocity profiles (heavy lines) required to maintain a stable propagating ripple form, compared with measured values (open circles), for two values of $R^*$ .	175
2.24	The surface-layer velocity profile over a bed form of small ( $O(10)$ ) aspect ratio viewed as the sum of a spatially averaged rotational profile and a local irrotational perturbation.	181
3.1	Sketch of the "horseshoe" vortex system about a cylindrical obstacle on a flat bed.	195
3.2	The three roughness elements around which skin-friction measurements were made in the first (isolated-element) series of runs.	209
3.3	One of the flush-mounted hot-film sensors used in the first series of runs, together with the grid used to position the roughness elements.	211
3.4	Locations where the skin-friction field was measured in the first series of runs.	213

Figure		Page
3.5	Calibration curves for single flush-mounted hot films used in the first series of runs.	215
3.6	(A) Photograph and (B) plan of the sensor array used to gather skin-friction data in the second (full-field) series of runs.	217
3.7	Calibration curves for the seven skin-friction sensors of the array shown in figure 3.6.	220
3.8	The metal-clad hot-wire sensor used to measure velocity in the second (full-field) series of runs.	223
3.9	The calibration curve for the velocity sensor shown in figure 3.8.	227
3.10	Plan view of roughness unit cells for the (A) sparse and (B) dense arrays used in the full-field runs.	231
3.11	Mean-velocity profiles measured over the sparse ( $\lambda = 0.00845$ ) array of hemispheres at the two positions shown in figure 3.10.	233
3.12	(A) and (B) Photographs of a plaster plate showing the direction field behind an isolated hemisphere.	239
3.13	Direction fields behind isolated obstacles, determined from plaster plates like that shown in figure 3.12.	241
3.14	The skin-friction magnitude field interpolated from measurements behind isolated obstacles at the points shown in figure 3.4, nondimensionalized by the reference (free-stream) value.	247
3.15	The root-mean-square skin-friction field interpolated from measurements behind isolated obstacles at the points shown in figure 3.4, nondimensionalized by the reference (free-stream) skin friction.	258
3.16	The horizontal divergence of the time-averaged skin-friction field.	270
3.17	Mean-velocity profiles measured in the four full-field runs.	287

Figure		Page
3.18	Mean-velocity profiles for the four full-field runs nondimensionalized according to the scheme of Wooding <u>et al.</u> (1973).	293
3.19	Mean-velocity profiles for the four full-field runs, nondimensionalized as in figure 3.18 but excluding the factor $\phi$ introduced by Wooding <u>et al.</u> (1973) to account for the effect of the streamwise extent of roughness elements on the roughness length $z_{ot}$ .	295
3.20	Sketches of the vortex system behind an isolated hemisphere (A) with no stratification and (B) with stable stratification.	303
3.21	The two-dimensional region of influence for a measuring station S in a boundary-layer profile.	313
3.22	Roughness-averaging scales for a series of regions upstream of a hypothetical boundary-layer measuring station (circle), based on the data in Table 3.5.	317

## List of Tables

Table	Page
2.1 General experimental conditions for runs over two-dimensional current ripples	79
2.2 Skin-friction skewness as a function of sensor position and roughness and bulk Reynolds numbers	152
2.3 Skin-friction kurtosis as a function of sensor position and roughness and bulk Reynolds numbers	153
2.4 Skin-friction skewness and kurtosis measured in smooth flow	154
2.5 Comparison of nondimensional spatially averaged skin-friction velocities calculated according to the method of Einstein and Barbarossa (1952) with values measured in this study	168
2.6 Comparison of Engelund's (1966) method for calculating form drag with the results of this study	170
3.1 Correspondence between calibrations shown in figure 3.5, correlation coefficients for fitted power-law curves, and chronological run numbers for the first (isolated-element) series of runs	225
3.2 Experimental conditions for runs of the first (isolated-element) series	244
3.3 Experimental conditions for runs of the second (full-field) series	281
3.4 Time-averaged skin-friction magnitude at the seven positions shown in figure 3.6	283
3.5 The limits of the upstream region that influences each height in a hypothetical current-meter array, and the roughness averaging scale $L_r$ in each region, for a typical $z_{ot}$ of 0.1 cm	322

## 1. Introduction.

1.1. General. Much of physical sedimentology involves consideration of the motion of fluid and sediment over boundaries irregular on one or more scales. Bed forms are among the commonest sources of irregularity, and they are of particular importance geologically because in many cases they produce a sedimentary record that is distinctive and potentially rich in paleoenvironmental information. In the analysis of modern environments, bed forms play an important role as natural current meters; the information they provide is potentially most valuable in places such as the deep ocean where direct measurement of currents is difficult and expensive. Interpreting both the ancient and the modern bed-form records amounts to deducing flow properties from observations of bed-form characteristics. This may be viewed as an inverse problem in which the forward problem is to determine the properties of bed forms developed under a given imposed flow field. This forward problem in itself is extremely complex: the simplest elements to which it can be reduced form a coupled, turbulent system of flow and sediment transport under locally nonuniform conditions. In the face of this it is not surprising that the most productive approach from a sedimentological viewpoint has been direct and empirical (Southard, 1971; Dalrymple et al., 1978; Harms et al., 1982).

As in any branch of science, however, such empirical information must always be supplemented by analysis aimed at providing an understanding of why the results have the form they do. Apart from the aesthetic pleasure such understanding provides, without it we cannot assess the stability of empirical results to changes in conditions from those under which they were obtained. Spatial and temporal variations in scale and magnitude of flow and in sediment properties all affect bed forms in nature; to evaluate the effects of all of these empirically we would have to generate an enormous catalog of data. A more effective approach is one that combines theory with well-placed critical experiments.

So much for putting the general problem of bed-form dynamics into geological perspective; it still needs to be reduced substantially to bring it within range of the available means of attack. I mentioned above that any bed-form theory must involve consideration of both flow and sediment transport over irregular (henceforth "rough") boundaries. I have chosen to concentrate on the flow, because the flow field must be understood at least near the boundary before there is any hope of calculating the sediment transport. There are, however, complex problems relating to the sediment transport as well. Some of them will be discussed in section 2.53, but the main emphasis in this work will be on the flow and the tangential bottom stresses it sets up.



The nature of the boundary shear stress depends on the form of the boundary, as illustrated by the three cases shown in figure 1.1. In all three, it is assumed that the boundary layer is steady, uniform, and unstratified, and that no sediment transport is occurring. ("Boundary layer" will usually be used in a general sense to mean that part of a wall-bounded shear flow in which shear stresses generated near the wall are dynamically important. Occasionally, though, it will be necessary to distinguish among pipe, open-channel and developing boundary layers.) More detailed discussion of most of the following review can be found in Tennekes and Lumley (1972, ch. 5), Arya (1975), Townsend (1976, ch. 5), and Smith and McLean (1977).

Consider first a turbulent boundary layer developed over a perfectly smooth surface (figure 1.1a). (We will see presently that many real surfaces are "smooth enough".) Although the boundary layer is fully turbulent, as we approach the wall the viscosity must become important to satisfy the no-slip condition. Hence the flow near the wall is viscous-dominated; at the wall the Reynolds stress is extinguished and the instantaneous boundary shear stress  $T_0$  is given by  $T_0 = \rho \nu (\partial U / \partial y)_0$ , where  $\rho$  and  $\nu$  are the fluid density and kinematic viscosity respectively, and  $U$  is the instantaneous velocity at height  $y$  above the bottom (figure 1.2). The subscript zero indicates that both the stress and the vertical derivative are to be evaluated at the bed.

In a turbulent flow  $T_0$  and  $U$  can be divided into time-averaged and fluctuating parts. Nearly all of the flows to be considered in this work will be turbulent; variables describing them will be distinguished as follows. All literal references will be to time-averaged quantities unless stated otherwise. Among symbolic references, lower-case letters or overlining will denote time-averaged quantities, primed lower-case letters will denote temporal fluctuations, and upper-case letters will denote total instantaneous quantities. Thus  $A = a + a'$  where  $a = (1/t_a) \int_0^{t_a} A dt$ , and  $t_a$  is a time scale long compared with those of the turbulent fluctuations.

Anticipating that  $\tau_0$  as well as  $\nu$  may influence the flow field near the smooth wall, we define a kinematic mean shear stress  $u_* = (\tau_0/\rho)^{1/2}$  having units of velocity and called the friction velocity or shear velocity. Then a natural length scale is  $\nu/u_*$  and the velocity field near the bed is given by

$$\frac{u}{u_*} = f_S\left(\frac{u_* y}{\nu}\right) \quad 1.1$$

Far from the wall, in the outer part of the flow, the turbulence begins to be affected by the finite height of the boundary layer  $D$ , so  $D$  becomes the length scale. Since the outer scaling is to be viewed as being applied from the surface downward, we refer the velocity to the surface velocity  $u_s$ ; it should also scale with  $u_*$ , on the grounds that whatever is the overall driving force on the flow

Figure 1.1. Sketches of smooth, rough, and macrorough flows (left) and corresponding mean-velocity profiles (right). Multivalued profiles are for different streamwise positions.

VDL - Velocity-defect layer

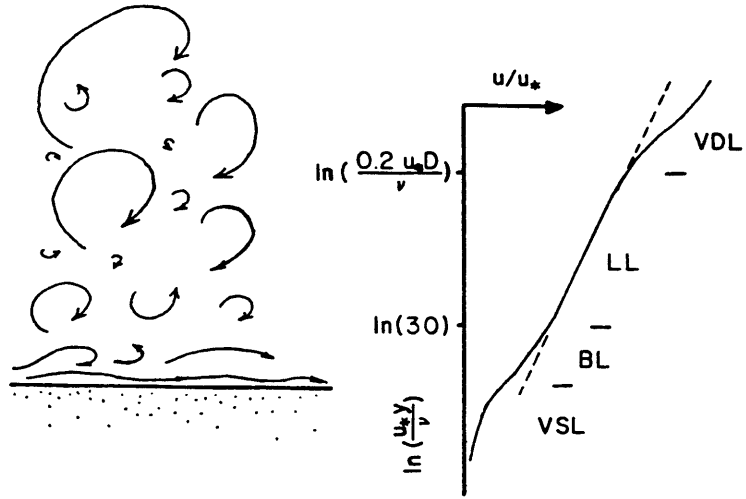
LL - Logarithmic layer

BL - Buffer layer

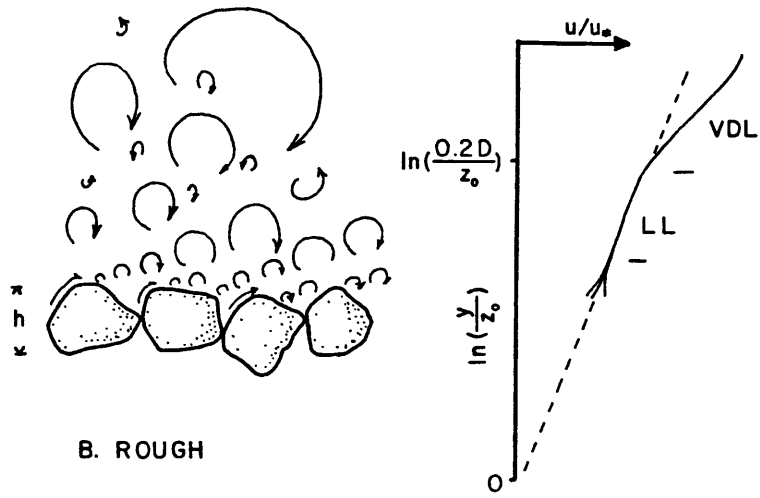
VSL - Viscous sublayer

ILL - Integrated logarithmic layer

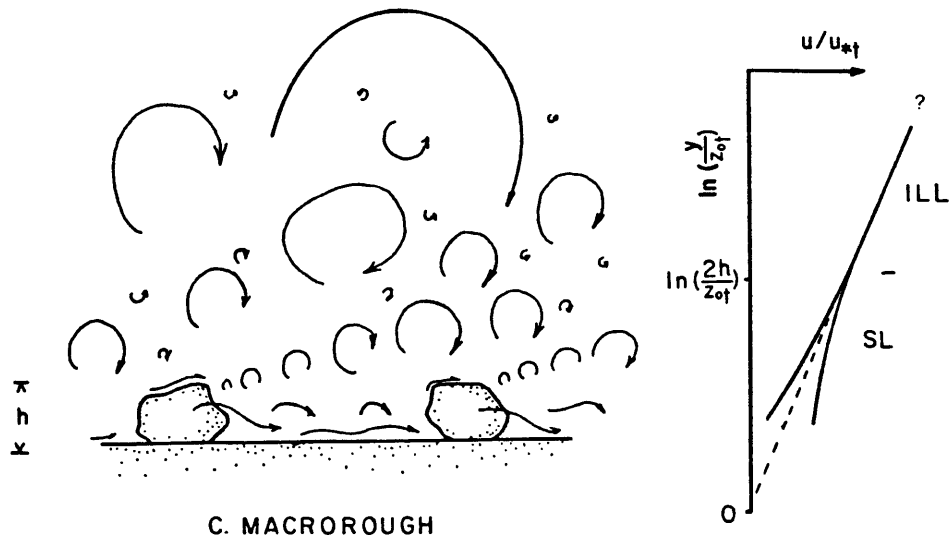
SL - Surface layer



A. SMOOTH



B. ROUGH



C. MACROROUGH

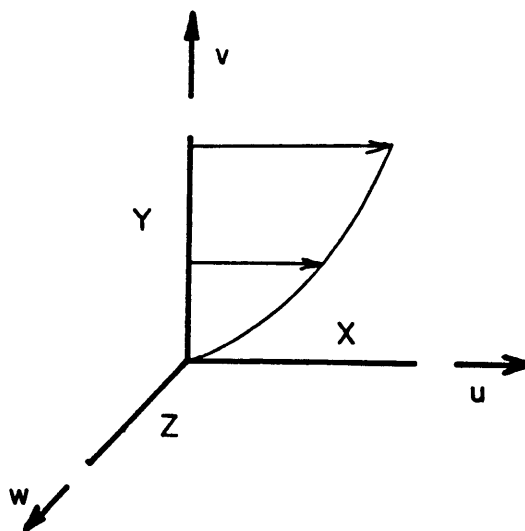


Figure 1.2. General Cartesian coordinate system  $(x,y,z)$   
and corresponding velocity components  $(u,v,w)$ .

(usually gravity or pressure), it must be balanced by the boundary shear stress. Hence for the outer layer

$$\frac{u_s - u}{u_*} = g \left( \frac{y}{D} \right) \quad 1.2$$

Millikan (1939) showed that by requiring that both (1.1) and (1.2) hold in some "overlap region" the velocity profile there is specified to within two empirical constants:

$$\frac{u}{u_*} = a_1 \ln \left( \frac{u_* y}{\nu} \right) + a_2 \quad 1.3$$

This relation was originally derived in a different way, so to maintain consistency  $a_1$  is usually written as  $1/\kappa$  where  $\kappa$  is called the von Karman constant. Much has been written about the constancy of  $\kappa$ ; it certainly has the value 0.4 in smooth flow for the three general types of boundary layer named above over the range of Reynolds numbers attainable in the laboratory. This makes (1.3) a very powerful tool: it is relatively difficult to measure  $u_*$  directly, particularly in field experiments, but it can be determined from (1.3) as  $u_* = \kappa du/d(\ln(y))$ . Making the required velocity-profile measurements is usually relatively straightforward.

The numerical value of  $a_2$  is of less interest for our purposes. It is similarly constant at about 5.0.

So for a smooth turbulent boundary layer the velocity profile looks as shown in figure 1.1a. Immediately above the bed there is a viscous-dominated region called the viscous sublayer in which the profile is linear:  $(u/u_*) = (u_* y / \nu)$ . This is overlain by a buffer or transitional region and then

the logarithmic layer; the velocity profile there is often loosely referred to as the "law of the wall" although strictly speaking this governs the two layers below as well. Beyond this is the outer or "velocity-defect" region, governed by a form of (1.2) that varies according to whether the boundary layer is fully developed in a pipe or in an open channel, or is not fully developed.

Now consider a turbulent boundary layer over a uniform bed of coarse sand of diameter  $h$  (figure 1.1b). By analogy with flow about an isolated sphere one would expect that, if velocities near the bed are large enough, flow separation should occur around the grains and the resulting wakes should disrupt the velocity field. We define a roughness Reynolds number  $R^* \equiv u_* h / \nu$ ; empirically, if  $R^*$  is greater than about 5, the viscous sublayer is affected by the presence of the grains, and if  $R^*$  is greater than about 70 (fully rough flow) it is completely destroyed in a formal sense. Of course, there must still be a viscous-dominated region on the surface of each grain to satisfy the no-slip condition, and with it a viscous shear stress. Continuing our analogy with the behavior of an isolated sphere, however, we expect the dominant part of the drag on the grains to be pressure or form drag induced by the separated flow about the grains. The boundary shear stress, in which this drag is averaged over the bed, is thus independent of viscosity and so of  $R^*$ .

The scaling arguments outlined for smooth flow can be extended to the fully rough case, provided we exclude from consideration the region very near the bed where the grains affect the flow field individually (figure 1.1b). The length scale in the law of the wall includes the viscosity, which is clearly inappropriate here; it is natural instead to choose  $h$ , the grain height, as the inner length scale. We retain  $u_*$  as the scaling velocity and write the law of the wall as

$$\frac{u}{u_*} = f_r\left(\frac{y}{h}\right) \quad 1.4$$

The outer flow, on the other hand, includes no explicit dependence on  $\nu$  so there is no reason to modify (1.2) for rough flows. In an overlap region where (1.4) and (1.2) are both valid, we obtain the rough-bed equivalent to (1.3):

$$\frac{u}{u_*} = a_3 \ln\left(\frac{y}{h}\right) + a_4 \quad 1.5$$

It is one of the most fundamental and remarkable results of the study of turbulent boundary layers that  $a_3 = a_1$ ; that is, that the relation between  $u_*$  and  $du/d(\ln(y))$  in the logarithmic region is the same in both smooth and rough flows. On the other hand,  $a_4$  is different from the smooth case and depends on the geometry of the roughness. It is usual to rewrite (1.5) as

$$\frac{u}{u_*} = \frac{1}{\kappa} \ln\left(\frac{y}{z_0}\right) \quad 1.6$$

where  $z_0$  is called the roughness length; it is a length scale proportional to the scale of the roughness. The constant of proportionality depends on the roughness geometry. (Here I



am generalizing slightly from the example of closely packed sand under consideration to similar kinds of small-scale, uniformly distributed roughness.) For closely packed sand-grain roughness,  $z_o=h/30$ .

It is possible to imagine sediment transport under either smooth or rough conditions as described above, although for the smooth case the viscous sublayer is disrupted by the moving grains (Gust and Southard, in press) and the length scale in  $R^*$  may need to be redefined. In any case the force propelling the sediment is the boundary shear stress  $\rho u_*^2$ : for both kinds of boundary layer considered so far, this is the average tangential force per unit area on the grains.

Now suppose we have a similar situation -- a bed roughened with large (say a few centimeters), closely packed spherical grains -- but imagine them to be laid in a single layer on a flat, smooth surface. Water flows over the bed so that  $u_*$  is about 1 cm/s and  $R^*$  is a few hundred, comfortably above the limit for fully rough flow. What happens if we remove grains one at a time, leaving individual grains surrounded by smooth surface (figure 1.1c)? (It would be necessary to adjust the mean velocity continuously to keep the boundary shear stress constant.) The large grains still separate the flow, exert form resistance, and shed wakes that locally disrupt the viscous sublayer. But the no-slip condition implies the existence of a viscous-dominated region near the wall: at the bed surface the boundary shear stress has the same

viscous form as it does on a smooth wall:  $\tau_o = \rho \nu (\partial u_p / \partial y_n)_o$ , where  $y_n$  is locally normal to the bed and has its origin at the bed surface, and  $u_p$  is the velocity locally parallel to the surface. Such small-scale, local shear stress is known as skin friction. Due to gradients in pressure and turbulence intensity induced by the presence of the large grains, the skin friction varies with position over the bed.

We may define the total bottom stress  $\tau_{ot}$  as

$$\tau_{ot} = \frac{1}{A} \left( \int_{A'} p_o n_y dA' + \int_{A'} \rho \nu \left( \frac{\partial u_p}{\partial y_n} \right)_o n_y dA' \right) \quad 1.7$$

where  $A$  is an averaging area that includes a number of roughness elements,  $A'$  is a true wetted surface area,  $p_o$  is the local pressure on the boundary,  $n_y$  is the vertical component of a unit vector normal to the surface, and  $u_p$  is the velocity parallel to the surface. This is the total boundary shear stress acting against the flow, so that in a wide, uniform open channel of depth  $D$  and slope  $S$ ,

$$\tau_{ot} = \rho g D S \quad 1.8$$

The first term in (1.7) is called the form drag ( $\tau_{of}$ ); it is meaningful only in a spatially averaged sense. On the other hand, the skin friction ( $\tau_{os}$ ) is the integrand in the second term; it is a well-defined local quantity although it enters the total bottom stress in spatially integrated form.

The boundary layer over a bed of widely and perhaps irregularly spaced roughness elements is thus considerably more complicated than either a rough or a smooth boundary layer; it really combines elements of both. The work to be

described in this thesis is aimed at clarifying aspects of this type of flow, which will be referred to as macrorough. Most of the further discussion of macrorough flow will be left to later, more detailed sections, but a few additional general comments should be made here. First, each of the three boundary shear stresses in (1.7) --  $\tau_{ot}$ ,  $\tau_{of}$ , and  $\tau_{os}$  -- can be converted to a friction velocity  $u_* = (\tau_o)^{1/2}$ . In light of the role of  $u_*$  in scaling velocity profiles, embodied in (1.2), (1.3) and (1.6), one would expect the composite nature of the boundary shear stress to be reflected in the velocity field. We can get a rough idea of how this works by considering the consequences of a general increase in the length scale of the turbulence with height, which in turn is a simple kinematic result of the increasing distance of the eddy centers from the wall (Townsend, 1976, p. 156 ff.). As eddies become larger, they respond more slowly to changes in strain rate, and as their distances from the wall increase, they are advected more quickly by the mean velocity; the net result of both effects is that the area of the bed to which the turbulence responds increases with height in the flow (Townsend, 1965a). (These ideas will be developed in more detail in section 3.53.) Since the total bottom stress  $\tau_{ot}$  is spatially averaged by definition (1.7), it can be a valid scaling parameter only above some height at which the turbulence is large enough to average the variable bottom stress. This height cannot be less than some small

distance above the tops of the roughness elements (empirically, it will be seen in section 2.32 to be about one roughness height), because the form drag, included in (1.7) as an integral of pressure on the boundary, appears in the flow as excess Reynolds stress generated in the wakes of the roughness elements. One must be somewhere above the tops of the roughness elements before the wakes will have merged to produce a Reynolds-stress field that is uniform in the streamwise direction. Below this, the velocity and turbulence fields vary spatially in response to the rough topography.

Combining all of the above, the following picture emerges. In macrorough flow, the spatially integrated region well above the tops of the roughness elements corresponds to the logarithmic layer given by (1.6); it will be referred to here as the integrated logarithmic layer (ILL). In deriving the profile law (1.6) for fully rough flow, a single friction velocity equivalent to  $u_*^t$  emerged naturally as the velocity scale because there was no need to consider the details of the viscous shear stress on the grain surfaces. But in macrorough flow there are areas between roughness elements where the boundary shear stress is purely viscous; furthermore the disposition of this viscous stress and its contribution to the total boundary shear stress both depend on the geometry and arrangement of the roughness elements.

These complications make it necessary to distinguish explicitly in macrorough flow between the resistance to flow caused by local, viscous stress -- the skin friction -- and that caused by the integrated boundary pressure field -- the form drag. In the ILL, however, both contributions are combined. To find an image of the variable skin friction in the velocity field, we must look at flow closer to the bed.

Below the ILL, the flow field varies spatially in response to the rough topography; such a region will be referred to here as a surface layer. In the smooth areas between roughness elements, extension of our scaling argument for purely smooth boundary layers suggests a surface-layer velocity profile scaled with a local "skin-friction velocity"  $u_{*s} = (\nu \partial u_p / \partial y_n)_o)^{1/2}$  and the viscosity. Here one must be careful because it is not obvious to what extent the wakes affect flow near the bed. This will be discussed in more detail later on, but the possibility of such a locally governed sublayer should be kept in mind.

The careful distinction that has been drawn between the two components of the total bottom stress may seem pedantic, but it is not. Think again of our prototypical macrorough bed: large, isolated roughness elements arranged on a flat surface. Now imagine that this surface is made of sand fine enough that the flow is locally smooth, at least as long as no sediment transport is occurring. The forces on these small grains are determined by conditions in their immediate

vicinity. They are not directly dependent on the form drag carried by the large roughness elements; rather the tangential stress on the fine sand at any point is given by the skin friction. To understand sediment transport on the bed, knowledge of the distribution of skin friction is absolutely necessary -- although, as mentioned earlier, once the sand begins moving, this can itself alter the skin-friction field. It is straightforward to extend this picture to the more familiar one of sand moving over a field of ripples or dunes (figure 1.3). The elements of macrorough flow described above are all present: flow separation occurs at the bed-form slip face, giving rise to a strongly turbulent wake and to form drag, and there is a local skin-friction field that varies spatially. The main additional complication is that bed slope as well as wake relaxation contributes to the variability in skin friction. The behavior of a sediment wave is determined by the relation between the topography and the variation in sediment transport over it (Smith, 1970; Middleton and Southard, 1977, p. 7.26 ff.). The latter depends on the skin-friction field, which in turn is controlled in large part by the topography. Thus, understanding the skin-friction field and its relation to topography is an essential part of understanding bed-form stability and dynamics.

Several more general points about macrorough flow are worth mentioning before we move on. As we have seen, the ILL is equivalent to the logarithmic layer in smooth and rough flow;

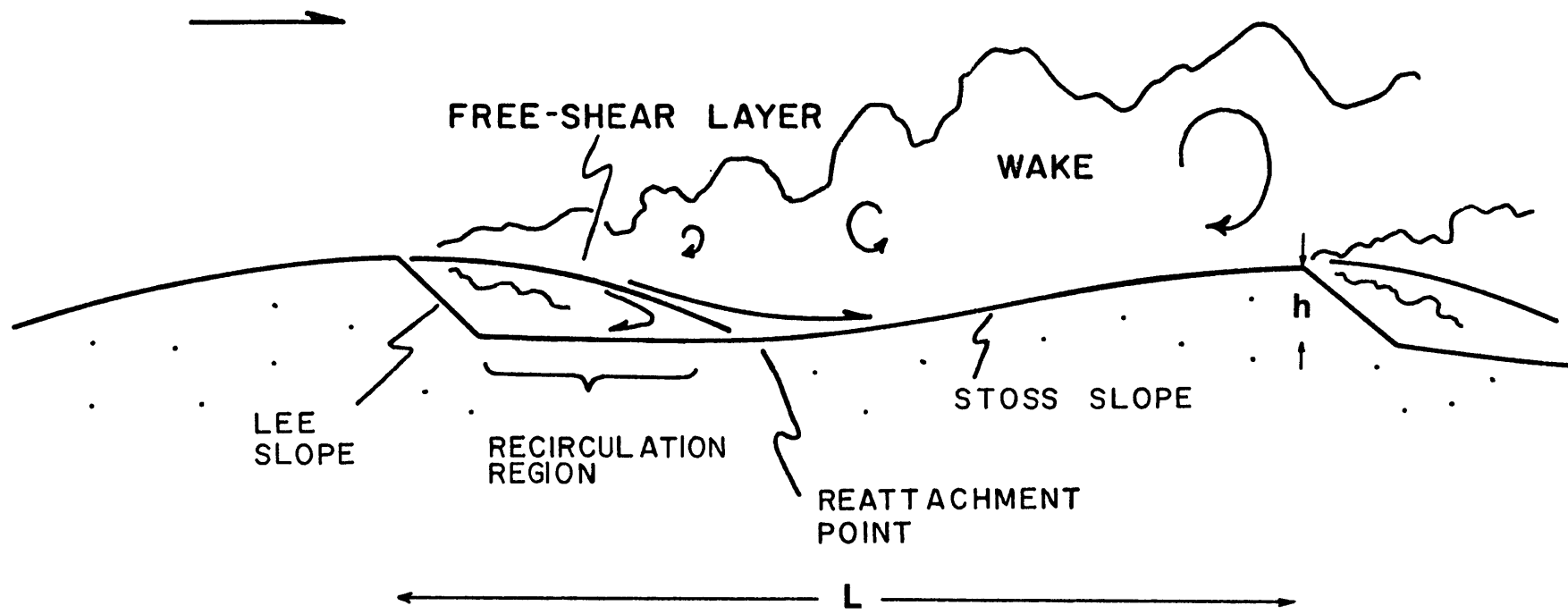


Figure 1.3. General features of a bed form and its associated flow field.

its velocity scale is  $u_*t$  and its length scale is  $z_{ot}$ . These are both integrated scales, characteristic of the bed as a whole. The friction velocity  $u_*t$  is defined implicitly through (1.7); the roughness length  $z_{ot}$  is a function of the geometry of the bed. A few general relations giving  $z_{ot}$  as a function of the size, spacing, and shape of roughness elements have been suggested (Lettau, 1969; Kondo, 1971; Wooding et al., 1973), but none have been shown to be accurate over a wide range of conditions (Yaglom, 1979). The roughness length also plays a role in generalizing the Reynolds-number criterion for fully rough flow given above for uniform, closely packed sand roughness: if  $z_o$  has been determined for a given bed, one can identify an equivalent sand roughness as  $k_s = 30z_{ot}$ . The criterion for fully rough flow is then  $u_*tk_s/\nu > 70$ .

Although a profile scaled with a bottom parameter like  $z_{ot}$  (as opposed to  $D$ ) is generally called an "inner law", for macrorough flow there is a surface layer to which explicit attention must be paid below the integrated logarithmic layer. The terms "inner" and "outer" are confusing in this context and will not be used in this work.

In both rough and macrorough flows, the irregular form of the lower boundary makes it unclear where the plane defined by  $y=0$  (the "zero plane") should be placed. Since the position of the zero plane is uncertain to within the height of the roughness elements, this is a problem only if



measurements are to be made less than a few tens of roughness heights above the bed. Unfortunately, for most laboratory investigations of macrorough flow (including this one) this is necessary because of depth limitations, so the location of the zero plane (the "zero-plane displacement") is important in describing flow in the ILL. There is no universally accepted technique for finding the zero-plane displacement, although commonly it is chosen to optimize agreement between measured data and equation (1.6) (Perry et al., 1969). A theoretical study of the zero-plane displacement done by Jackson (1981) does not yield a straightforward method for its determination. Methods used in this study for fixing the zero plane vary and will be described as they appear.

In deriving the logarithmic law for the velocity profile over smooth and rough beds, recourse was made to an outer or velocity-defect law (1.2) that governs flow between the logarithmic layer and the top of the boundary layer. In principle, there is no reason why there should not be a velocity-defect region over macrorough beds, but investigations so far have not revealed one (O'Loughlin and Annambhotla, 1969; Sadeh et al., 1971; Bayazit, 1976; Smith and McLean, 1977; Nowell and Church, 1979). There is no velocity-defect region in the results reported here, either. The reason for this is presumably to be found in the large values of relative roughness  $h/D$  ( $O(0.1)$  or more) that characterize all of these studies. The development of a

velocity-defect region probably requires that the bed length scale and the overall length scale (roughly  $h$  and  $D$  respectively) be separated by at least two orders of magnitude. In any event, the absence of a velocity-defect region in many examples of macrorough flow is noted but will not be discussed further in this work.

Finally, we return to the skin friction, whose behavior on macrorough beds forms the main theme of this work. Our idea of skin friction must be generalized somewhat. As mentioned above, the form given in (1.7) is valid only when the macrorough boundary is locally smooth, so that the local boundary shear stress is purely viscous. But this need not be the case. If grains are in motion they can exert a tangential force on the bed through collisions; or the sediment may be coarse enough for conditions to be rough even at the smallest scale (imagine that the flat bed with isolated large grains discussed above is made of coarse sand). Skin friction, then, is any local boundary shear stress: it is the time-averaged tangential force on the bed per unit area averaged over an area of a few grain diameters squared; in the limit as the grain size becomes small the definition implied by (1.7) holds. What is considered skin friction evidently depends to some extent on what problem one is interested in. Here, we are ultimately concerned with the transport of uniformly sized sediment, so the skin friction is taken to be the average local stress on the grains

regardless of whether it is purely viscous or includes a small-scale form-drag or grain-impact component. Our concern is to distinguish the skin friction from form drag induced by features larger than the grains themselves. Thus a macrorough bed should be thought of as one that is hydrodynamically rough at any length scale or scales larger than the grain size.

This discussion sets the stage for the work to be described, which consists of investigations of velocity, total bottom stress, and skin friction over beds with two kinds of macroroughness elements: two-dimensional current ripples and crag-and-tail marks. In both cases the bed forms are idealized representations of common natural forms and in both cases the bed is immobile. The intent has been to focus on the variable skin-friction field caused by the macrorough boundary in the absence of additional complications due to sediment transport.

## 1.2. Experimental Methods

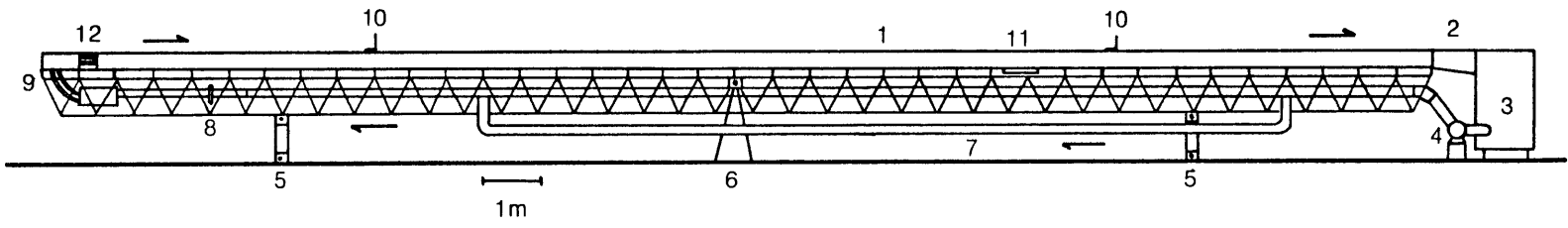
1.21. General. This section describes only principles and methods relevant to both chapters 2 and 3. The properties of macrorough flow whose measurement, intercomparison, and interpretation form the theme of this work are total bottom stress, time-averaged velocity, and skin friction. Equipment and methods used to measure each of these will be discussed in turn.

1.22. The flume. The experiments were done in a recirculating flume whose channel is 20 m long, 0.6 m wide and 0.3 m deep (figure 1.4). The channel can be tilted about its midpoint by means of two coupled sets of screw jacks to maintain uniform flow. Discharge and hence mean velocity were determined to within 3% using a calibrated orifice-plate/manometer system. Two rails running along either side of the channel carry a rolling frame to which instruments can be fastened. Velocity profiles were made using a vertical traversing device mounted on the frame that could be positioned to within 0.05 mm.

The flume was equipped with two point gauges about 12 m apart for measuring water-surface slope, from which total bed shear stress was determined using (1.8). Each point gauge could be read to within 0.05 mm, and the measured differences in height were typically 1 - 5 mm. However, because of turbulent fluctuations in the water surface the overall precision of measurements of slope (and hence of shear stress) is about 5%.

Figure 1.4. The flume in which all the experiments were done.

1. Main channel; the position of the number corresponds to that of the test section where the measurements were made.
2. Hinged expansion section
3. Tail box
4. Pump
5. Screw jacks for adjusting the channel slope
6. Pivot
7. Return pipe
8. Orifice plate, connected to a U-tube manometer to measure discharge
9. Manifold and inlet box
10. Point gauges
11. Square well in which plates could be mounted flush with the channel bed
12. Flow straighteners



When surface-slope measurements in a channel with smooth sidewalls are used to estimate the total bottom stress on a rough bed using (1.8), the estimate is biased by the drag of the sidewalls; (1.8) is strictly valid only for infinitely wide flows. In all the data reported here, this has been corrected for by the method of Vanoni and Brooks (1957), which was found by Knight and MacDonald (1979) to be accurate to within 20% over a wide range of conditions. The magnitude of the correction to the bottom stress is about 20% in the results reported in chapter 2 and 10% for those in chapter 3.

1.23. Thermal anemometry. Thermal anemometers are used to measure fluid motion indirectly by measurement of the rate of transfer of heat to the fluid from a small surface. In this work they have been used to measure both velocity and skin friction. The former is the more common and easily understood application, so I will begin there.

Velocity measurement: hot wires. If an infinitely long cylinder immersed in a moving fluid is heated, it loses heat at a rate that depends on the temperature difference between cylinder and fluid, on the component of the free-stream velocity normal to the cylinder axis, on the dimensions of the cylinder, and on the physical properties of the fluid (figure 1.5; Hinze, 1975, ch. 2; Comte-Bellot, 1976). The latter include viscosity, density, coefficient of thermal expansion, and specific heat. There has been considerable theoretical work on heat transfer from cylinders immersed in moving fluids, beginning with the classic study of King (1914). Hinze (1975) and Comte-Bellot (1976) provide the following semi-empirical formula for the heat transfer:

$$\frac{R_w I^2}{(R_w - R_a)} = A + BU^{0.5} \quad 1.10$$

where  $R_w$  is the resistance of the wire at operating temperature,  $R_a$  its resistance at the ambient (fluid) temperature,  $I$  is the current in the wire,  $U$  is the component of the free-stream velocity normal to the wire, and  $A$  and  $B$  are empirical constants.



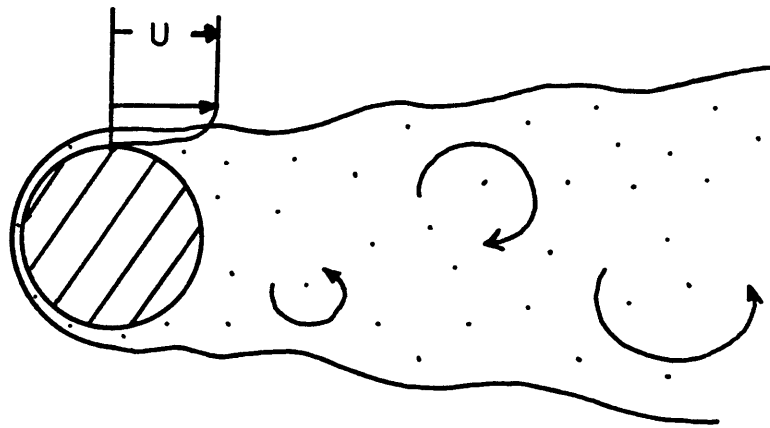


Figure 1.5. Schematic section of flow and the thermal boundary layer (stippled) about a hot wire (cross-hatched).

If  $R_w$  and  $R_a$  are known, (1.9) could in principle be used to relate the current or voltage measured in the cylinder to  $U$ . In practice even semi-empirical relations like (1.9) are not very useful, mainly because of effects arising from the finite length of real hot wires. These induce heat losses to the wire supports and temperature gradients across the wire, neither of which are accounted for in (1.9) (Hinze, 1975, ch. 2; Comte-Bellot, 1976). The result of all this is that hot wires must be calibrated for use. Because the physical properties of the wires themselves change with time and because it is impossible to control experimental conditions completely, it is important that this be done as often as possible.

The calibration of thermal anemometers in the same fluid and at the same temperature (and, if possible, at about the same Reynolds number) at which the measurements are to be made eliminates the need for explicit consideration of the physical properties of the fluid and sensor. Hence we are left with the temperature difference between fluid and sensor and the free-stream velocity as free parameters. The former can be treated in either of two ways. If the current  $I$  in the sensor is kept constant the temperature of the sensor, and hence its resistance, becomes a function only of the velocity. On the other hand, if the temperature of the sensor is kept constant against the fluctuating velocity by a fast feedback system, the applied voltage is uniquely related

to the velocity. The latter arrangement is preferred for most purposes and has been used here: because the wire is kept at constant temperature the response of the system is not limited by thermal lag in the wire (Comte-Bellot, 1976).

The reason for using a wire of finite length is, of course, to permit truly local measurement of the velocity field. On the other hand, if the wire is not many times longer than its diameter it responds to velocity components parallel to its long axis and loses directional sensitivity. The wire transmits heat to the fluid via a thermal boundary layer: a region of heated fluid that diffuses into the surrounding fluid much as vorticity does in the more familiar viscous boundary layer (figure 1.5). The velocity that the wire senses is that at the edge of this boundary layer. If the wire is many times longer than it is thick, the thickness of the wire plus its associated thermal boundary layer is still much less than the length, so the latter may be thought of as the spatial averaging scale for the wire.

Application. Velocity measurements in this study were carried out with commercially available anemometers manufactured by Thermo-Systems Incorporated (TSI). Different sensors were used in each part of the study; they will be discussed in the next two chapters. The electronic measuring and processing units used in the anemometry system are also manufactured by TSI; they are shown schematically in figure 1.6. The sensor forms one leg of a Wheatstone bridge, which

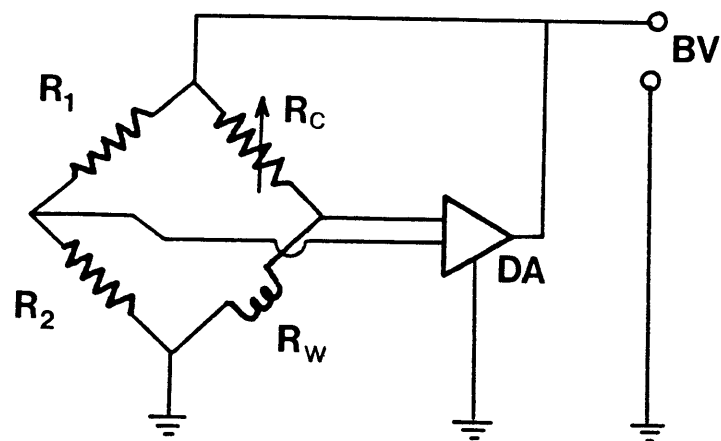


Figure 1.6. Simplified diagram of the circuitry for a constant-temperature thermal anemometer.  $R_1$  and  $R_2$  are fixed bridge resistors,  $R_c$  is a fixed control resistor,  $R_w$  is the heated sensor, DA is a direct-current differential amplifier, and BV is the bridge output voltage.

is kept balanced by a fast amplifier when the sensor is being run. With the amplifier turned off, the bridge can be used to measure the 'cold' (ambient-temperature) resistance of the probe,  $R_a$ , using the variable resistor shown. The operating resistance  $R_w$  is calculated from the overheat ratio  $A_r = R_w/R_a$ , set on the variable resistor and maintained by the amplifier, whose voltage output is read as a measure of the velocity. The overheat ratio is chosen by the investigator. A large  $A_r$  gives a high operating temperature and increases the sensitivity of the system but makes the sensor more susceptible to contamination by material suspended in the water. For the hot wires used in this work  $A_r = 1.05$  was found to be a reasonable compromise.

There are several operating details that must be attended to to ensure optimal performance of the anemometer system. Coaxial cables must be used wherever possible to minimize noise. The cable connected to the sensor must have its impedance compensated for before the ambient-temperature resistance  $R_a$  is measured. The gain and bias of the bridge amplifier must also be adjusted for each sensor to provide maximum frequency response without introducing feedback noise.

Two aspects of the fluid system are especially relevant to the operation of thermal anemometers: temperature stability and suspended material in the water. The temperature must be controlled because it affects the overheat ratio  $A$ , via the

ambient-temperature resistance  $R_a$ . Variation in temperature may be compensated by changing  $R_w$ , but since this is done using a control resistor that cannot be varied continuously, small changes in temperature cannot be precisely corrected for. In addition, it was found that calibrations made at different temperatures at the same overheat ratio did not always agree. Therefore, a copper cooling coil was mounted in the flume tailbox and connected to a source of cold tap water. Before beginning each run, the water temperature was raised to an operating value several degrees above that of the cooling water. The operating temperatures varied between 20.00 °C (winter) and 26.00 °C (summer). By varying the rate of cooling water flow, these temperatures could be maintained to  $\pm 0.05$  °C, as monitored on a mercury thermometer that could be read to  $\pm 0.02$  °C. Temperature control to  $\pm 0.05$  °C has also been recommended by Comte-Bellot (1976).

All the experimental work described here was done in tap water. If there is any material suspended in the water, it collects on the heated sensor and eventually attenuates the bridge signal. The sensing elements were cleaned before every reading was taken, using an artist's paint brush (occasionally dipped in acetone). The water was replaced every few days and was always charged with algicide. Filtering the water through fiberglass was attempted but was found to produce no noticeable improvement and so was not continued.

All the velocity measurements reported here were obtained by reading the time-averaged analog voltage produced by the bridge/amplifier system. The signals were not linearized. The bridge output was fed through an averaging circuit with a 10 s time constant and was read over a period of about two minutes to  $\pm 0.01$  v from a digital voltmeter. The quality of the data was checked by repeating measurements, by recalibrating sensors, and by observing the output voltage at the free surface, where the velocity was measured to  $\pm 3\%$  (standard error) by timing surface floats. Based on these methods, the absolute accuracy of the velocity data is 6%, the relative accuracy of points in successive velocity profiles is 3%, and the relative accuracy of successive points in a profile is 1%, unless otherwise noted.

Calibration. The hot-wire probes were calibrated by placing them in a series of flows of known velocity and measuring the output voltage; this was done in the flume in which data were taken, and at similar Reynolds numbers. Calibration curves and methods for individual experiments will be referred to in the sections dealing with them. Earlier calibrations are simple polynomial fits to the measured points; later it was found that some of the variability between curves could be removed by using the form

$$v - v_0 = Au^B \quad 1.11$$

where  $v$  is the unlinearized bridge output voltage recorded

for mean velocity  $u$  and  $v_0$  is that at  $u=0$  (the free-convection voltage), and  $A$  and  $B$  are empirical constants.

Skin-friction measurement: flush-mounted hot films.

Measurement of skin friction using heated elements mounted flush with the surface is based on the same principles as hot-wire anemometry. For both hot-wire and hot-film sensors the velocity field varies rapidly in the neighborhood of the sensor, because each forms a boundary on which the no-slip condition applies (figures 1.5, 1.7). It is really this boundary layer that controls the rate of heat transfer; in the case of hot wires the boundary layer is controlled by the velocity at its edge for fixed operating conditions, so the anemometer can be calibrated in terms of the velocity without explicit reference to the details of the boundary layer. A similar argument applies to flush-mounted hot films. In this case, however, the boundary layer near the sensor is not imposed by the presence of the sensor, which does not disturb the flow field at all if it is truly flush-mounted and the bed is locally smooth. Rather, the velocity field results from the presence of the wall and is governed by (1.1) since the film presents a locally smooth surface. If the temperature of the fluid is held fixed, the kinematic viscosity  $\nu$  is constant, so the only variable parameter is  $u^*$ ; one can thus obtain a unique calibration relating  $u^*$  to the output voltage. The use of flush-mounted hot films to



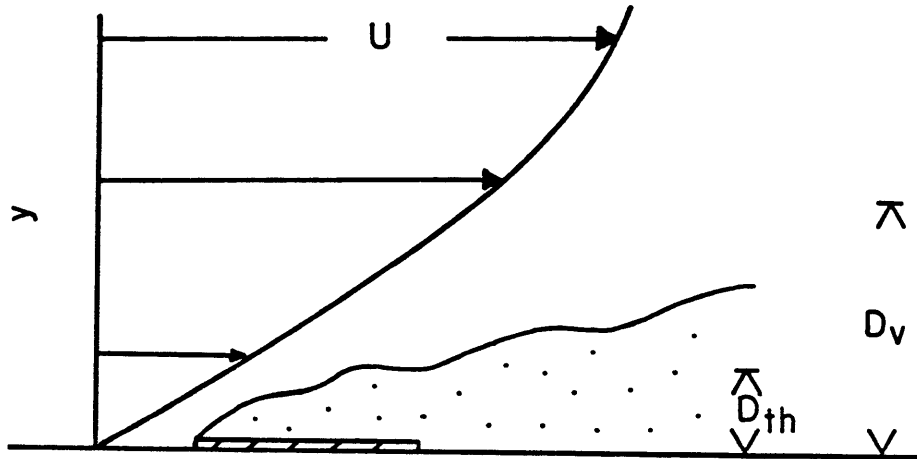


Figure 1.7. Schematic diagram of flow and the thermal boundary layer (stippled) over a flush-mounted hot film (cross-hatched).  $D_{th}$  is the thickness of the thermal boundary layer and  $D_v$  that of the viscous sublayer.

measure skin friction has become a standard practice in turbulence research (Bellhouse and Schultz, 1966; Brown, 1967; Wallace et al., 1976; Blackwelder and Eckelmann, 1977; Sreenivasan and Antonia, 1977; Kreplin and Eckelmann, 1978). Related work has also been done using flush-mounted mass-transfer analogs of hot films (Hanratty et al., 1977; Zilker and Hanratty, 1979).

Ludwig (1950) and Liepmann and Skinner (1954) did early theoretical work on hot-film anemometry; a somewhat more sophisticated treatment is that of Brown (1967). Using dimensional analysis and linearized boundary-layer equations for heat and momentum, these authors obtain a relation analogous to (1.10):

$$\frac{I^2 R_w}{R_w - R_a} = A \tau_o^{1/3} \quad 1.12$$

where A is a constant that depends on the physical properties of the sensor and the fluid.

There is a vertical scale associated with hot films; it is the height of the thermal boundary layer (figure 1.7). This is not an averaging distance but rather defines the region near the wall within which the similarity relation (1.1) must be identical in both calibration and test conditions in order for the calibration to be valid. A formula for the height  $D_{th}$  of the thermal boundary layer has been derived by Ludwig

(1950) using similarity theory; it reads

$$D_{th} = 1.86 \left( \frac{a \mu L}{\tau_{os}} \right)^{1/3} \quad 1.13$$

where  $a$  is the diffusivity of heat of the fluid,  $\mu$  is its dynamic viscosity, and  $L$  is the sensor length.

For a typical  $\tau_{os}$  of 1 dyne/cm<sup>2</sup>,  $D_{th}$  for the hot-film sensors used here is about 0.025 cm. As discussed by Liepmann and Skinner (1954) and Brown (1967), the most important way in which velocity similarity in the thermal boundary layer may be confounded is the presence of a pressure gradient in the test case. The pressure gradient may be used to form a vertical length scale  $L_p$  (Yaglom, 1979):

$$L_p = \frac{\rho u_*^2}{\left( \frac{\partial p}{\partial x} \right)} \quad 1.14$$

The effect of the pressure gradient on the velocity profile is negligible at heights less than  $L_p$  so transference of hot-film calibrations to flows with pressure gradients is valid as long as  $D_{th} < L_p$ . The validity of the skin-friction measurements reported here will be checked using this criterion in the next two chapters.

In theoretical work heat is assumed to be transferred only from the film to the fluid, but in practice a substantial amount may be transferred to the fluid or lost via the substrate (Brown, 1967). As with hot wires, accurate relations between skin friction and voltage can only be

obtained by calibrating the sensors.

Application. Flush-mounted hot films were used in this study in a variety of configurations. In all cases the sensing elements were square films 1.8 mm on a side manufactured by Micromeasurements, Incorporated (Model WTG50A). Their use as skin-friction meters was pioneered by G. Gust. The conducting element itself is not a continuous film but a fine nickel grid embedded in an epoxy film. Typically these devices have a resistance of about 50  $\Omega$  at room temperature, substantially higher than those of common thermal-anemometry probes. The overheat ratio can thus be kept constant against temperature changes with relatively fine sensitivity using a discrete control resistor. The overheat ratio  $A_T$  used was 1.05, resulting in a temperature difference between sensor and fluid of 9 °C.

The quality of the skin-friction data has been checked by recalibrating the sensors, by repeating measurements, and by comparison of the mean skin friction as determined from the sensor and from smooth-flow slope measurements (see next section) during runs. Based on these methods, the absolute error in the measured skin friction is 10%, the relative error among sensors in an array is 5%, and the relative error among data collected sequentially in the same run with the same sensor is 2%.

The frequency response of the skin-friction sensors was determined by G. Gust (personal communication) by using the square-wave test (Freymuth, 1967) to compare their frequency

response with that of a probe for which it had been determined dynamically (Perry and Morrison, 1971). The test indicated that the frequency response of the sensors used here is flat to at least 20 Hz.

Calibration. In this study, skin-friction sensors were calibrated by mounting the sensors in smooth flow at depths of 7-10 cm, measuring the bridge output voltage, and determining the shear stress by measuring the surface slope and using (1.8). For a finite-width flow with smooth sidewalls, the depth in (1.8) must be replaced by the hydraulic radius (the cross-sectional area of the flow divided by the wetted perimeter). The sensor to be calibrated was placed along the centerline of the flume about 12 m downstream of the inlet. The aspect ratio was always at least 6; according to Knight and MacDonald (1979a) this is sufficient to ensure that the skin friction averaged over the wetted perimeter, given by (1.8), is within 5% of that at the centerline. Also, Gust and Southard (in press) made skin-friction transects across the flume used here at an aspect ratio of 6, using a movable hot film, and found variations of less than 2% across the central 0.5 m of the channel.

Individual calibrations will be discussed as the data are presented. They have the form

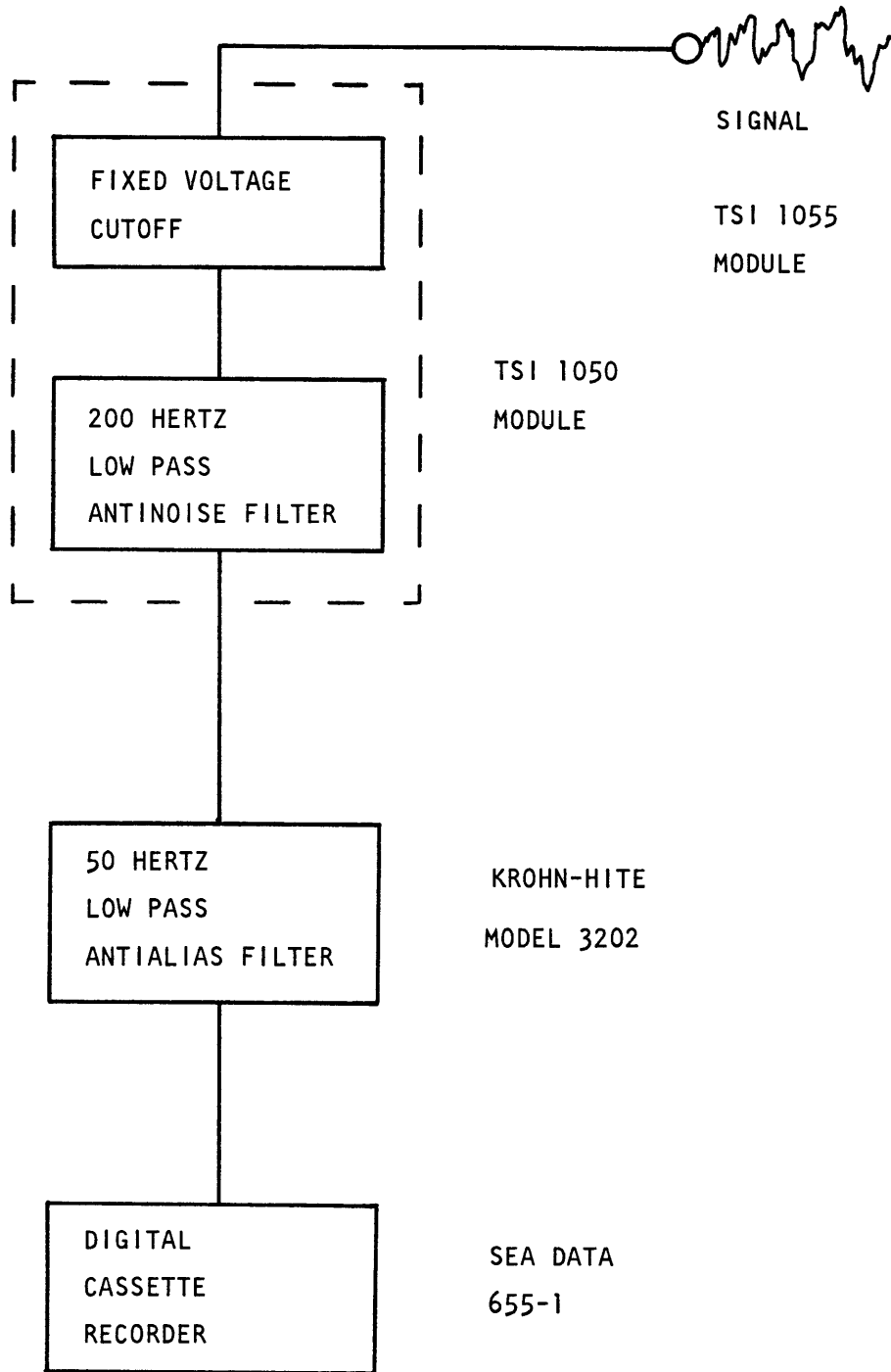
$$v-v_0 = A(\tau_{0S})^B \quad 1.15$$

where A and B are empirical constants.

1.24. Data processing. In this study, recordings were made of skin friction and, to a limited extent, of velocity. Signals were recorded as voltage time series through the chain shown in figure 1.8. A fixed integer voltage was first removed from the signal to bring it within the 5-volt range of the recorder; then it was low-pass filtered at 200 Hz to suppress noise within the anemometer system. When either one or two channels were being recorded, the recorder operated at 128 Hz and the 4-pole anti-alias filter was set at 50 Hz. A few three-channel recordings were also made at 64 Hz and a filter frequency of 25 Hz. Only two such time series were used in this study; they are identified where they appear.

The data recording and processing system used here has been designed and used by Gust (1982a) for marine turbulence research. Recording was done onto tape cassettes using a Sea Data Model 655-1 burst recorder. The recorder has a range of 5 volts and a resolution of 12 bits; files were recorded over the maximum possible duration of 4.3 minutes. The tapes were read and processed using a Sea Data reader linked to a DEC MINC minicomputer at the University of South Florida. First the time series were sorted and transferred to nine-track tape. Then a linear calibration for the A/D converter in the recorder, determined by recording fixed, accurately known ( $\pm 0.01$  v) voltages, was applied to convert the raw data into a voltage time series. The appropriate calibration curve was applied next to obtain the desired velocity or shear-stress time series.

Figure 1.8. The instrument chain used for recording digital data.





Each time series was operated on to provide time-domain and frequency-domain statistics. The former include moments and probability density functions, which were calculated according to standard methods (Otnes and Enochsen, 1972; Tennekes and Lumley, 1972, ch. 6). The latter include only spectra. The data were divided into blocks 2048 words long and the time-domain statistics and spectral estimates were calculated for each block. The calculations were preceded by removal of the mean and first-order trend from the data and, for the spectra, by application of a 10% cosine taper to the ends of each block. The spectral estimates for each block are four-frequency moving averages of the squared fast Fourier transform of the data. The final statistics for each file are averages over all the blocks.

There are two sources of error in the time-domain statistics: the finite length of the records used to estimate them, and errors in calibrating the sensors. If a random signal of bandwidth  $B$  is measured for a time  $t_a$ , the standard error of the estimated standard deviation (rms value) is  $1/\sqrt{Bt_a}$  (Bendat and Piersol, 1966, sec. 5.4.2). The rms skin friction is defined by

$$(\sigma_\tau)^2 = (1/t_a) \int_0^{t_a} (\tau_{os} - \bar{\tau}_{os})^2 dt \quad 1.16$$

where  $t_a$  is an averaging time equal to 4.3 minutes in the present experiments. Taking for the bandwidth the point at which the spectrum is attenuated by 10 dB gives  $B = 5$  Hz (section 2.42) and a contribution to the error of about 3%.

The magnitude of the error from sensor calibration<sup>•</sup> has been estimated as follows. The calibration curve may be taken to be approximately linear over the range of the fluctuations, so the rms skin friction is related to the rms voltage  $\sigma_v$  by  $\sigma_\tau = (d\tau/dv)\sigma_v$ . For a typical calibration curve (nine points,  $r^2 = 0.97$ ), the standard error of the slope  $d\tau/dv$  (Wonnacott and Wonnacott, 1972, ch. 12), and hence of  $\sigma_\tau$ , is 7%. Adding the two contributions, the overall error in the rms skin friction is about 10%. The overall error in the  $n^{\text{th}}$  skin-friction moment is about 10n%.

Confidence intervals for the spectral estimates  $\phi$  have the endpoints A,B where (Otnes and Enochsen, 1972, section 5.3):

$$A = N\phi/\chi^2_{N;\alpha/2} \text{ and } B = N\phi/\chi^2_{N;1-\alpha/2} \quad 1.17$$

where N is the number of degrees of freedom in the spectral estimate (between 84 and 90 for the data reported here),  $\chi^2$  is a point of the chi-squared distribution, and  $\alpha = 1-p$  where p is the significance level (always taken as 0.95).

## 2. Flow and skin friction over two-dimensional current ripples.

2.1. Introduction. Current ripples form under a wide range of conditions where water flows over fine sandy surfaces, and their cross-laminated remains are common enough in the sedimentary record to have attracted the attention of geologists for over a hundred years. Natural current ripples are three-dimensional in plan form under most if not all circumstances (Allen, 1969; Harms, 1969; Banks and Collinson, 1975; Allen, 1977). However, in many cases their crests cross the flow steeply enough that their lee eddies are closed (Allen, 1968, ch. 7), so two-dimensional forms are a natural first approximation that includes the essential features of separation and reattachment at a level of complexity far below that of natural beds.

A number of workers have studied flow over current ripples in the laboratory. Vanoni and Hwang (1967) immobilized fully developed rippled beds using a plastic spray. They measured the overall resistance properties of the ripple fields and made velocity profiles with a Pitot tube. Because of the large size of the tube (3.2 mm) they were unable to make detailed measurements near the bed, nor were they able to measure the skin friction. The main conclusion drawn from their velocity profiles was that the velocity responds more strongly to the topography near the bed than it does farther away.

Znamenskaya (1967) studied the flow field over ripples by filming tracer particles. She divided the flow field into three parts: (1) the stable recirculation eddy, (2) a thin zone of high shear on the stoss slope, and (3) a "transit zone" above the first two where the streamlines are sinusoidal.

McQuorquodale and Giratella (1973) studied the flow field over stabilized natural ripples and idealized, two-dimensional ripples of triangular section, using hot-wire and Pitot-tube anemometry. They found no significant differences between the two types of bed under the same flow conditions. They also compared streamwise profiles of turbulent and mean velocities made at thirteen bed-form heights and less than one height above the bed forms. The former show almost no variability; the latter, not surprisingly, vary considerably. The ripples used were rather small (6 cm long and 5 mm high), so it was impossible to obtain detailed velocity profiles on the stoss slope below crest level. There were no skin-friction measurements.

Raudkivi (1963, 1966) presents the most detailed set of laboratory measurements that has yet appeared, including Reynolds shear stress, two components of turbulence intensity, mean velocity, skin friction, and pressure over an isolated bed form 38 cm long and 2.9 cm high (a small dune). The turbulence quantities were measured with hot-film anemometers, the mean velocity and skin friction with Pitot and Preston tubes respectively. The data show strikingly the

strong effect of the wake on the flow near the bed: it manifests itself as a bulge in profiles of all turbulence quantities that relaxes going downstream from the crest. The mean velocity does not show a clear wake signature, but there is a region of strong shear about at crest level that also relaxes downstream. Streamwise variability in the mean velocity appears to be negligible by about one bed-form height above the crest. The skin-friction data show substantial scatter but clearly increase monotonically from reattachment to the crest. Unfortunately, the velocity profiles, taken with a Pitot tube, are not sufficiently detailed near the bed to determine how the profile there is related to  $u_*s$ .

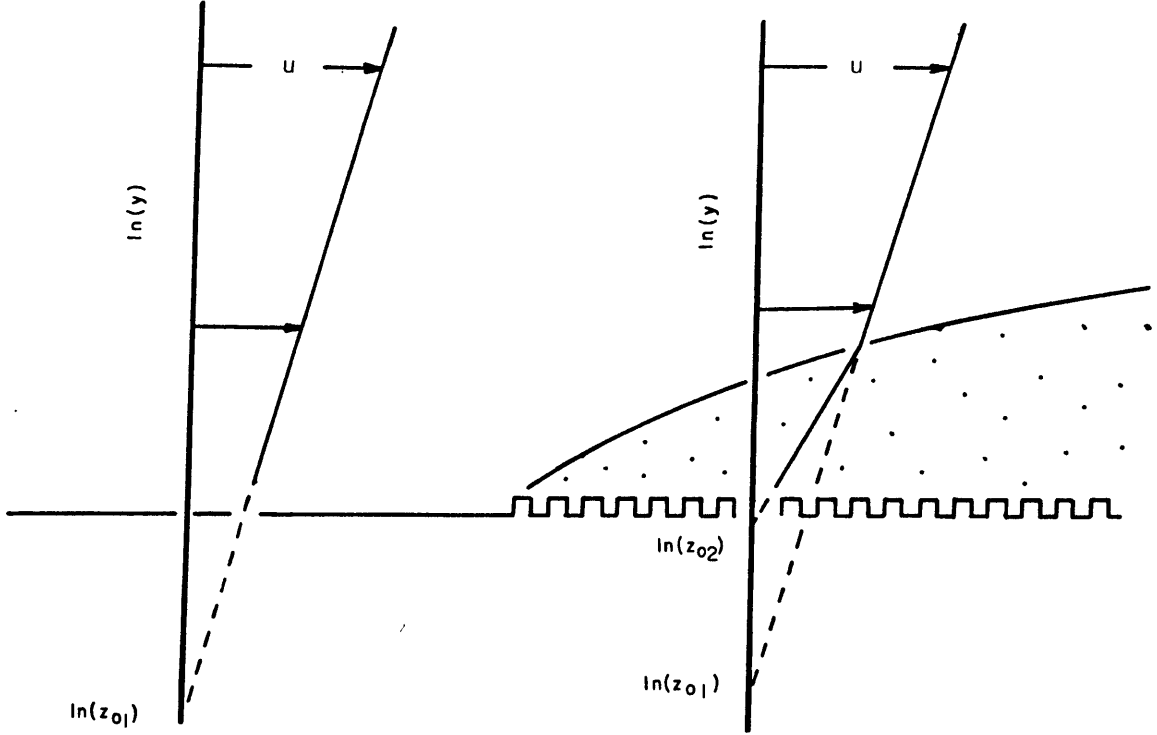
None of the data sets obtained over current ripples provides a detailed account of the variation of skin friction over the bed together with the near-bed velocity field associated with it. As a result, it is not surprising that in none of the above studies is there any attempt at modelling flow near the bed, despite its fundamental importance to bed-form dynamics. The most sophisticated approach to this problem so far is that of Smith and McLean (1977). They obtained data over sand waves in the Columbia River, measuring mean and turbulent velocity fields, and, to a limited extent, skin friction. Their results are presented in terms of a flow-field model that requires an understanding of the "boundary layers within boundary layers" known as

internal boundary layers (IBLs). We will examine these in some detail before considering their application to bed forms.

2.11. Internal boundary layers. When a developed boundary layer encounters a change in bottom roughness, the response takes the form of an internal boundary layer that adjusts to the new roughness and grows into the old boundary layer much as a classical boundary layer grows on a flat plate (Elliot, 1958; Townsend, 1965a,b; Rao et al., 1974; figure 2.1). It is natural to ask how closely IBLs resemble their more familiar counterparts. In an early attempt to describe the behavior of IBLs, Elliot (1958) suggested that the boundary layer downstream of transition could be divided into two parts: in the lower part (the IBL) the velocity profile is given by (1.6) scaled with  $u_*2$  and  $z_{o2}$ , representing respectively the total bottom shear stress and roughness length of the downstream surface. The upper part preserves flow in equilibrium with former conditions; the velocity is again given by (1.6) but scaled with  $u_*1$  and  $z_{o1}$ , both characteristic of the upstream surface.

This point of view implies that the entire region affected by the new surface is in equilibrium with it, and that the shear stress changes discontinuously from  $\rho(u_*2)^2$  to  $\rho(u_*1)^2$  at the top of the IBL. More sophisticated approaches have been devised by a number of investigators, of which the most extensively developed is due largely to Townsend (1965a,b; 1966). He showed that conditions for self-preserving flow

Figure 2.1. Simplified diagram of an internal boundary layer (stippled) developing at a smooth-to-rough transition ( $z_{o2} > z_{o1}$ ), after Elliot (1958).





(of which Elliot's postulated field is a special case) in an IBL would be met for a wide range of roughness changes, but his calculated velocity profiles show a region governed by (1.6) scaled with  $u_*^2$  and  $z_{o2}$  (an equilibrium region) only in the lowermost part of the IBL. An extensive set of field measurements by Bradley (1968) supports this view of the velocity field, as does a second-order numerical solution calculated by Rao et al. (1974). Rao et al. explicitly resolved the thickness of the equilibrium region within the IBL and found it to be of the order of 0.1 times the total thickness.

The top of an IBL may be defined as the point where the velocities in the IBL and the preexisting boundary layer match, leading to a relation for the height of the IBL in terms of distance downstream of transition and the roughness lengths of the two surfaces. Despite the fact that Elliot's (1958) calculation of the IBL height is based on an inaccurate description of the velocity field, his results for the height have been supported by subsequent workers (Bradley, 1968; Rao et al., 1974): extension of (1.6) through the entire IBL gives a good estimate of its thickness although not of its velocity distribution. For both smooth-to-rough and rough-to-smooth transitions, the growth of the IBL height  $D_i$  is proportional to  $x^{0.8}$ , where  $x$  is distance downstream of the transition, and is bounded by

$$D_i < 0.1x$$

2.1

The growth of the equilibrium layer depends on the sense of the transition, occurring more slowly if it is rough-to-smooth than the reverse. In the former case the lowermost 5% of the IBL is in equilibrium, so the logarithmic sublayer grows as

$$D_{ln} < x/200 \quad 2.2$$

2.12. Application of IBL theory to flow over macrorough beds. Arya (1975) has used IBL theory to describe the boundary layer developed over regular arrays of two-dimensional or three-dimensional bluff obstacles (obstacles that induce flow separation) on flat surfaces. His model applies when the elements are sufficiently far apart that reattachment occurs on the intervening flat surface. It is assumed that an IBL begins to grow near reattachment; this may be thought of as an extreme case of a rough-smooth transition. Above the IBL is a region influenced by the wake of the roughness element immediately upstream and then an integrated logarithmic layer (ILL) as described in section 1.1. Arya assumes that within the entire IBL the velocity profile is given by (1.6) scaled with  $u_*s$  and  $z_{0s}$ , the latter being the roughness length of the surface between the macroroughness elements. In this respect his theory follows that of Elliot (1958). If the surface is smooth,  $z_{0s}$  may be written as  $0.14\nu/u_*$  to make (1.6) equivalent to (1.3).

An IBL developed between roughness elements is an example of a surface layer whose velocity field is locally determined

by the skin friction, a possibility raised in section 1.1. A surface layer in which the velocity field is given by (1.6) in appropriate local form will be called an equilibrium surface layer (ESL).

Arya goes on to assume that the wake of the roughness element immediately upstream has relaxed sufficiently that it can be ignored and the IBL velocity profile matched directly to the integrated logarithmic layer to complete the description of the velocity field. By assuming that the IBL develops at the same rate as it does under a change in bed roughness, this matching scheme can also be used to calculate the skin-friction field. By ignoring the wake the range of applicability of the analysis is restricted to beds on which the roughness elements are far apart (at least a few tens of element heights); otherwise the flow may still be distorted substantially from its equilibrium form by the time the next roughness element reseparates it.

Smith and McLean (1977) modelled the flow over sand waves in the Columbia River in similar terms. The bed forms had spacings  $L$  of 60-100 m and heights  $h$  of 1-3 m, so their aspect ratio ( $L/h$ ) was about 50. Unlike the idealized situation considered by Arya (1975), flow separation did not always occur over the sand waves. Whether it did or not, an IBL was presumed to develop over essentially the whole length of the bed form (figure 2.2). As in Arya's model, the equilibrium profile (1.6) was taken to be valid throughout

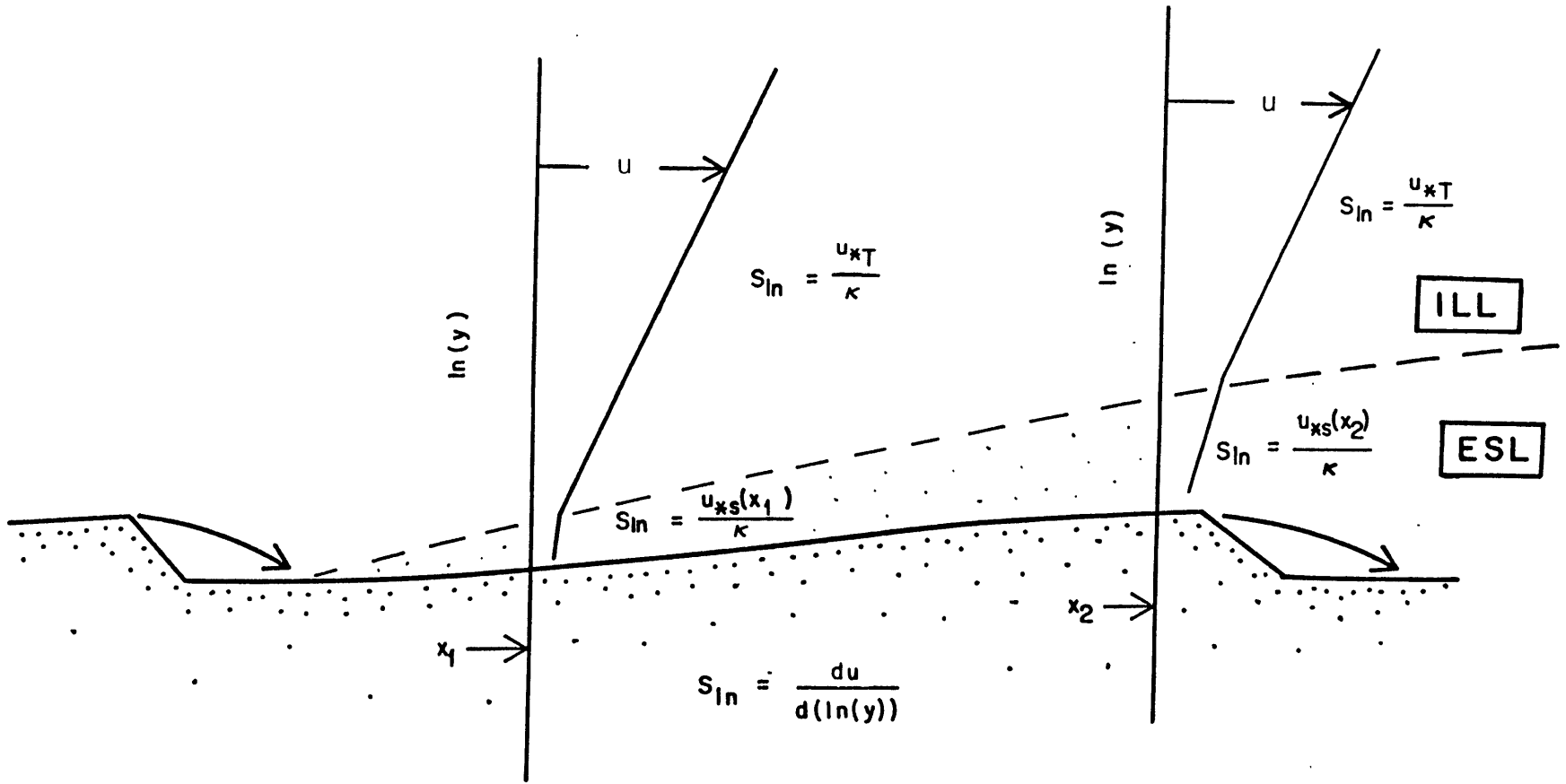
the IBL and was matched to the integrated logarithmic layer at the average height of the IBL. Smith and McLean concentrated on describing the flow field averaged over one bed-form wavelength. Thus although their model involves a local description of the flow field, embodied in (1.6) scaled with  $z_{os}$  and  $u_*s$ , it is compared with data only on a spatially averaged basis. The data include all mean-velocity and Reynolds-stress components, all measured using ducted-propeller current meters that the authors claim have a frequency response of 5 Hz. The velocity measurements were made to within 3 cm (of the order of 0.01 bed-form height) of the bed. There are also some Preston-tube skin-friction measurements.

The spatially averaged velocity profile that results from the models of Arya (1975) and Smith and McLean (1977) has a distinctive form. The velocity profile in the integrated logarithmic layer is given by (1.6) scaled by spatially averaged quantities ( $u_*t$  and  $z_{ot}$ ), so spatial averaging leaves it unchanged. For the ESL, the velocity profile given by (1.6) depends on  $x$  only parametrically, via  $u_*s$ . Denoting the spatial average by angle brackets so that  $\langle a \rangle = (1/\lambda) \int_0^\lambda a dx$ , we obtain in the equilibrium surface layer

$$\frac{\langle u \rangle}{\langle u_*s \rangle} = \frac{1}{\kappa} \ln \left( \frac{y}{z_{os}} \right) \quad 2.3$$

Since  $u_*t$  includes both  $\langle u_*s \rangle$  and  $u_*f$ , it is larger than  $\langle u_*s \rangle$  and the logarithmic slope  $du/d(\ln(y))$  is greater in the

Figure 2.2. An internal boundary layer model for the velocity field over bed forms of large aspect ratio ( $O(100)$ ), after Smith and McLean (1977). The IBL is stippled; within it the semilogarithmic slope  $du/d(\ln(y))$  increases linearly with  $u_*s$  going from reattachment to the crest.



integrated region than in the surface layer. Qualitatively, the spatially averaged velocity profiles look as shown in figure 2.3, with a characteristic kink at about one bed-form height reflecting the transition from the ESL to the ILL. This is an idealized general form expected for velocity profiles on macrorough beds. The data of Smith and McLean (1977) show it clearly, as do those of Nowell and Church (1979), O'Loughlin and Annambhotla (1969) and Raupach et al. (1980). Although the measurements behave approximately as shown in figure 2.3, they generally show a transition between the equilibrium surface and integrated layers, rather than a sharp break. This reflects the influence of the wake as well as the limited extent of the IBL to which (1.6) may be rigorously applied (section 2.11).

The idea of the two-part logarithmic profile shown in figure 2.3 has also been applied to the interpretation of field measurements. A two-part profile observed in the deep sea has been seen by Chriss and Caldwell (1982) as evidence for an undetected bed form upstream of their sensor array. The general ubiquity of macrorough beds in nature and the two-part profile form led Gust (1982b) to caution against attempting to infer skin friction and sediment transport from logarithmic profiles measured far above natural boundaries.

Several questions come to mind in connection with the view developed so far of the boundary layer over bed forms. First, although the Smith-McLean model describes the local form of the near-bed velocity profile, the model is compared with

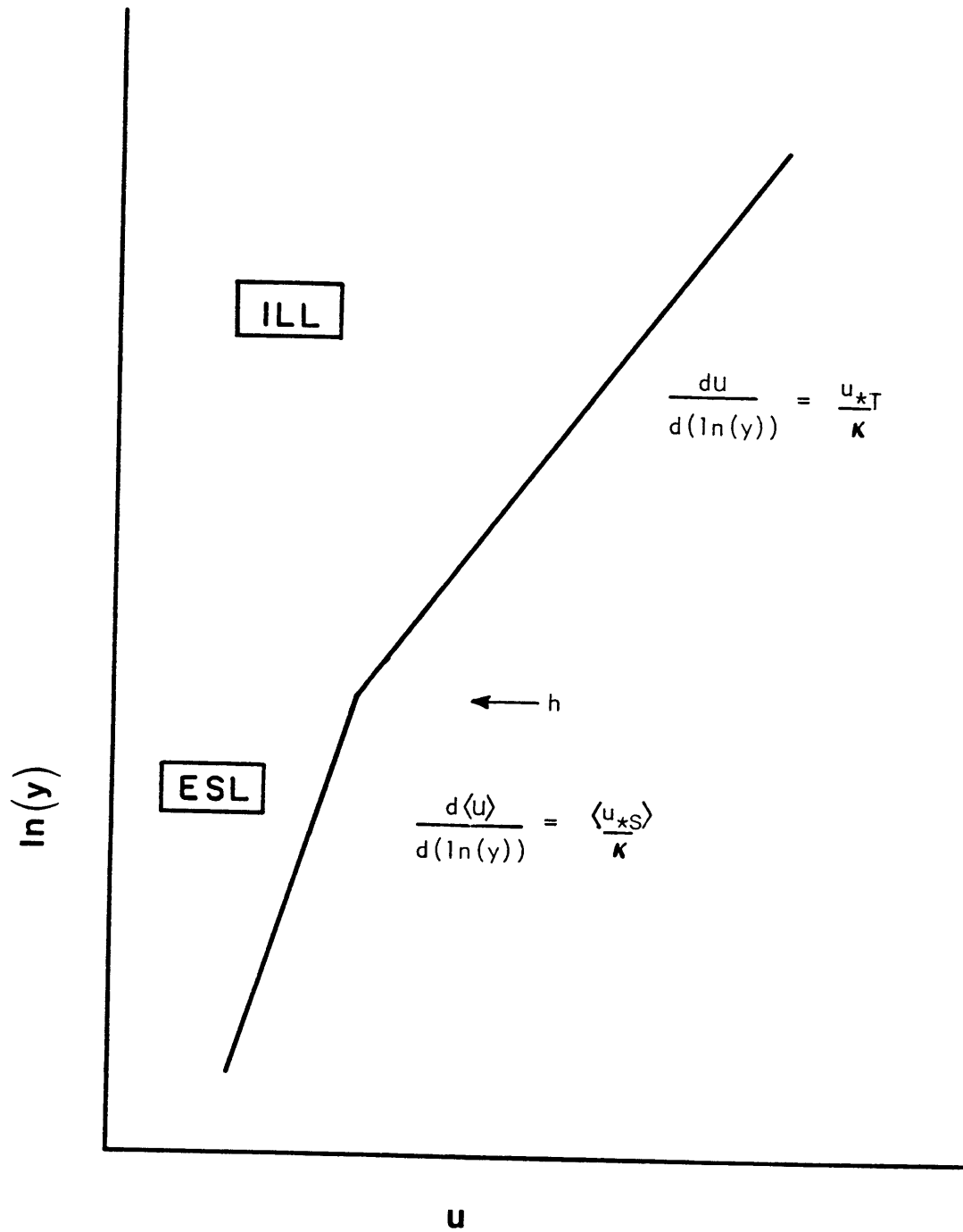
data only on a spatially averaged basis; it is natural to wonder how well it works for individual profiles. Second, the model involves extrapolation of (1.6) throughout the boundary layer, effectively ignoring the wake. As I mentioned in connection with Arya's (1975) model, this requires that the spacing of the macroroughness elements be large compared with their height; applied to bed forms it means that their aspect ratio must be large.

This brings us to an important point, for there are three other respects in which the aspect ratio may be important in determining the way the boundary layer develops over bed forms. First, the relations for the rate of IBL growth used by both Smith and McLean (1977) and Arya (1975) to find the skin-friction distribution were developed for IBLs developing in the absence of strong external pressure gradients. In Arya's idealized roughness field this condition is met because the area between macroroughness elements is flat, but this is not true on bed forms. By continuity the flow accelerates up their backs, so there must be a concomitant pressure decrease. Qualitatively one would expect the magnitude of the pressure gradient to increase with the slope, and hence inversely with the aspect ratio, so the pressure gradient should become increasingly important as the aspect ratio decreases.

The second reason for including aspect ratio in the analysis is related to the rate of growth of the IBL. As discussed in section 2.11, the equilibrium region of an IBL



Figure 2.3. The idealized two-part semilogarithmic form of the spatially averaged mean-velocity profile in macrorough flows possessing an equilibrium surface layer.



grows no more rapidly than about  $D_{1n} = x/200$ . So the thickness of the equilibrium surface layer at the crest compared with the bed-form height is bounded by

$$D_{1n}/h < L/200h \quad 2.4$$

$D_{1n}/h$  goes directly as the aspect ratio; if  $L/h$  is of order 10,  $D_{1n} \ll h$ . Based on observations such as those of Nowell and Church (1979), Raudkivi (1963, 1966), and Vanoni and Hwang (1967), and for the physical reasons outlined in section 1.1, the integrated logarithmic layer does not extend below about  $lh$  above the crest. So if  $D_{1n} \ll h$ , there must be another layer between the equilibrium surface layer and the integrated logarithmic layer. One would expect such a layer to be strongly influenced by the wake.

The third reason for considering the influence of aspect ratio on bed-form dynamics is also closely connected with possible effects of the wake. Wakes, as mentioned earlier, are sites of vigorous generation of turbulence (this is because of strong shear between the rapidly moving free-stream fluid and the slowly moving fluid stranded by the obstacle), so the reattachment region where the wake plays on the bed may be expected to be an area of large fluctuating skin friction. Sediment transport is known to be a nonlinear function of mean shear stress under turbulent uniform conditions; if this is true instantaneously as well, such fluctuations may dominate sediment transport in the reattachment region. The reattachment distance is a fixed, small number of obstacle heights downstream of the obstacle

(about 7.5 when it occurs on a horizontal surface: Eaton and Johnston, 1981), so the relative fraction of the bed form influenced by the wake increases with decreasing aspect ratio. In computing the sediment-transport pattern from only the mean skin-friction field, as was done in Smith and McLean (1977), for example, the possible effects of such fluctuations are ignored; it is not clear at present under what conditions this is acceptable.

How variable are the aspect ratios of natural bed forms? The bed forms studied by Smith and McLean (1977) are in the range commonly cited for sand waves: about 20 to 200 (Dalrymple et al., 1978). The smaller two-dimensional dunes have aspect ratios of the same order (Costello, 1974). Three-dimensional dunes, however, show less scatter and a smaller mean value of about 15 (Costello, 1974). Current ripples show the smallest and the least variable aspect ratio of the unidirectional bed forms: about 10 (Costello, 1974).

Over bed forms of large aspect ratio, then, there is good reason to expect the surface layer to be in equilibrium. But as the aspect ratio decreases, the effects of wakes and pressure gradients associated with the bed forms may change this picture significantly. The experiments described in this chapter have been designed to measure the mean skin-friction and velocity fields over bed forms of small aspect ratio, concentrating on the surface layer, to determine whether there is an ESL present or not. They have also been designed to provide basic data on the fluctuating

skin-friction field in order that its importance to sediment transport may be evaluated. The bed forms were two-dimensional, immobile current ripples; the measurements include the mean velocity to within 1 - 3.5 mm of the bed at three streamwise locations, and the mean and fluctuating skin friction at four streamwise locations. Experimental methods are described in the next section, followed by sections on mean fields and the fluctuating skin-friction field, and finally by a discussion of the implications of the results.

## 2.2. Experimental Methods.

All the experiments were carried out in the 20 m flume shown in figure 1.4. General experimental conditions are given in Table 2.1.

The bed. Construction of the rippled bed was begun by smoothing a bed of fine quartz sand (mean size 0.2 mm) about 10 cm thick using a plastic blade mounted on the rolling carriage (section 1.22). Then a similar blade mounted normal to the channel axis was used to make defects 1 cm long and a few millimeters deep spaced every 10 cm along the length of the channel. This spacing is typical of ripples in fine sands (Costello, 1974). The bed was then exposed to a weak flow (about 15 cm/s) at a water depth of 10 cm for several hours until the entire exposed surface had been shaped by the flow; during this time the developing two-dimensional bed forms migrated about half a wavelength and their height increased to approximately 1 cm, giving them a typical ripple aspect ratio of about 10 (Costello, 1974). The development of the bed was stopped when random small disturbances began to appear in the crest lines. These irregularities affected no more than a fraction of a percent of the bed; otherwise the ripples were extremely two-dimensional, with spanwise variations in height and spacing of only a few percent.

The water was then carefully drained and the bed allowed to dry until the surface was damp but free of standing water. It was dusted with 1-3 mm of sieved concrete made with sand identical to that in the bed; the concrete was sprayed with

<u>R*</u>	<u>D</u>	<u><math>\bar{u}</math></u>	<u>R</u>	<u><math>\tau_{ot}</math></u>
150	10.64 (cm)	15.1 (cm/s)	16,100	2.08 (dynes/cm <sup>2</sup> )
184	10.50	19.7	20,700	3.13
236	10.00	23.3	23,300	5.14
259	10.56	28.4	30,000	6.20
313	10.39	32.9	34,200	9.02

Table 2.1. General experimental conditions for runs over two-dimensional ripples.

water mist from an atomizer and allowed to harden. The resulting surface was reasonably strong and no rougher than the sand mixed into it.

Velocity measurement. One of the major objectives of this part of the study was to determine the relationship between skin friction and flow in the surface layer. This required detailed velocity measurements within one crest height (1 cm) of the bed, so a small hot-wire sensor especially designed for near-wall studies (TSI 1218 20W) was selected for use (figure 2.4). The sensing element comprises a substrate on which a platinum film is deposited and an outer quartz coating for work in water; the element is 1 mm long and 50  $\mu\text{m}$  in diameter. At an overheat ratio of 1.05 the wire is 19  $^{\circ}\text{C}$  warmer than the fluid. These sensors are particularly susceptible to calibration drift, presumably due to contamination by debris in the water as well as wire aging and strain (Perry and Abell, 1975; Gust, 1982a). Because it was considered essential to obtain reliable absolute values for the mean velocities, the probes were calibrated on the day of each run. The output voltage was measured at three different surface velocities (figure 2.5), corresponding to three different discharges. The velocity was measured by timing a float on the water surface to a precision of about 3% (standard error). The final discharge, intermediate in magnitude among the three, was that at which the run was to be made. At the end of each profile, the sensor was raised to the surface to check that no drift had occurred, to within



Figure 2.4. The TSI hot-wire sensor used to measure velocity in the two-dimensional ripple experiment. The heavy grid lines have a spacing of 1 cm.

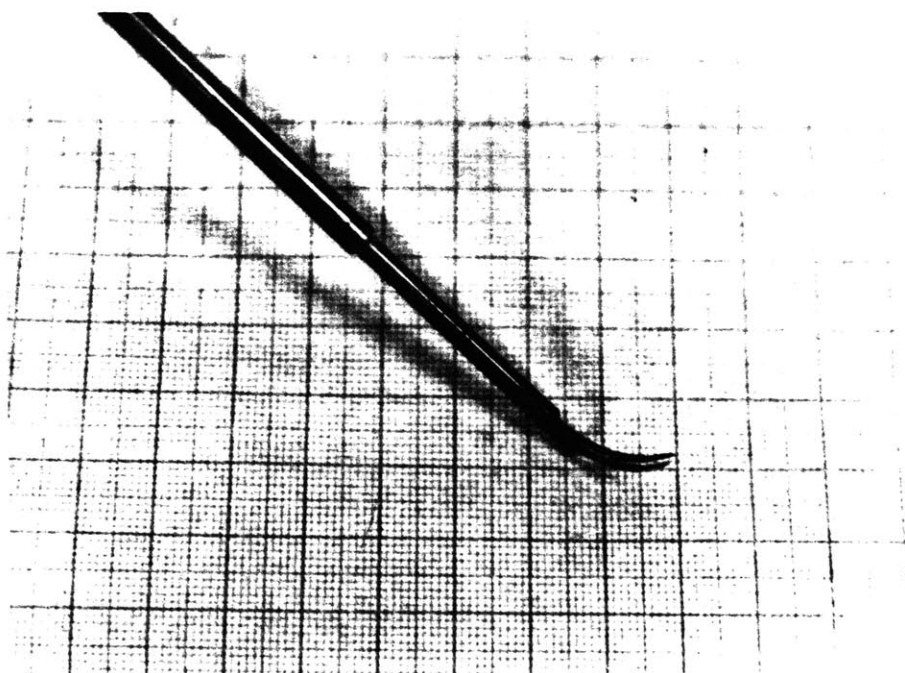
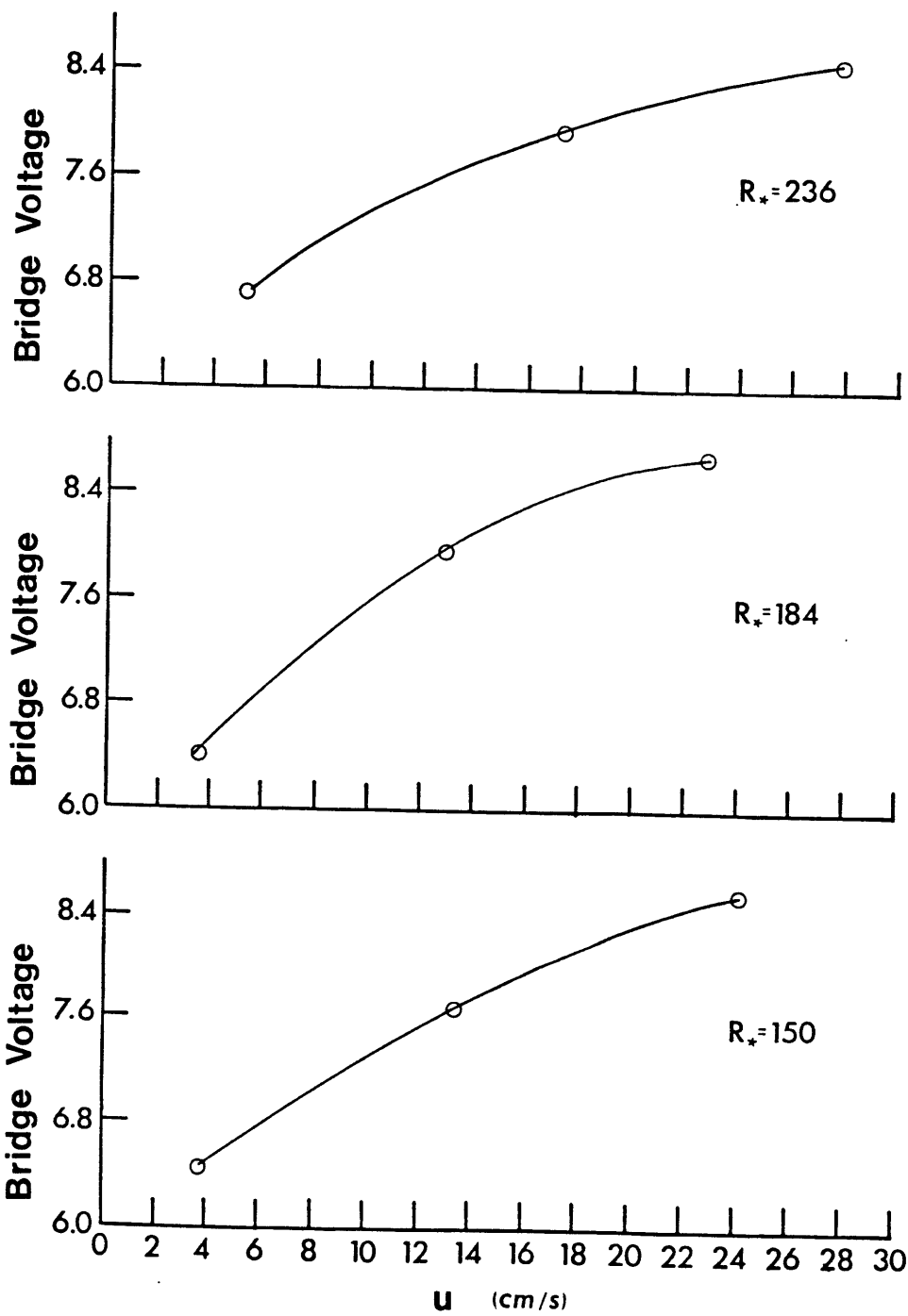


Figure 2.5. Hot-wire calibration curves for each of the three runs in which velocity measurements were made.



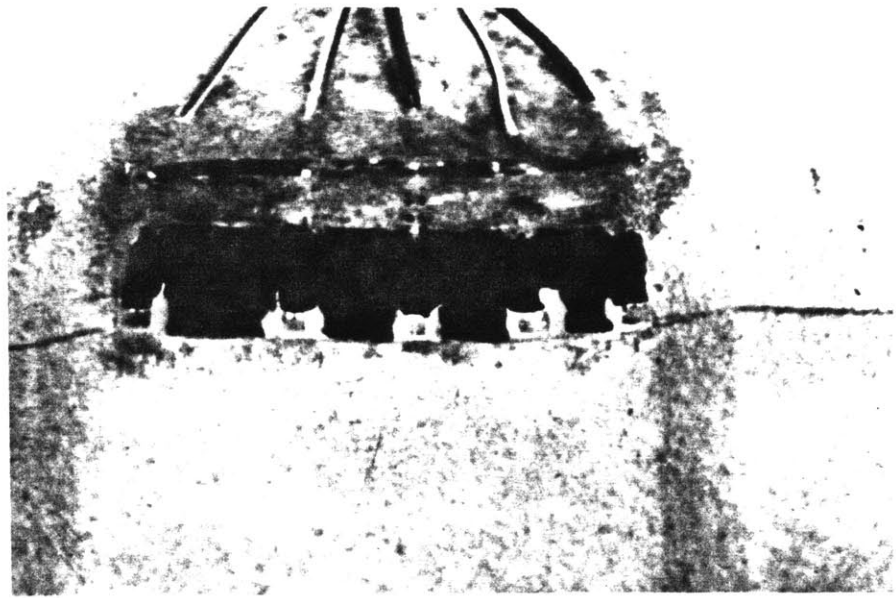
the error margin of 3% for these experiments.

The skin-friction array. A linear array of five flush-mounted skin-friction sensors (Micromeasurements Corp. WTG 50A) was built for the experiments (figure 2.6). The sensors were mounted on a flexible substrate of rubber backed with a thin aluminum strip. The five sensors were calibrated in the flume before the ripples were made by mounting the array in a metal plate. After the ripples had been immobilized, a slot to accept the array was cut in the stoss side of a test ripple, the array was bent to shape and fitted, and the edges were smoothed with cement. It was discovered after the array was in place that sensor 4 (at reattachment) had failed, so no data were obtained from it. After the experiment was completed, the array was removed, the bed was broken up and removed, and the sand was removed from the flume. The array was recalibrated in the flat metal plate. The pre-experimental and post-experimental calibrations are shown in figure 2.7. Sensors 1, 2, and 5 recalibrated well but sensor 3 suffered drift during its ten months under water. From observations of zero-flow voltages and repeated measurements, the drift appears to have been roughly linear with time, so this approximation was used to correct the data from sensor 3. The mean data were not affected, since they were taken soon after emplacement of the array, and the effect on the fluctuations is not great because only the coefficient and not the exponent in the power-law calibration curve changed (figure 2.7).

It was necessary to check that the curvature of the substrate needed to fit the array into the ripple did not affect the calibration of the sensors. Accordingly a single sensor was made up like those in the array and calibrated in the flow near the free surface (that is, as a velocity sensor) mounted both on a flat plate and on a pipe whose radius of curvature was smaller than any encountered in the ripple. The axis of the pipe was mounted parallel to the flow so that the sensor would not be affected by the pressure gradient induced by curvature in the direction of flow. The resulting calibrations proved to be identical (figure 2.8).

As discussed in section 1.23, the use of constant-pressure calibrations for flush-mounted hot films is valid in flows with pressure gradients as long as  $D_{th} < L_p$ , where  $D_{th}$  is the thickness of the thermal boundary layer on the sensors (0.025 cm) and  $L_p$  is the pressure-gradient length scale. The latter has been estimated using the results of section 2.32; its minimum value is 0.05 cm for all the runs discussed in this chapter. Hence the condition  $D_{th} < L_p$  is satisfied and the calibration procedure is valid.

Figure 2.6. (A) Photograph and (B) section of the hot-film array used to measure skin friction in the two-dimensional ripple experiment.



A



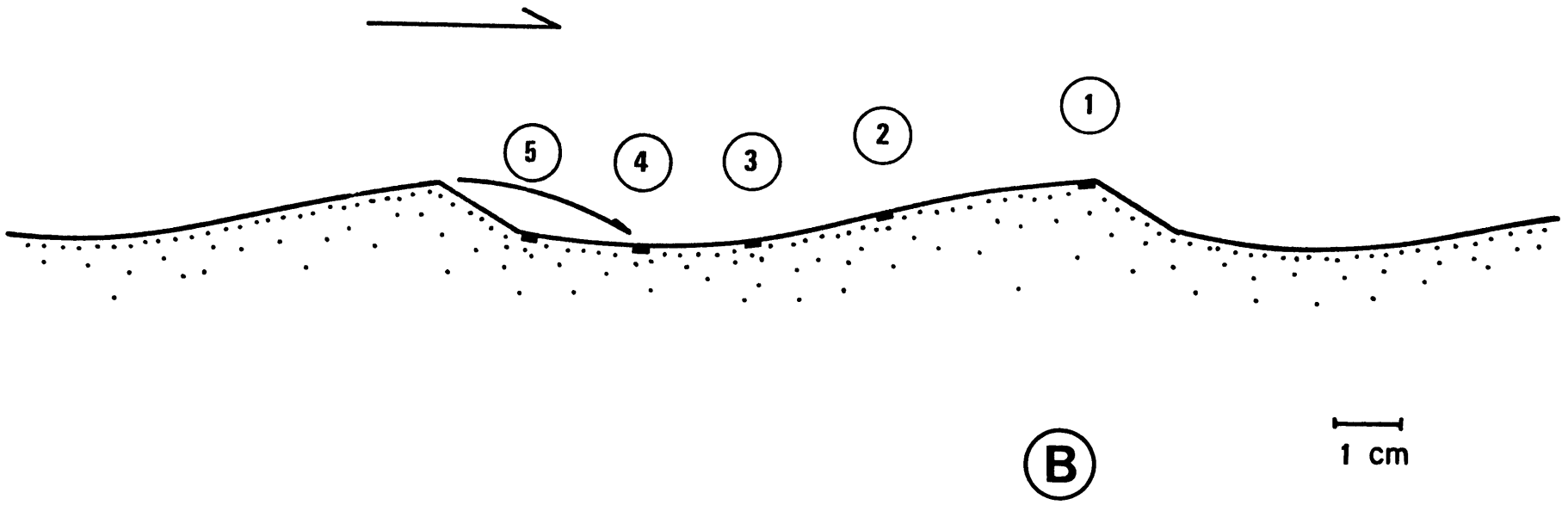
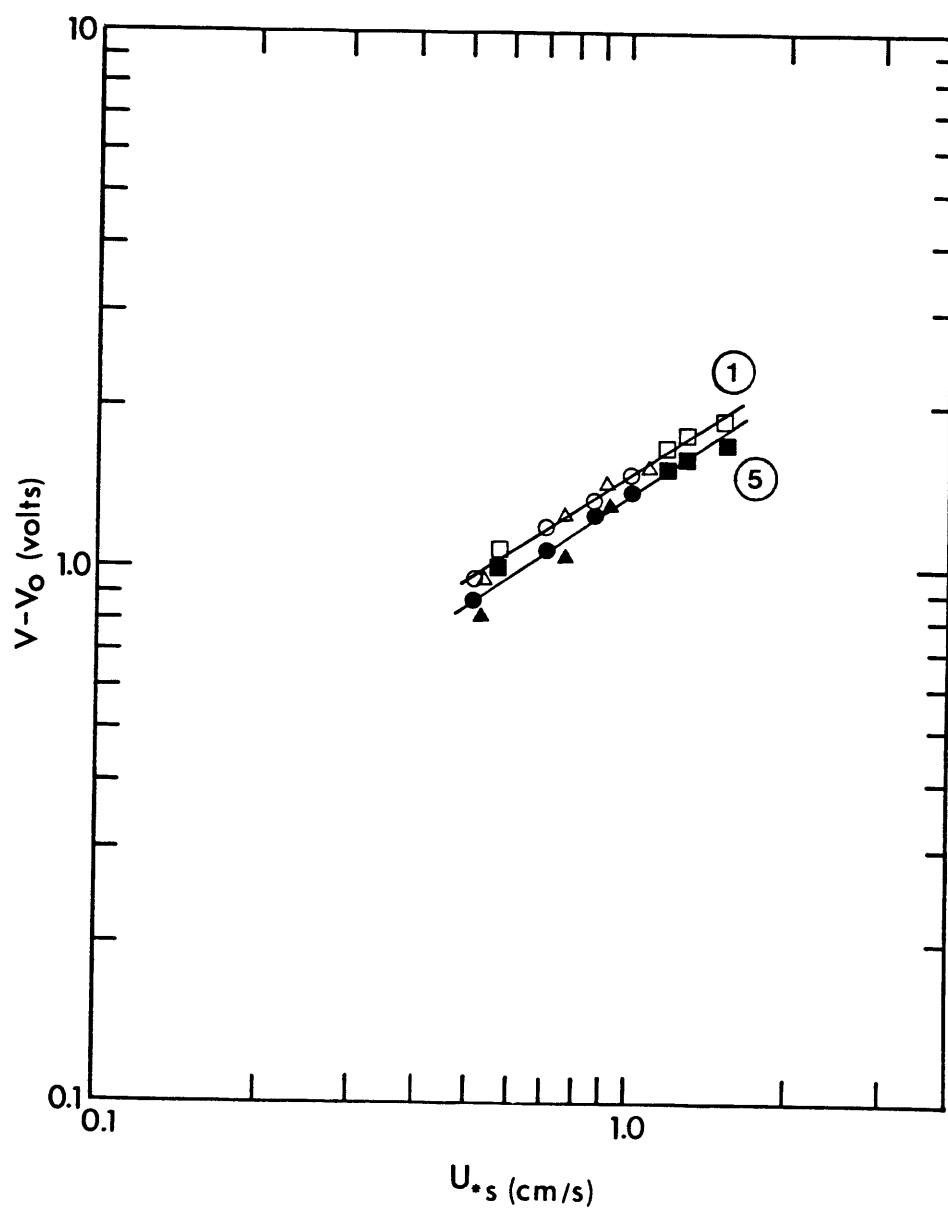


Figure 2.7. Calibration curves for the skin-friction array shown in figure 2.6. Filled and open symbols denote different sensors, squares and circles give results for two calibrations made before data were gathered, and triangles give results for a calibration made after data were gathered. Values of  $r^2$  for the lines are:

(1)	0.993
(2)	0.990
(3 before)	0.983
(3 after)	0.970
(5)	0.986



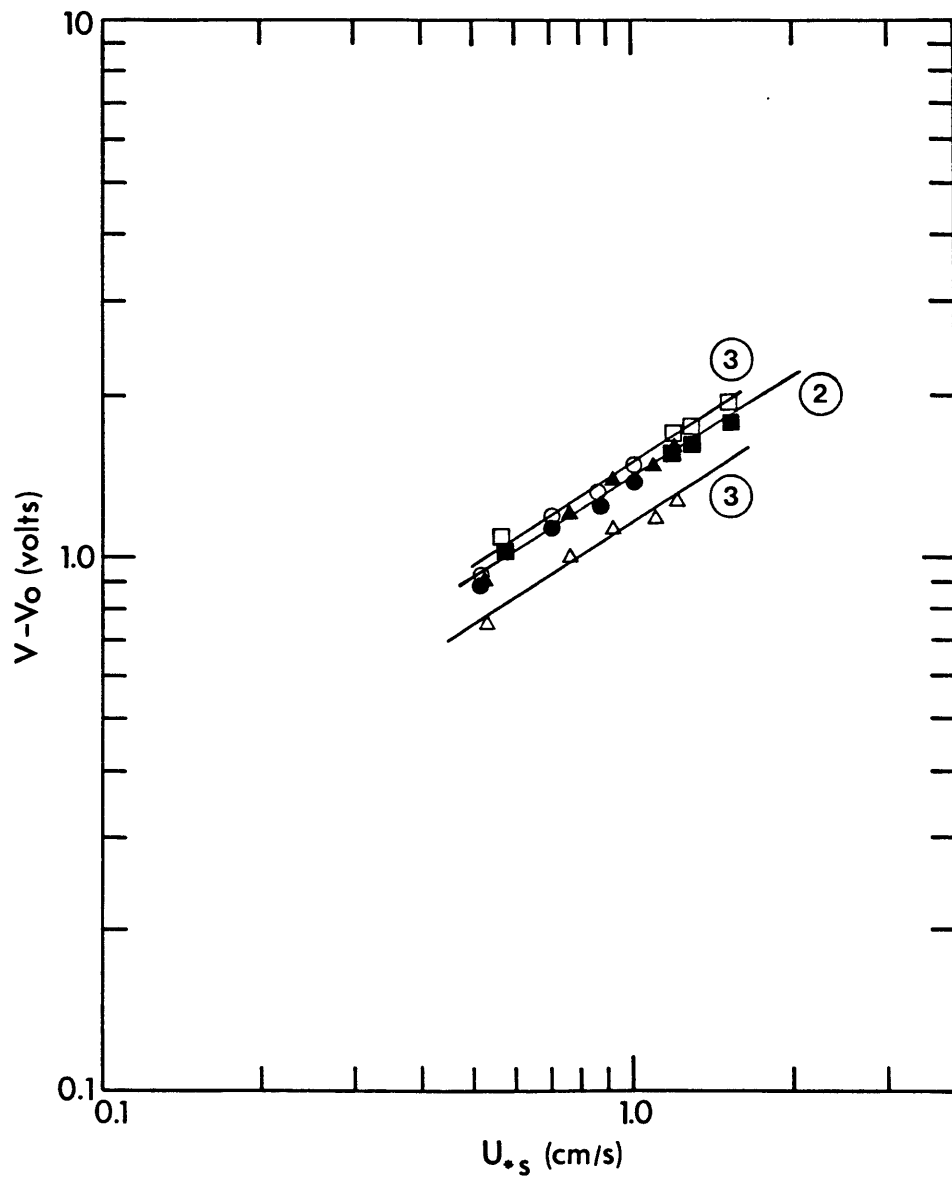
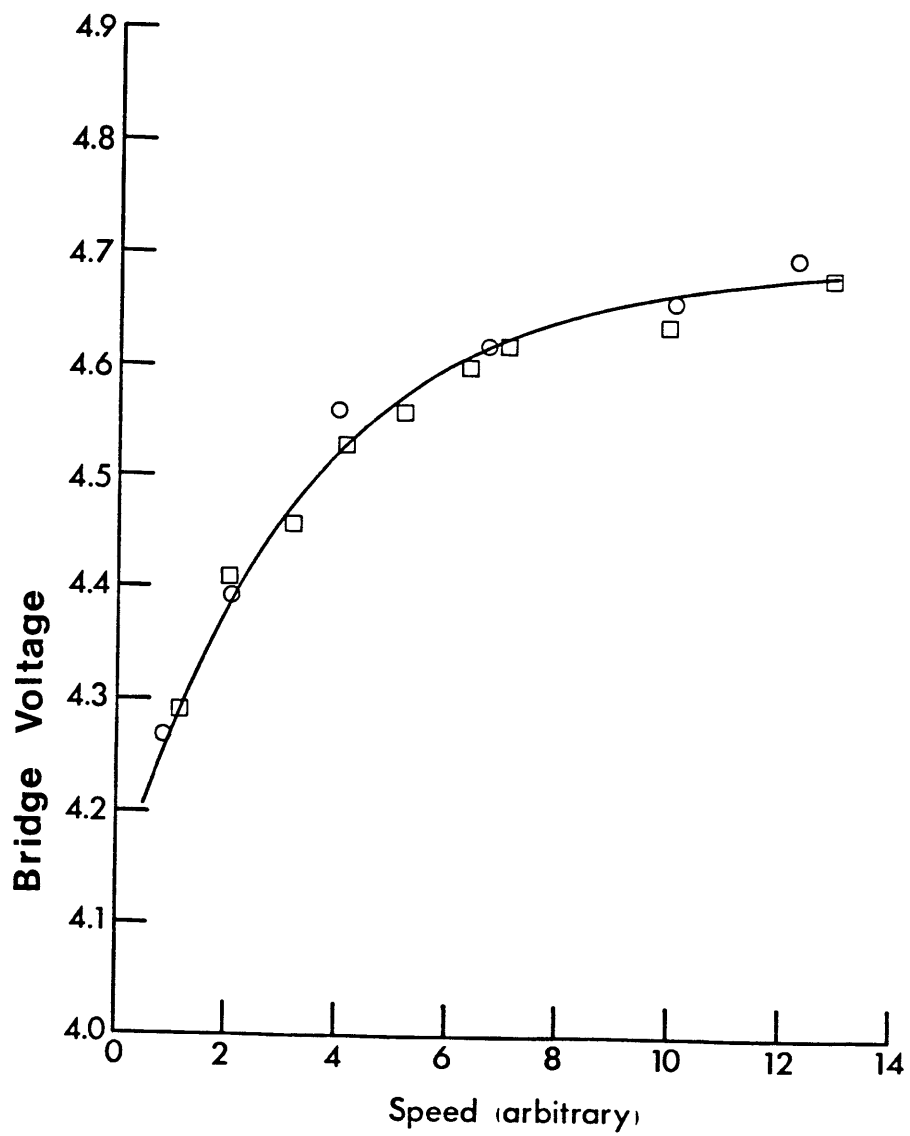


Figure 2.8. Comparison of the output voltage of a hot film mounted on a rubber substrate that is flat (squares) and curved normal to the direction of flow (circles) for different values of flow speed given in arbitrary units (the range of speeds is about 3 - 40 cm/s).



### 2.3. Results: Mean Quantities.

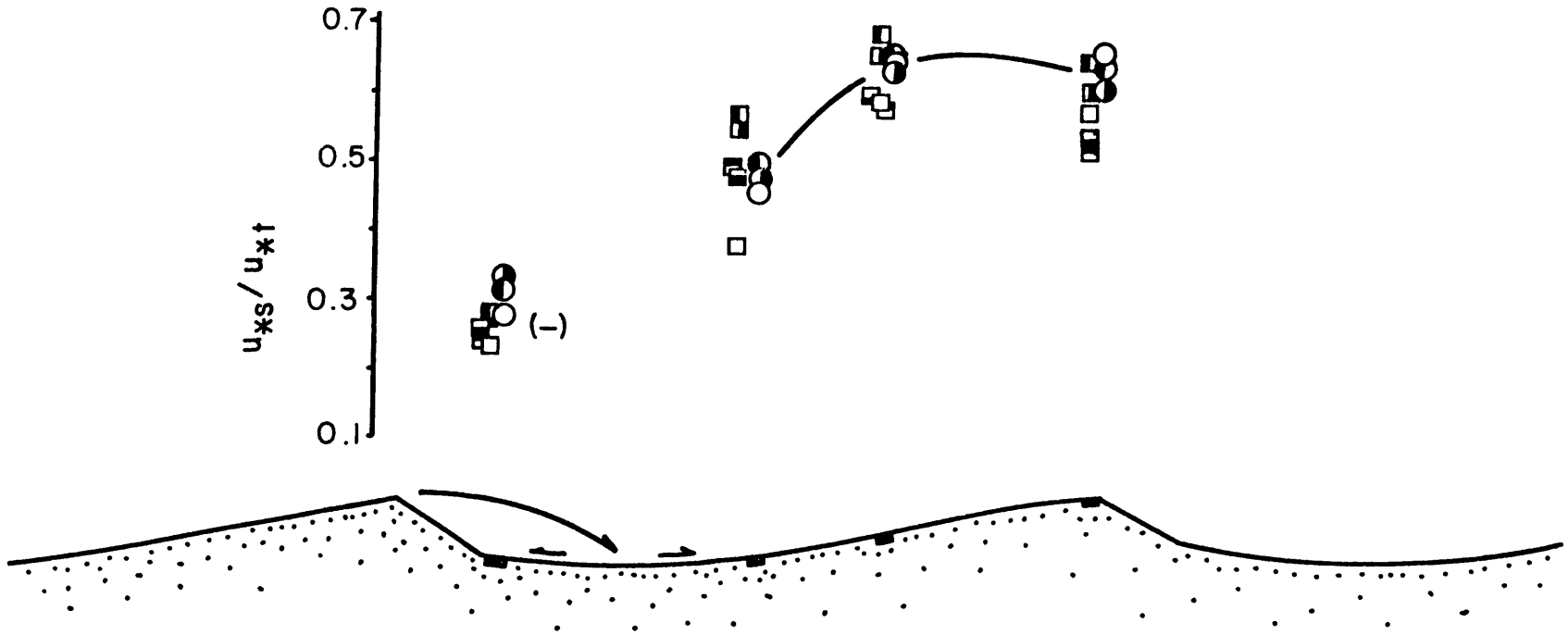
2.3.1. Skin friction. Values of the mean skin friction for each of the four working sensors are shown in figure 2.9, nondimensionalized with the total bottom stress. Measurements are shown for three Reynolds numbers  $R_*$ , defined using  $u_*$  derived from the total bottom stress and the bed-form height (1.04 cm). The data shown include mean values computed from recorded time series and from the analog signal averaged through a 10 s filter. It is not clear why the analog means show less scatter than the recorded means, but the overall ratios  $u_{*s}/u_{*t}$  computed using both types of data agree fairly well. There is no residual systematic behavior evident in figure 2.9, so nondimensionalizing the skin friction field by  $u_{*t}$  collapses the data satisfactorily.

The measured skin friction is smallest in the trough. It has about the same value at the mid-stoss and crest positions; the stress at mid-stoss is augmented by the favorable pressure gradient there. This is a manifestation of the phase shift between shear stress and near-bed velocity over wavy beds that has been invoked frequently in the stability analysis of bed forms (Engelund and Fredsoe, 1982) and has been measured by Zilker (1976) for flow over a sinusoidal boundary. There is also a substantial shear stress in the region of reverse flow upstream of reattachment, equal to about 23% of the value at the crest.

The roughness Reynolds number  $R_*$  used to index runs in this series of experiments is defined using overall bed quantities  $h$  and  $u_*\tau$ . A roughness Reynolds number may also be defined using the diameter of the sand from which the bed was made (0.02 cm) and the skin friction. The largest value of this "skin-friction Reynolds number" encountered in these experiments is about 3.6, below the upper limit of 5 given in section 1.1 for smooth flow. Hence there is no reason to expect that the small-scale roughness of the ripple surface has any direct effect on the near-bed flow field; nor is there any hydrodynamic difference between the surface presented by the skin-friction sensors and the ripple surface adjacent to them.



Figure 2.9. Mean values measured with the skin-friction array shown in figure 2.6, nondimensionalized with  $u_*^2$ , as a function of  $R_*$  and sensor position. Values obtained by averaging the unlinearized analog bridge voltage are shown as circles and those obtained by averaging digital time series are shown as squares.



ANALOG	$R_*$	DIGITAL	$R_*$
○	150	□	150
●	184	■	184
●	236	■	236
		■	259
		■	313

### 2.32. Velocity.

Coordinate system. The mean-velocity data will be analyzed and presented in the framework of a curvilinear coordinate system, as follows. As discussed in section 1.1, the velocity field far from the bed (above about one crest height) responds to the bed only in a spatially averaged sense; it is insensitive to streamwise position. Here the coordinate system should be rectilinear, and the correct vertical scale is the height above some uniform reference level. On the other hand, near the bed the flow follows the surface, so the vertical coordinate there should be the local distance from the bed. The velocity measurements were all made in the forward-going part of the flow, whose lower surface coincides with the bed only downstream of reattachment. Upstream of this point, the lower boundary lies in the free-shear layer, at the top of the recirculating region (figure 1.3). The shape of this composite surface may readily be approximated by a sine wave (Znamenskaya, 1967). For a sinusoidal lower boundary, a natural choice for a vertical coordinate that has the characteristics given above is  $\zeta$  (figure 2.10) given by:

$$y = \zeta + ae^{-k\zeta}\cos(kx) \quad 2.5$$

where  $a$  is the wave amplitude and  $k$  its wavenumber.

The sinusoidal approximation used here for the bottom boundary of the flow is shown in figure 2.10. It fits the bed well downstream of reattachment and incorporates a reattachment distance that is in good accord with the

distance estimated by observation of neutrally bouyant particles (about one-third of the spacing). Values of  $\zeta$  were calculated iteratively, using this boundary profile and input values of the local height, with program YBL (Appendix). It will be shown presently that lines  $\zeta = \text{constant}$  are equivalent to streamlines obtained from linear potential theory for an infinitely deep flow over a sinusoidal boundary.

Results. Mean-velocity profiles for the upper part of the flow field referred to the curvilinear  $(x, \zeta)$  coordinate system are given in figure 2.11, nondimensionalized by  $u_* t$ . It should be noted that this choice of coordinate system eliminates the zero-plane displacement as a free parameter: the vertical coordinate far from the bed is referred by definition to a plane lying halfway between crest and trough. The velocity profiles shown in figure 2.11 yield mean regression estimates for von Karman's constant  $\kappa$  of 0.445 and a roughness length ( $z_0$ ) of 0.03 cm. (All points above  $\zeta = 1.5$  cm were used and the minimum value of  $r^2$  is 0.97; the standard error of the estimated  $\kappa$  is 0.03). A common laboratory value for  $\kappa$  is 0.41 (Daily and Harleman, 1966, p. 234). In view of the fact that the zero-plane displacement was not adjusted and that errors in measurement of both velocity and total stress (section 1.23) affect the estimates, agreement with the expected value is considered acceptable.

Mean-velocity profiles for the surface layer are shown in

Figure 2.10. Sketch of the curvilinear vertical coordinate  $\zeta$  in comparison with the rectilinear coordinate  $y$ .

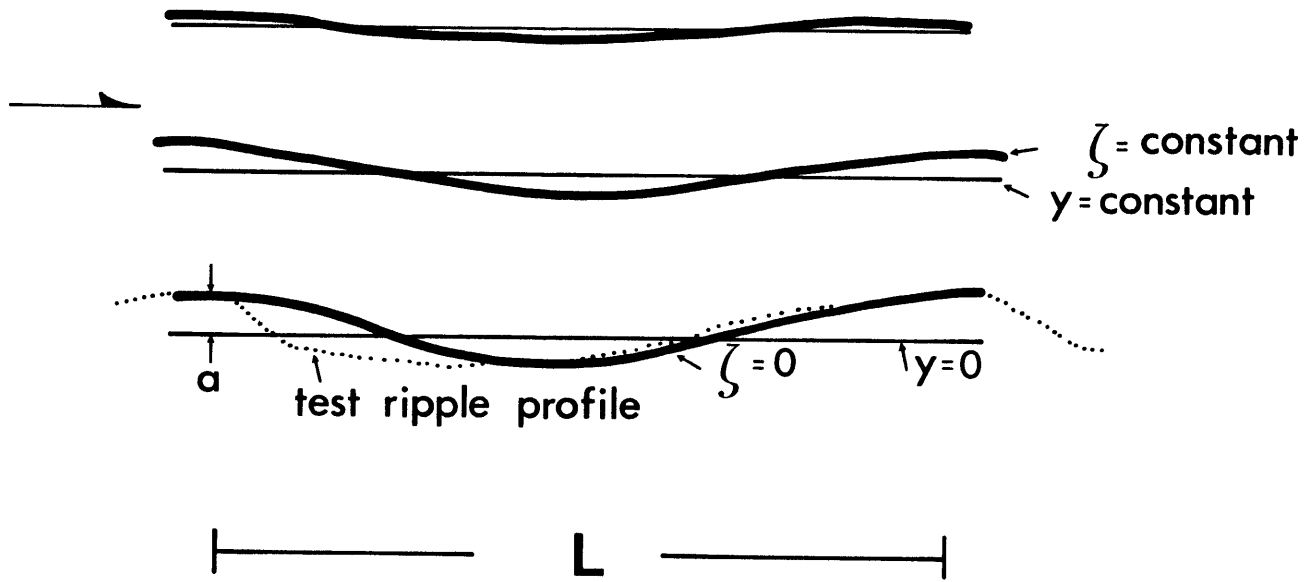


Figure 2.11. Mean-velocity profiles measured over two-dimensional ripples, nondimensionalized with the total friction velocity  $u_*\tau$ . Only the upper part of the measured flow field is shown.

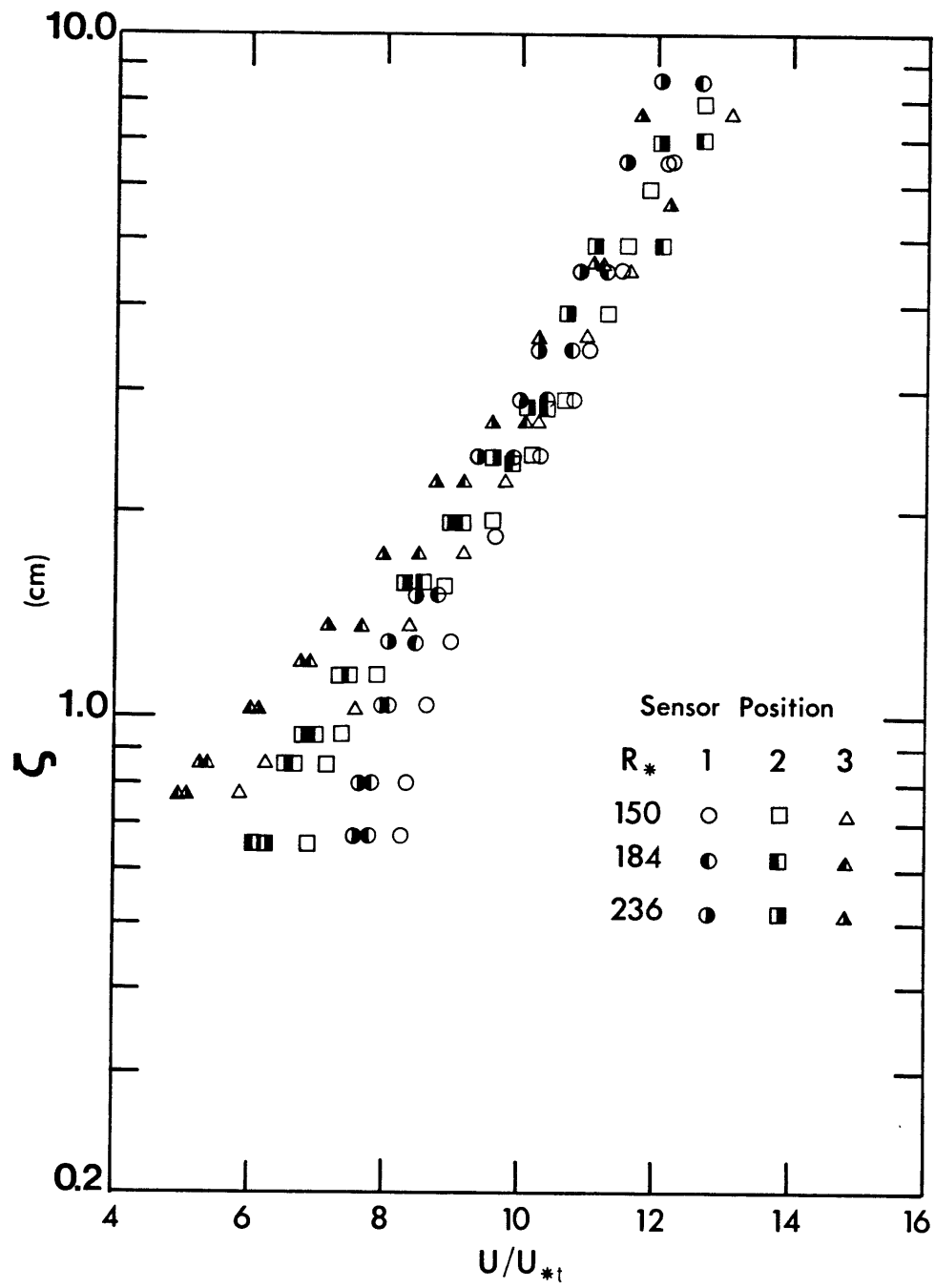




figure 2.12: the velocities in this case are nondimensionalized with  $u_*s$ . If (1.6) were obeyed locally in this region, all the profiles shown would have the same slope  $du/d(\ln(\zeta))$ . It is clear from figure 2.12 that this is not the case. For each sensor position, an apparent value  $\kappa_A$  for von Karman's coefficient can be calculated as  $\kappa_A = u_*s/(du/d(\ln(\zeta)))$ ; these are given in figure 2.12. The slopes  $du/d(\ln(\zeta))$  were determined from least-squares fits to the lowermost six points in each profile. All the correlation coefficients  $r^2$  were greater than 0.99 and the standard error of the fitted slopes gives a standard error for  $\kappa_A$  of 5%. Hence the differences between the calculated  $\kappa_A$  at positions 1 and 3 and the expected local-equilibrium value of 0.4 are highly significant.

One would immediately suspect the pressure gradient induced by the wavy bed as the cause of the distortion, but this is not the case. Pressure measurements over bed forms by Vanoni and Hwang (1967) and by Raudkivi (1963, 1966) show that the pressure field over the stoss slope is qualitatively what one would expect (from potential theory, for instance): it is approximately sinusoidal and out of phase with the bed by  $180^\circ$  referred to the crest. Thus the pressure gradient is largest at mid-stoss (position 2), where agreement with local-equilibrium expectations is best.

The data may be interpreted more successfully by applying potential flow theory, so I will discuss some elements of this before returning to the problem at hand.

Potential flow. By taking the curl of the Navier-Stokes equation<sup>1</sup>

$$U_{i,t} + U_j U_{i,j} = -(1/\rho) P_{,i} + \nu U_{i,jj} \quad 2.6$$

and simplifying, one arrives at an equation for the vorticity  $\Omega_k = \epsilon_{jik} U_{i,j}$  (see, for example, Tritton, 1977, sec. 6.5)):

$$\frac{D\Omega_i}{Dt} \equiv \Omega_{i,t} + U_j \Omega_{i,j} = \Omega_j U_{i,j} + \nu \Omega_{i,jj} \quad 2.7$$

If the viscous term is neglected, one has

$$\frac{D\Omega_i}{Dt} = \Omega_j U_{i,j} \quad 2.8$$

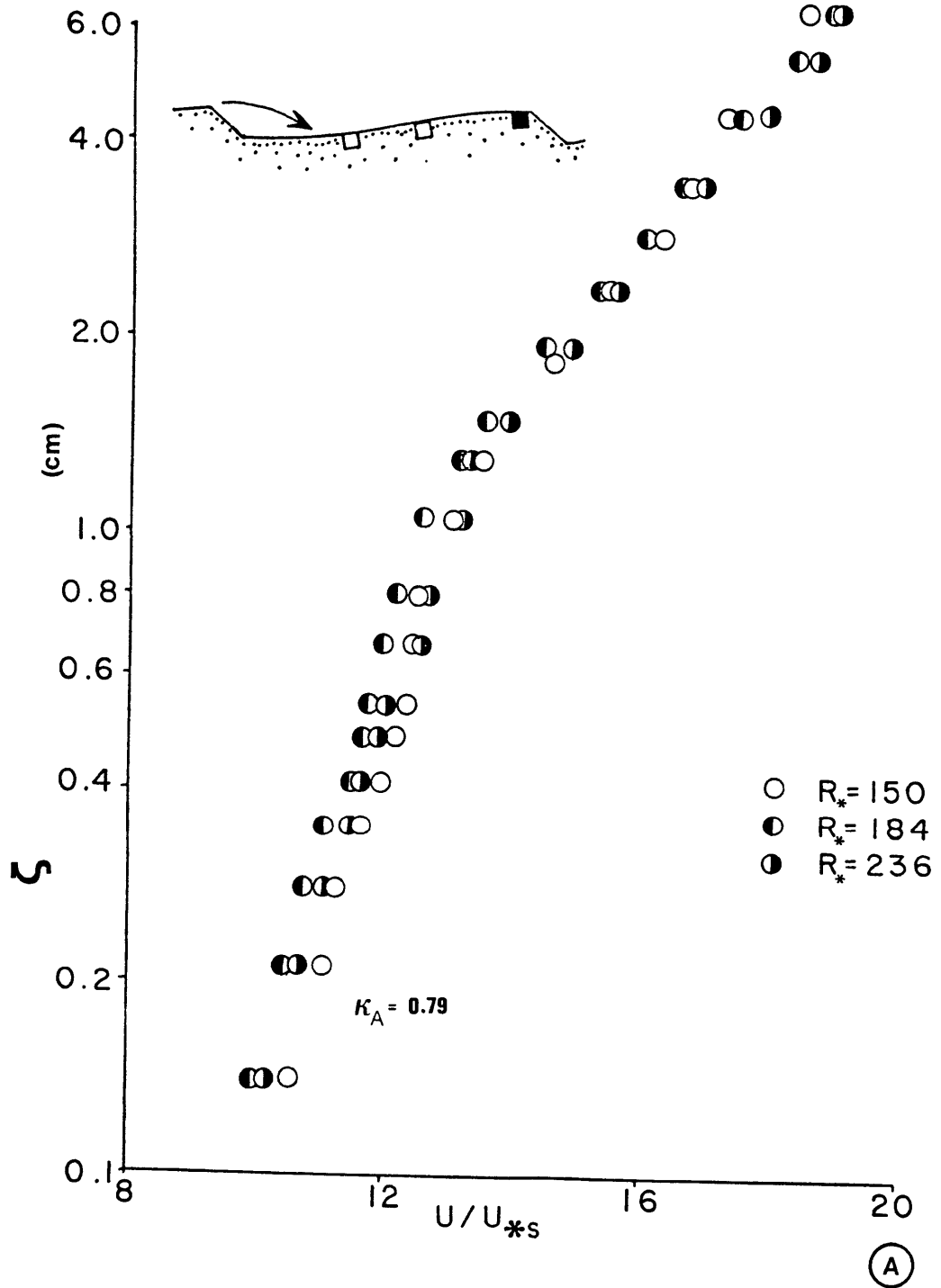
The term on the left represents the change in vorticity experienced by a fluid particle as it is advected by the velocity field. If the vorticity field  $\Omega_i$  is ever zero globally, then it is always zero: the vorticity of a moving particle can change only through the action of the velocity field on a pre-existing vorticity field. This classical result establishes a strong connection between inviscid flows ( $\nu=0$ ) and irrotational flows ( $\Omega_i=0$ ).

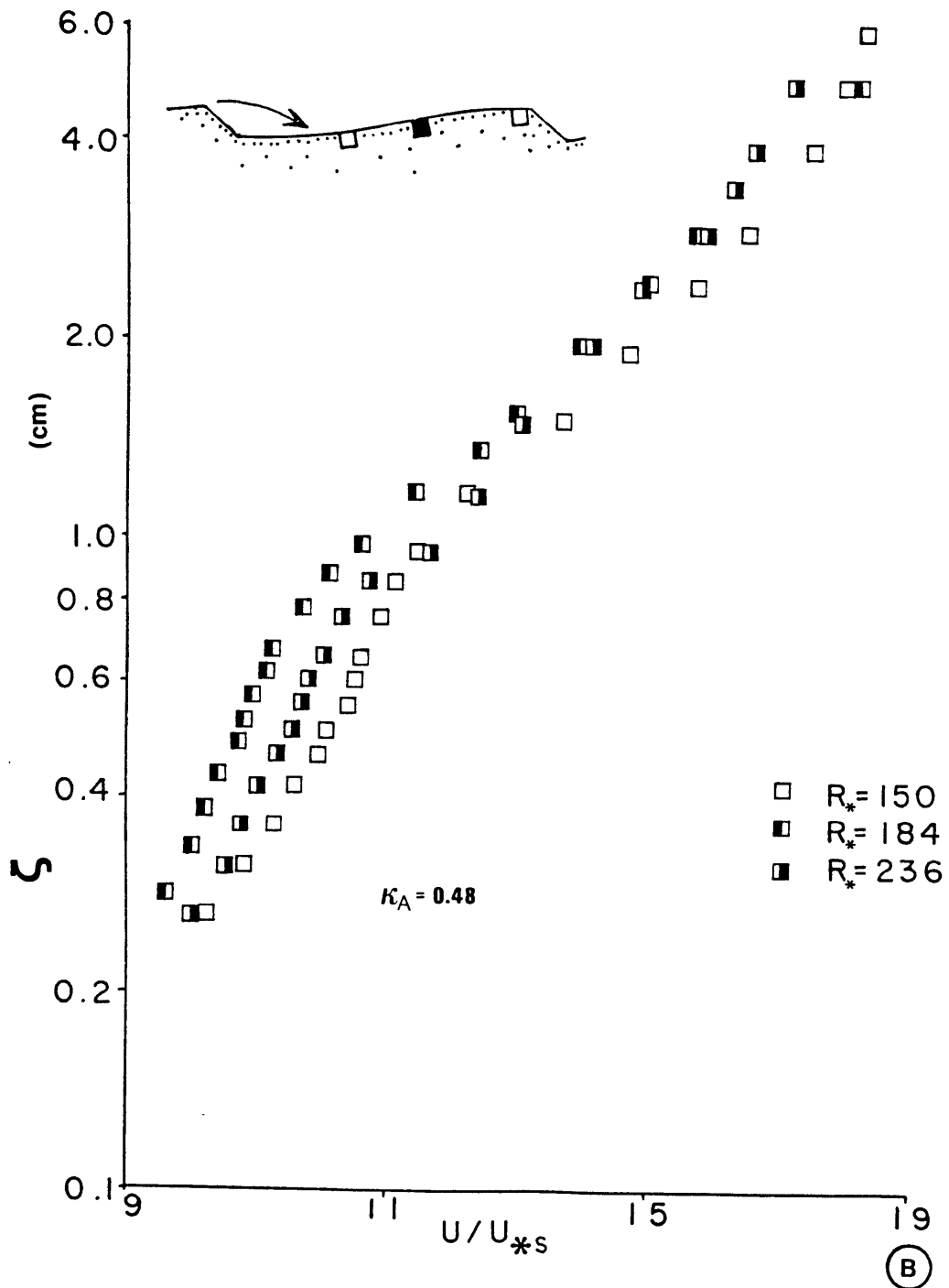
The condition  $\Omega_i=0$  may be satisfied by writing the velocity

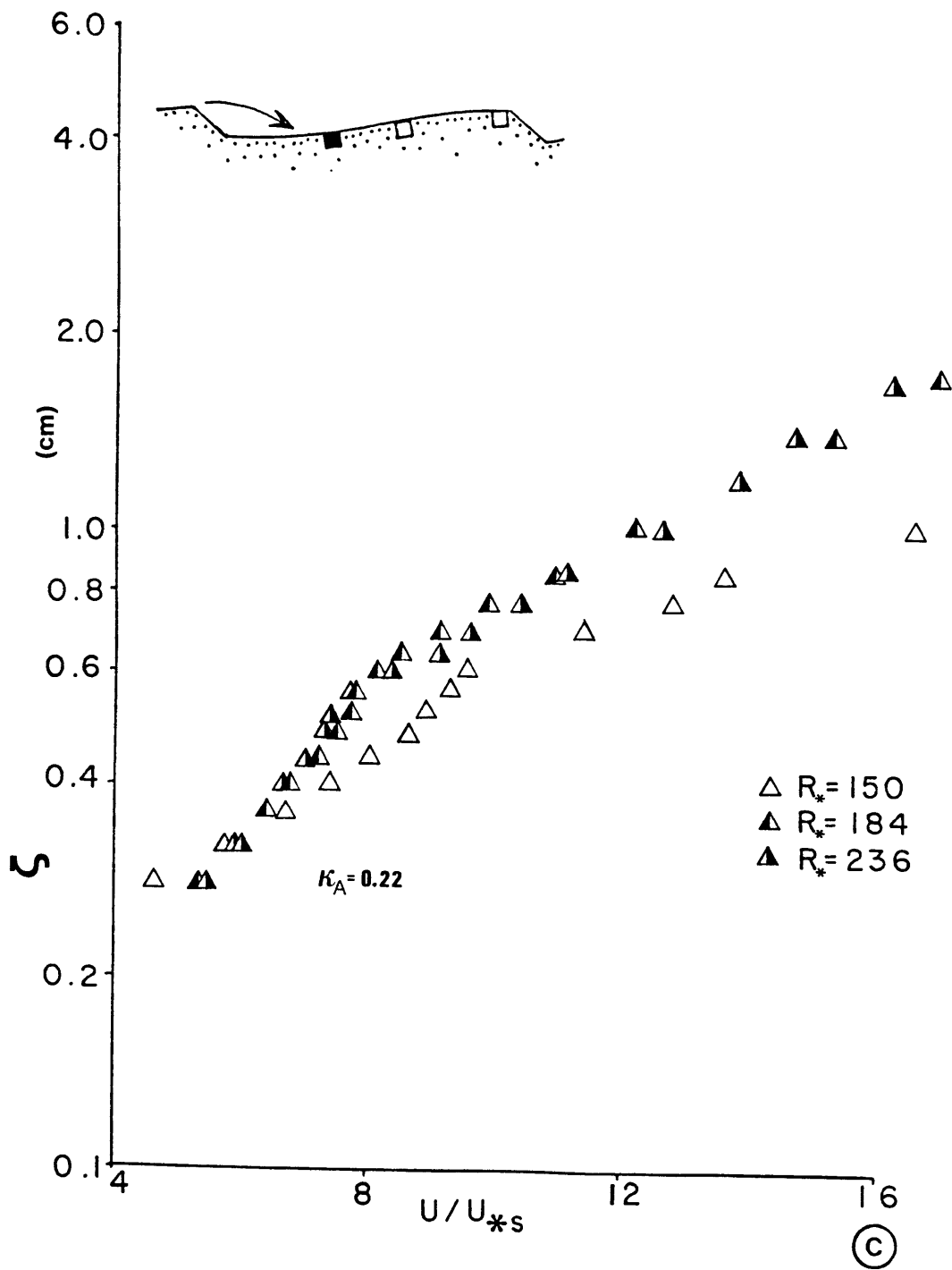
---

<sup>1</sup>Vector equations will usually be written in tensor notation in this work:  $t$  is time, all other subscripts are directions in a right-handed coordinate system (figure 1.2), a comma denotes differentiation by the variables following it, and repeated indices indicate summation over the three coordinates.

Figure 2.12. Mean-velocity profiles measured over two-dimensional ripples, nondimensionalized with the local skin friction velocity  $u_*^s$ , for skin friction measuring positions 1 (A), 2 (B) and 3 (C). The apparent von Karman coefficients  $\kappa_A$  are derived from semilogarithmic regression fits to the lowermost six points in each profile.







field as

$$U_i = \phi_{,i} \quad 2.9$$

where  $\phi$ , the velocity potential, is a scalar function of position that satisfies Laplace's equation  $\phi_{,ii} = 0$  if the fluid is incompressible. This is a major simplification: the problem of solving the nonlinear system (2.6) has been replaced by that of solving Laplace's equation, which is linear and has been extensively studied by mathematicians and physicists.

What is the physical meaning of an irrotational velocity field? Clearly, (2.8) cannot exactly describe the flow of a real fluid; these always have finite viscosity. Furthermore, since  $\nu$  multiplies the highest-order derivative in (2.6), the viscous term can never be ignored throughout an entire flow field, regardless of the outcome of any overall scaling arguments. To satisfy all the boundary conditions constraining solutions to (2.6), including the no-slip condition, the viscous term must become important at least near solid surfaces (this is lucidly discussed in Schlichting, 1979, ch. 4). This idea is at the heart of boundary-layer theory; as discussed in section 1.1, it plays an important role whether the boundary layer is rough or smooth.

Generall, one uses solutions to (2.9) to describe the flow field outside the boundary layer. Think of flow over a curved surface like a wing or a wavy bed. Regardless of the

details of the flow response, the fluid must conserve mass, speeding up where it is constricted and slowing down where it expands. This forces a response described by the Bernoulli law, given for inviscid flow by:

$$\frac{p}{\rho} + \frac{(U_i U_i)}{2} = C \quad 2.10$$

where  $C$  is a constant throughout the flow field. The pressure variation arises in direct response to the changes in the velocity field required to conserve mass: where the fluid accelerates, the pressure must decrease downstream to provide the necessary force. Inspection of (2.6) shows that, without the viscous term, the equation of motion (the Euler equation) simply expresses this balance between acceleration and pressure gradient. So the irrotational solution for a given boundary geometry may be thought of as the simplest possible response of the flow to the geometry: mass is conserved and the pressure field adjusts to drive the resultant accelerations. This is a purely kinematic response. The velocity field is determined from (2.9), together with the boundary conditions, and the pressure field is calculated from it using (2.10). Because of the neglect of the viscous term in (2.9), the flow is free of shear stresses. For the time-averaged component of turbulent flow, governed by the Reynolds equation

$$u_i',t + u_j u_i',j = -(1/\rho)p',i + (v u_i',j - \overline{u_i' u_j'}),j \quad 2.11$$



where the overbar denotes time averaging, the equivalent argument requires that we drop the stress term  $(\nu u_{i,j} - \overline{u'_i u'_j})_{,j}$  to obtain potential flow.

A simple problem related to flow over bed forms to which (2.9) can be applied can be set up as follows. Consider an irrotational two-dimensional flow over a flat surface in the absence of a pressure gradient. The velocity field is given by  $u = u_0$  (a constant); that is,  $\phi = u_0 x$ . (This is a trivial solution to (2.9).) What is the disturbance to the flow caused by the presence of low-amplitude (small aspect ratio) sinusoidal waves on the boundary? Let the bottom surface be given by  $\eta = a \cos(kx)$ . In the small-amplitude approximation, the lower boundary condition, that there must be no flow into or out of the bounding surface, may be applied at  $y=0$ . A solution to (2.9) that also dies off with distance from the boundary is given by

$$u = u_0 + u_0 a k e^{-ky} \cos(kx) \quad 2.12$$

The pressure field, calculated from (2.10), is given to first order in  $(ak)$  by

$$p/\rho + u_0^2 a k e^{-ky} \cos(kx) = C \quad 2.13$$

The flow field described by (2.12) is shown in figure 2.13.

Application to flow over ripples. The boundary layer developed over current ripples cannot be described correctly by (2.9). The Reynolds stresses in this region, enhanced by vigorous generation of turbulence in the wakes of the roughness elements (Raudkivi, 1963, 1966), are not

negligible; nor do the velocity profiles shown in figure 2.12 look like the inviscid ones in figure 2.13. The former are distinctly rotational in that they possess strong velocity shear. Nonetheless the irrotational solution can be used to describe the local variation seen in the measured profiles, as follows. Suppose the velocity field is written as

$$u = \langle u \rangle + u'' \quad 2.14$$

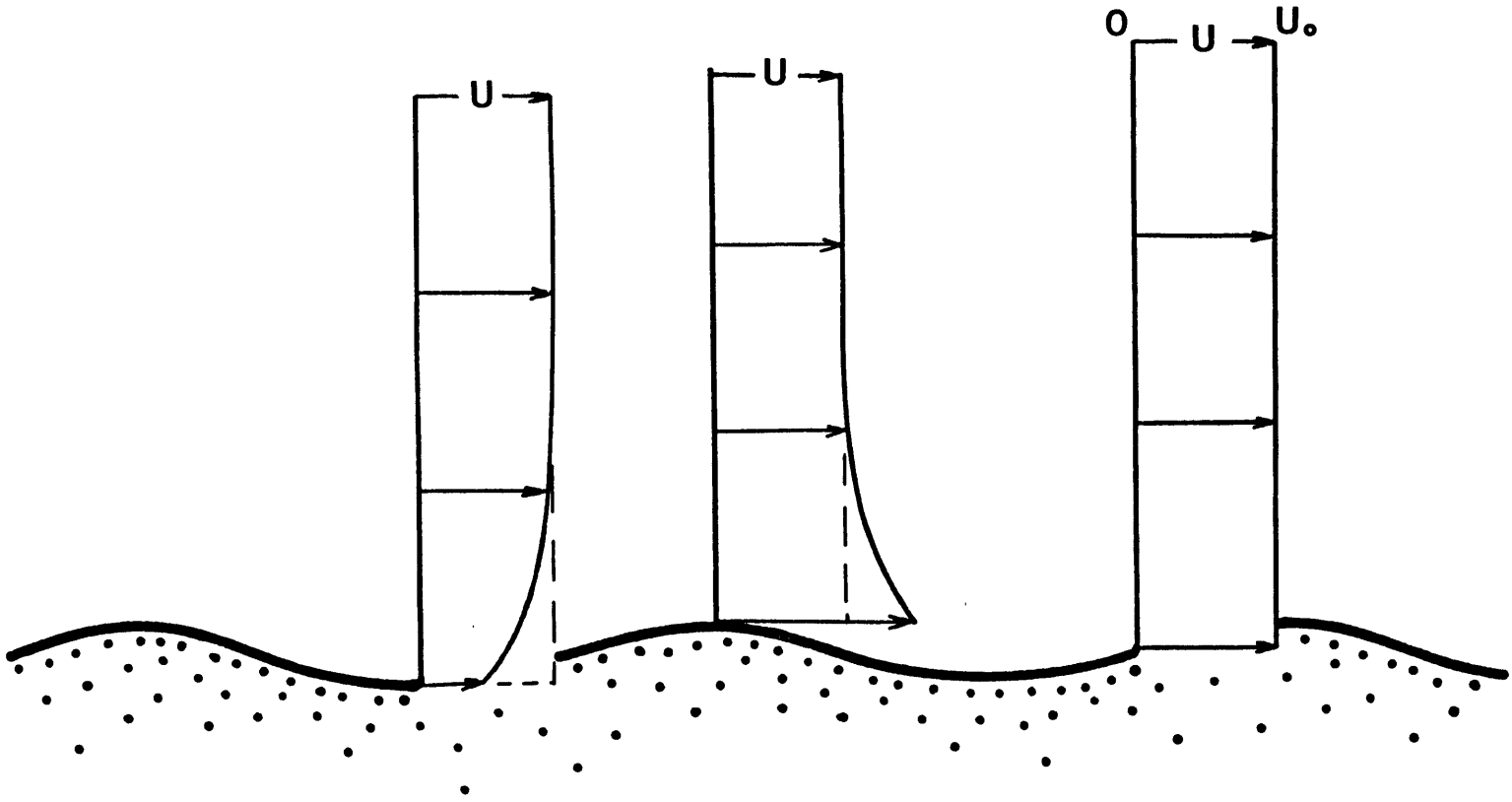
where  $u''$  is the inviscid solution (2.12) and  $\langle u \rangle$  is a spatially averaged velocity given by

$$\langle u \rangle = (1/\lambda) \int_0^\lambda u dx \quad 2.15$$

Describing the velocity field by (2.14) amounts to suggesting that all the vorticity in the velocity profile is contained in the spatially averaged part  $\langle u \rangle$ , so that the flow responds locally only by conserving mass. It should be noted that the form (2.12) for the inviscid response is correct even though the rippled bed is not sinusoidal, because the bottom of the forward-going part of the flow is approximately sinusoidal, as discussed earlier in connection with the curvilinear  $(x, \zeta)$  coordinate system.

The first step in comparing the data with the conjecture (2.14) is to find the spatially averaged profile  $\langle u \rangle$ . The inviscid solution  $u''$  disappears when  $\cos(kx)=0$ ; thus a velocity field given by (2.14) reduces to  $\langle u \rangle$  at the zero-crossings of the bed. The middle position (2 in figure 2.6) at which velocity profiles were measured is a

Figure 2.13. Sketch of the velocity field given by first-order potential theory for flow over a sinusoidal bed.



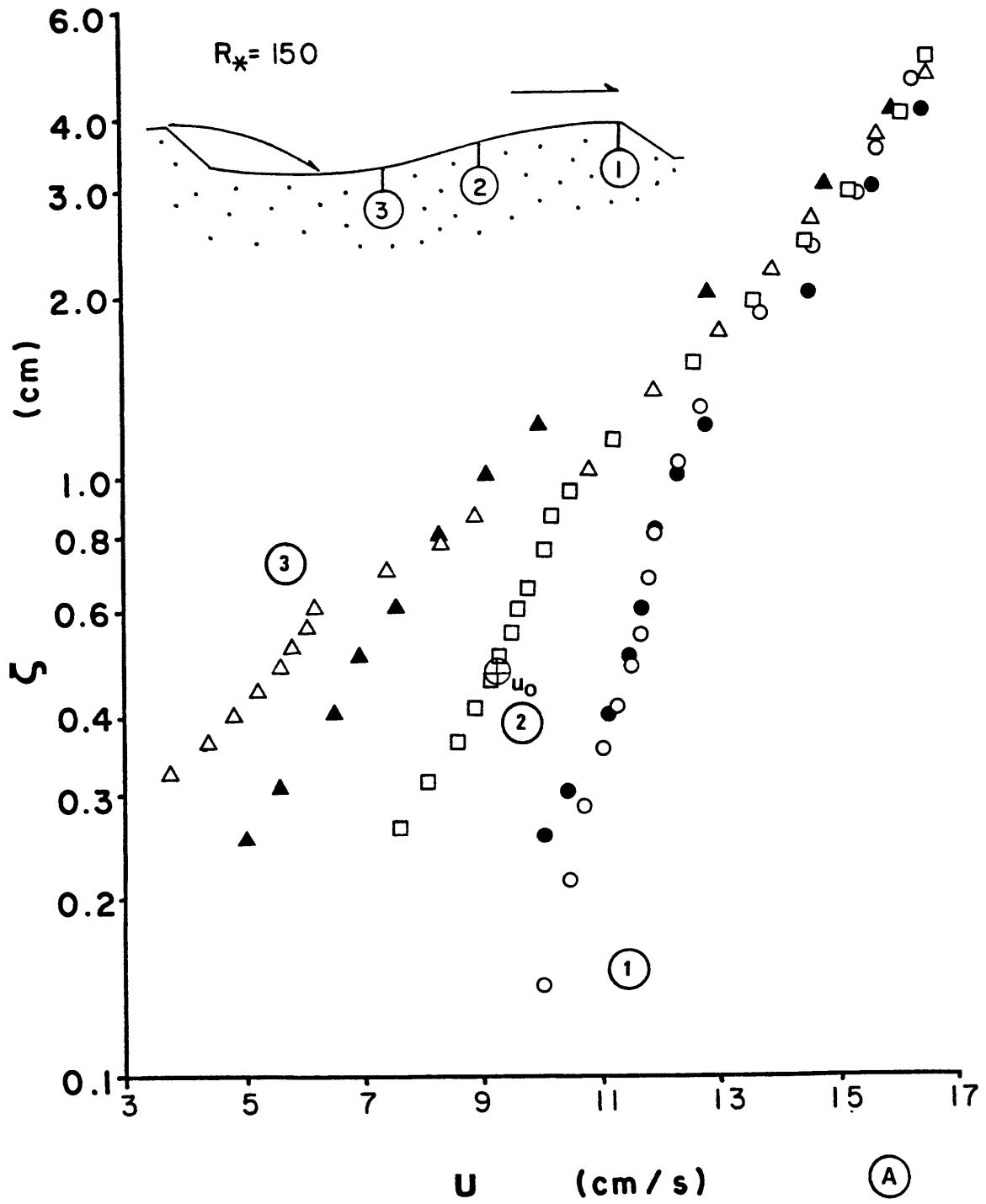
zero-crossing so the profiles measured there at each Reynolds number have been taken to be the spatially averaged part of the velocity field  $\langle u \rangle$ .

In deriving (2.12) the underlying spatially averaged flow is given by a constant  $u_0$ , which then appears in it as a scaling velocity. In applying (2.12) to an underlying flow with shear, the correct choice for the scaling velocity is not clear. Originally, I used half the surface velocity as an arbitrary but consistent choice. The location of this reference velocity is shown on the spatially averaged profiles in figure 2.14; it can be seen that it is given to good accuracy by the unperturbed velocity at the crest height. This way of seeing the reference velocity makes more physical sense than the original definition, although numerically there is little difference for the present set of measurements.

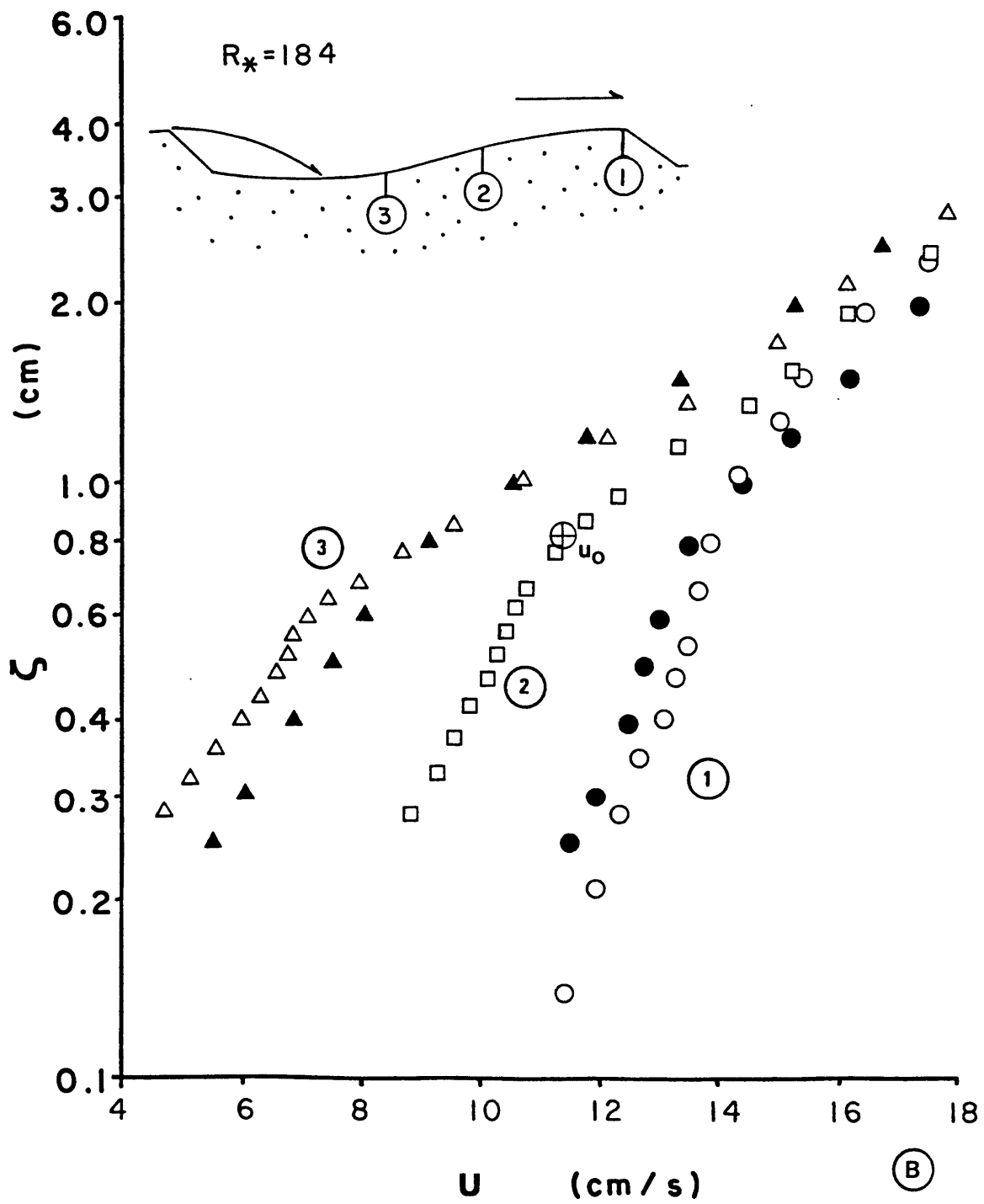
The results of applying the model (2.14) to the measured unperturbed profiles are shown in figure 2.14. This scheme gives good agreement with the crest profiles but seems to do less well with those near reattachment. This is reasonable; based on our having eliminated the shear stresses from consideration in deriving the potential flow description, one would expect it to be least applicable where the disturbance to the Reynolds stress is largest. However, part or all of the disagreement is due to systematic bias induced in the mean-velocity data by the strong turbulence near reattachment. Since the voltage-velocity calibration is

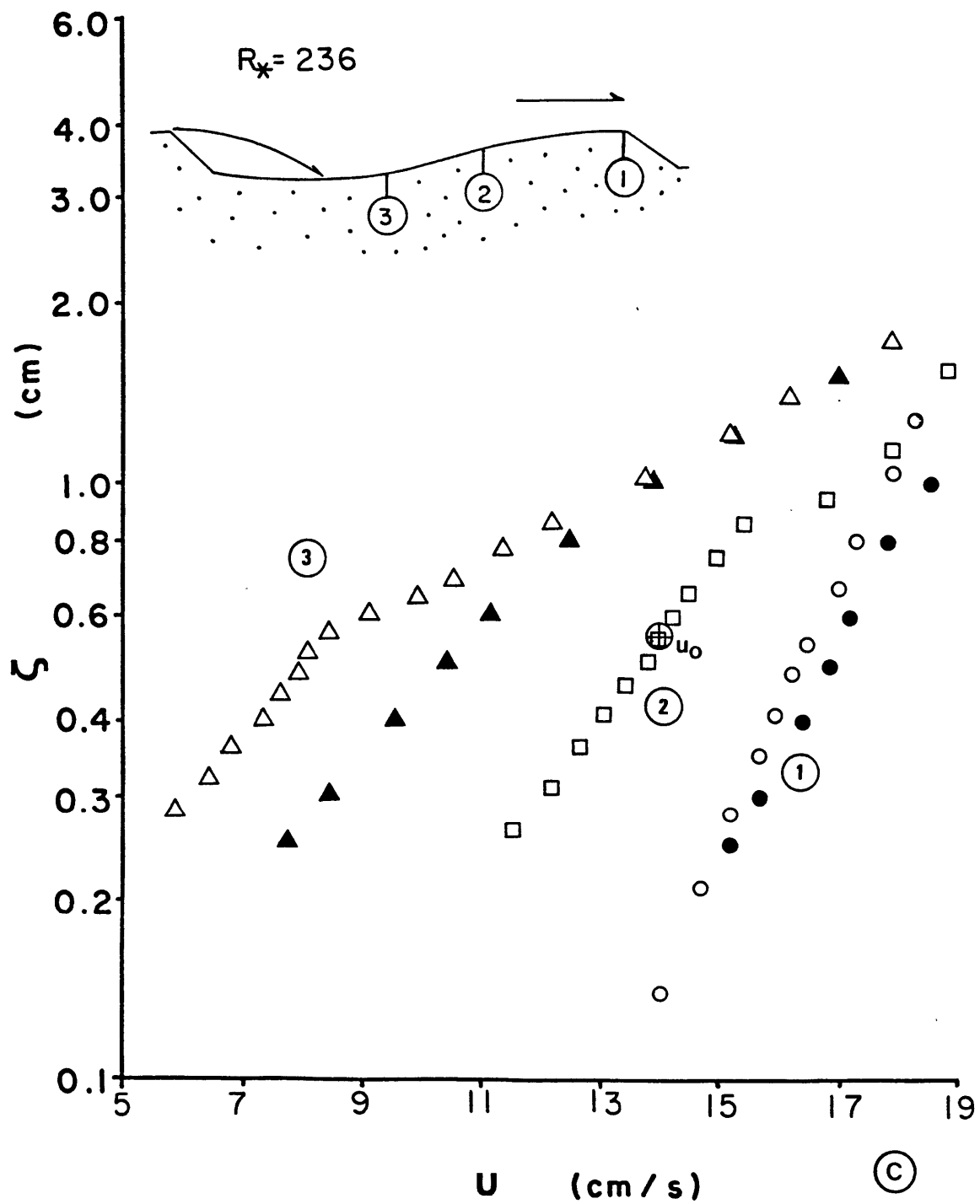
nonlinear (figure 2.5), estimating the mean velocity from the mean analog voltage introduces bias because positive turbulent fluctuations contribute relatively less to the mean voltage than negative ones do. The estimated velocities are thus too low. This problem can be avoided only by linearizing the voltage signal or by digitally recording the voltage, obtaining the complete velocity time series, and calculating the mean velocity directly. Both methods require equipment that was not available for this part of the study. Later on, however, digital recordings of velocities at selected points over the bed were made for correlation analysis. Comparison of these with velocities estimated from analog averages of nonlinearized voltages indicates that, in the strongly turbulent region below one crest height above the bed, the velocities nearest reattachment are about 20% too low. Hence the local-inviscid model may be fairly accurate even near reattachment. In any case, it predicts correctly the sense of change of the semilogarithmic velocity slope  $du/d(\ln(\zeta))$  going downstream over the stoss slope, which the local-equilibrium model does not. If the surface layer were an ESL, the slope would increase going downstream, but it is observed to decrease, as the local-inviscid model requires.

Figure 2.14. Measured dimensional mean-velocity profiles (open symbols) compared with the results (filled symbols) of adding a first-order inviscid solution to the profile measured at position 2. The location in the position-2 profile of the scaling velocity  $u_0$  is given by the cross-hair symbol.









## 2.4. Results: fluctuating quantities.

2.41. Root-mean-square intensity. Graphs showing the rms intensity of the fluctuating skin friction ( $\sigma_\tau$ , defined by  $\sigma_\tau \equiv \sqrt{(\overline{\tau'_{OS}{}^2})}$ ) are shown in figure 2.15. The intensity falls off by a factor of about 2.5 going from the measuring point nearest reattachment (number 3) to that at the crest (number 1); this of course is a reflection of the downstream relaxation of the wake. Somewhat more surprisingly, the rms intensity is quite low in the recirculation region (position 5); it is much lower there than at a similar distance from reattachment going downstream (position 3).

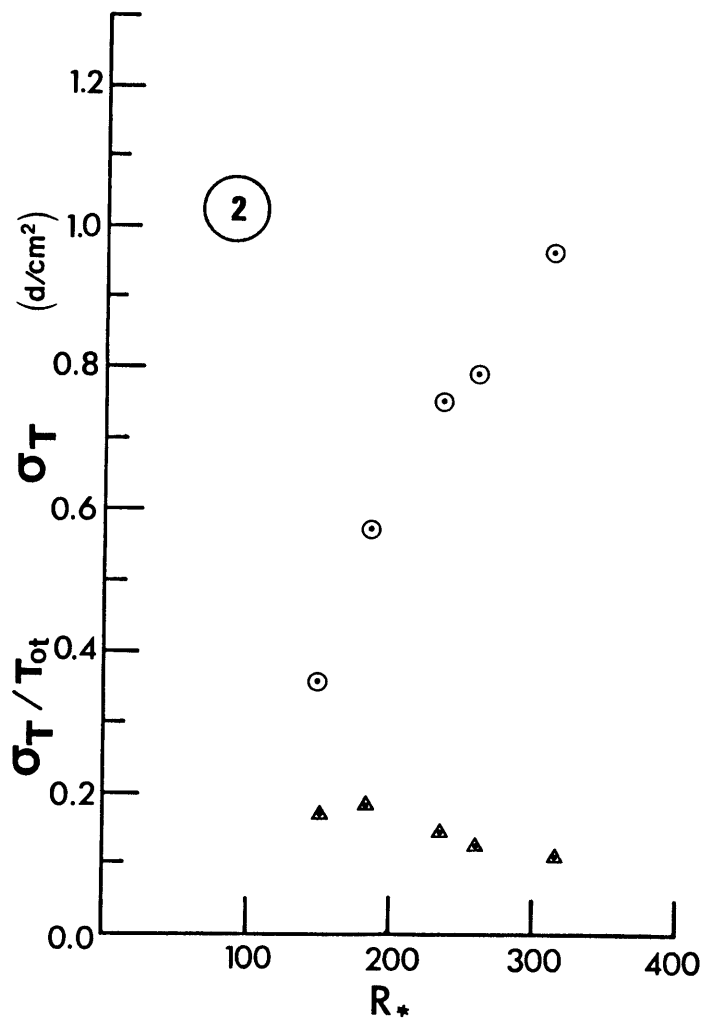
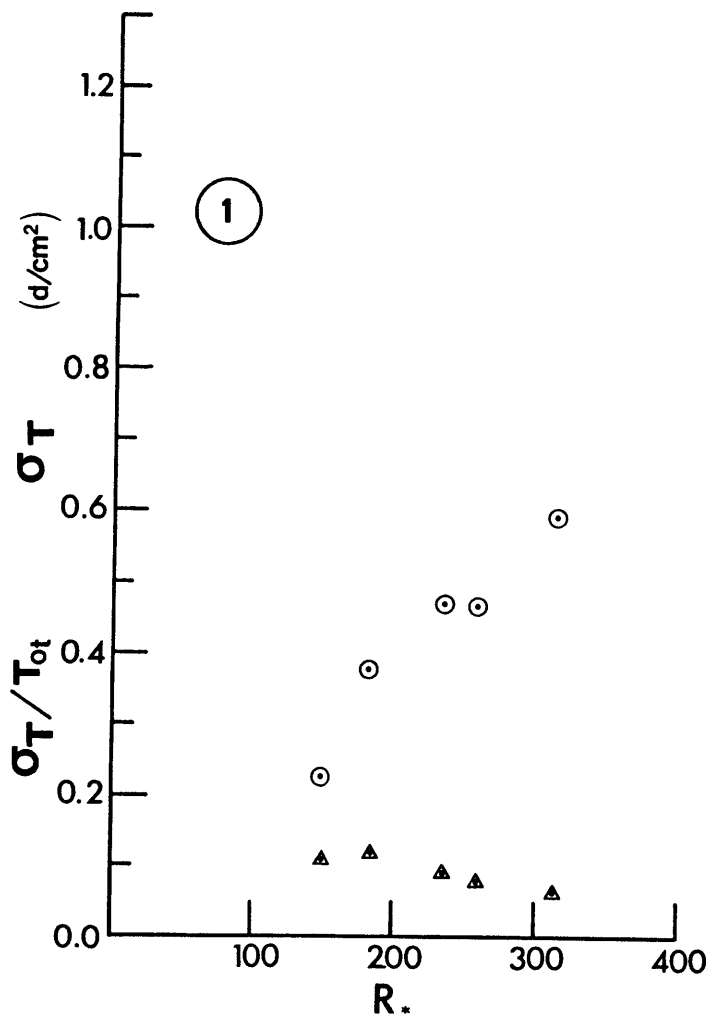
Figure 2.15 also shows the results of attempting to nondimensionalize the rms intensity using the total boundary shear stress, as was done for the mean skin friction (figure 2.9). The nondimensionalization reduces the scatter in the data considerably, although there is residual systematic variation present; the nondimensional fluctuation intensity decreases with Reynolds number. This variation is just within the error margin of the estimates (15%) so it is not clear whether or not it is significant. The decrease in nondimensional fluctuation intensity suggests that the intensity may not increase with  $R^*$  as fast as the mean skin friction does (linearly; figure 2.9). This can also be seen by examining the ratio of rms intensity to the time-averaged value (the relative fluctuation intensity  $\sigma_\tau/\tau_{OS}$ ), shown in figure 2.16. The relative fluctuation intensity decreases systematically with  $R^*$ . The greatest decrease is near

reattachment; at station 3 the value at  $R^* = 313$  is 58% of that at  $R^* = 150$ .

For comparison, four recordings were made of the skin friction in a smooth flow during calibration of the sensors. Data obtained for these conditions are shown in figure 2.17. There is also a decrease in  $\sigma_\tau/\tau_{OS}$  with  $R \equiv \bar{u}D/\nu$  where  $\bar{u}$  is the bulk velocity (discharge divided by cross-sectional area) and  $D$  the depth (7.51 cm for the smooth-flow data). Comparison of figures 2.16 and 2.17 shows that the values of the relative fluctuation intensity encountered at the crest are somewhat smaller than those for smooth flow at similar values of  $R$  (the range of bulk-flow Reynolds numbers associated with the results shown in figure 2.16 is similar to that shown in figure 2.17: see Table 2.1). This is not surprising in view of the favorable pressure gradient over the back of the ripples; such a pressure gradient causes the viscous sublayer to thicken and under extreme circumstances can cause the entire boundary layer to become laminar (Yaglom, 1979).

Kreplin and Eckelmann (1979) reviewed data on the relative fluctuation intensity in smooth flows gathered by various investigators using flush-mounted wall sensors. The reported range of values is 0.205 to 0.3, measured in air and water at overall Reynolds numbers of 5,000 to 25,000. The different values come from different studies and do not show systematic dependence on  $R$ . On the other hand, Blinco and Simons (1974) report a strong Reynolds-number dependence, based on flush mounted hot-film data: the relative fluctuation intensity

Figure 2.15. The rms value  $\sigma_\tau$  of the fluctuating skin friction as a function of  $R^*$  and sensor position, in dimensional form (dynes/cm<sup>2</sup>; circles) and nondimensionalized with the total bottom stress  $\tau_{ot}$  (triangles).



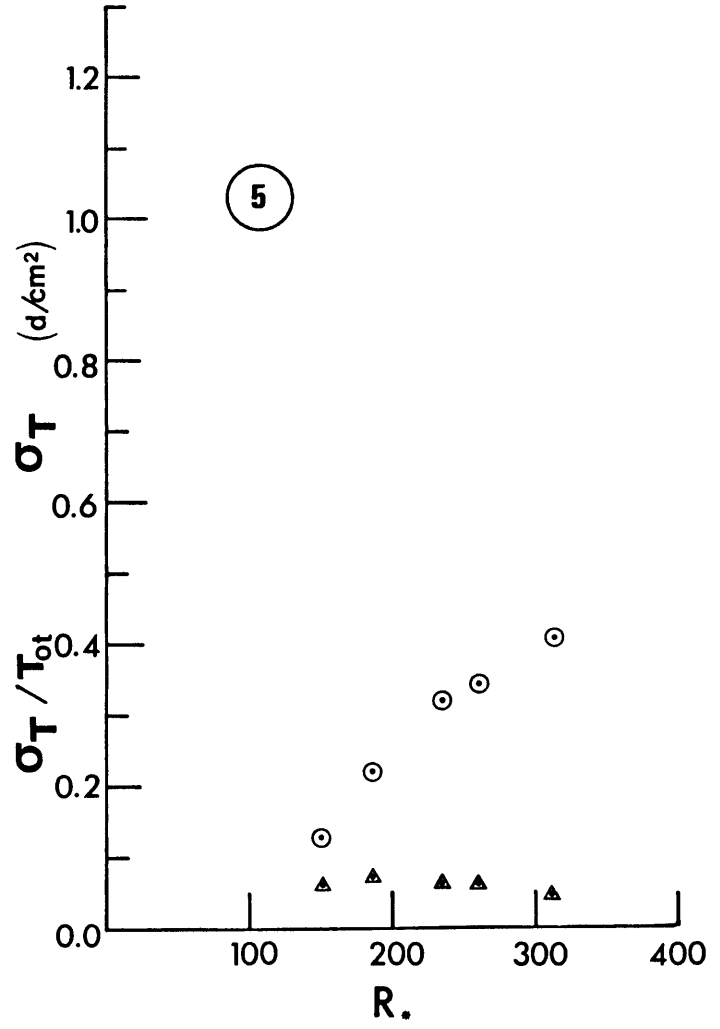
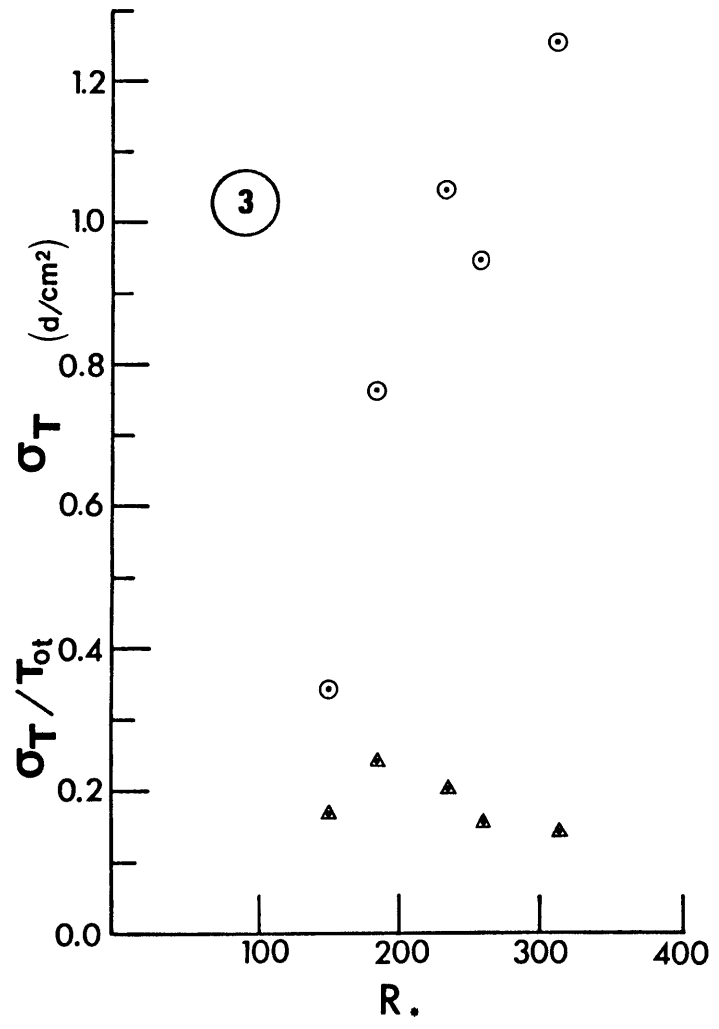


Figure 2.16. Relative fluctuation intensity  $\sigma_\tau/\tau_{0S}$  of skin friction measured over two-dimensional ripples as a function of sensor position and  $R^*$ .



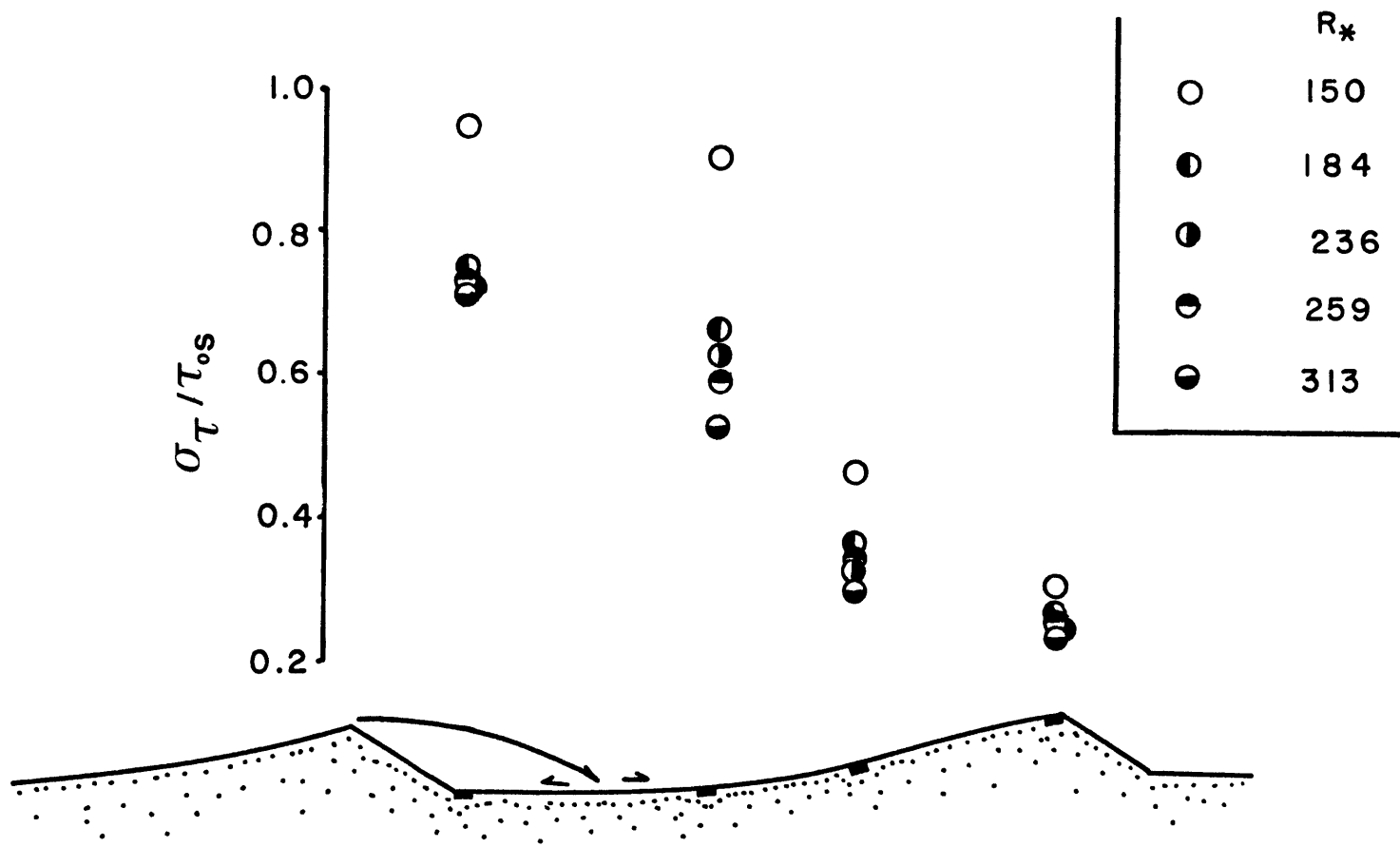
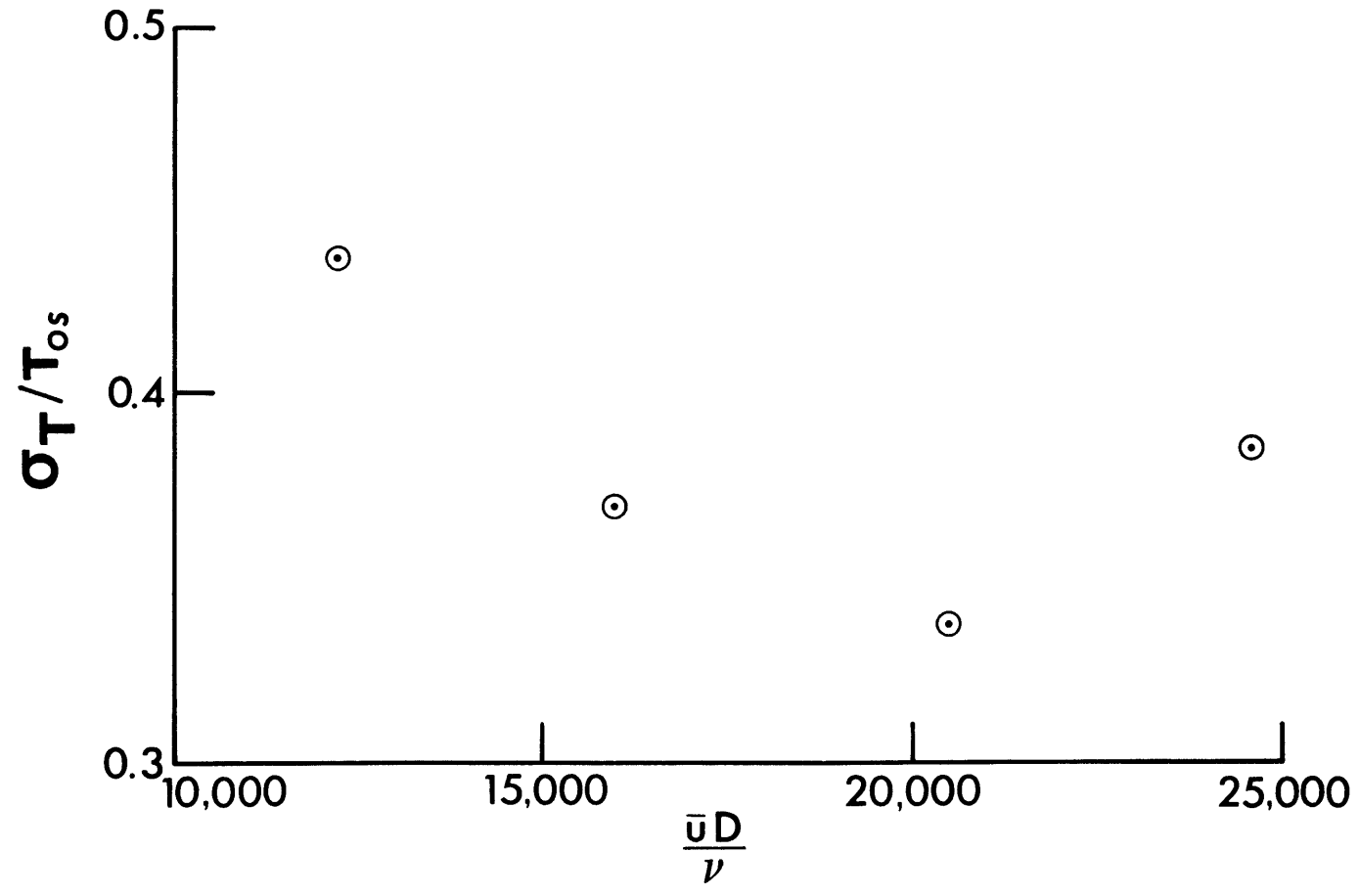


Figure 2.17. Relative fluctuation intensity  $\sigma_\tau/\tau_{0S}$  of skin friction as a function of bulk Reynolds number  $D\bar{u}/\nu$  for smooth flow.



falls from 1.2 at  $R=6,000$  to 0.22 at  $R=136,000$ . Kreplin and Eckelmann themselves report a value of 0.25 at  $R=7,700$ . Their experiment was conducted in oil whose viscosity  $\nu$  is six times that of water, and it included velocity measurements down to  $(u^*y/\nu)=2$ . The relative fluctuation intensity of the velocity increases from 0.25 at the wall to 0.38 at  $(u^*y/\nu)=5$ . It is possible that the large sensors (1.8mm long) used in this study give erroneously large values for  $\sigma_\tau/\tau_{OS}$  because they develop a relatively thick thermal boundary layer (section 1.23) compared with those of Kreplin and Eckelmann, which are 0.15mm long. However, the sensors used by Blinco and Simons, who obtained results similar to those reported here, are only 0.25mm long. No conclusion can be drawn at present as to whether the relative fluctuation intensity varies with Reynolds number, sensor length, or both. A careful intercomparison of sensors of different lengths over Reynolds numbers in the range  $10^3 - 10^5$  is needed to resolve this question.

It is striking that the relative fluctuation intensity falls off with  $R^*$  much more rapidly near reattachment than at the crest. Without a full turbulence model it is difficult to determine the reason for this, but it is clear that the contribution of the wake, which is most important near reattachment, increases more slowly with  $R^*$  than do either the mean skin friction or contributions to the fluctuating skin friction from other sources (sublayer bursting (Cantwell, 1981) or forcing by the outer flow, for instance).

It is worth noting that this effect is not related to variation in the position of the reattachment point with  $R^*$  (and hence  $R$ ). There was no observable variation in the position of reattachment over the range of Reynolds numbers examined here; nor would any be expected on the basis of observations of reattachment behind simple backward-facing steps (Eaton and Johnston, 1981).

The relative fluctuation intensity in the recirculating region is comparable in magnitude to that at position 3 a similar distance downstream of reattachment, indicating that, at least near the wall, the fluid swept upstream of reattachment is relatively as turbulent as that swept downstream.

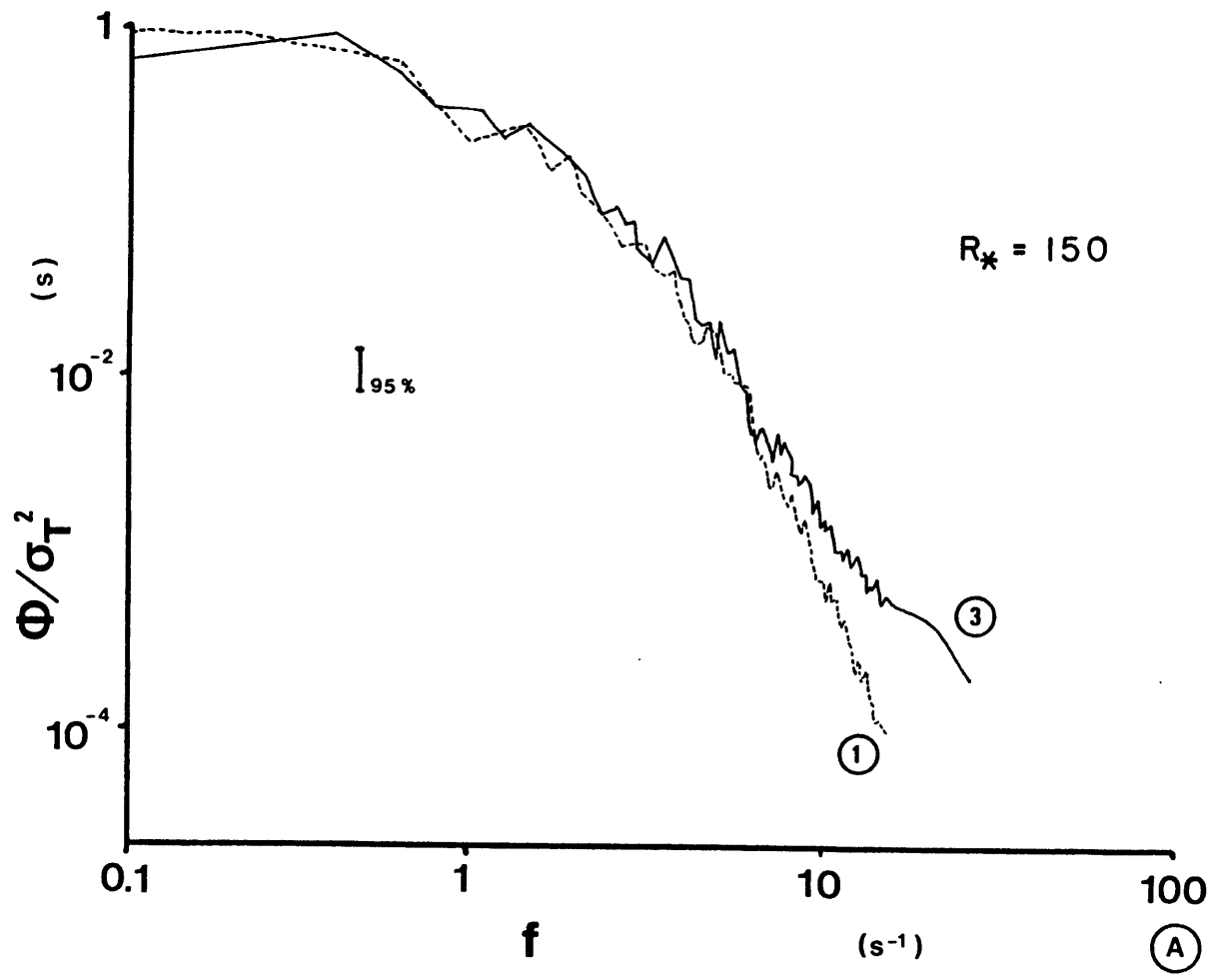
2.42. Spectra. Skin-friction spectra from sensors 1 (at the crest) and 3 (near reattachment) are shown in figure 2.18. The ordinate, the power density, has been normalized by the total variance of the signal ( $\sigma_\tau^2$ ) so that the curves shown all integrate to unity.

It is clear from figure 2.18 that there are no significant differences in spectra taken near reattachment and at the crest. This is somewhat surprising in view of the strong, coherent fluctuations known to exist in free-shear layers (Wyganski and Fiedler, 1970; Brown and Roshko, 1974), which the former workers report as giving rise to peaks in spectra measured near the edges of the layers. One might expect such peaks to appear in skin-friction spectra measured near reattachment. Their characteristic frequency may be

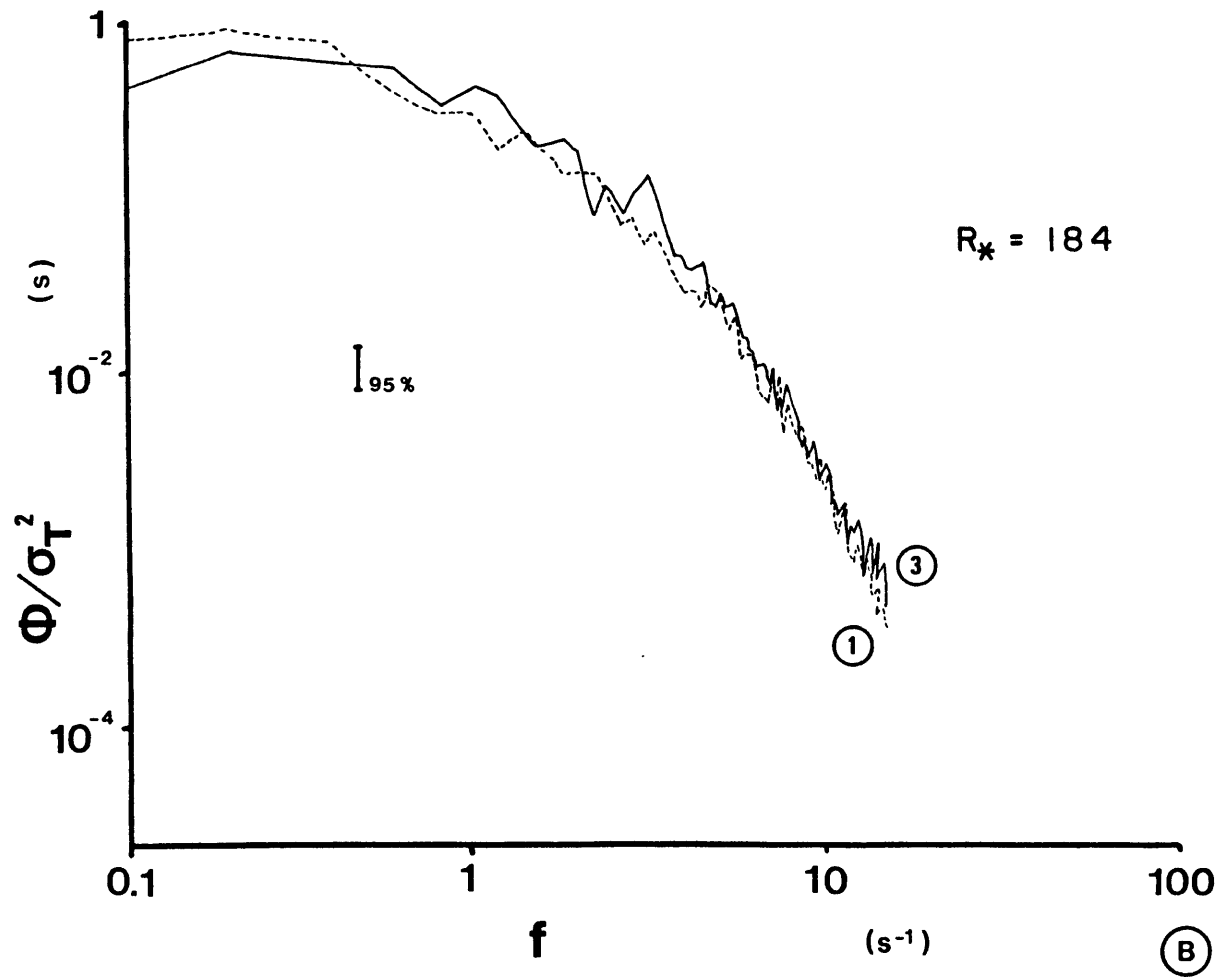
estimated as follows. Both Wygnanski and Fiedler (1970) and Brown and Roshko (1974) find that the wavelength of the large coherent eddies they observe increases linearly with distance from the beginning of the free-shear layer; the coefficients are about 0.5 and 0.6 respectively. Near position 3, the distance from separation is about 4 cm, so the expected wavelength is about 2 cm. Taking for the convection velocity the measured value at the midpoint of the eddy (that is, at  $z = 1$  cm in the mid-stoss profile) gives an expected frequency of about 5 Hz at  $R^* = 150$  and 7 Hz at  $R^* = 236$ . Both of these values are well within the resolution of the sensors used here (section 1.23). Apparently either the large eddies are not present in the mixing layer behind current ripples or they do not impart a characteristic peak in the skin-friction spectra. The latter seems the more likely explanation. If this is accepted, some light may be shed on the behavior of large eddies at reattachment points. Bradshaw and Wong (1972) have suggested that such eddies are torn in two as the flow splits at reattachment, while Kim et al. (1980) propose that instead they move alternately upstream and downstream from the reattachment area. In the latter case a spectral peak associated with the alternate passage of large eddies is to be expected; since none is observed the data presented here support the eddy-tearing hypothesis of Bradshaw and Wong.

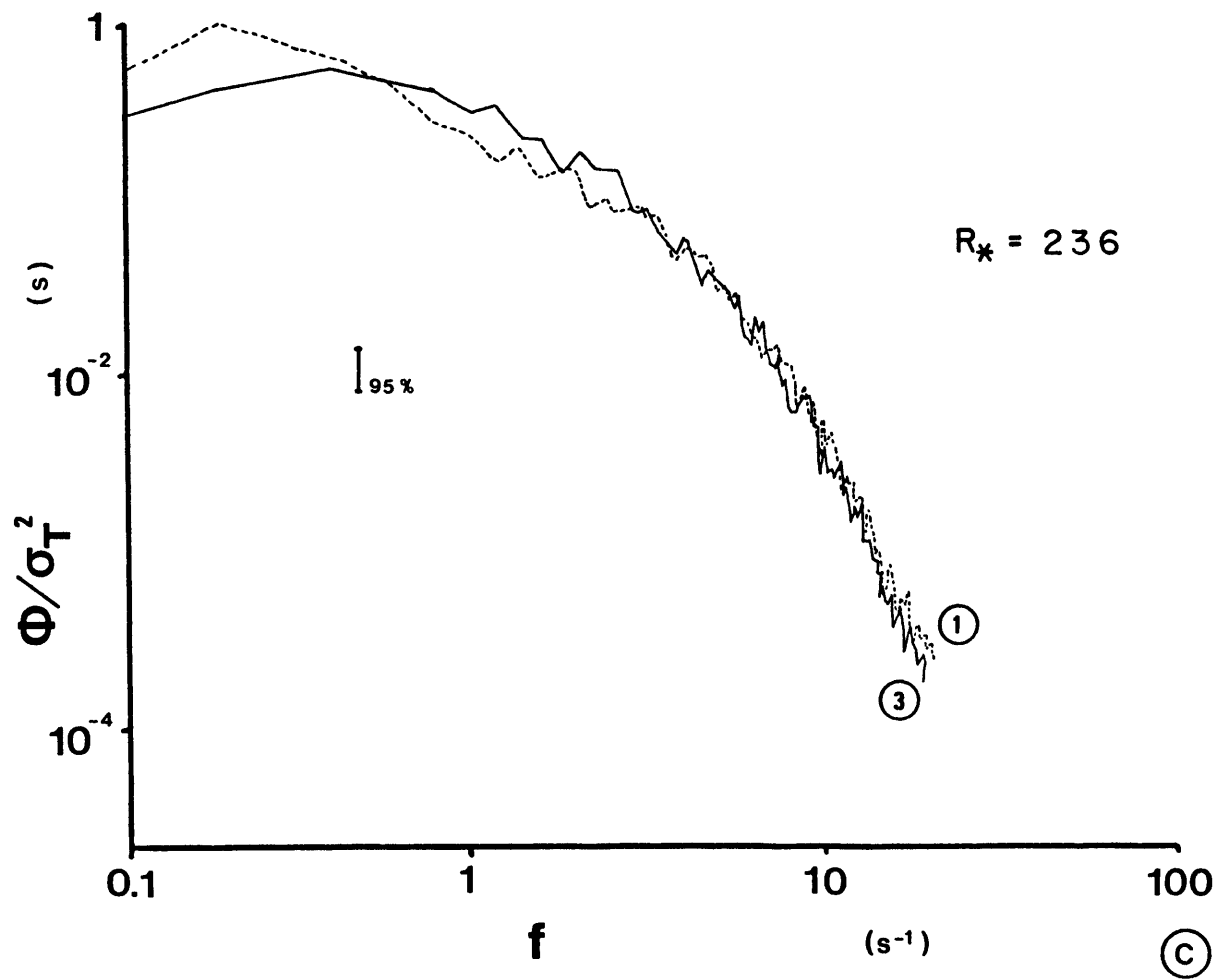
Figure 2.19 is a comparison of crest spectra with smooth-flow spectra obtained at similar Reynolds numbers. In

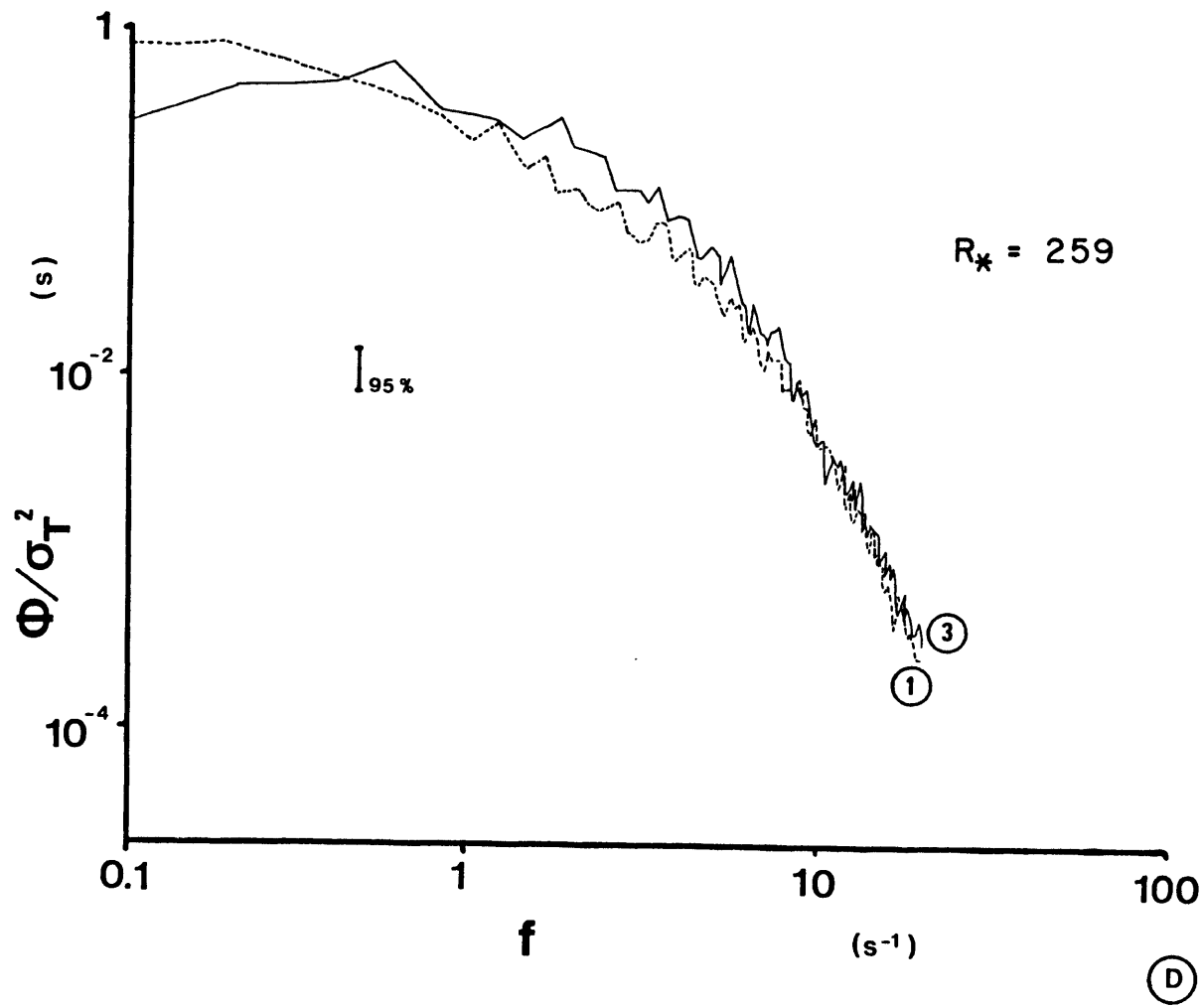
Figure 2.18. Power spectral density  $\phi$  of the skin friction, normalized by the total variance of the signal  $\sigma_\tau^2$ , as a function of frequency  $f$ . The data shown were measured at the crest (1) and near reattachment (3).











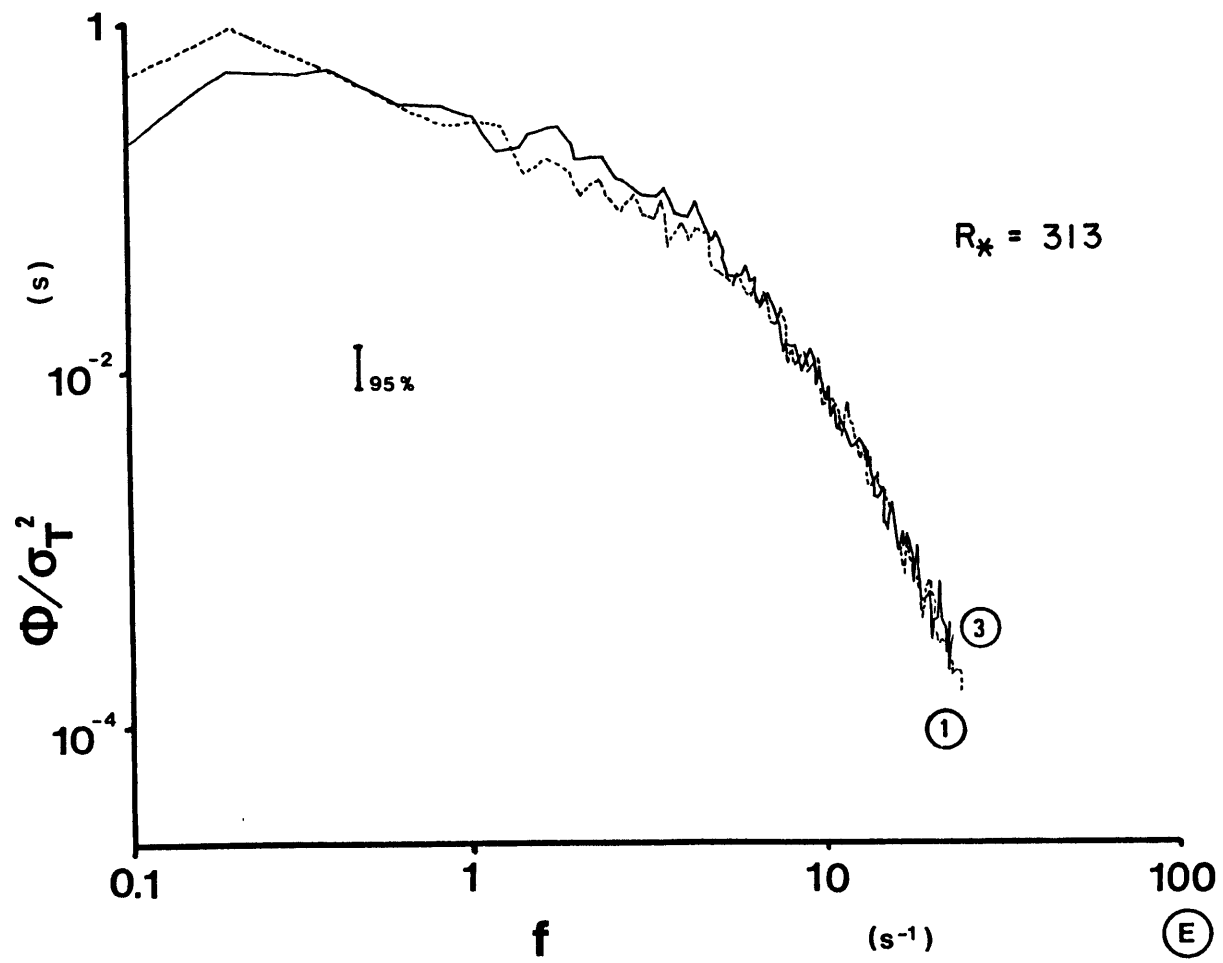
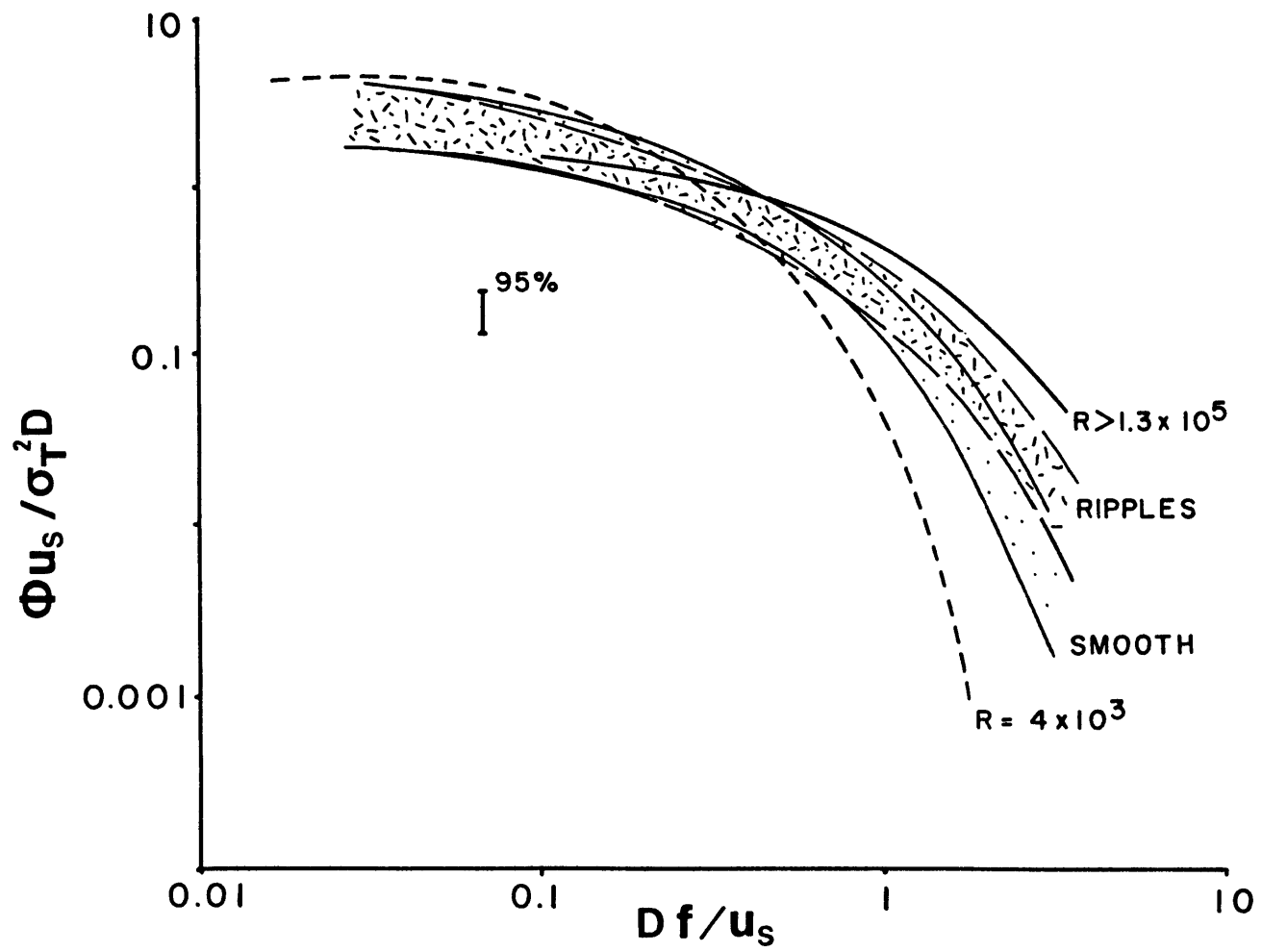


Figure 2.19. Nondimensional skin-friction spectra measured on two-dimensional ripples and in smooth flow. The frequency scale is  $u_s/D$ , where  $u_s$  is the free-surface velocity and  $D$  the depth. The solid and dashed curves are from smooth-flow data obtained at Reynolds numbers above and below those used here; they are taken from Sreenivasan and Antonia (1977).



addition to having been normalized by the variance  $\sigma^2$  as in figure 2.18, all the spectra have been nondimensionalized using the characteristic frequency  $u_s/D$ , where  $u_s$  is the surface velocity and  $D$  the depth. The nondimensionalization was applied to all five measured crest spectra, spanning a Reynolds number range of 16,100 to 34,200, and to four smooth-flow spectra, spanning a range of 12,400 to 24,600. Among each of these two sets the nondimensionalized spectra were found to overlap to within the 95% confidence interval so only the envelopes containing all the data are shown. The two envelopes differ systematically: there is relatively more energy at high nondimensional frequencies in the ripple spectra than in the smooth-flow spectra.

Sreenivasan and Antonia (1977) also found  $u_s/D$  to be effective in collapsing smooth-flow skin-friction spectra. However, they found that nondimensionalized spectra obtained by various investigators over a wide range of Reynolds numbers exhibit systematic variation: energy is shifted from low to high nondimensional frequencies as  $R$  increases. Two of the spectra included by Sreenivasan and Antonia in their synthesis are shown in figure 2.19 for comparison with ours. The two spectra bound the ones presented here with respect to  $R$ , and ours plot between them, as expected. It is possible that the observed differences between smooth-flow and ripple spectra are due to such a Reynolds-number effect, since the latter were obtained at somewhat higher Reynolds numbers. The Reynolds-number ranges for both sets of spectra are

greater than the differences between the sets, however, and within each set the nondimensionalization collapses the spectra to within the 95% confidence band. The differences in shape between smooth-flow and ripple skin-friction spectra probably reflect the contribution to the latter of relatively small-scale (hence high-frequency) turbulence generated in the wakes of the ripples.

2.43. Probability density functions (PDFs). Skin-friction PDFs are shown as a function of sensor position and  $R^*$  in figure 2.20. Since the probability density function  $p(T_{OS})$  of a random variable  $T_{OS}$  has unit integral by definition, only the shapes of the distributions can vary, so those shown in figure 2.20 are arbitrarily normalized to constant maximum value.

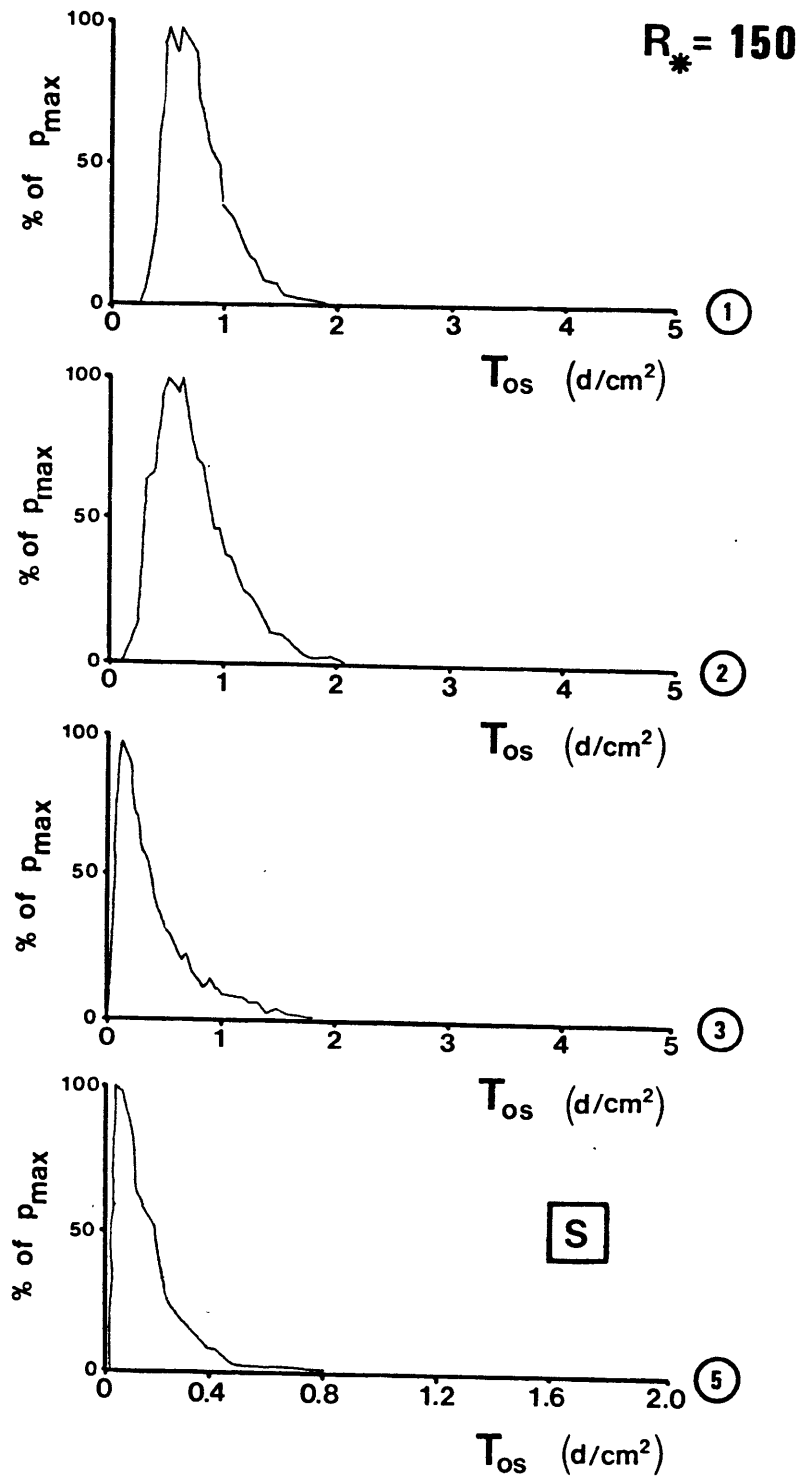
Unlike the spectra, the shapes of the PDFs vary strongly with position but not with  $R^*$ . The moments of PDFs are commonly used as measures of their shapes; the first (mean) and second (variance) were discussed in sections 2.31 and 2.41. The normalized third moment is called the skewness ( $Sk$ ) and is defined by

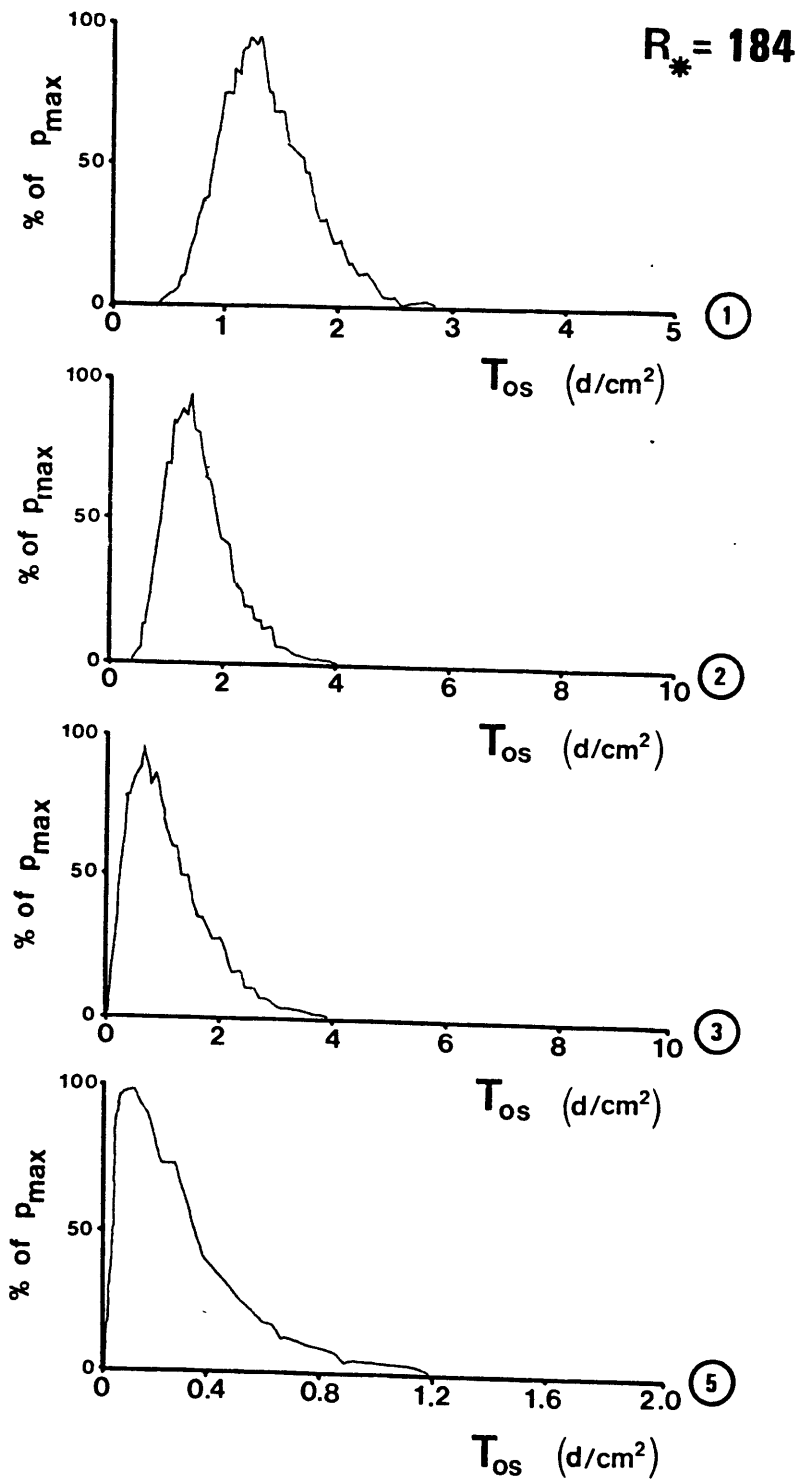
$$Sk = 1/\sigma_{\tau}^3 \int_{-\infty}^{\infty} p(\tau'_{OS}) \tau'_{OS}{}^3 d\tau'_{OS} \quad 2.16$$

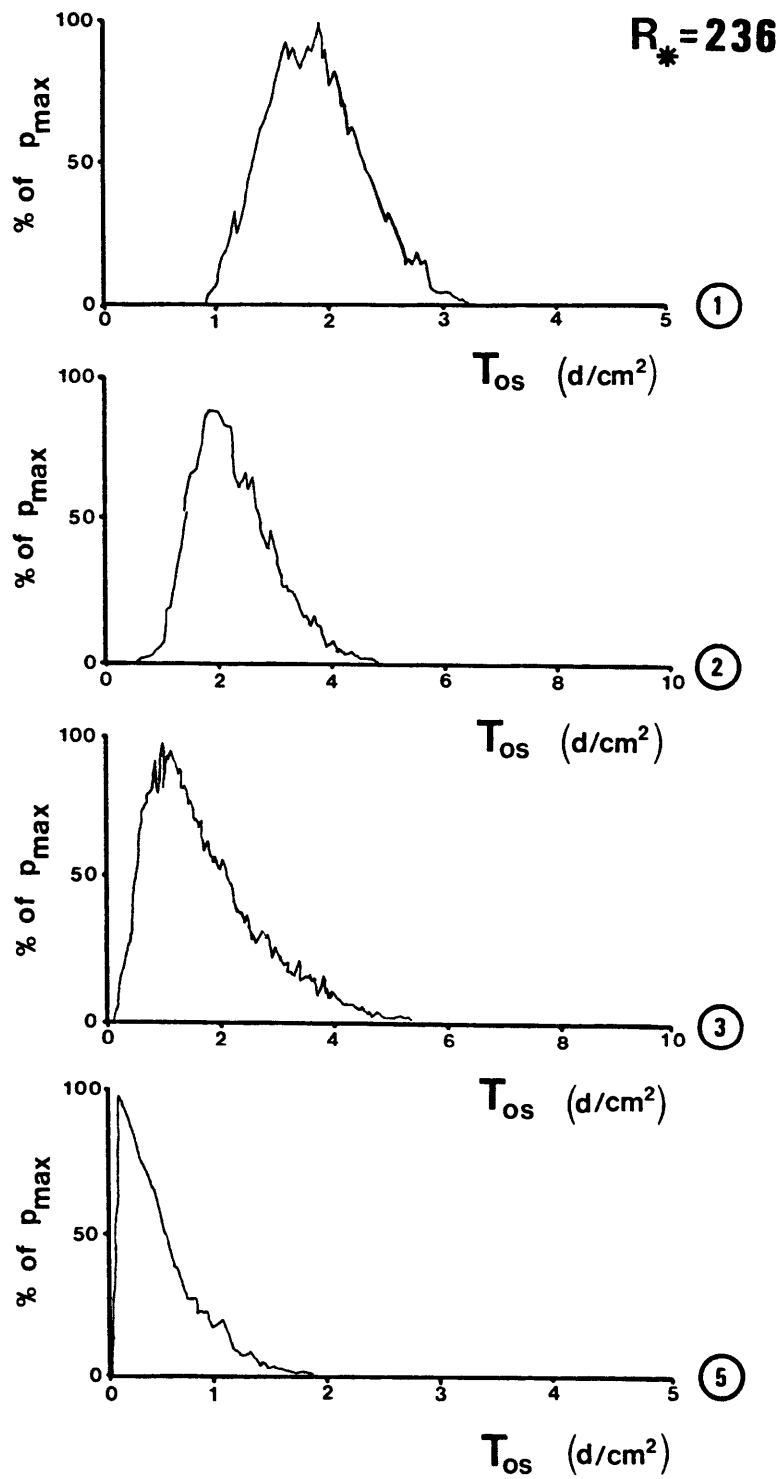
Since  $Sk$  is an odd nonlinear function of  $\tau'_{OS}$ , it is sensitive to asymmetry in the distribution; a positive skewness indicates that positive fluctuations tend to be large and infrequent relative to negative ones. The skewness of a Gaussian PDF is zero.



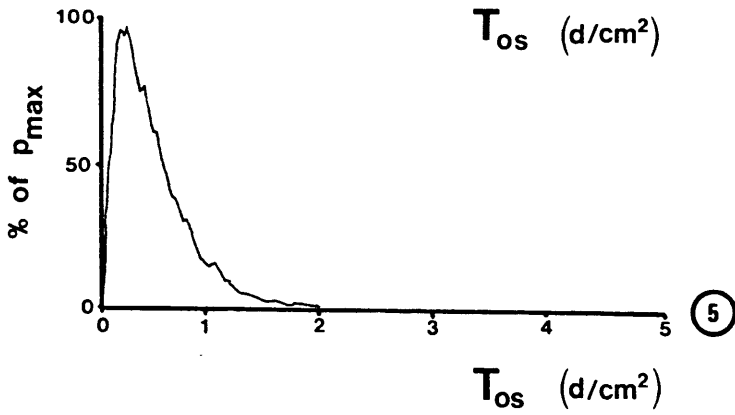
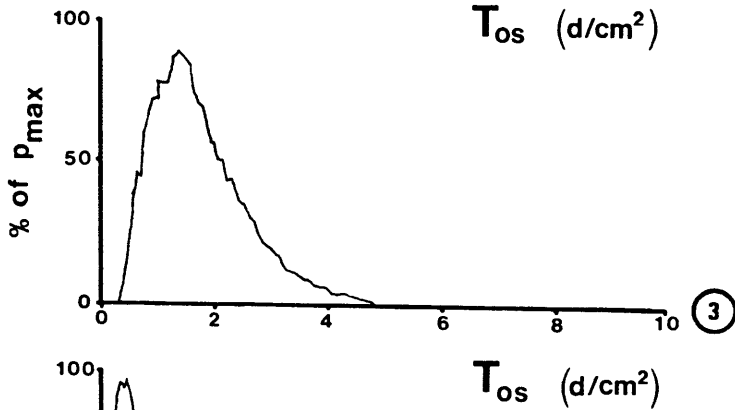
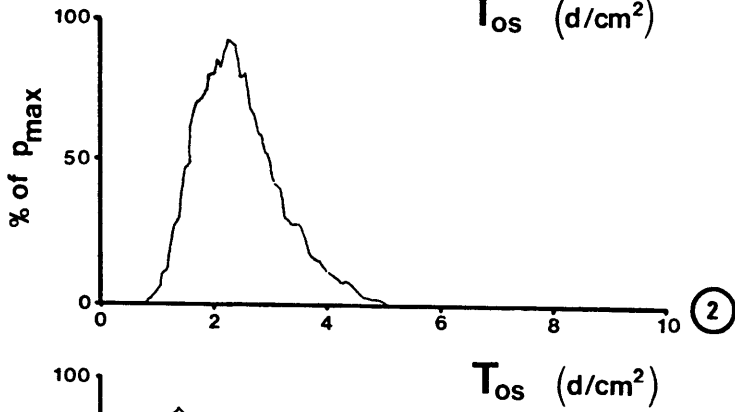
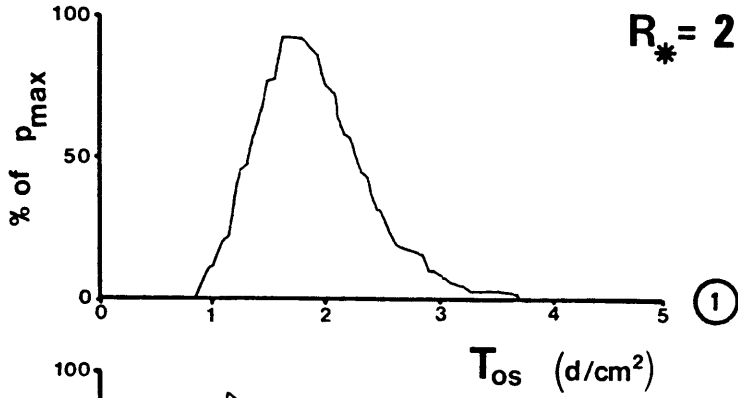
Figure 2.20. Probability density functions of the instantaneous skin friction  $T_{OS}$  for all sensor positions and roughness Reynolds numbers  $R^*$ . The PDFs are normalized to constant height. For graphs marked "S" the sampling rate was 64 Hz; for the others the sampling rate was 128 Hz.



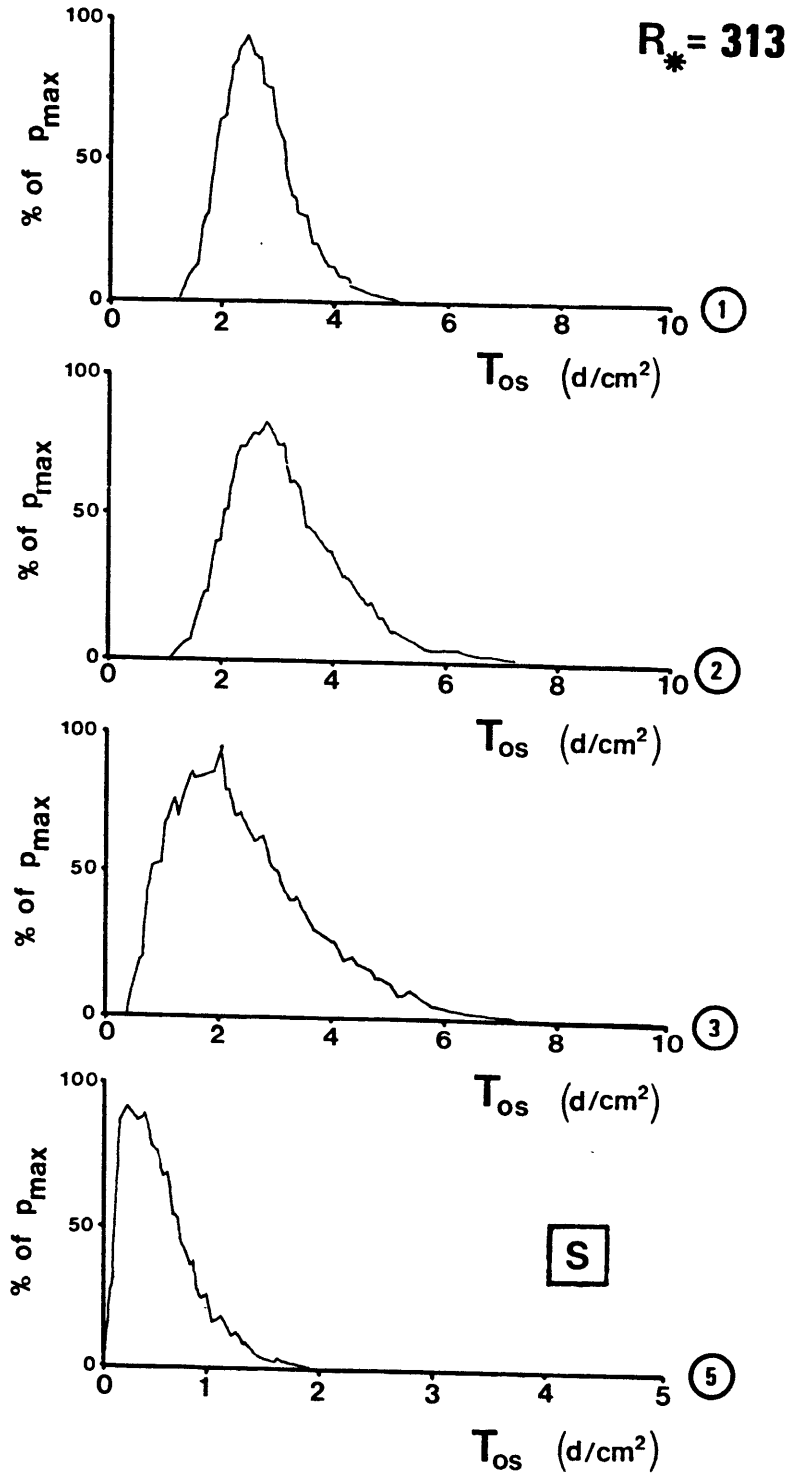




$R_* = 259$



D



The normalized fourth moment is called the kurtosis (Ku) and is given by

$$Ku = 1/\sigma_{\tau}^4 \int_{-\infty}^{\infty} p(\tau'_{os}) \tau'_{os}{}^4 d\tau'_{os} \quad 2.17$$

This is an even function of  $\tau'_{os}$  but because of the large power to which  $\tau'_{os}$  is raised in the integrand it is mainly sensitive to extreme fluctuations. Hence a large kurtosis reflects a distribution dominated by large, infrequent fluctuations from the mean in both directions -- in other words, a peaked time series. The kurtosis of a Gaussian PDF is 3.0.

The skewness and kurtosis values corresponding to the measured PDFs are given in Tables 2.2 and 2.3. The skewness is always positive, as we have observed in smooth flows (Table 2.4) at comparable bulk Reynolds numbers. Both skewness and kurtosis increase going from crest to trough. The crest values show no strong trend with  $R^*$  but the trough values decrease with increasing  $R^*$ . The maximum values are consistently found in the recirculating region (position 5); these show no clear trend with  $R^*$ . Evidently the reattaching flow contributes to the skin friction in large, infrequent pulses, and this effect is relatively stronger for positive fluctuations than for negative ones. It is noteworthy that the kurtosis is consistently greater than the Gaussian value of 3.0. Skin-friction time series are apparently relatively peaked, particularly when strongly disturbed by a reattaching free-shear layer.

Sensor Position	R = 16,100	20,700	23,300	30,000	34,200
	R* = 150	184	236	259	313
1	0.99	0.86	0.67	0.83	0.78
2	1.15	0.99	0.97	0.92	0.81
3	1.52	1.33	1.15	1.16	1.01
5	1.88	1.39	1.24	1.44	1.40

Table 2.2. Skin-friction skewness as a function of sensor position and roughness and bulk Reynolds numbers (R\* and R respectively).



Sensor Position	R = 16,100	20,700	23,300	30,000	34,200
	R* = 150	184	236	259	313
1	4.50	4.05	3.72	3.99	3.93
2	4.77	4.35	4.32	4.08	3.84
3	5.49	5.25	4.38	4.53	4.05
5	7.56	5.37	4.65	5.88	5.40

Table 2.3. Skin-friction kurtosis as a function of sensor position and roughness and bulk Reynolds numbers (R\* and R respectively).

	$\frac{\bar{u}D}{\nu}$	=	12,400	16,000	20,500
			_____	_____	_____
Skewness			1.11	0.95	0.80
Kurtosis			4.98	4.38	4.02

Table 2.4. Skin-friction skewness and kurtosis measured in smooth flow.

## 2.5. Discussion.

2.5.1. Why is the local response inviscid? Before attempting to answer this question I would like to put the results of the previous section in context by comparing them with a theoretical study that contains a locally inviscid region. Jackson and Hunt (1975; henceforth JH) considered the response of the atmospheric boundary layer to a hill of small, smoothly varying slope. They divided the flow into two layers. In the lower layer, the zero-order flow is that of the undisturbed boundary layer upstream translated onto the hill surface. In the upper layer, an inviscid response similar to (2.12) occurs. The pressure field it sets up is applied to the inner layer and causes it to vary from its zero-order form. The inner layer is analogous to the internal boundary layers discussed in section 2.11 in that it is a form of surface layer. It differs from an IBL, however, in that changes in it are driven by the pressure field imposed by the outer layer and are not the result of boundary layer growth; the latter is not present in the JH model because the boundary layer is never reset by the appearance of separated / reattaching flow. All changes in the Reynolds-stress field associated with the hill are confined to the inner layer as it adjusts to the variable pressure field. The outer layer responds in an inviscid manner because the Reynolds-stress field there is not affected by the hill. Clearly, this cannot be the case in the locally inviscid

region described by (2.14), since this is just where the large Reynolds stress maximum associated with the wake field occurs (Raudkivi, 1966). The problem, then, is to determine what conditions have to be met in order that (2.14) may accurately describe the flow field in this region.

First we need a formal decomposition for the spatially averaged and fluctuating parts of the flow; for simplicity this is done in Cartesian coordinates. The flow is governed by the Reynolds equation (2.11). The spatial averaging operator is defined as in section 2.32 by  $\langle a \rangle = (1/\lambda) \int_0^\lambda a dx$ . In this section, the notation follows that of section 2.32 except that double overlining is used in addition to angle brackets to denote spatial averages. Double primes denote spatial fluctuations.

Substituting  $u_i = \bar{u}_i + u''_i$ ,  $p = \bar{p} + p''$ , and  $\tau_{ij} = \bar{\tau}_{ij} + \tau''_{ij}$  into (2.11) we obtain equations analogous to the Reynolds equations; for the averaged field,

$$\bar{u}_{i,t} + \bar{u}_j \bar{u}_{i,j} = -(1/\rho) \bar{p}_{,i} + \bar{\tau}_{ij,j} - \langle u_j u_i \rangle_{,j} \quad 2.18$$

and for the fluctuating field,

$$u''_{i,t} + \bar{u}_j u''_{i,j} + u''_j \bar{u}_{i,j} = -(1/\rho) p''_{,i} + \tau''_{ij,j} \quad 2.19$$

The next step, given that equation (2.19) governs the spatially fluctuating momentum field, is to find sources of

vorticity in it. Taking the curl of (2.19) gives

$$\begin{aligned} & (\epsilon_{lik} u^{i,l})_{,t} + \bar{u}_j (\epsilon_{lik} u^{i,l})_{,j} + \epsilon_{lik} \bar{u}_{j,l} u^{i,j} \\ & + \epsilon_{lik} u^{j,l} \bar{u}_{i,j} + u^{j,l} (\epsilon_{lik} \bar{u}_{i,l})_{,j} = \epsilon_{lik} (\tau^{ij,j})_{,l} \end{aligned} \quad 2.20$$

However

$$\begin{aligned} \epsilon_{lik} \bar{u}_{j,l} u^{i,j} &= \epsilon_{lik} \bar{u}_{j,j} u^{i,l} - \epsilon_{lji} \bar{u}_{j,l} u^{k,i} \\ &+ \epsilon_{lik} \bar{u}_{i,l} u^{j,j} - \epsilon_{lji} \bar{u}_{k,i} u^{j,l} - \epsilon_{lik} \bar{u}_{i,j} u^{j,l} \end{aligned} \quad 2.21$$

Substituting (2.21) into (2.20) and using  $u^{j,j} = \bar{u}_{j,j} = 0$  gives

$$\begin{aligned} & (\epsilon_{lik} u^{i,l})_{,t} + \bar{u}_j (\epsilon_{lik} u^{i,l})_{,j} = -u^{j,l} (\epsilon_{lik} \bar{u}_{i,l})_{,j} \\ & (\epsilon_{lji} u^{j,l}) \bar{u}_{k,i} + (\epsilon_{lji} \bar{u}_{j,l}) u^{k,i} + \epsilon_{lik} (\tau^{ij,j})_{,l} \end{aligned} \quad 2.22$$

In classical vector notation this is

$$\frac{\overline{D}\vec{\omega}}{Dt} = -\vec{u} \cdot \nabla \vec{\omega} + \vec{\omega} \cdot \nabla \vec{u} + \vec{\omega} \cdot \nabla \vec{u} + \nabla \times (\nabla \cdot \underline{\tau})$$

where  $\underline{\tau}$  is the spatially fluctuating stress tensor and the total derivative  $\overline{D}/Dt$  incorporates advection by the spatially averaged field only:  $\overline{D}/Dt \equiv (\partial/\partial t + \vec{u} \cdot \nabla)$ .

The terms on the left-hand side of (2.22) represent the change in spatially fluctuating vorticity following a particle as it is advected by the spatially averaged velocity. The terms on the right are possible source terms. The first represents transfer of mean vorticity to

the fluctuating field by advection and will be discussed presently. The next two represent vortex-stretching; they are identically zero in two-dimensional flows such as those considered here. The last term embodies production of vorticity by shear stresses, the familiar source term in real-fluid flows.

In a two-dimensional flow, then, there are only two sources of vorticity, the first and fourth terms on the right side of (2.22). The first represents advection of mean vorticity by the spatially variable velocity; it is zero for the present case because the spatial averaging was done relative to the curvilinear  $(x, \zeta)$  system. Since the averaging has been carried out along lines  $\zeta = \text{constant}$ , the only component of the gradient of the spatially averaged vorticity is  $\partial^2 \bar{u} / \partial \zeta^2$ , normal to these lines. But the curves  $\zeta = \text{constant}$  were chosen specifically because they represent streamlines of the inviscid solution (2.12); hence there is no velocity component normal to them, in the direction in which  $\bar{u}$  changes. As a result,  $\vec{u} \cdot \nabla \bar{\omega} \equiv 0$ .

This leaves only the last term on the right-hand side of (2.22) to consider. There are no data sets obtained over bed forms comparable to those used here that include all the Reynolds-stress components, but it seems reasonable to focus attention on the component  $\tau''_{\zeta x}$ , which is known to be large in the wake region (Raudkivi, 1966; Etheridge and Kemp, 1978), and which is capable of inducing rotation in the plane

of the two-dimensional flow under consideration here. In particular, if the vertical gradient of this stress  $\partial \tau''_{\zeta x} / \partial \zeta$  is zero everywhere, then the production term will also be zero. Is this possible?

The extensive set of measurements by Zilker (1976) may be used to answer this question. The data include mean and fluctuating velocity components and skin friction, all measured over a series of sinusoidal beds whose wavelength was fixed at 5 cm and whose amplitude was systematically increased. The bed that most closely approximates the ripples has an aspect ratio of 8:1 and clearly caused flow separation. From a complete set of streamlines measured by Zilker, it is apparent that the bottom of the forward-going flow, deformed by the separation region, was not sinusoidal. To apply the inviscid model to this data, it was necessary first to approximate the observed bottom surface of the flow. Then the inviscid response was obtained by finding the Fourier-series representation of the surface and summing the contributions of each harmonic. None of the observed profiles turns out to be unperturbed, so the closest one (that at  $x/L = 0.8$ ) has been chosen and the others are calculated relative to it. The scaling velocity is that of the unperturbed profile at the crest height and, as is the case for the ripple data, it is about equal to the original choice, half of the surface velocity. The results are shown in figure 2.21. It can be seen that the agreement between

measurements and calculations is excellent, even right at reattachment ( $x/L = 0.6$ ).

The shear stress  $\tau''_{\zeta x}$ , incorporated in the only remaining source of vorticity in equation (2.22), comprises the spatially variable part of the Reynolds shear stress plus a negligible viscous contribution. The vorticity production depends on the vertical gradient of this stress; the above evidence that the local response is irrotational suggests that the gradient ( $\partial \tau''_{\zeta x} / \partial \zeta$ ) must be zero. This amounts to requiring that Reynolds-stress profiles measured at different streamwise positions be parallel to one another. This is not an intuitive result but the measurements of Zilker (1976), shown in figure 2.22, bear it out remarkably well in the region to which the inviscid model applies (figure 2.21).

The data presented by Raudkivi (1966) do not include the detailed structure of the mean velocity field near the bed, so they cannot be used to test the inviscid model in detail. However, Raudkivi did determine the pressure field over his artificial dune; as mentioned earlier it is roughly sinusoidal in shape and out of phase with the bed by  $180^\circ$ . Solving (2.13) for  $\Delta p$ , the pressure difference between crest and trough, we obtain

$$\Delta p = 4 \pi \rho U_o^2 a / L \quad 2.23$$

For Raudkivi's measured  $\Delta p$  (1966, Figure 3), this can be solved to give an approximate reference velocity  $U_o = 22$  cm/s. The lowermost velocity measured at the  $3L/4$  position



Figure 2.21. Mean-velocity profiles measured by Zilker (1976) at different streamwise positions over a sinusoidal bed (open symbols) compared with the results (filled symbols) of adding a first-order inviscid solution to the profile measured at  $x/L = 0.8$ . The scaling velocity  $u_0$  used in the inviscid solution is given by the cross-hair symbol.

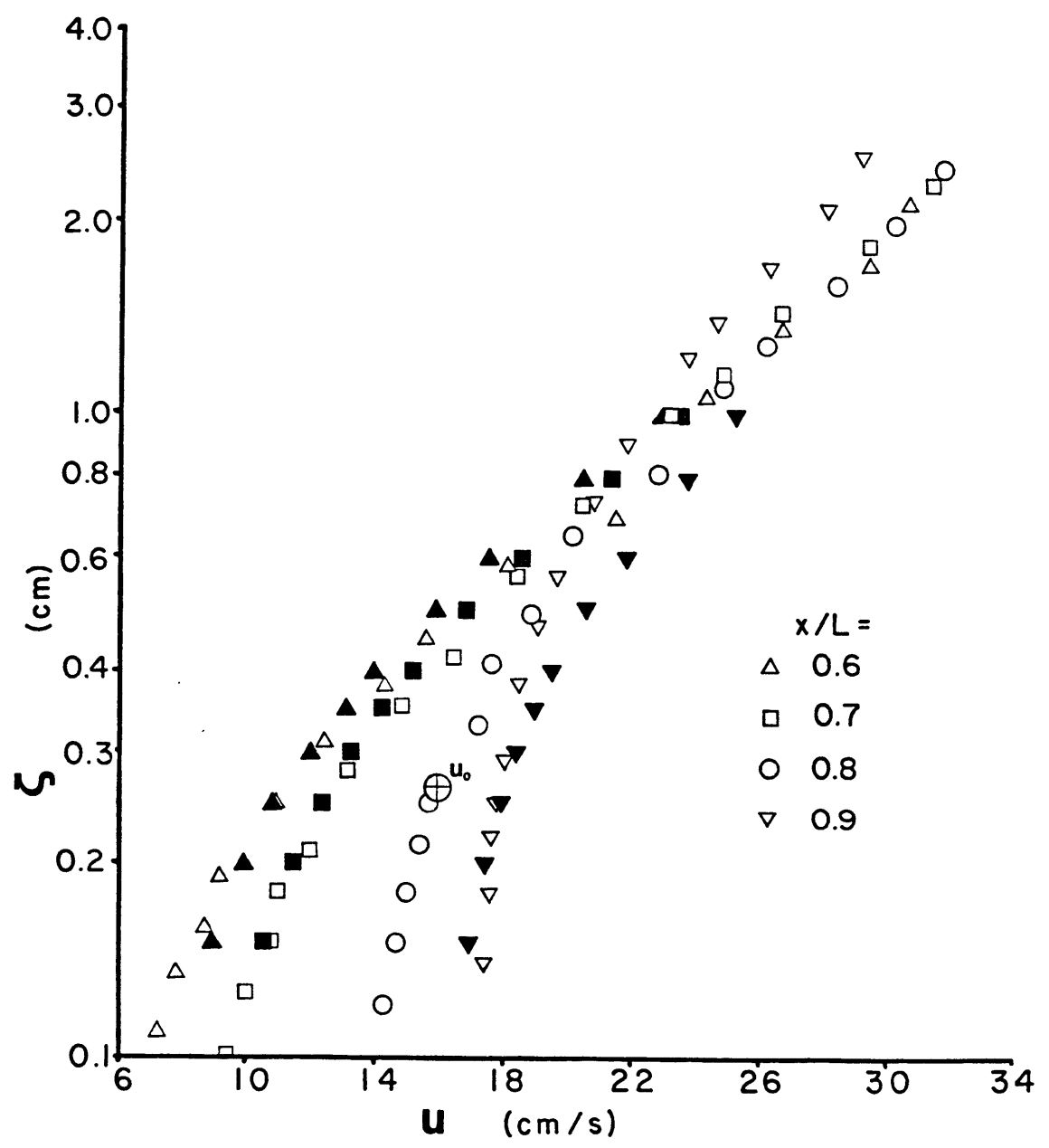
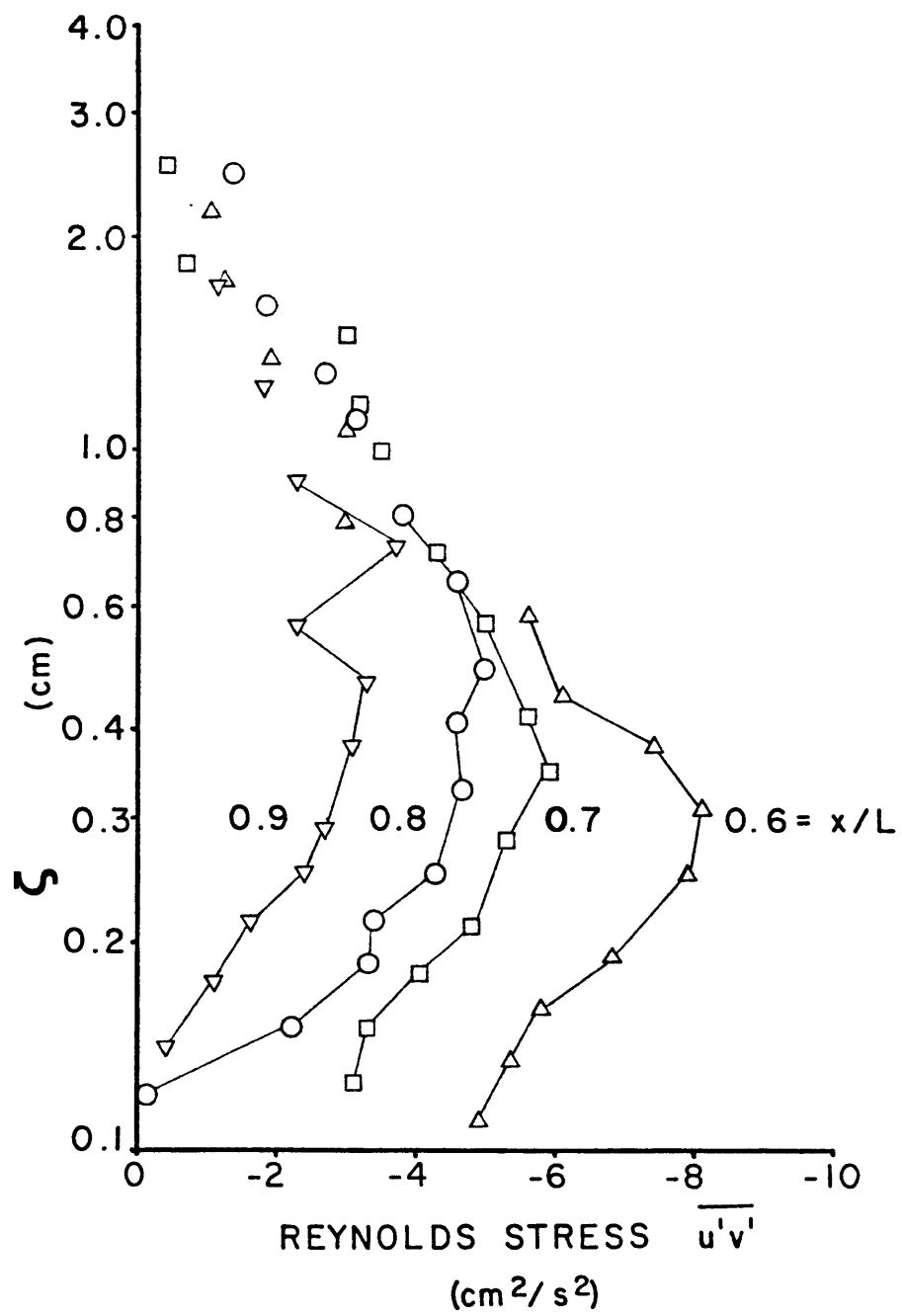


Figure 2.22. Profiles of Reynolds shear stress obtained by Zilker (1976) at different streamwise positions over a sinusoidal bed.



(that of the unperturbed profile) is 26 cm/s and was taken slightly above the ripple crest. Hence our inviscid scaling velocity is approximately consistent with Raudkivi's measured pressure field.

Inspection of Raudkivi's (1966, Figure 4) Reynolds-stress profiles indicates qualitative disagreement with Zilker's results, shown in figure 2.22; the characteristic bulge associated with the production of Reynolds stresses in the wake disappears well upstream of the next bed-form crest. However, these results have been disputed by Etheridge and Kemp (1978), who made similar measurements using more sophisticated techniques. The latter workers suggest that Raudkivi's data are off in just the sense expected on the basis of the preceding theory; that is, that the Reynolds-stress bulge is more persistent than Raudkivi reports. The data of Etheridge and Kemp were unfortunately obtained behind a step on a flat bed so the acceleration that occurs over the back of a dune or ripple is not present. There is a clear need for high-quality measurements of the complete momentum field over the backs of bed forms to determine the relation between Reynolds-stress and velocity profiles as the aspect ratio increases from  $O(10)$  to  $O(100)$ .

2.52. Comparison of the results with drag-partition theories. The separation of  $\tau_{ot}$  on a macrorough bed into its components  $\tau_{of}$  and  $\tau_{os}$  is called drag partitioning. Einstein and Barbarossa (1952) approached the problem by dividing the total hydraulic radius  $r_h$  (the cross-sectional area of the flow divided by the wetted perimeter) into two parts,  $r_{hs}$  related to the skin friction and  $r_{hf}$  related to the form drag. They proposed that  $r_{hs}$  could be determined as follows. By vertically averaging the velocity profile (1.6) over a depth  $D$ , one obtains for the average velocity  $\bar{u}$

$$\frac{\bar{u}}{u_*} = \frac{1}{\kappa} \left[ \ln \left( \frac{D}{z_o} \right) - 1 \right] \quad 2.24$$

For a wide channel  $r_h \approx D$  and the formal division of the hydraulic radius given above allows us to write

$$\frac{\bar{u}}{\sqrt{(gD_s S)}} = \frac{1}{\kappa} \left[ \ln \left( \frac{D_s}{z_{os}} \right) - 1 \right] \quad 2.25$$

where  $z_{os}$  is the roughness length associated with the skin friction. Equation (2.25) implicitly incorporates the idea of the double logarithmic layer outlined in section 2.12 since it relates the skin friction to the surface roughness length through the local-equilibrium law (1.6).  $D_s$  should thus be equal to the height of the equilibrium surface layer. The additional assumption that makes (2.25) useful in practice is that  $\bar{u}$  may be approximated as the mean velocity averaged over the whole depth, not just the surface layer as implied in the derivation. For known  $\bar{u}$ , then, (2.25) can be

used to find  $D_S$  implicitly and  $\langle \tau_{OS} \rangle$  can then be found from

$$\langle \tau_{OS} \rangle = \rho g D_S S \quad 2.26$$

The Einstein-Barbarossa method was applied to the present data with the results given in Table 2.5 in the form  $u_*^s/u_*^t$ ; the measured values are given for comparison. The overall calculated mean is 0.62; the measured value is 0.57, so the results agree to within 9%. The fact that the method overestimates the skin friction is presumably due in part to the use of the whole depth-averaged velocity rather than that in the surface layer. Accordingly, an iterative scheme was attempted in which the first calculated value of  $D_S$  was used to estimate  $\bar{u}$ , which was then used to improve  $D_S$ , and so forth. The iteration does not converge, however; the calculated values of  $D_S$  and  $\bar{u}$  decrease continuously. This is because (2.25) is not accurate unless (1.6) describes the flow in the surface layer, which it does not in the present set of experiments. There is no clear justification for cutting off the iteration at any particular point, so the original estimates must be accepted even though they are somewhat too large.

An even simpler approach to drag partition is to calculate the form drag from the Carnot formula for the energy loss through a series of expansions. This reads (Engelund, 1966):

$$S_f = \frac{\bar{u}^2}{2gL} \left(\frac{h}{D}\right)^2 \quad 2.27$$

where  $S_f$  is that part of the energy slope (the free surface

$R^*$	$\frac{\langle u^*_s \rangle}{u^*_t}$ Calculated	$\frac{\langle u^*_s \rangle}{u^*_t}$ Measured	$\frac{\langle u^*_s \rangle_{calc}}{\langle u^*_s \rangle_{meas}}$
150	0.58	0.52	1.12
184	0.62	0.64	0.97
236	0.59	0.61	0.97
259	0.65	0.54	1.20
313	0.63	0.58	1.09

Table 2.5. Comparison of nondimensional spatially averaged skin-friction velocities calculated according to the method of Einstein and Barbarossa (1952) with values measured in this study.



slope in uniform flow) that is consumed by form losses,  $h$  is the height of the bed forms, and  $L$  their wavelength. This relation is derived by calculating the loss in kinetic energy required as the flow passes through each expansion and summing; it is assumed that the free surface remains undeformed, so it is valid when the squared Froude number ( $F^2 = \bar{u}^2/gD$ ) is small. This condition is met in the present case;  $F^2$  never exceeded 0.11. The form drag  $\tau_{of}$  may be calculated from (1.8) using the total depth  $D$  and  $S_f$ . Values of  $\tau_{of}$  calculated in this way are given as ratios of calculated to measured values in Table 2.6. The overall mean is 0.90, so this simple method also gives fairly good agreement with the data.

$R^*$	$\frac{(u_*f)_{\text{calculated}}}{(u_*f)_{\text{measured}}}$
150	0.84
184	0.98
236	0.87
259	0.92
313	0.89

Table 2.6. Comparison of Engelund's (1966) method for calculating form drag with the results of this study.

### 2.53. Application to sediment-transport calculations.

Both spectra and probability density functions of skin friction bear on calculating sediment transport over bed forms. The relevance of the observed spectra can best be considered in terms of the response times of grains. Grant and Madsen (1982) estimated the time required for a grain of very fine sand to reach 90% of its final velocity upon sudden imposition of a steady shear stress, under conditions of strong sediment transport. They found it to be about 0.01 s, implying that under these circumstances the sediment would respond in a quasi-steady manner to shear stresses fluctuating at up to O(100 Hz).

This estimate indicates that the response of typical grains to fluctuating shear stresses becomes attenuated only at frequencies far greater than those of the energy-containing (or even measurable) region of the skin-friction spectrum. Hence the full skin-friction time series contributes to sediment transport.

In the absence of frequency-dependent effects, the time-averaged bed-load transport of sediment  $q_s$  by a fluctuating shear stress  $T_{os}$  is given by

$$q_s(\tau_{os}) = \int_0^{\infty} k_s(T_{os})p(T_{os})dT_{os} \quad 2.28$$

where  $k_s$  is a kernel function giving the instantaneous transport rate as a function of instantaneous skin friction  $T_{os}$ .

If  $k_s$  were known, (2.28) could be used to calculate local rates of sediment transport over the back of a ripple, but it is not. Since  $p(T_{0s})$  assumes a relatively simple form in smooth flows (Kreplin and Eckelmann, 1979), (2.28) could conceivably be inverted if  $q_s(\tau_{0s})$  were known for such conditions. But for transport conditions where ripples are stable they cannot be suppressed; as a result measured transport rates already include the effects of the varying mean and fluctuating skin friction that we would like to investigate. Another way to determine the kernel function  $k_s$  would be to take it to be the transport law for laminar-flow conditions, which could be measured. Such a project is beyond the scope of this work, but apparently progress in this direction has been made by Grass (1982 personal communication). Unfortunately the data are not yet available.

A qualitative understanding of the role of skin-friction fluctuations in bed-form mechanics may be gained by assuming that if fine sand could be transported on a flat bed under flow conditions for which ripples develop, it would obey the same transport law that coarse sediments do under similar conditions. Consider the continuity equation for bed-load transport of sediment (Middleton and Southard, 1977, p. 7.25):

$$\frac{\partial q_s}{\partial x} = -C \sigma \frac{\partial \eta}{\partial t} \quad 2.29$$

where  $\eta$  is the height of the bed and  $C_o$  is the volume concentration of sediment in the bed.

If a bed form propagates without change in form at a speed  $\sigma$ ,

$$\frac{\partial \eta}{\partial t} = \sigma \frac{\partial \eta}{\partial x} \quad 2.30$$

By eliminating  $\partial \eta / \partial t$  between (2.29) and (2.30), the shape  $\eta(x)$  can be related to the transport pattern  $q_s(x)$ :

$$-C_o \sigma \frac{\partial \eta}{\partial x} = \frac{\partial q_s}{\partial x} \quad 2.31$$

First  $\sigma$  must be determined. At the crest, all sediment transported moves over the edge to avalanche down the lee face so the transport rate there is related to the migration rate by

$$q_s = \sigma h C_o \quad 2.32$$

where  $h$  is the ripple height.

To calculate  $q_s$  we use the Meyer-Peter/Muller empirical transport law (Meyer-Peter and Muller, 1948):

$$q_s = \frac{8}{(s-1)g} (u_*^2 - u_{*c}^2)^{3/2} \quad 2.33$$

where  $d$  is the grain size,  $s$  is the specific gravity of the sediment, and  $u_{*c}$  is the critical skin-friction velocity for the initiation of sediment motion.

Our initial supposition was that this relation would

describe the motion of fine sand under flat-bed conditions. It is consistent with this to apply (2.33) at the crest to find the migration speed using (2.32), since the relative fluctuation intensity there is comparable to that in smooth flow (section 2.41).

We now have an initial value of  $q_s$  (that at the crest) and a migration speed. With these values and the measured ripple profile  $\partial\eta/\partial x$ , (2.31) can be used to calculate an apparent transport profile  $q_s(x)$ . Two low values of  $R^*$  were chosen to examine the behavior of the transport profile as the skin friction increases from near-critical conditions, where the fluctuations would be expected to be most important. The value for  $u^*_{sc}$  used in the calculations, 1 cm/s, is typical of fine sands (Miller et al., 1977).

In calculating  $u^*_{sc}$  the effect of the bed slope must be accounted for. If the bed slopes upward in the direction of flow at an angle  $\beta$  the revised value of  $u^*_{sc}$ , denoted by  $u^*_{sc\beta}$ , is given by (Madsen, 1975, ch. C):

$$(u^*_{sc\beta})^2 = (u^*_{sc})^2 \cos(\beta) \left(1 + \frac{\tan(\beta)}{\tan(\psi)}\right) \quad 2.34$$

where  $\psi$  is the angle of repose of the sediment, here taken to be  $30^\circ$ .

The results of the calculation are shown in figure 2.23. Qualitatively, the variation in  $u^*_s$  needed to maintain a stable bed is consistent with that measured. The greatest discrepancy occurs near reattachment and, as expected, the measured mean values are too low. The vertical bars in

Figure 2.23. Calculated profiles of skin-friction velocity (heavy lines) required to maintain a stable propagating ripple form, compared with measured values (open circles), for two values of  $R^*$ . The vertical lines extending from each circle represent one standard deviation ( $\sigma_{u_*}$ ) in the measured data.

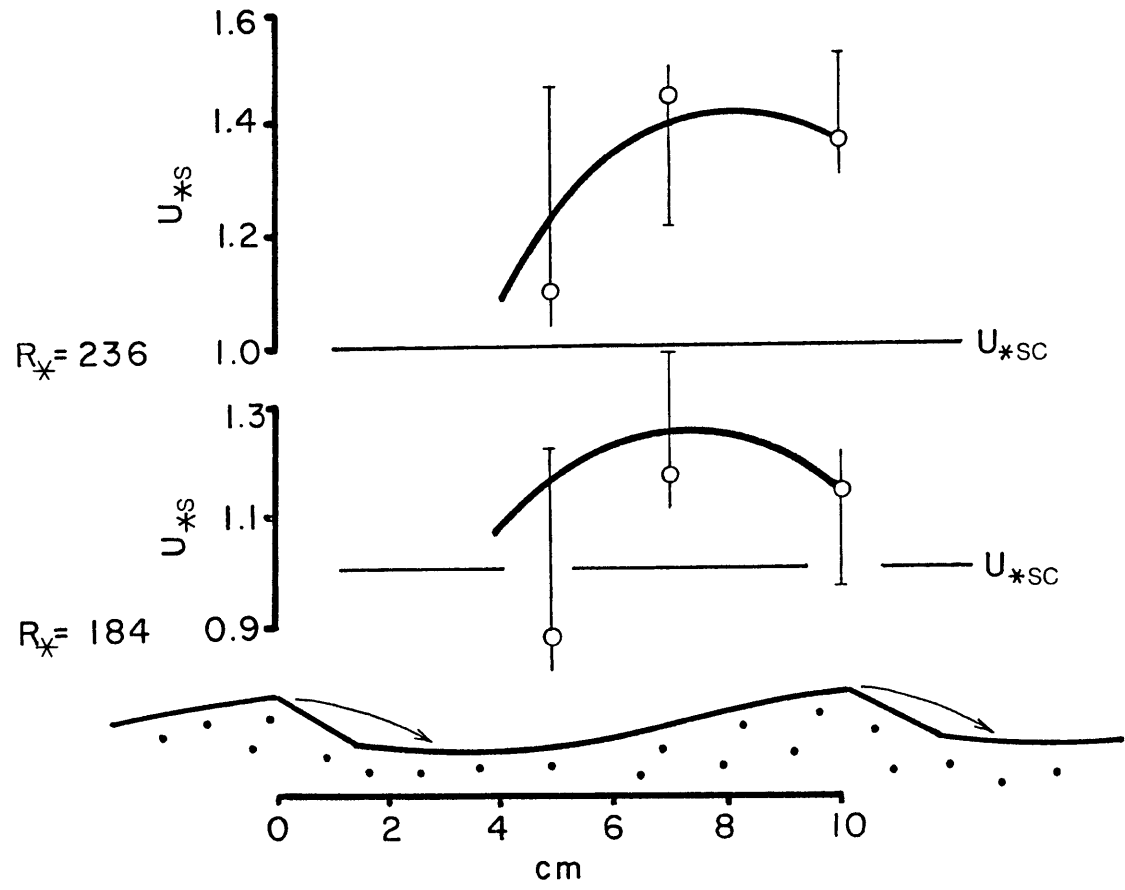




figure 2.23 show one standard deviation in the measured skin friction for comparison with the computations. To maintain a stable bed under the transport law (2.33) at  $R^* = 184$ , the combined mean and fluctuating skin friction near reattachment would have to transport sediment at a rate equal to that for a flat-bed skin friction nearly one standard deviation above the mean. This would require that the function  $k_S(T_{OS})$  be nonlinear, with an exponent greater than one, in which case the mean transport near reattachment would be enhanced by the strong positive skewness of the fluctuating skin friction there (figure 2.20). Also shown in figure 2.23 are the minimum (horizontal-bed) values of  $u_{*SC}$  encountered on the bed form. For  $R^* = 184$ , the measured  $u_{*S}$  near reattachment is well below this, resulting in the relatively large difference between the measured and calculated values. This is not the case for  $R^* = 236$ , and here the discrepancy between measured and calculated  $u_{*S}$  near reattachment is much smaller. Comparison of the computations for both values of  $R^*$  suggests that the importance of the fluctuations in transporting sediment is greatest for near-critical conditions and diminishes as the total bottom stress increases. Consistent with this, it was observed that if the ripples were dusted with a layer of fine sand about one grain diameter thick and the flow was increased slowly from subcritical conditions, initial motion occurred first in the trough, where the fluctuations are largest, rather than on the crest, where the mean is largest.

2.54. Implications for bed-form dynamics and classification. The behavior of the boundary layer over current ripples described in this study differs fundamentally from that proposed by Smith and McLean (1977) for flow over sand waves. The systems examined differ in two important respects: scale and aspect ratio. Both must be considered in comparing the two studies.

Smith and McLean measured the flow field over bed forms of the order of 1 m high and with an aspect ratio of order 50 in water 10 m deep. They modelled the flow in terms of two layers: a lower equilibrium surface layer and an outer integrated logarithmic layer. Although a model for the whole flow field was developed, it was compared with data only on a spatially averaged basis.

The present set of experiments was conducted over current ripples 1 cm high, whose aspect ratio was 10, in water 10 cm deep. The velocity data from the lower part of the surface layer display semilogarithmic profiles (to a typical  $r^2$  value of 0.99 for the lowermost six points; figure 2.15), so they may be compared with the spatially averaged law of the wall (2.3) derived by Smith and McLean. The apparent von Karman coefficient (the ratio of the skin friction  $\langle u_* \rangle$  to the semilogarithmic slope  $d\langle u \rangle / d(\ln(\zeta))$ ) that results is 0.50, comparable with the commonly accepted equilibrium-flow value of 0.4. However, I regard this as coincidence: intuition and a good deal of laboratory work (Bradshaw and Wong, 1972; Castro, 1979; Chandrsuda and Bradshaw, 1981) suggest that the

transfer of momentum beneath a reattaching free-shear layer is strongly influenced by the energetic large-scale turbulence generated in the layer and is thus qualitatively different from that over a flat bed. This is corroborated by applying the same analysis to the data of Zilker (1976; figure 2.21): here the apparent von Karman coefficient is 1.2.

In both Zilker's data and those reported here, the spatially averaged velocity profiles can be used to derive the remainder of the velocity field downstream of reattachment by applying potential theory, as summarized in figure 2.24. Further experimentation on similar flows should concentrate on this averaged profile. In particular, if the rotational part of the flow field always varies semilogarithmically near the wall, more data are required to determine what, if any, scaling velocity and length would make a relation analogous to (2.3) generally applicable. On the other hand, in the absence of an ESL, there is no reason that surface-layer velocity profiles need be semilogarithmic; the data reported here do not exclude the possibility that they may become curved near the bed in response to either wake-generated turbulence or spatial acceleration of the flow. In any case, it is clear from the results of the present experiments that agreement of spatially averaged data with (2.3) does not imply that the surface layer is in local equilibrium.

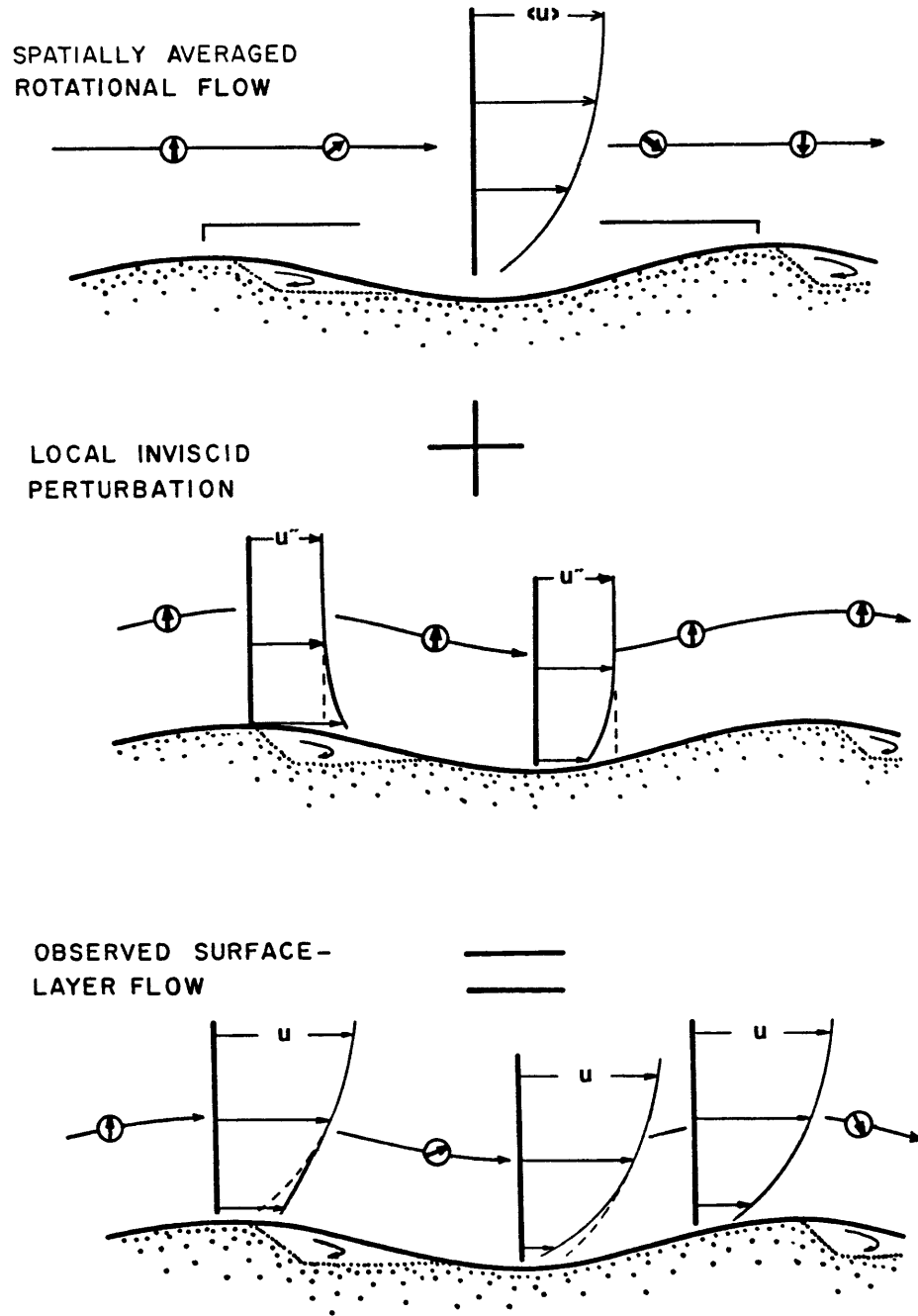
The absence of an ESL in the data presented here and those

of Zilker (1976) is not surprising in view of (2.2), which suggests that the ESL thickness is much less than the height of the crest unless the aspect ratio is  $O(100)$ . This relation, however, is based on IBL theory that assumes the growing boundary layer to be fully turbulent. (In this case the relation is scale-independent by virtue of Reynolds-number similarity). For the laboratory-scale flows considered here, this may not be true; the ESL may be no more than the local viscous sublayer required by the no-slip condition. In this case the ESL grows as a laminar boundary layer, and using (2.2) amounts to overestimating its thickness. This may contribute to the absence of an ESL in the data presented here, but based on (2.2) flow in the surface layer can never be fully in equilibrium for bed forms of small aspect ratio ( $O(10)$ ) regardless of scale.

On the other hand, Smith and McLean (1977) worked in the Columbia River on bed forms whose aspect ratio was some 5 times larger than those discussed above; all the boundary-layer elements relevant to this discussion were undoubtedly fully turbulent. Based on (2.2), for this case it is reasonable to expect an ESL that is a substantial fraction of the bed-form height in thickness.

One of the effects of reducing the aspect ratio, then, is to reduce the distance (relative to the crest height) over which an ESL can develop and so to restrict its height. There are two other contributions to the breakdown of an ESL

Figure 2.24. The surface-layer mean-velocity profile over a bed form of small ( $O(10)$ ) aspect ratio viewed as the sum of a spatially averaged rotational profile and a local irrotational perturbation.



model based on IBL theory as the aspect ratio becomes small, both of which concomitantly favor a locally inviscid response as described in section 2.32. The first is the development of a favorable pressure gradient. From the Bernoulli relation (2.10) it may be seen that the maximum pressure gradient goes inversely as the aspect ratio; the inviscid estimate is

$$\frac{1}{\rho} \frac{\partial p}{\partial x} \Big|_{\max} = u_o^2 a k^2 \quad 2.35$$

The pressure-gradient length scale  $L_p$  (section 1.22) then becomes

$$L_p = u_{*ss}^2 / u_o^2 a k^2 \quad 2.36$$

where  $\rho u_{*ss}^2$  is some representative skin friction; the spatially averaged value will be used here. If we estimate the surface-layer height as  $h$ , then the parameter that determines whether the pressure gradient is important in governing its dynamics is

$$\left(\frac{L_p}{h}\right) = \frac{u_{*ss}^2}{u_o^2 a k^2 h} = \frac{C_D}{2\pi^2} \left(\frac{L}{h}\right)^2 \approx 5 \times 10^{-4} \left(\frac{L}{h}\right)^2 \quad 2.37$$

where  $C_D$  is a drag coefficient equal to  $(u_{*ss}/u_o)^2$ ; it is about 0.01 for the present measurements.

If  $L_p/h < 1$ , then the surface layer is influenced by the pressure gradient. This is clearly necessary for an inviscid response, in which the pressure gradient is the only term available to balance the convective acceleration induced by

the surface topography, and for  $L/h = 10$  this condition is satisfied. On the other hand, application of IBL theory such as that outlined in section 2.11 requires that  $L_p/h > 1$  since the theory and empirical coefficients all refer to the constant-pressure case. If  $h/L = 100$ , this requirement is satisfied.

The other requirement for a locally inviscid response as discussed in section 2.51 is that the vertical gradient of the spatially variable Reynolds shear stress must be zero. Qualitatively it was shown in section 2.51 that this is true for Zilker's (1976) measurements, the only data set against which it could be checked. It is evident from figure 2.22 that this parallelism of shear-stress profiles measured at different positions is the result of the overwhelming perturbation to the Reynolds stress induced by the presence of the free-shear layer, which causes a pronounced bulge in the Reynolds-stress profiles. Similar Reynolds-stress behavior near reattachment may be seen in the data of Etheridge and Kemp (1978), Castro (1979), and Chandrsuda and Bradshaw (1981), although these measurements were all made behind steps on flat surfaces. It is clear from all three of these reports that the strong Reynolds-stress bulge relaxes to a relatively flat profile a few tens of step heights downstream. Hence the condition that there be no local source of vorticity required for a locally inviscid response cannot be satisfied unless a new free-shear layer forms



before the one upstream has relaxed significantly. Again, the condition is satisfied as the aspect ratio becomes small. Since the above argument involves only the Reynolds stress, which is dominated by large-scale elements of the turbulence, Reynolds-number similarity applies and the argument is independent of scale.

All of the above suggests that surface layers developed over bed forms of large and small aspect ratio are fundamentally different from one another. On bed forms of large aspect ratio, a surface layer in local equilibrium with the skin friction is to be expected; on bed forms of small aspect ratio, the local response is inviscid because the Reynolds-stress field, perturbed strongly by separation and the development of a free-shear layer, is far from equilibrium and is dominated by relaxation effects. The response of the surface layer to these large stresses occurs only in a spatially averaged sense. On bed forms of large aspect ratio, there is a thick ESL between the bed and the ILL in which the Reynolds stresses are locally generated (e.g. Townsend, 1976, ch. 5). On bed forms of small aspect ratio, surface-layer Reynolds stresses are dominated by the wake of the bed form upstream. This implies that the crests of bed forms of small aspect ratio interact with one another much more strongly than do those of bed forms of large aspect ratio.

Do these differences in surface-layer response have any

manifestation in the behavior of natural bed forms? It has been observed that, generally speaking, bed forms of large aspect ratio are long-crested while those of small aspect ratio are short-crested and highly three-dimensional. This is true at both laboratory (Costello, 1974) and field scales (Boothroyd and Hubbard, 1975; Dalrymple et al., 1978). I have observed that the transformation of a two-dimensional ripple field such as the one immobilized for this study to a typical three-dimensional pattern occurs by the growth of small kinks in the bed-form crests and by their propagation downstream to successive crests. It is the latter process in which the strong crest-to-crest coupling described above is implicated; hence the results of this study are consistent with, although not predictive of, the plan-form behavior of bed forms of varying aspect ratio.

## 2.6. Conclusions.

1. The surface layer over bed forms of small ( $O(10)$ ) aspect ratio is not locally in equilibrium; rather it can be decomposed into a spatially averaged rotational component and a local inviscid component. The local response is inviscid because Reynolds-stress profiles in the surface layer are parallel to one another. This view of the surface layer is fundamentally different from, but complementary to, that developed by Smith and McLean (1977) for the surface layer over bed forms of large aspect ratio ( $O(100)$ ). The differences can best be appreciated by comparing figures 2.2 and 2.24.

2. The relative fluctuation intensity of skin friction ( $\sigma_\tau/\tau_{0S}$ ) decreases going from reattachment to the crest and decreases with increasing Reynolds number. The latter trend also appears to occur in smooth flow although this contradicts the results of some previous studies.

3. The shape of the skin-friction spectrum does not change significantly with position on the ripple but, for all positions, energy is shifted slightly to high frequencies relative to smooth-flow spectra if the spectra are nondimensionalized with the free-surface velocity and the depth.

4. The fluctuating skin friction is strongly positively skewed near reattachment but becomes more symmetric going toward the crest. The fluctuating part of the skin friction plays an important role in transporting sediment, at least

for near-critical conditions.

5. The observed skin-friction and total bottom stress data are consistent within 20% with the simple drag-partition formulas of Einstein and Barbarossa (1952) and Engelund (1966).

### 3. Flow and skin friction over three-dimensional macrorough beds.

3.1. Introduction. Most natural bed forms are three-dimensional in that their morphology varies across the flow. This is true in particular of ripples and many dunes; nonetheless it was decided not to extend the work on flow over current ripples to the three-dimensional case. As discussed in section 2.54, rippled beds are associated with strong interaction between successive bed-form crests; furthermore the plan form of three-dimensional ripple fields is extremely complex (Allen, 1969; Harms, 1969). But the wakes of three-dimensional obstacles, even when they are of relatively simple geometry, are considerably more complicated than those of two-dimensional obstacles, and the effects this has on patterns of skin friction and sediment transport are not well known. So it was decided to investigate three-dimensional macrorough flow at a somewhat simpler level than that of natural current-ripple fields by restricting attention to obstacles of simple geometry, in isolation and in arrays sparse enough to avoid strong wake interaction.

In addition to being a logical first step towards understanding flow and skin friction over more complex three-dimensional bed-form fields, the macrorough beds studied here have been chosen so that the results have direct sedimentological application. There are a variety of bed forms, known from many environments and having no

two-dimensional counterparts, that are the result of local erosion and deposition induced by randomly arranged, bluff obstacles (macroroughness elements) on the bed.

Small-scale examples include crag-and-tail marks, current crescents, and sand shadows. These bed forms are fundamentally different from ripples and dunes in that, under the correct conditions, the latter arise spontaneously on flat beds and migrate; they may be thought of as free bed forms. On the other hand, the bed forms considered in this section owe their existence entirely to the presence of obstacles on the bed, to which they are bound; they may be thought of as trapped bed forms. Such stationary bed forms developed behind obstacles will be referred to here as "obstacle-trapped bed forms" (OTBs).

Before examining OTBs in more detail, it is worth noting some changes in measuring strategy from the preceding chapter; like the simplifications in bed configuration just discussed, they are made necessary by the complexity of three-dimensional macrorough flows. Instead of focusing on flow in the surface layer in relation to skin friction, we will be concerned in this chapter with the skin-friction field and the integrated logarithmic layer. Because these two elements of the flow field are separated by a very complex surface layer that will not be investigated directly, the connection between velocity and skin-friction data will not be as clear as it was in the last chapter. Nonetheless, from a sedimentological point of view, it makes sense to

begin investigating three-dimensional macrorough beds at this level. The importance of the skin-friction field has already been made clear (section 1.1): it determines the pattern of sediment transport. It would be desirable to study the surface layer in conjunction with the skin friction, but making a sufficient number of accurate velocity measurements in a three-dimensional, highly turbulent surface layer is well beyond the scope of this work. In the face of this, it is natural to focus instead on the ILL. It contains information (albeit in spatially averaged form) about the flow beneath it (in  $u_*t$ ), and about the geometry of the bed as it affects the flow (in  $z_{ot}$ ). In addition, the ILL is often the lowest part of the boundary layer that can be directly measured in field and laboratory studies. So it is useful to ask, even if only at a qualitative level, how far changes in skin-friction pattern are reflected in the ILL. Furthermore, skin-friction measurements made in conjunction with ILL measurements are needed for testing drag-partition formulas analogous to those discussed in section 2.52; these are the only means available to estimate the skin friction if, as is often the case, only ILL data are available. Finally, ILL measurements are important in their own right in the formulation of general drag laws for use in calculating sediment transport in natural situations. This last point involves a number of complications that will be discussed further in the final section of this chapter.

Obstacle-trapped bed forms. There are a variety of obstacle-trapped bed forms (OTBs) reported in the literature, and a somewhat greater variety of names. Dzulynski and Sanders (1965), working with firm mud beds, termed such features "scour marks" and classified them as longitudinal, diagonal, transverse, and crescentic. Allen (1965) reported on a number of occurrences of OTBs in snow. He extended the classification of Dzulynski and Sanders somewhat, adding a category to longitudinal scours that he called "scour-remnant ridges". These are ridges of sediment left upstanding in the lee of obstructions during general deflation of the bed, and they appear to be equivalent to the "crag-and-tail marks" (or just "sediment tails") well known from the sea floor (Heezen and Hollister, 1971, ch. 9; Swift et al., 1983).

Crag-and-tail marks are centimeter-scale to decimeter-scale elongate mounds or ridges of sediment formed in the lee of dropstones, animal mounds, or other obstructions in areas of active sediment transport. They are among the most common bed forms on Earth. Allen restricts the term "scour-remnant ridges" to features resulting from deflation; it is not certain that crag-and-tail marks can be similarly restricted. This is also the reason the neutral term "obstacle-trapped bed forms" is preferred in this work to "scour marks".

It is not entirely clear how the various OTBs are related to sediment type or to overall rates of accumulation or erosion on the bed. Allen (1965) describes occurrences of sedimentary tails under conditions that are clearly



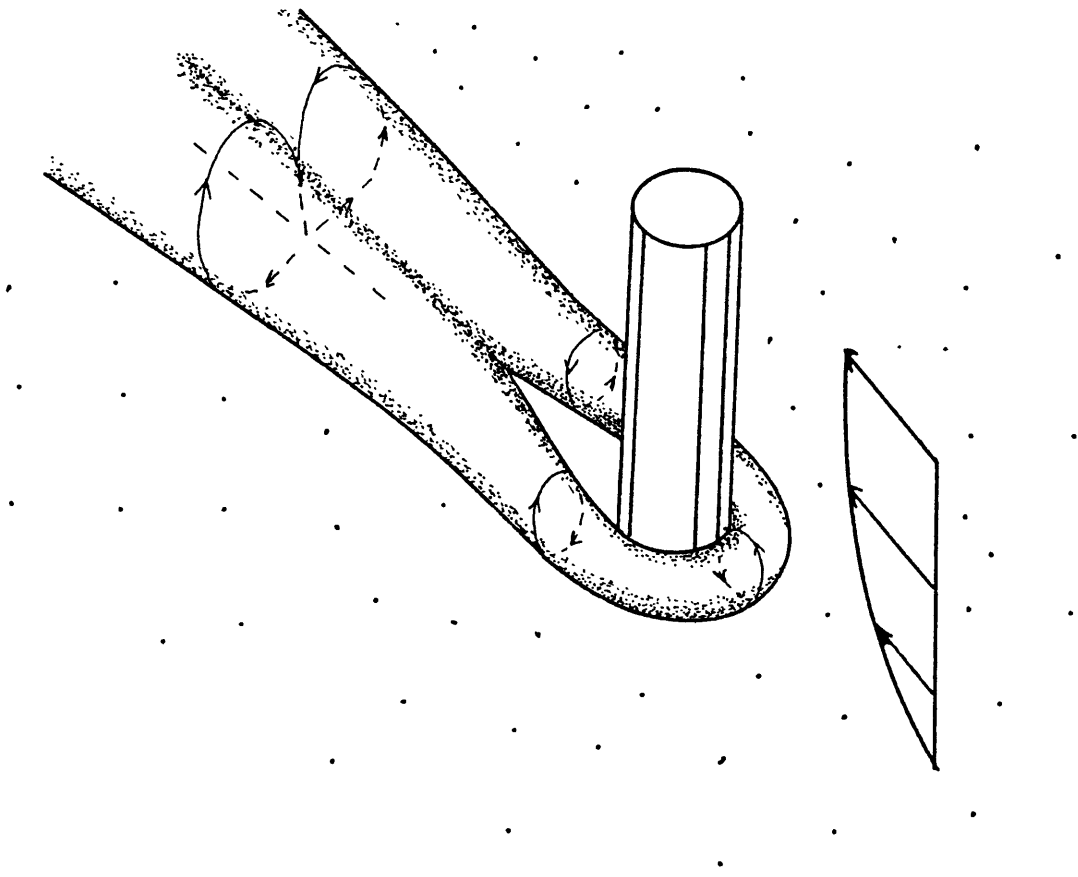
erosional, in which the tails are upstanding remnants of old, hard snow. However, he also reports finding depositional tails; these represent the only new snow added to the areas in which they occur. The old snow had been subjected to a melt-freeze cycle, so it was a form of cohesive sediment. The bed forms developed during a subsequent snowstorm, in which there was extensive drifting; it is uncertain whether the fresh snow should be thought of as cohesive or not. Allen also shows small-scale scour-remnant ridges on a moist (hence cohesive) sand surface undergoing deflation by the wind.

Karcz (1968) made observations of OTBs after floods in wadis in the Negev desert. He reports typical current crescents upstream of obstructions and sediment tails with scales of centimeters to decimeters downstream, but was evidently unable to determine the overall sense of sedimentation in the areas he examined. Both cohesive and apparently cohesionless sediments were involved, and the sediment type does not seem to play an important role in determining the size of the bed forms; this is thought to depend mainly on obstacle size and sediment supply.

A number of writers have also considered the relation of OTBs to patterns of fluid flow about obstacles on the bed. The general nature of the flow has long been known to engineers (Hawthorne, 1954; Hawthorne and Martin, 1955; Richardson, 1968). Consider, for example, a cylinder mounted vertically on the bed in a two-dimensional turbulent boundary

layer. As the fluid in the plane of the flow and the cylinder axis approaches the cylinder it is brought to rest against it, raising the pressure in accordance with Bernoulli's law ((2.10) but note that in a real fluid  $C$  is a constant only along streamlines, and then only as long as energy losses are negligible). Since the velocity decreases towards the bed, so does the pressure. The resultant vertical pressure gradient along the front of the cylinder drives fluid downward there, forming a vortex as shown in figure 3.1. As the flow diverges around the cylinder, the vortex is stretched and intensified, giving rise to the classic "horseshoe" vortex system (Richardson, 1968). The upstream part of this system is responsible for the excavation of the crescentic pits commonly observed upstream and alongside of obstacles on the bed ("current crescents"; Peabody, 1947). The formation of a sediment tail to the lee of the obstacle is thought by Allen (1965) and Karcz (1968) to be the result of a reduction in fluid speed (and hence, presumably, of skin friction) in the wake, although Allen is careful to note that the extent of the region of deposition is limited by the position of the intense vortex filament as it wraps around the obstruction. In the vortex system shown in figure 3.1, flow behind the centerline of the obstacle (that is, over the crest of the tail) forms the common downgoing limb of a pair of counter-rotating streamwise vortices. Hence, as sketched by Allen (1965), fluid moves down the flanks of the tail and into the paired erosional

Figure 3.1. Sketch of the "horseshoe" vortex system about a cylindrical obstacle on a flat bed.



furrows usually found adjacent to it.

Hawthorne (1954) made an extensive theoretical study of the vortex system around vertical struts. He found that the shape of the strut in section strongly influences the induced flow field: it is much attenuated if the strut has sharp rather than rounded upstream and downstream edges. Hawthorne also looked at the patterns of sedimentation around two such differently shaped struts; they closely reflect the variation in strength of the induced vortex system. For neither shape, however, is a tail-like structure formed. Deposition downstream takes the form of lobes removed from the strut and displaced from the plane of the flow and the axis of the strut.

The most extensive study so far of the nature of flow about obstacles in relation to patterns of sedimentation is that of Werner et al. (1980), who made field observations in the Baltic of OTBs at scales of tens of meters (using side-scan sonar) and centimeters to meters (by diving). The most common large-scale features they observed are called "comet marks"; these are lanes tens to hundreds of times longer than wide downstream of boulders or outcropping bedrock in which the thin (tens of centimeters) sand veneer covering most of the shelf has been eroded away, leaving a coarse, reflective pavement. The width of the lanes appears to be a few times that of the generating obstacle. Observations by divers indicate that these comet marks are usually accompanied by downstream tails several obstacle heights long made of

well-sorted medium to fine sand. Evidently all of the sand sheet is in transport episodically, this being controlled by storms that also dominate bed-form development.

Werner et al. (1980) also conducted a series of flume experiments on the bed forms they observed, making velocity measurements with a Pitot tube to within a few millimeters of the bed and visualizing the direction of flow in the immediate vicinity of the bed using oil paint. They were mainly concerned with the genesis of comet marks, so they concentrated on obtaining data from far downstream of isolated obstacles (natural pebbles a few centimeters in diameter). The Pitot-tube measurements show a velocity defect immediately behind the obstacles that persists for only about three obstacle heights downstream; beyond this there is a velocity excess at the centerline, flanked by relative minima. This structure, known as the "negative wake" (Schlichting, 1979, p. 656) is still detectable eighty diameters downstream. Based on the oil-paint flow visualization, Werner et al. concluded that this velocity structure is associated with divergent flow at the bed along the centerline and convergent flow adjacent to it, as shown in figure 3.1. As noted by Schlichting (1979, p. 656), the paired vortex system set up downstream by the obstacle draws high-momentum fluid from the upper boundary layer down to the bed at the centerline, giving rise to the velocity excess there. Low-momentum fluid from near the bed is driven to the sides and then up, giving rise to flanking areas of

relatively slowly moving fluid.

The flume experiments of Werner et al. (1980) included a number of runs in which bed-form patterns in fine sand were generated by isolated obstacles. Again, the main focus was on effects far downstream of the obstruction. It was found that the length of the erosional lane along the centerline increases with the undisturbed (free-stream) bed shear stress, rapidly becoming very large near the value corresponding to the ripple-dune transition. What is particularly striking with regard to the present discussion, however, is that depositional tails were not produced behind the obstacles in any of the runs, despite their having covered a wide range of conditions of bed shear stress and sediment supply.

Eckman et al. (1980) measured the magnitude of the skin friction at various points about isolated vertical cylinders that acted as models for worm tubes common on the sea floor. The measurements were made with a single flush-mounted hot film. They found two areas of reduced skin friction disposed symmetrically about the centerline, qualitatively similar to the areas of low near-bed velocity reported by Werner et al. (1980). Eckman et al. expected these to be areas of sediment accumulation, possibly providing an important food source for the occupants of the tubes.

Neither the direction-field visualization made by Werner et al. (1980) nor the magnitude measurements of Eckman et al. (1980) are sufficient to determine whether skin-friction

patterns in the wakes of isolated obstacles are responsible for the existence of sedimentary topography behind them. The skin friction may be thought of as a two-dimensional vector field: in the coordinate system shown in figure 1.2, the skin-friction vector  $\tau_m$  has components ( $\tau_x = \sigma_{yx0}$ ,  $\tau_z = \sigma_{yz0}$ ), where  $\sigma_{ij}$  is the stress tensor, to be evaluated in this case at the bed. (The tensor subscripts  $m$  and  $n$  range only over the two horizontal coordinate directions  $x$  and  $z$ .) The rate of bed-load transport can also be viewed as a two-dimensional vector field  $(q_s)_m$ . The sediment continuity equation, introduced in section 2.53, then has the form

$$\eta_{,t} = -(1/C_0)(q_s)_{m,m} \quad 3.1$$

where  $\eta$  is the bed elevation and  $C_0$  is the volume concentration of sediment in the bed.

The transport rate  $q_s$  is usually written as a power-law function of the skin friction (section 2.53); for purposes of illustration we may use the following simple form:

$$(q_s)_m \propto |\tau|^a \tau_m \quad 3.2$$

where  $a$  is an exponent of order 1 and  $|\tau| = (\tau_n \tau_n)^{1/2}$ . Then (3.1) becomes

$$\eta_{,t} = -(1/C_0)a|\tau|^{a-1} \tau_{m,m} \quad 3.3$$

The sign of  $\eta_{,t}$ , which determines whether there is erosion (negative) or deposition (positive), is opposite to that of  $\tau_{m,m}$ . Also, if  $a$  is near unity (as in section 2.53), the



magnitude of  $\tau_{m,t}$  is largely controlled by that of  $\tau_{m,m}$ . Clearly, to understand the relation of sedimentation to the wake flow about an obstacle it is necessary to know how  $\tau_{m,m}$  behaves. Since there is significant variation in both the magnitude (Eckman et al., 1980) and direction (Werner et al., 1980) of the skin-friction field near the obstacle, both must be measured to calculate  $\tau_{m,m}$ . Furthermore, in view of the strong turbulence present in the wake flow, skin-friction variance may reasonably be expected to affect the pattern of sedimentation.

Flow over three-dimensional macrorough beds. Near-bed flow and skin friction affect the ILL through the spatially integrated parameters  $u_*t$  and  $z_{ot}$  that scale (1.6) there. The roughness length  $z_{ot}$  is of particular interest because it reflects in an averaged way the geometric properties of the bed as they affect the boundary layer; furthermore, together with the von Karman coefficient  $\kappa$ , it uniquely determines the velocity at any height within the ILL associated with a given total boundary shear stress. (This rather simple picture is correct only if a number of complicating factors common in field settings are not present. Many of these will be discussed further in section 3.53.)

Several authors have developed classification schemes for macrorough flows (Morris, 1955; Perry et al., 1969; Wooding et al., 1973; Knight and MacDonald, 1979b). The most analytical of these is that of Perry et al. (1969), as extended by Wooding et al. (1973). It is based on the

behavior of  $z_{ot}$  as a function of the areal density  $\lambda$ , defined by  $\lambda \equiv A_h/A_p$ , where  $A_p$  is the average area of the bed for each roughness element and  $A_h$  is the frontal area of one element. At the smallest densities ( $\lambda < 0.1$ ),  $z_{ot}$  is found to depend on the element height  $h$  and the interelement spacing  $B$ , for a given element shape. Such beds are called "h,B-rough". It is thought that there is negligible wake interaction in the h,B regime (Wooding et al., 1973). As  $\lambda$  approaches 0.1 the ratio  $z_{ot}/h$  reaches a maximum; such beds are called "h-rough". If  $\lambda$  is increased still further, holding the size and shape of the roughness elements constant,  $z_{ot}$  decreases in a manner that depends on the nature of the roughness. For irregular, three-dimensional roughness (natural sand beds, for example),  $z_{ot}$  continues to be proportional to  $h$  as it decreases, so the bed is still referred to as h-rough. On the other hand, for regular, two-dimensional roughness (for example, a uniform array of transverse square bars),  $z_{ot}$  becomes dependent on the flow depth or boundary-layer thickness  $D$ , and the bed is called "D-rough". Physically, on D-rough beds the roughness elements are so closely packed that recirculation regions occupy most of the space between them. The roughness length decreases because drag on the forward going part of the flow is exerted only by the top part of each element, reducing the effective roughness height. (This condition was termed "skimming flow" by Morris (1955).) The physical origin of the dependence of  $z_{ot}$  on  $D$  is somewhat less clear (Townsend,

1976, sec. 5.5)

Natural macrorough beds fall mainly into the first two categories. Bed forms of low aspect ratio, such as the current ripples discussed in the preceding chapter, are examples of h-rough beds, while those of high aspect ratio (two-dimensional dunes) are examples of h,B-rough beds. There is nothing to suggest that obstacle-trapped bed forms are restricted to either of these two groups, although in view of their apparent connection with the wakes of three-dimensional obstacles they probably could not form under D-rough conditions.

Wooding et al. (1973), in a comprehensive synthesis, attempted to find an expression relating  $z_{ot}$  to the size, shape, and spacing density of macroroughness elements under h,B conditions. The variability in the data they gathered is striking; for instance, reported values for von Karman's coefficient  $\kappa$  range from 0.24 to 0.62. Based on the data and on similarity theory, the authors suggest that  $z_{ot}$  is proportional to  $h\lambda\phi$ , where  $\phi=(h/s)^{0.38}$  and  $s$  is the streamwise length of the roughness elements. Hence, all other things being equal, lengthening roughness elements should reduce their resistance to flow.

Plan of the experiments. Combining the ideas discussed so far, one arrives at the following picture. Obstacles strewn randomly on flat surfaces in a wide range of natural settings commonly have on their lee sides sedimentary tails several obstacle heights long. It is natural to suppose that such

tails are simply a reflection of the wakes of the associated obstacles, but the experiments of Werner et al. (1980) suggest that the flow field in the wake may not be compatible with tail formation, because of the velocity maximum along most of the centerline. To the extent that wake flow does govern tail development, the extension of tails downstream may be self-limiting: based on the results of Wooding et al. (1973), the addition of sedimentary tails to bluff natural obstacles should reduce the total boundary shear stress for otherwise constant flow conditions. Inasmuch as the induced horseshoe vortex system that dominates the wake is closely connected to the total bottom stress (via both skin friction and form drag), adding sediment downstream should weaken the vortex system as well.

The foregoing discussion indicates that sedimentary tails are widespread, geomorphically important bed forms whose origin and effects on the flow are not completely understood. The experiments to be described in this chapter have been designed to answer the following questions:

(1) Is the pattern of skin friction behind a single representative bluff obstacle consistent with the formation of sedimentary tails as recorded in a variety of field environments? Allen (1965), Karcz (1968), and Richardson (1968) suggest that it is; the data of Werner et al. (1980) imply that it may not be.

(2) Does deposition of a sedimentary tail to the lee of a bluff obstacle change the skin-friction pattern there so that

a tail tends to grow once initiated?

(3) Do sedimentary tails reduce the overall drag of sparse (h,B) arrays of obstacles, as application of the work of Wooding et al. (1973) suggests?

Answering these three questions requires skin-friction measurements around isolated roughness elements and ILL measurements over arrays of similar roughness elements. In addition it was decided to try to link these two data sets by making skin-friction measurements at selected points around a test element in the arrays. A question arising naturally from this is:

(4) Can skin-friction measurements around isolated roughness elements be used to construct from a few measurements the skin-friction field in an array of like elements at h,B densities?

The full-field skin-friction data can also be used to test drag-partition formulas for macrorough beds. The usefulness of the data in this regard will evidently depend to some extent on the outcome of question (4).

### 3.2. Experimental methods.

General. The experimental program has two parts: (1) measurement of the skin-friction field around an isolated hemisphere at three different values of the free-stream skin friction (the skin friction with no roughness element), without tails and with tails of two different lengths, and (2) measurement of velocity profiles and skin-friction magnitudes at selected points in two sparse (h,B) arrays of hemispheres with and without the longer of the two tails used in the first series. All the experiments were carried out in the 20-meter flume described in section 1.22.

Roughness elements. The basic roughness elements were hemispheres 5.0 cm in diameter made from light plastic shells (kindly donated by the Bristol-Meyers Corporation) that were filled with plaster of paris and sanded flat. The model tails were tapered ridges triangular in plan and section; in the first set of experiments they were made of plaster and in the second, of Plasticine. At their upstream end their width was equal to the diameter of the hemispheres and they were shaped to fit snugly against them; Plasticine was used when necessary to give a smooth join. Two tail lengths were used; they were one roughness height (2.5 cm) and four heights (10.0 cm) long. The short tail was chosen to be somewhat shorter than the separated region behind the hemisphere, as determined by plaster-of-paris flow visualization (see below); the long tail was chosen to be substantially longer, representative of common observed features, and not so long

as to pose severe interference problems in the full-field runs. The three kinds of roughness elements are shown in figure 3.2.

Skin-friction sensors. In the first (isolated-element) series of runs, a single fixed hot-film skin-friction sensor (section 1.2) was used and the hemisphere was moved about a grid upstream of the sensor (figure 3.3). It was assumed that the skin-friction field was symmetric about the centerline, so data were gathered in half the section, at about forty points as shown in figure 3.4. The element could be positioned by eye to within 1 mm using the sighting lines visible in figure 3.3.

The sensor was mounted on the centerline of the flume and was calibrated as described in section 1.2. Ideally, the sensor was to be calibrated before and after each group of runs in which it was used. Unfortunately, this was prevented for three runs by unexpected sensor failures (figure 3.5). All the calibration curves for the first series are given in figure 3.5; they are associated with the appropriate runs and correlation coefficients in Table 3.1.

For the second (full-field) series of runs an array of fixed skin-friction sensors was constructed (figure 3.6). Sensing elements (Micromasurements Inc. Model WTG50A) were mounted on a flat PVC plate that fitted snugly into a square well 50 cm on a side cut into the bottom of the channel (figure 1.4). The plate was supported by four miniature screw jacks. The sensors were all located at

positions where data had been recorded in the isolated-element runs. The sensor array was calibrated before and after the second series of runs. All the calibration curves are shown in figure 3.7.

As discussed in section 1.23, the condition  $D_{th} < L_p$  must be satisfied to obtain accurate skin-friction data from flush-mounted hot films. Estimates of the pressure gradient are available only for the second series of runs (section 3.52); they have been arrived at as follows. First the spatially averaged skin friction as determined from the array just described is subtracted from the total bottom stress to give the form drag  $\tau_{of}$ . The pressure difference across each roughness element is then  $\tau_{of}/\lambda$  and the pressure gradient is estimated as  $\tau_{of}/\lambda L$ , where  $L$  is the length of the elements. Combining this with the measured skin friction gives values for  $L_p$  of about 1 mm for the full-field runs. This is safely above the estimated value of  $D_{th}$  (0.25 mm; section 1.23), so the use of sensors calibrated in smooth flow to measure the skin friction is valid.

Velocity. Velocity measurements were made only in the second (full-field) series of runs. The sensor used was developed by Gust (1982a) and built by Thermosystems Inc. (figure 3.8). The heated element is 4 mm long and 25  $\mu\text{m}$  thick, and is contained in a nickel tube 400  $\mu\text{m}$  in diameter. The sensor is extremely robust and insensitive to contamination. It is well suited to measuring mean velocity although not high-frequency (tens of Hertz) turbulence. The



Figure 3.2. The three roughness elements around which skin-friction measurements were made in the first (isolated-element) series of runs.

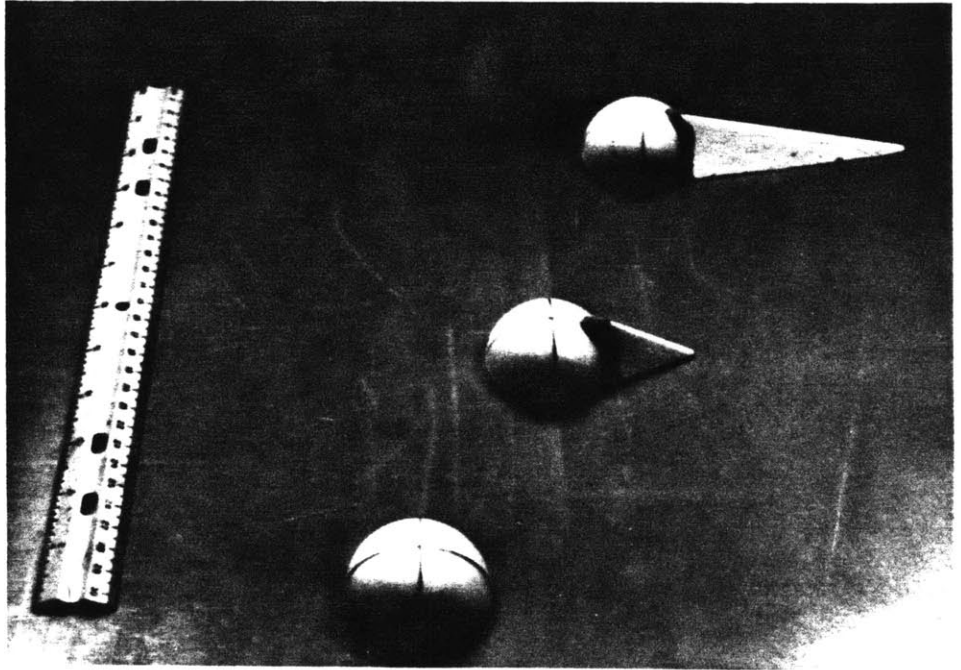


Figure 3.3. One of the flush-mounted hot-film sensors used in the first series of runs, together with the grid used to position the roughness elements.

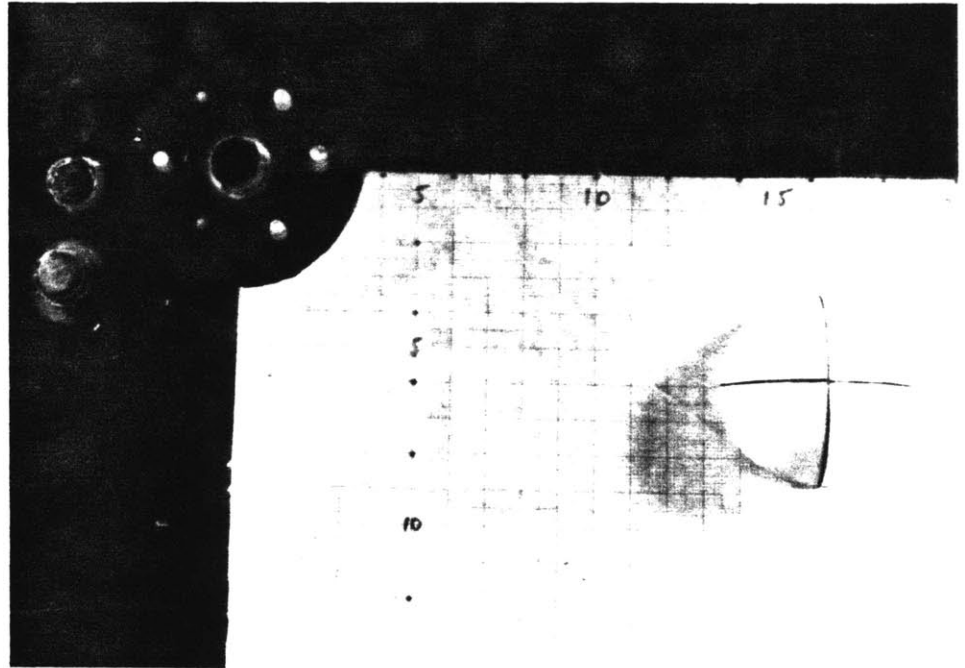


Figure 3.4. Locations where the skin-friction field was measured in the first series of runs.

Open circles - all runs except 176

Half-filled circles - not occupied in runs with  
the long tail

Filled circles - not occupied in runs with  
either tail

Small filled points - run 176 only

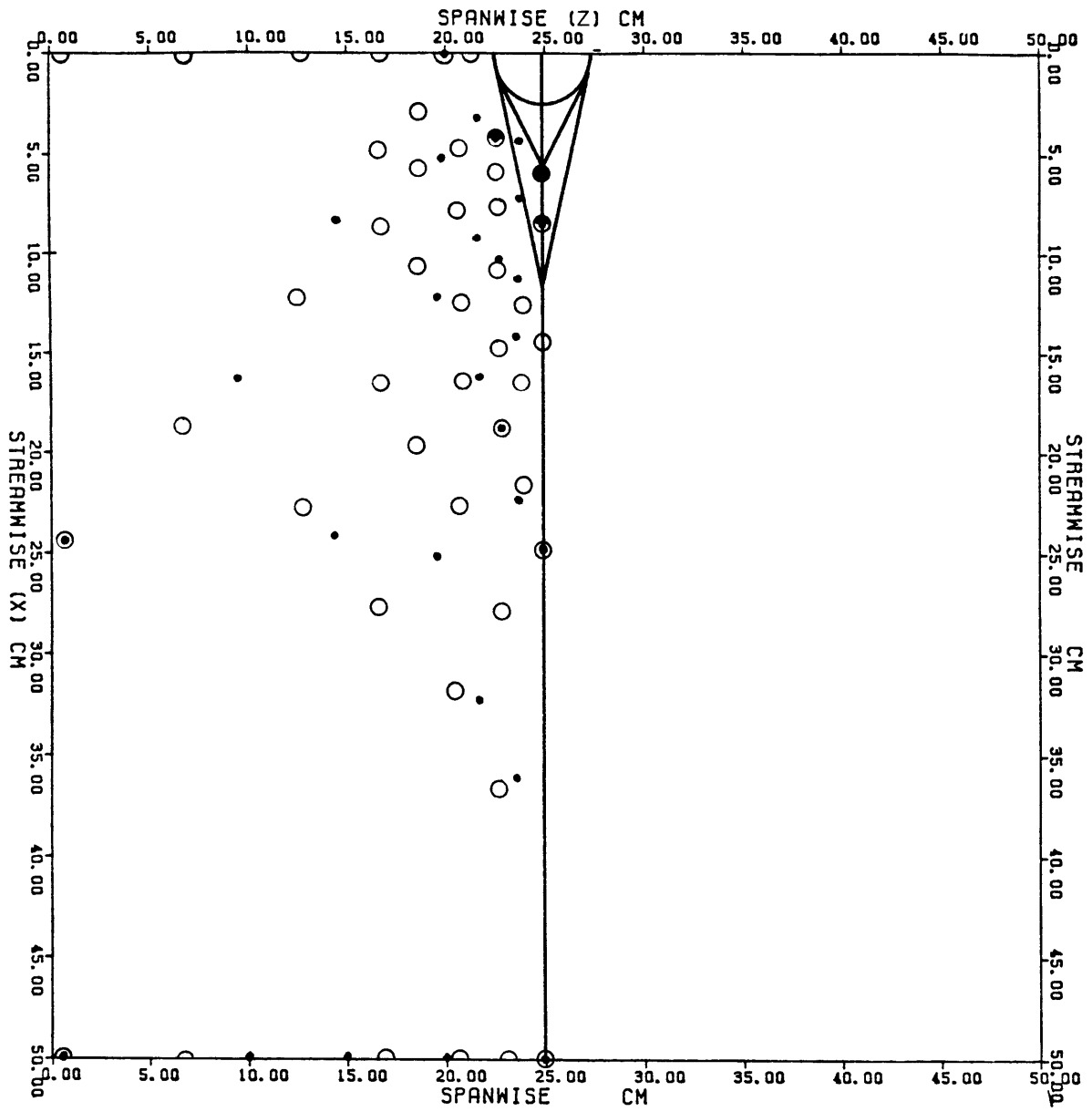


Figure 3.5. Calibration curves for single flush-mounted hot films used in the first series of runs. Different symbols represent different calibration runs. Open symbols represent runs made before data were gathered; filled symbols, runs after data were gathered; half-filled symbols, runs made among data-gathering runs. The data-gathering runs to which each curve applies are given in Table 3.1 along with correlation coefficients for each curve.

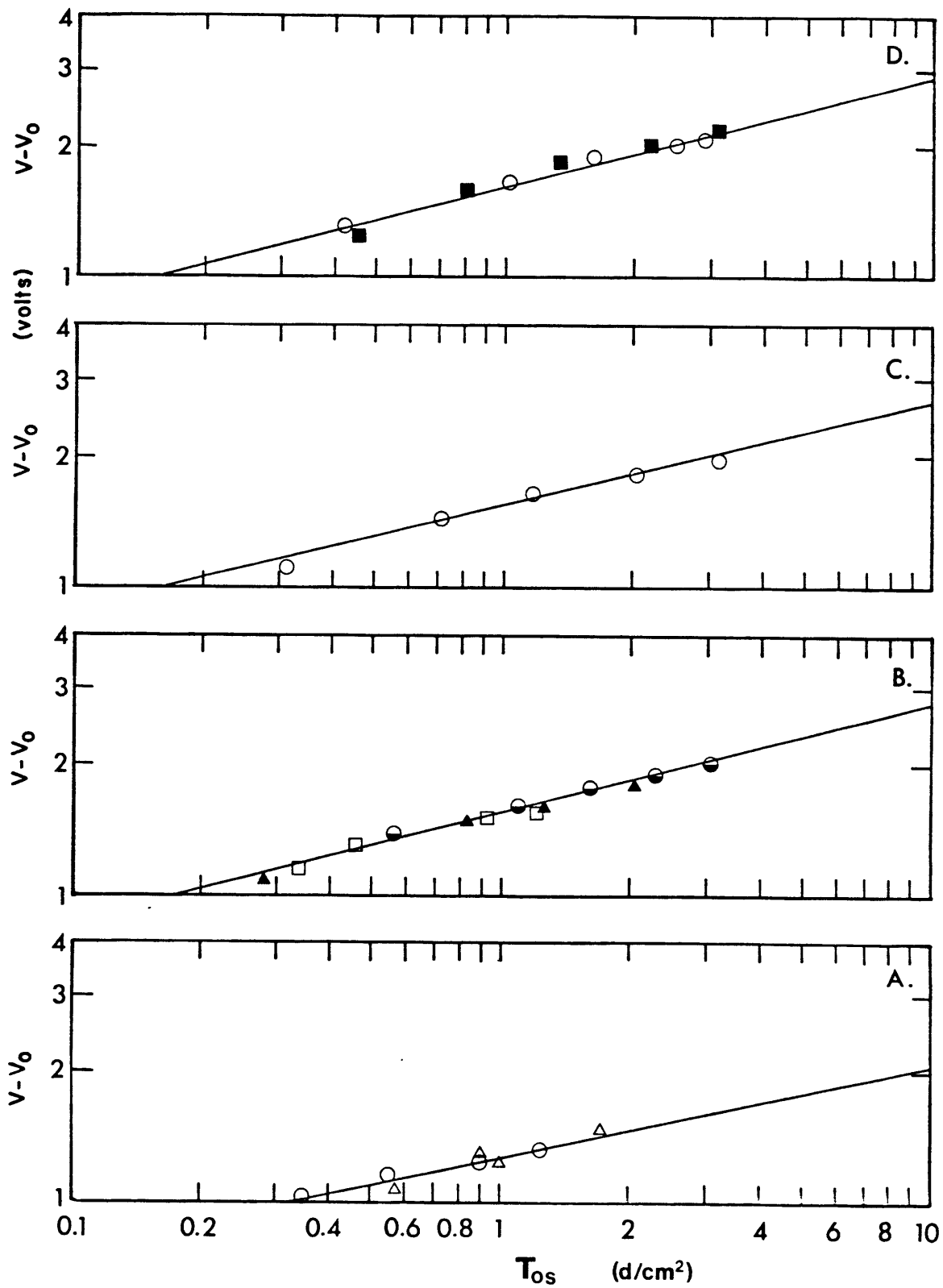
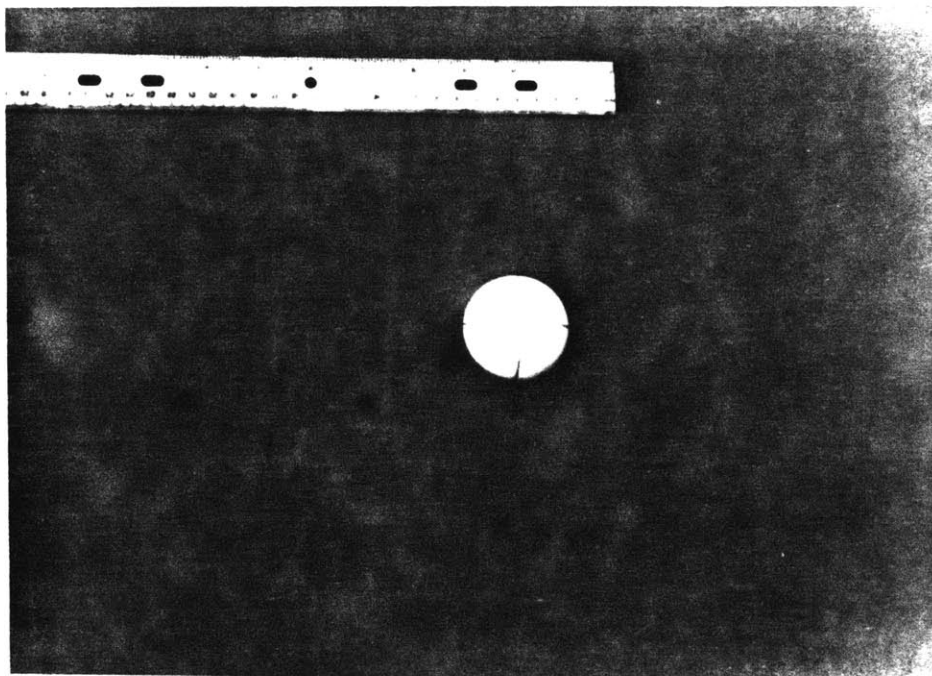




Figure 3.6. (A) Photograph and (B) plan of the sensor array used to gather skin-friction data in the second (full-field) series of runs.



A

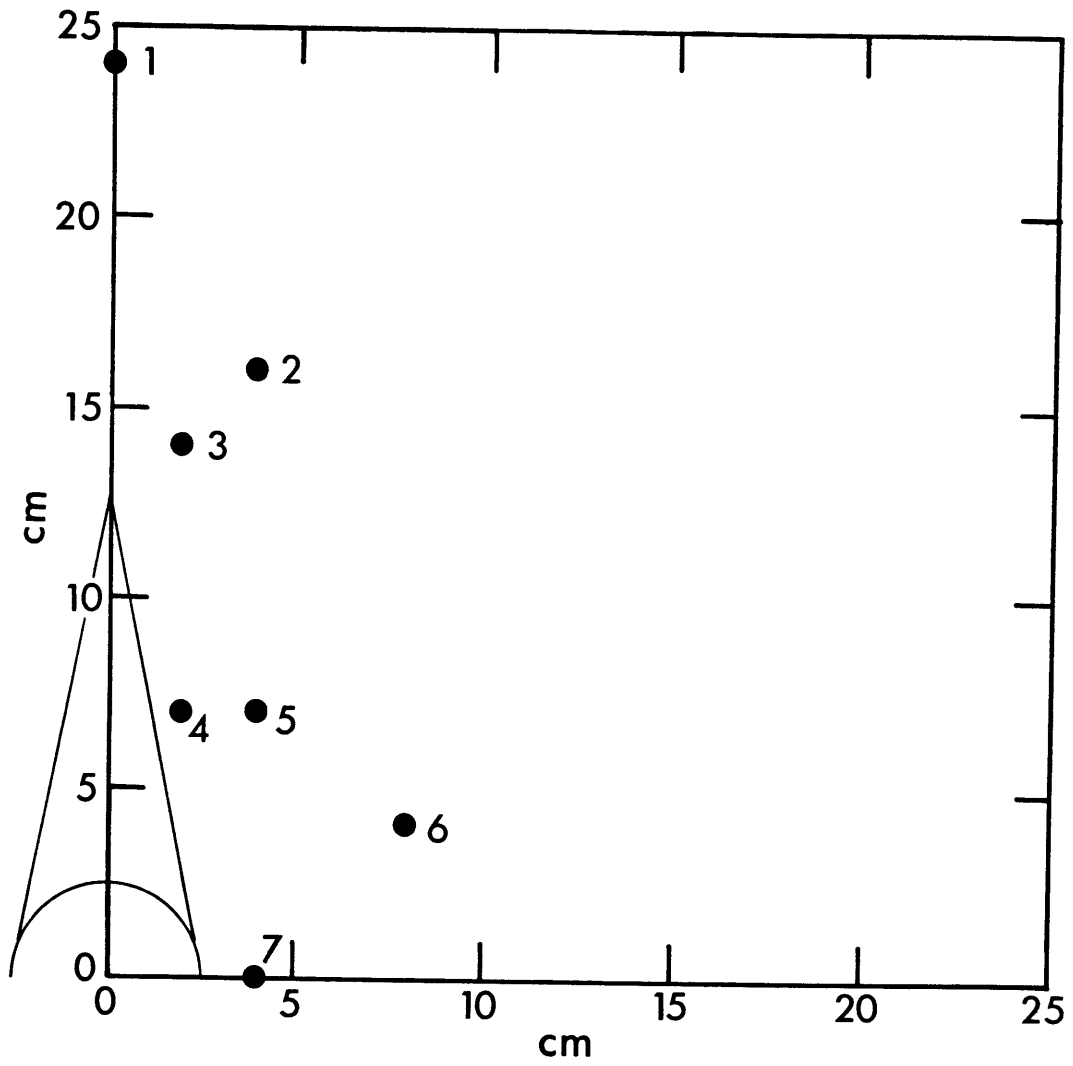
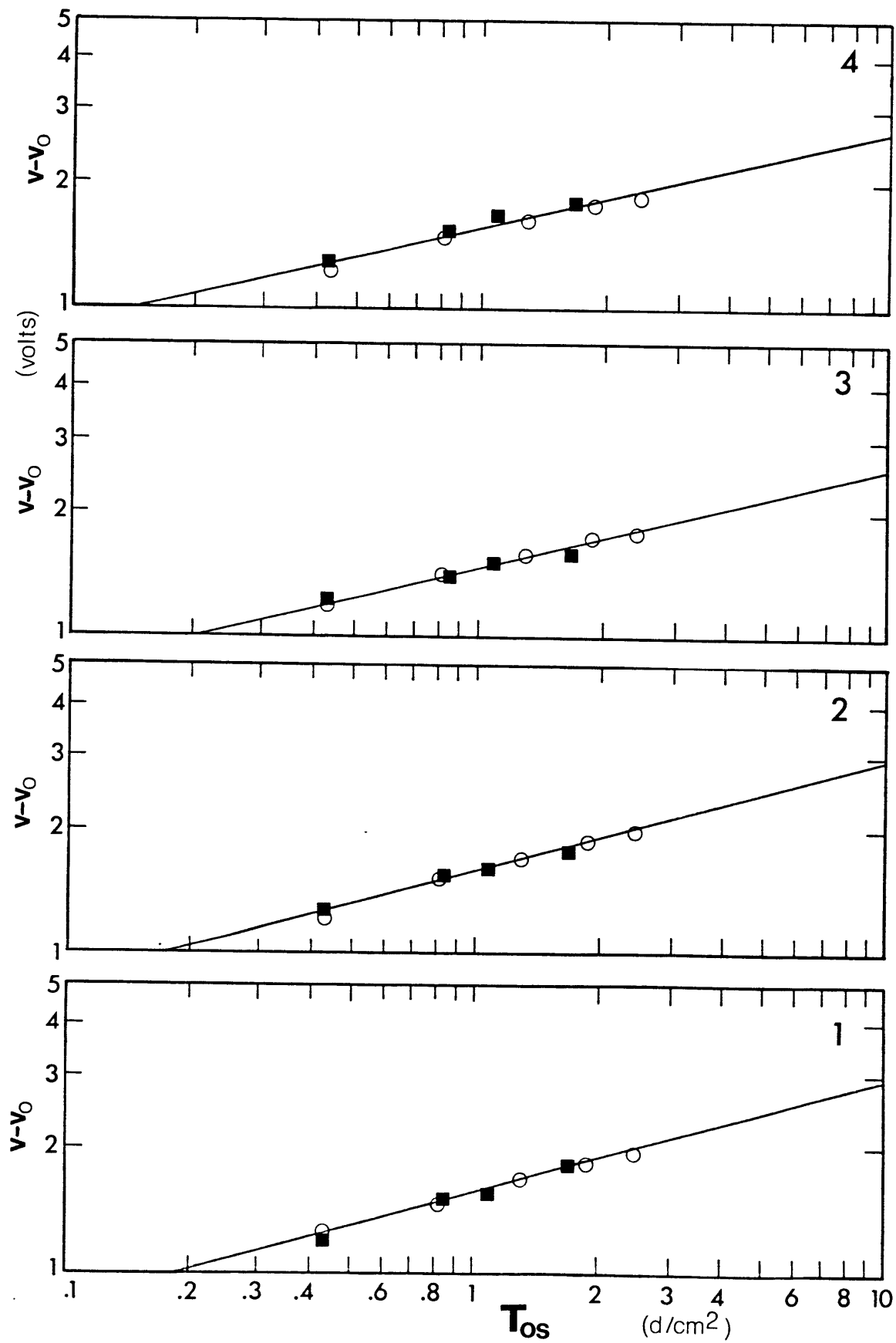
**(B)**

Figure 3.7. Calibration curves for the seven skin-friction sensors of the array shown in figure 3.6. Open symbols represent a calibration run made before data were gathered; filled symbols, a run made after data were gathered. Correlation coefficients for the curves are:

Sensor	$r^2$
1	0.97
2	0.98
3	0.98
4	0.96
5	0.97
6	0.98
7	0.94



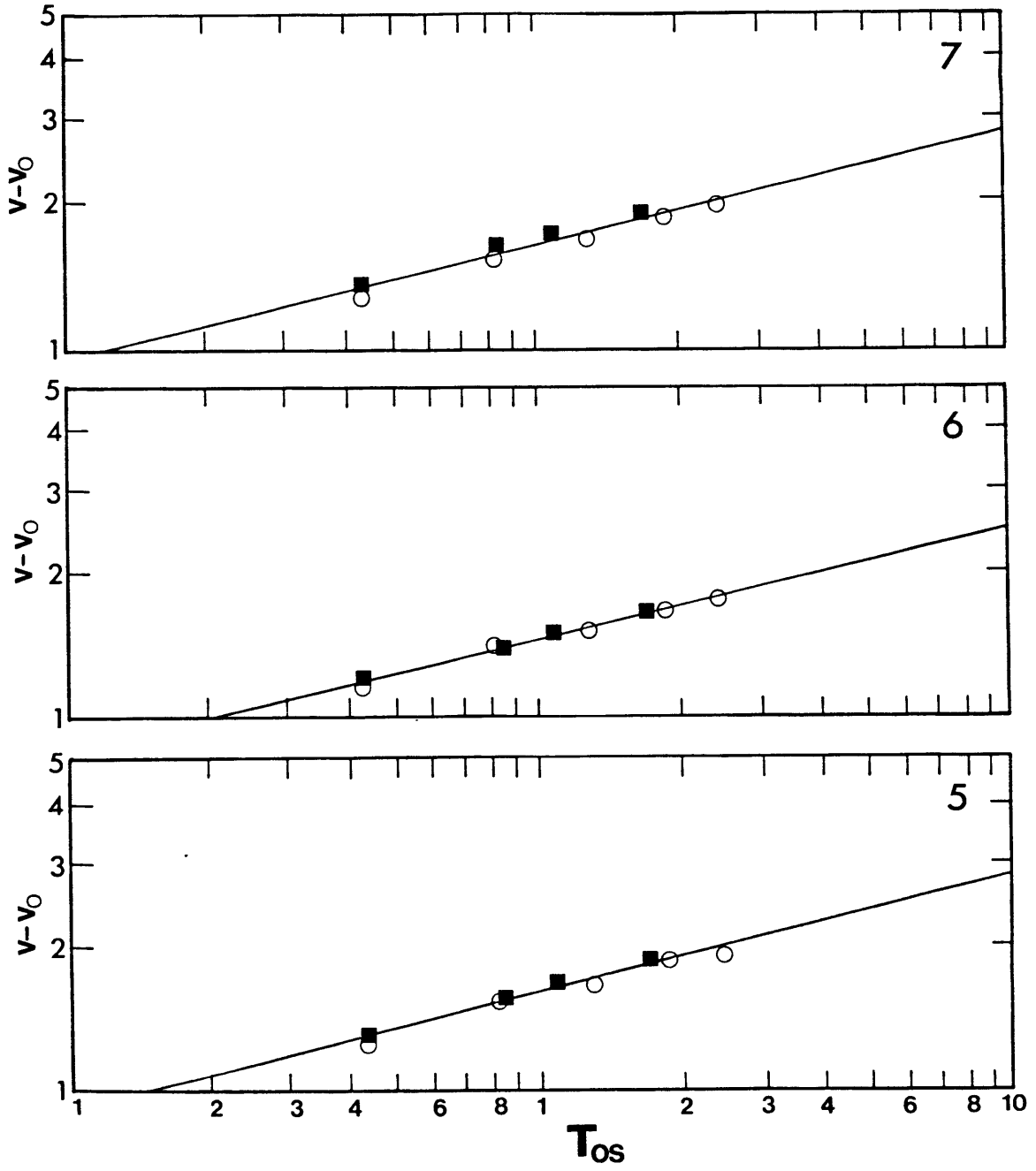
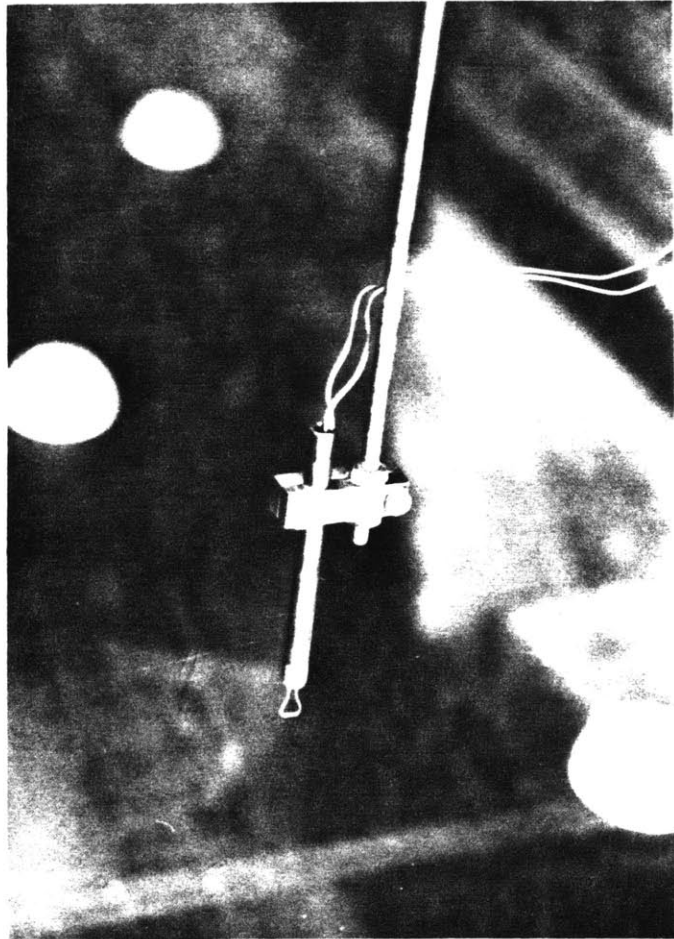


Figure 3.8. The metal-clad hot-wire sensor used to measure velocity in the second (full-field) series of runs.





<u>Calibration</u>	<u>Correlation Coefficient <math>r^2</math></u>	<u>Run Numbers</u>
A	0.95	176
B	0.98	178, 179, 181, 182
C	0.98	185, 186
D	0.98	188, 189

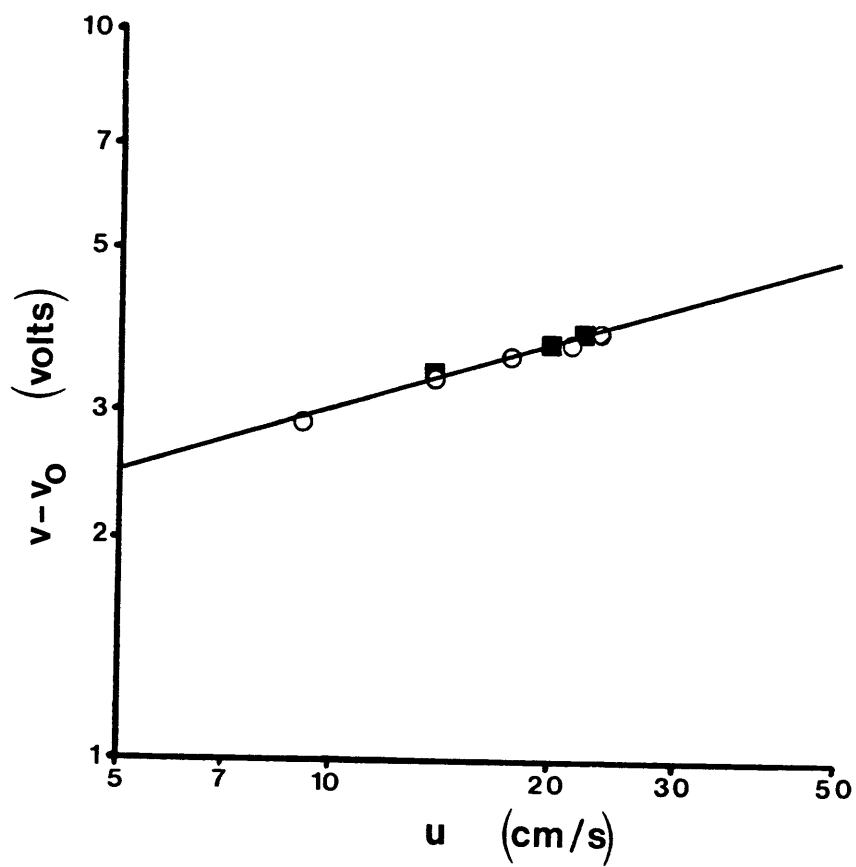
Table 3.1. Correspondence between calibrations shown in figure 3.5, correlation coefficients for fitted power-law curves, and chronological run numbers for the first (isolated-element) series of runs.

sensor was calibrated before and after the second series by reading the voltage at a series of velocities calculated from the discharge curve for the 20 meter flume. The calibration curve is given in figure 3.9.

Direction. The direction of flow at the bed was measured using plaster of paris according to a method devised by Allen (1966). It is based on the generation by surficial defects of wakes that extend downstream and erode small flutes (elongate scour pits) oriented in the local flow direction. Assuming that the vortices that create the flutes are roughly circular in section, the direction may be taken as that of the near-wall flow averaged vertically over a distance equal to the width of the defects. In the present set of experiments, flat plaster plates 50 cm square were marked with a grid of pits about 1 mm wide spaced every 1-2 cm. The plates were fitted into the square well in the channel shown in figure 1.4. Before beginning a run, the plate was carefully made flush with the bed and the desired roughness element was fixed at the upstream end of it. The plate was exposed to flow for several hours until flutes a few millimeters long had formed. The direction field was transferred to transparent plastic and then measured with a protractor at the desired locations. The overall precision of this method is  $\pm 1^\circ$ .

Plaster-of-paris flow visualization does not give readily interpretable results in areas of strong temporal directional variability or intermittent flow reversal. Pits in the

Figure 3.9. The calibration curve for the velocity sensor shown in figure 3.8. Open symbols represent a calibration run made before data were gathered; filled symbols, a run made after data were gathered. The curve has a correlation coefficient  $r^2$  of 0.97.



plaster surface in such areas become flared and enlarged but do not generate distinct flutes.

Full-field arrays. Roughness elements identical to those about which the skin-friction field had been measured were arranged in two configurations to form arrays over which ILL measurements could be made. The first configuration is shown in figure 3.10a. It has an areal density  $\lambda$  of 0.00845. The second is shown in figure 3.10b; it has an areal density of 0.0197, still well below the upper limit for h,B-rough behavior (0.1; Wooding et al., 1973). The roughness elements added to Configuration 1 to form Configuration 2 were staggered so that they filled as much of the cross-sectional area of the flow as possible. This was to avoid spanwise alterations in bottom roughness that could induce secondary flows (McLean, 1981).

All the runs involving arrays of roughness elements were made at a water depth of 20 cm, a depth chosen on the basis of two preliminary runs made using Configuration 1 at varying depth. Velocity-profile measurements were made on the flow centerline at two streamwise positions (figure 3.10), one directly above a roughness element (Position 1), and the other midway between two successive elements (Position 2). The results of the preliminary runs are shown in figure 3.11. At a depth of 10 cm, there is systematic disagreement between velocity profiles at the two streamwise positions even above one roughness height above the tops of the elements. Furthermore, both profiles show much less shear than would be

expected if they obeyed (1.6) scaled with  $u_*\tau$  (1.11 cm/s; the smaller of the two apparent von Karman coefficients  $\kappa_A$  is 0.95, determined from points between 4.5 and 7.5 cm above the bed at a correlation coefficient  $r^2$  of 0.89). For a flow depth of 15 cm both profiles coincide above a height of about 4 cm, and show a semilogarithmic slope that is somewhat less than would be expected for the measured  $u_*\tau$  (0.94 cm/s);  $\kappa_A$  is 0.52, determined from points between 5 and 11.5 cm at a correlation coefficient of 0.87. Similar observations have been reported by Bayazit (1976) for flow over closely packed hemispheres, but  $\kappa$  is not affected in this case until the relative roughness  $h/D$  is greater than 0.3.

It was decided to make the main body of measurements at a depth of 20 cm, both because the high value of  $\kappa_A$  suggests that true law-of-the-wall behavior may not occur at 15 cm and because 15 cm is equal to the spacing of the rows of roughness elements in Configuration 1. Since the channel is 60 cm wide, the chosen flow depth gives an aspect ratio of 3:1. It was decided that the measurements would be considered acceptable if the centerline velocity profiles were spatially integrated in the streamwise sense and semilogarithmic with a value of  $\kappa$  close to the standard one of 0.4.

Treatment of data. All the isolated-element skin-friction data were obtained using the digital recording system shown in figure 1.8 and described in section 1.24. Only time-domain statistics were computed, and of these only the

Figure 3.10. Plan view of roughness unit cells for the (A) sparse and (B) dense arrays used in the full-field runs. The filled points give the locations of velocity-profile stations 1 and 2.

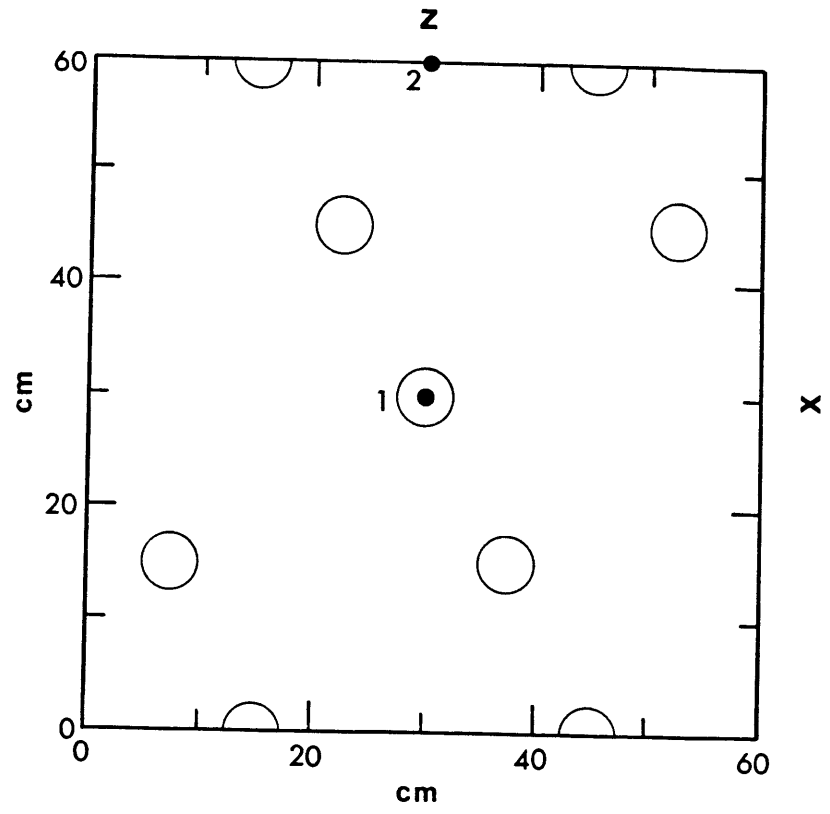
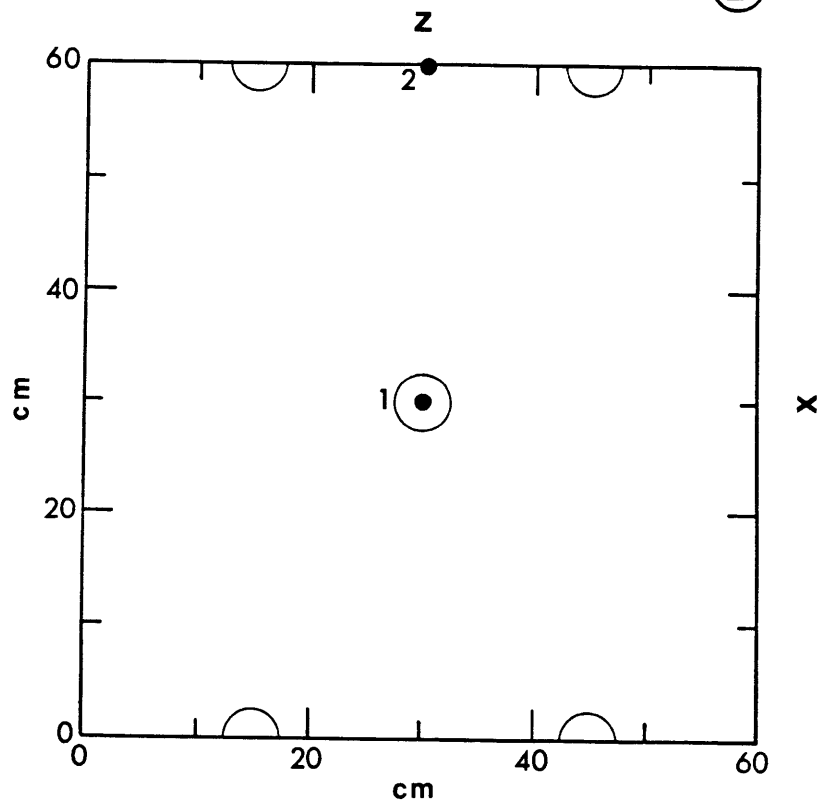
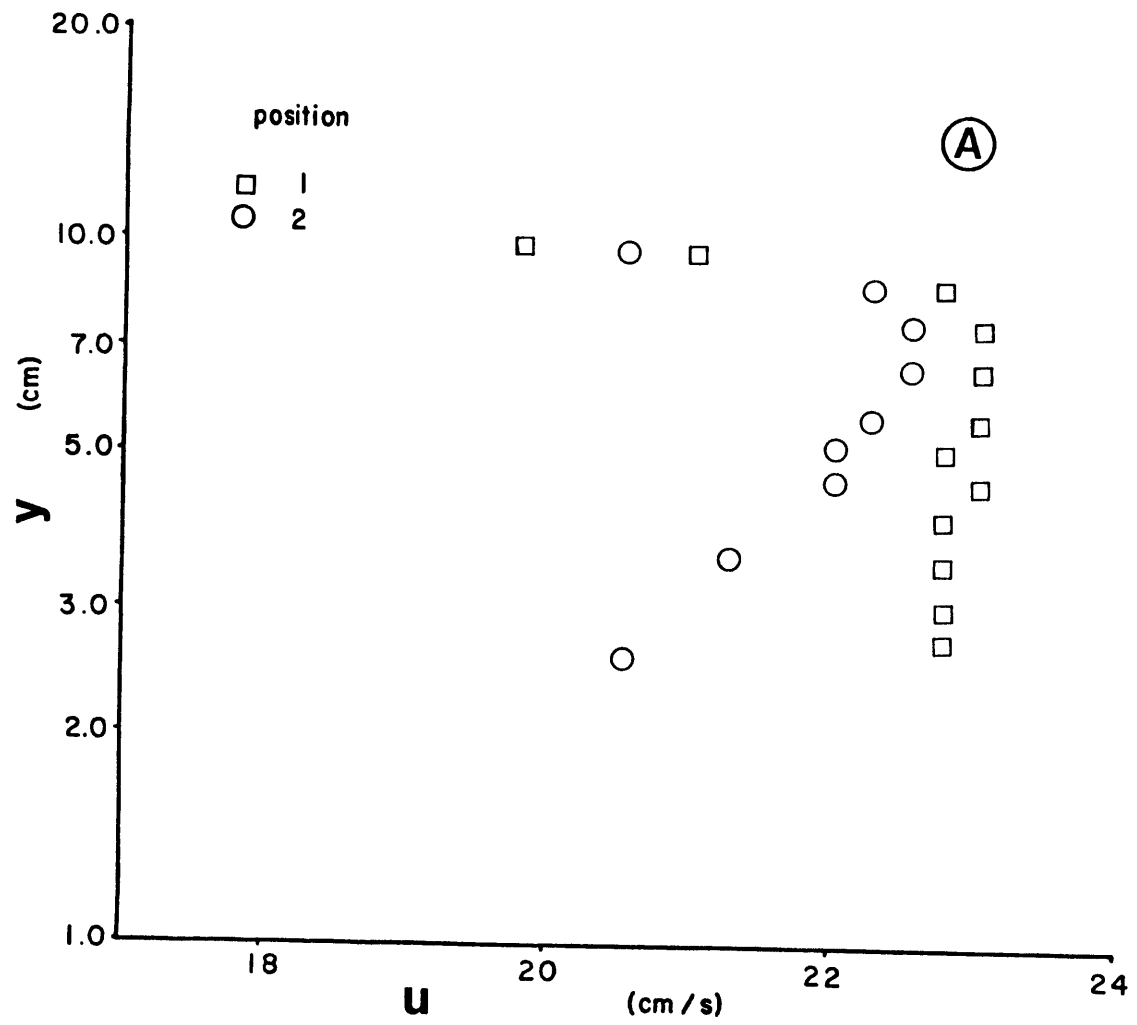
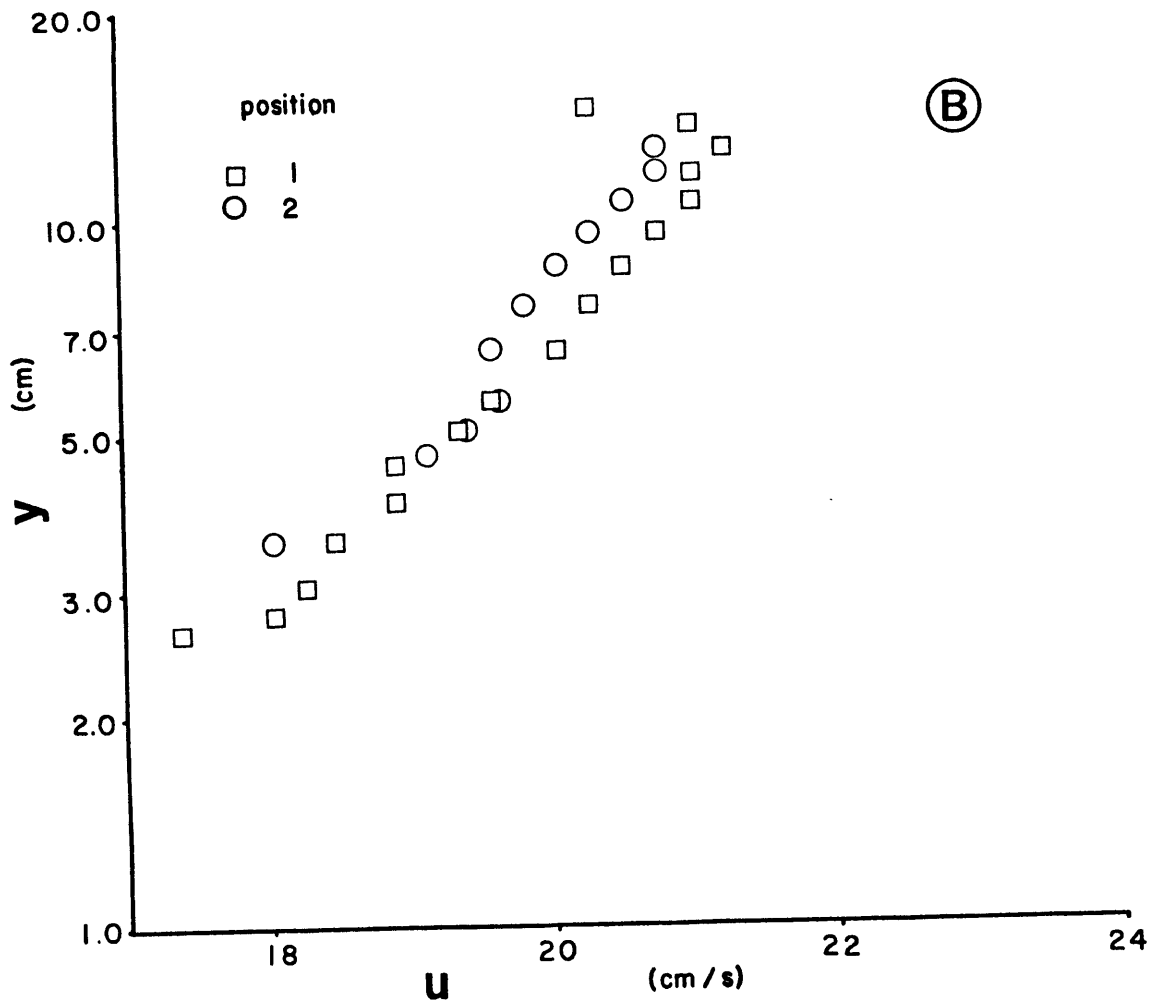
**(B)****(A)**



Figure 3.11. Mean-velocity profiles measured over the sparse ( $\lambda = 0.00845$ ) array of hemispheres at the two positions shown in figure 3.10. Experimental conditions for the two runs shown are:

<u>Index</u>	<u>D</u>	<u>u*<sub>t</sub></u>
A	10.02 cm	1.11 cm/s
B	15.20	0.94





first two moments (mean and standard deviation) will be discussed further. The mean, standard deviation, and direction at each point were combined to produce contour maps of the mean magnitude, rms magnitude, and horizontal divergence of the skin friction vector field  $\tau_m$ . This was all done by computer (program SKINFRIC, Appendix B). First the two mean vector components were determined from the input data at each measuring point; then all the data were reflected about the centerline of the measuring area. Next, a two-dimensional fourth-order interpolation routine (International Mathematical and Statistical Library routine IQHSCV, version 7) was applied to the data to provide estimates of all the fields on a uniform 1 cm grid. The magnitude and the horizontal divergence of the mean field were then calculated at each point; the latter was estimated at each interior point on the grid by taking the symmetric finite difference of the four adjoining points. The finite-difference estimate of the horizontal divergence  $(\tau_{m,m})_{\Delta}$ , is given for any interior point  $(x,z)$  by

$$(\tau_{m,m})_{\Delta} = \frac{\tau_x(x+\Delta x, z) - \tau_x(x-\Delta x, z)}{2\Delta x} + \frac{\tau_z(x, z+\Delta z) - \tau_z(x, z-\Delta z)}{2\Delta z}$$

3.4

where  $\Delta x$  and  $\Delta z$  are the horizontal grid spacings, both equal to 1 cm.

The magnitude along the two streamwise edges was averaged to provide an estimate of the reference (free-stream) skin friction for each run, and all the data were divided through

by this value to facilitate comparison of data from different runs. Contour maps of the data were calculated and plotted using an MIT library subroutine (FNCON1). For clarity, the horizontal divergence was divided into near and far fields that were contoured separately.

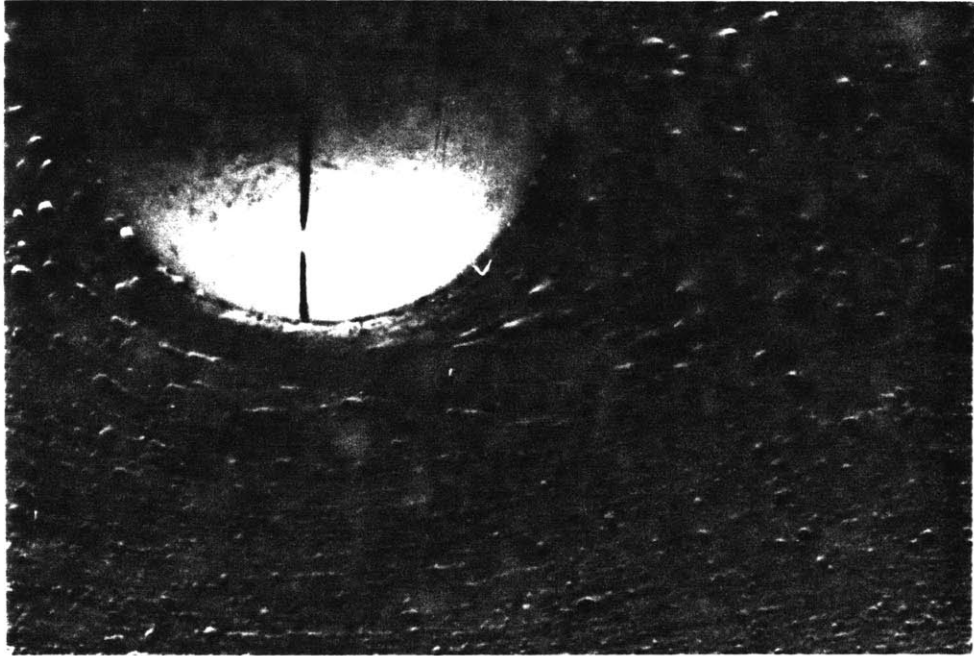
Naturally there were no measurements made at points covered by the roughness elements; in addition, in the region of separated flow immediately behind the plain hemispheres (figure 3.12), the direction-field measurements indicated the presence of strong directional variability and intermittent reversal in the near-bed flow. Since the simple flush-mounted hot films used here are sensitive to only the magnitude of the instantaneous skin friction and not to its direction (they sense a rectified skin-friction signal), they cannot be used to estimate the magnitude of the time-averaged vector in the presence of intermittent flow reversal. Unfortunately it was not possible to exclude from either the interpolation or the contouring points covered by the obstacle or by separated flow; these areas are marked where they occur and contours within them should be ignored.

3.3. Results: Isolated elements. Isolated-element results will be shown graphically in logical order going from no tails to long tails and from low to high Reynolds number. Plots are also labelled with chronological run numbers and the results are indexed that way in Table 3.2.

3.31. Direction. There was no discernible systematic variation in the direction fields with Reynolds number and very little with tail size. A typical plaster plate is shown in figure 3.12, and photographs of direction fields transferred to plastic sheets are given for each tail size in figure 3.13. They show general features similar to those described by Werner et al. (1980). The oncoming flow can be seen to diverge around the hemisphere, forming a narrow separation zone upstream and alongside of it. To the lee, there is a separated region, the end of which is marked by reattachment of the two diverted streams at about two roughness heights downstream of the trailing edge of the hemisphere. Downstream of this point, the direction diverges along the centerline and converges a few roughness heights to either side of it; this structure broadens slowly downstream. The observed pattern is that expected on the basis of the wake structure sketched in figure 3.1.

Figure 3.12. (A) and (B) photographs of a plaster plate showing the direction field behind an isolated hemisphere. The closeup view in (A) shows pits in the separated region behind the hemisphere. Flow is from right to left.

Ⓐ



Ⓑ

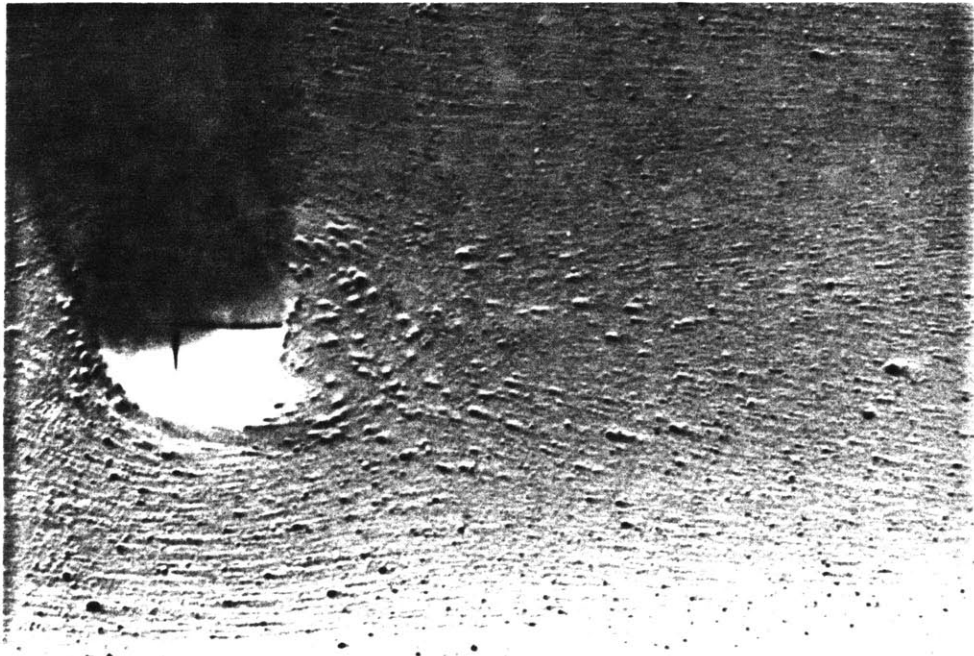
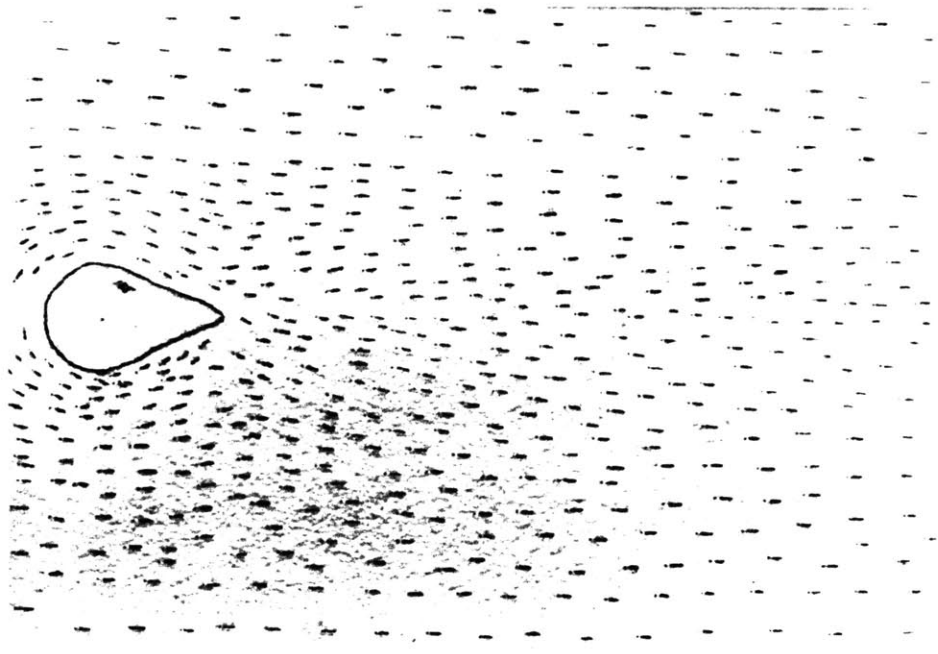


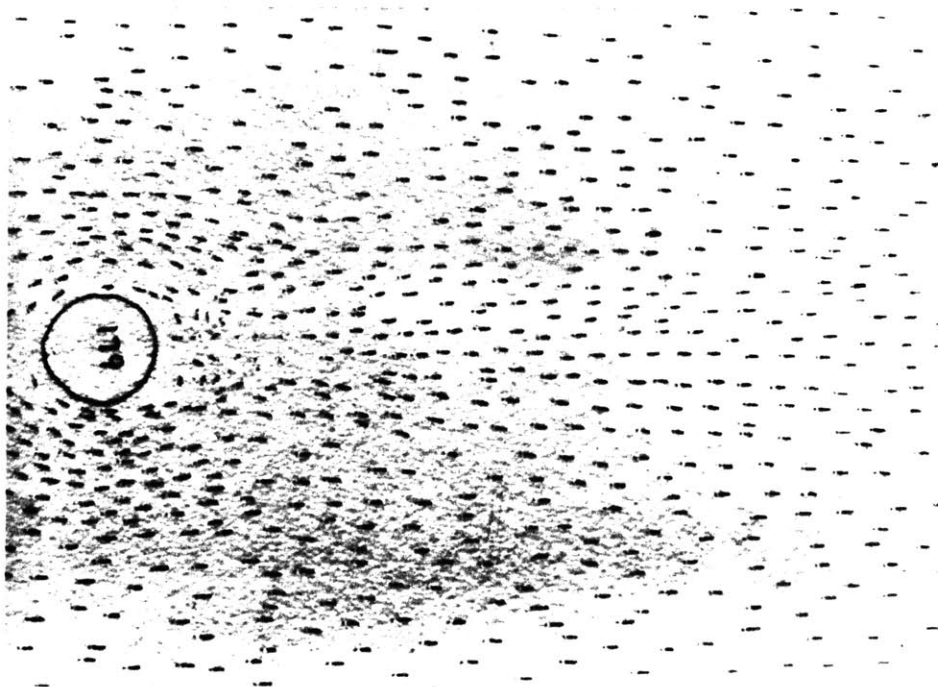


Figure 3.13. Direction fields behind isolated obstacles,  
determined from plaster plates like that shown  
in figure 3.12. Flow is from left to right.

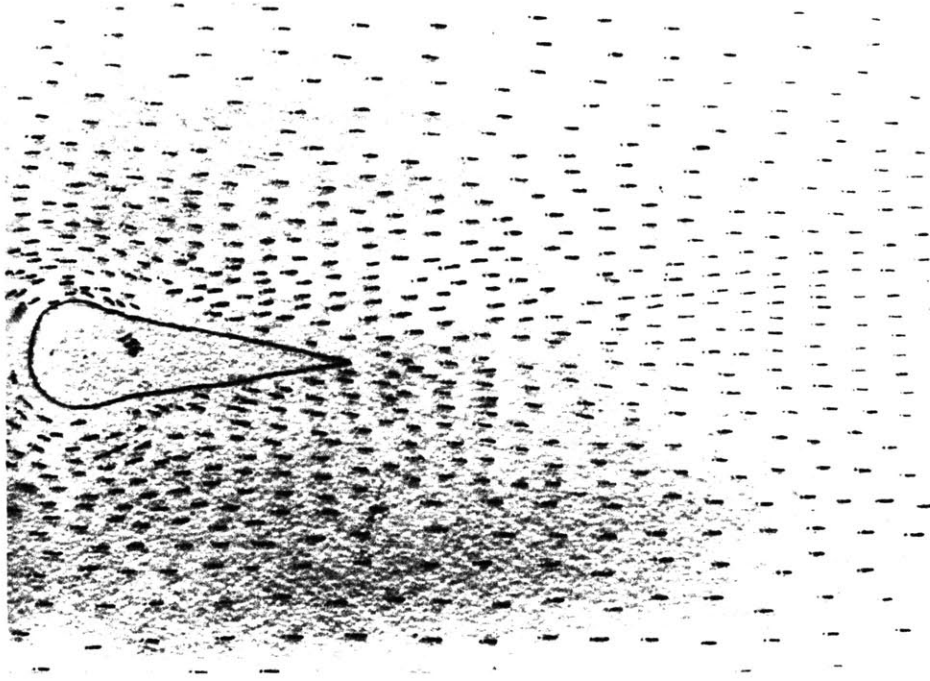
- (A) hemisphere
- (B) hemisphere with short tail
- (C) hemisphere with long tail



**B**



**A**



©

Run	Tail	Free-stream Skin Friction	Bulk Velocity $\bar{u}$	Reynolds Number $\bar{u}D/\nu$
176	none	0.86 d/cm <sup>2</sup>	19.2 cm/s	20,300
178	none	0.39	13.2	13,300
179	none	1.44	26.2	26,700
181	short	0.81	19.1	20,300
182	short	0.40	13.4	13,400
185	short	1.48	26.3	26,700
186	long	1.46	25.9	26,700
188	long	0.91	19.1	20,300
189	long	0.40	13.4	13,300

Table 3.2. Experimental conditions for runs of the first (isolated-element) series.

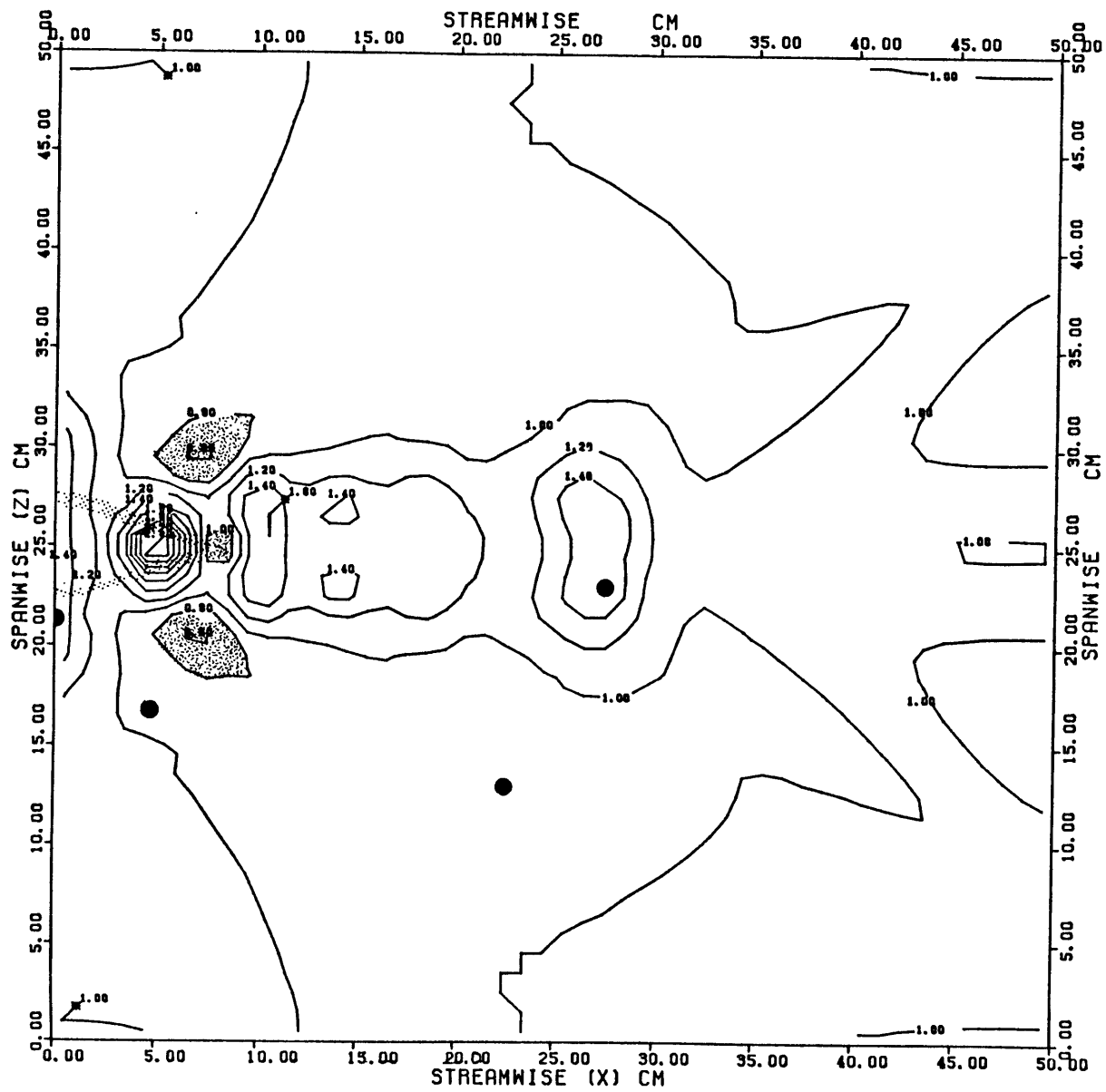
3.32. Mean skin-friction magnitude. Contour maps of the skin-friction magnitude nondimensionalized by the free-stream values are given in figure 3.14. The fields all have the following general properties. Pronounced maxima are generated on either side of the hemisphere as the flow is accelerated around it, and there is another maximum a few element heights downstream along the centerline. The magnitude then generally decreases downstream along the centerline, but there is a secondary maximum a few roughness heights downstream of the first. The magnitude always decreases to either side of the centerline. About ten heights downstream this variation becomes indistinguishable from that introduced by the interpolation. The flanking lows are qualitatively similar to those reported by Eckman et al. (1980); the minimum magnitude is about 80% of the free-stream value and it appears at roughly two element heights downstream of the midpoint and two heights off the centerline.

As the Reynolds number increases the nondimensional values of the maxima in the immediate vicinity of the element decrease, from about 2.0 to about 1.5. The values of the centerline maxima show a similar although reduced trend. The nondimensional values of the flanking minima remain fairly constant, however. The data suggest that the skin-friction magnitude is not proportional to the free-stream skin friction, particularly near the obstacle.

The main effect of varying the tail length is on the maxima along the centerline. Addition of the short tail does not affect the position of maxima, although it appears to reduce their magnitude somewhat. This is partly because the measuring station near reattachment could not be occupied with the tail present. Addition of the long tail moves the first maximum downstream to the end of the tail but does not affect its magnitude. The position of the secondary maximum is also moved downstream, although not as far as that of the first. Neither the strength nor the position of the flanking minima appears to be affected by the tails.

Figure 3.14. The skin-friction magnitude field interpolated from measurements behind isolated obstacles at the points shown in figure 3.4, nondimensionalized by the reference (free-stream) value. Conditions for each run are given in Table 3.2; the graphs are arranged in order of increasing tail length and increasing Reynolds number. Stippled bands show the borders of areas covered by the obstacles or by separated flow. Shaded regions in the field are lows. The marked points are locations where data were not obtained, usually because of problems with the recorded digital cassette tapes. Contours more than about 10 cm off the centerline reflect mainly variation introduced by the interpolating program. Contour intervals for each graph are:

Run	Contour interval
178	0.2
176	0.2
179	0.1
182	0.1
181	0.09
185	0.08
189	0.2
188	0.1
186	0.1

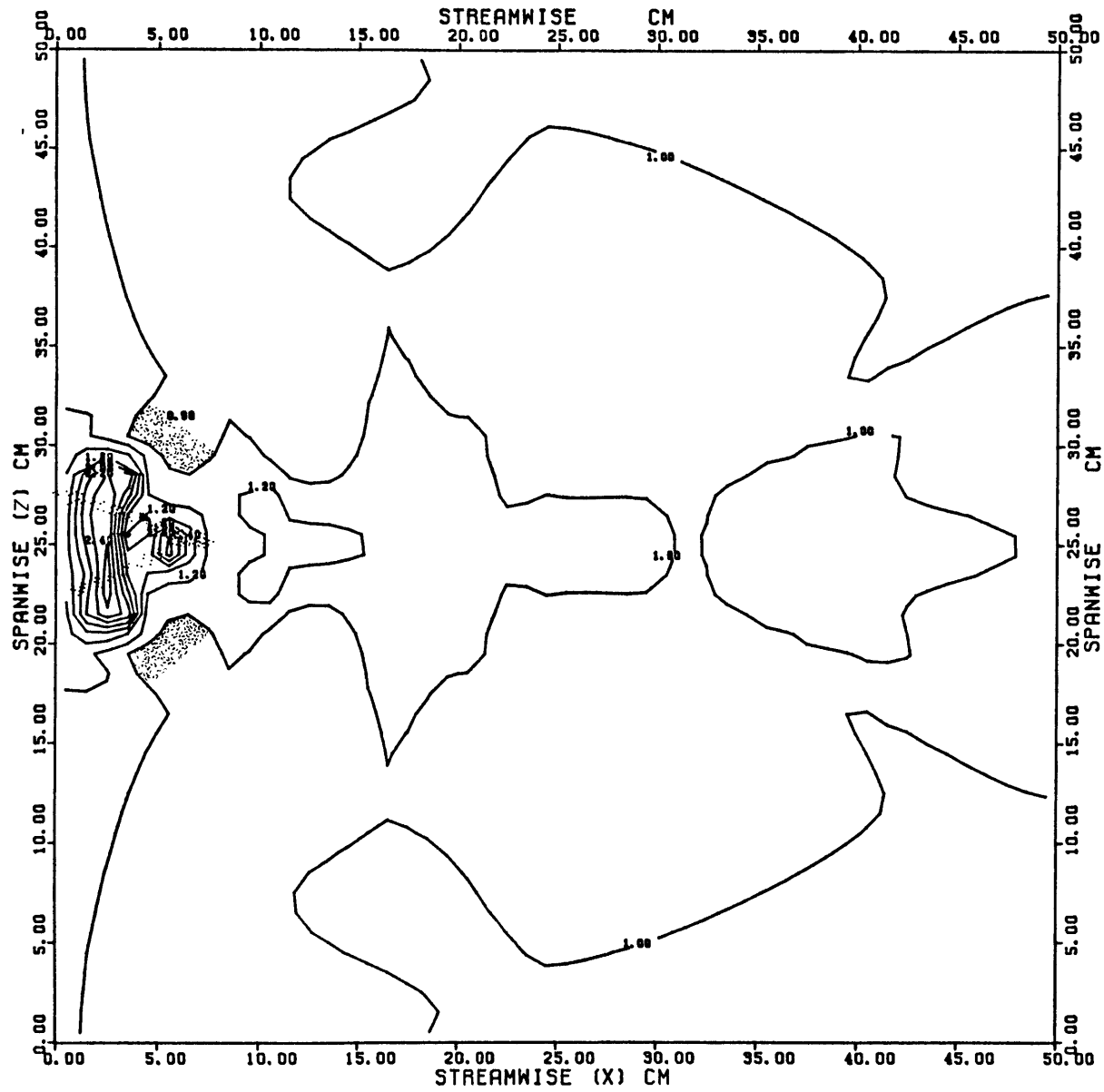


MEAN STRESS

REF = 0.385 DYNE/CM<sup>2</sup>

RUN 178

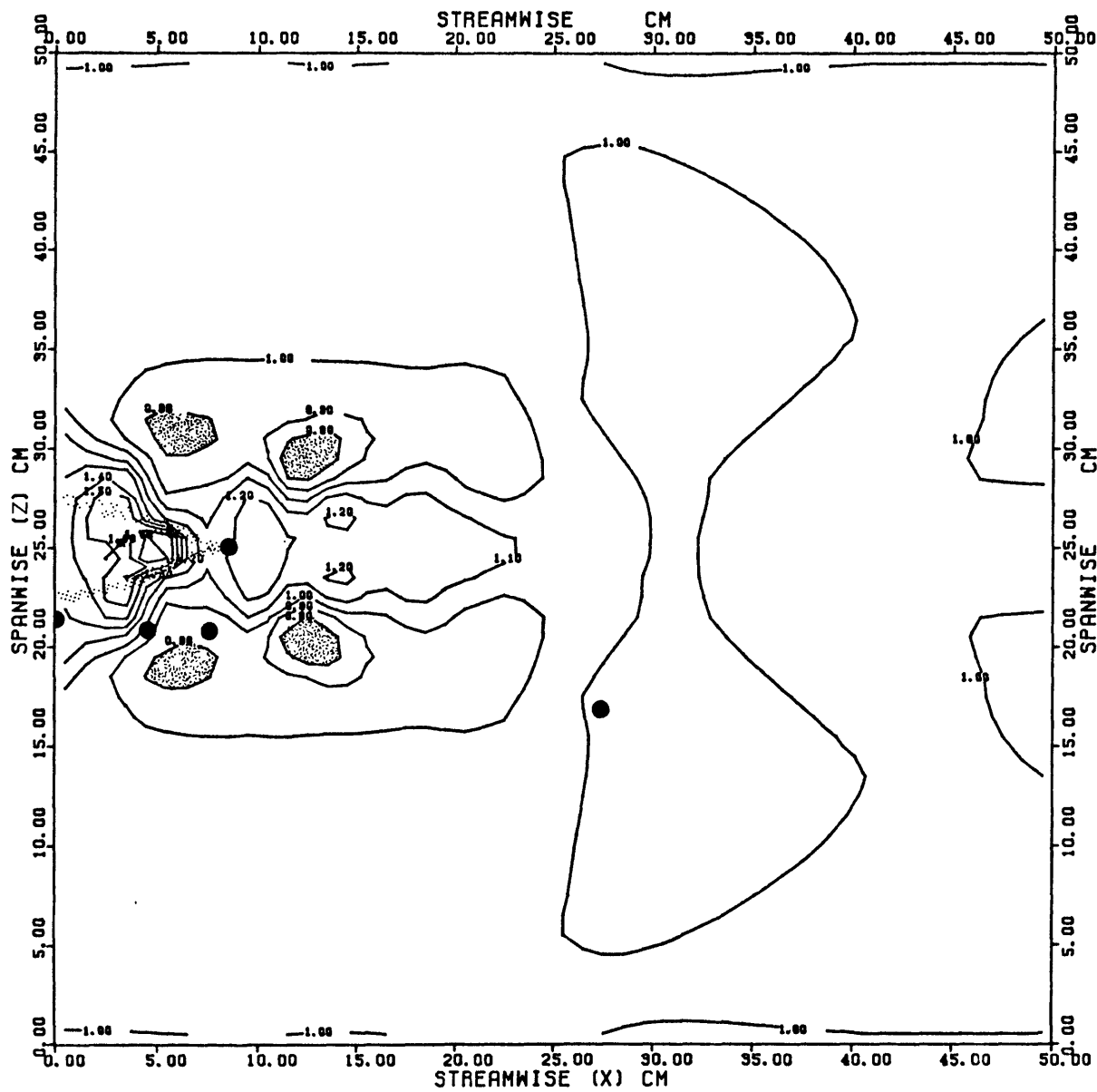




MEAN STRESS

REF = 0.857 DYNE/CM<sup>2</sup>

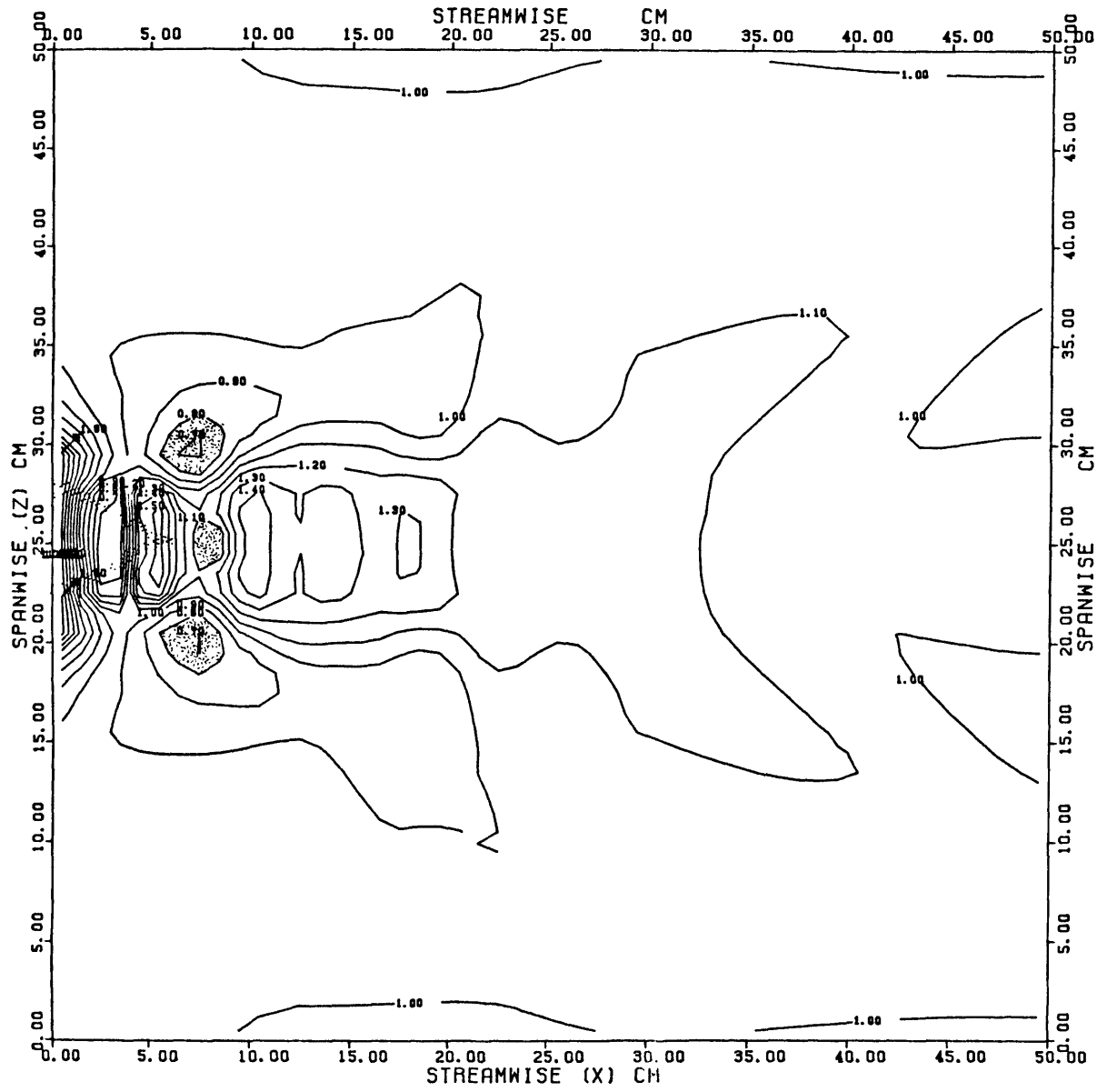
RUN 176



MEAN STRESS

REF = 1.442 DYNE/CM<sup>2</sup>

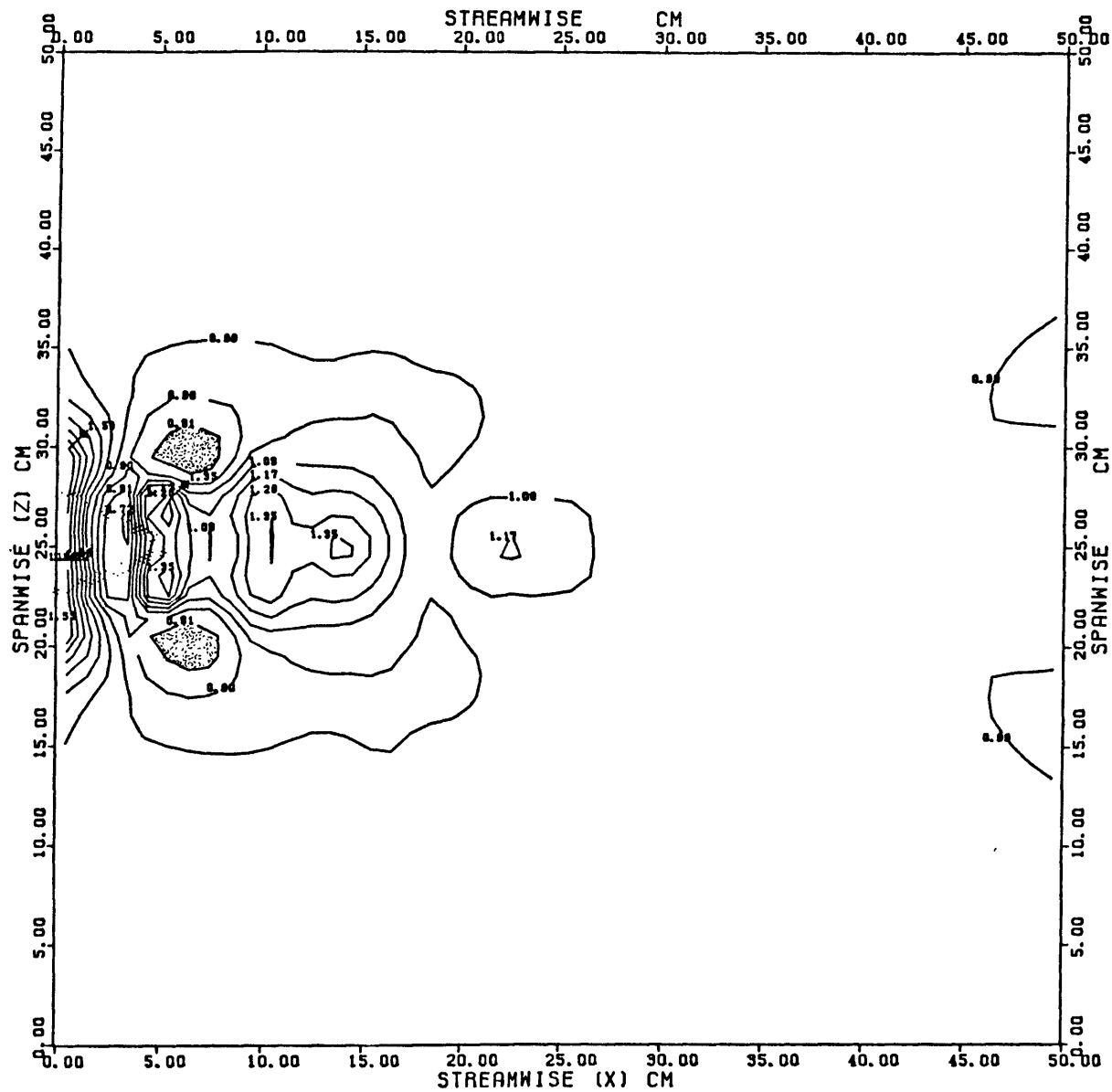
RUN 179



MEAN STRESS

REF = 0.396 DYNE/CM<sup>2</sup>

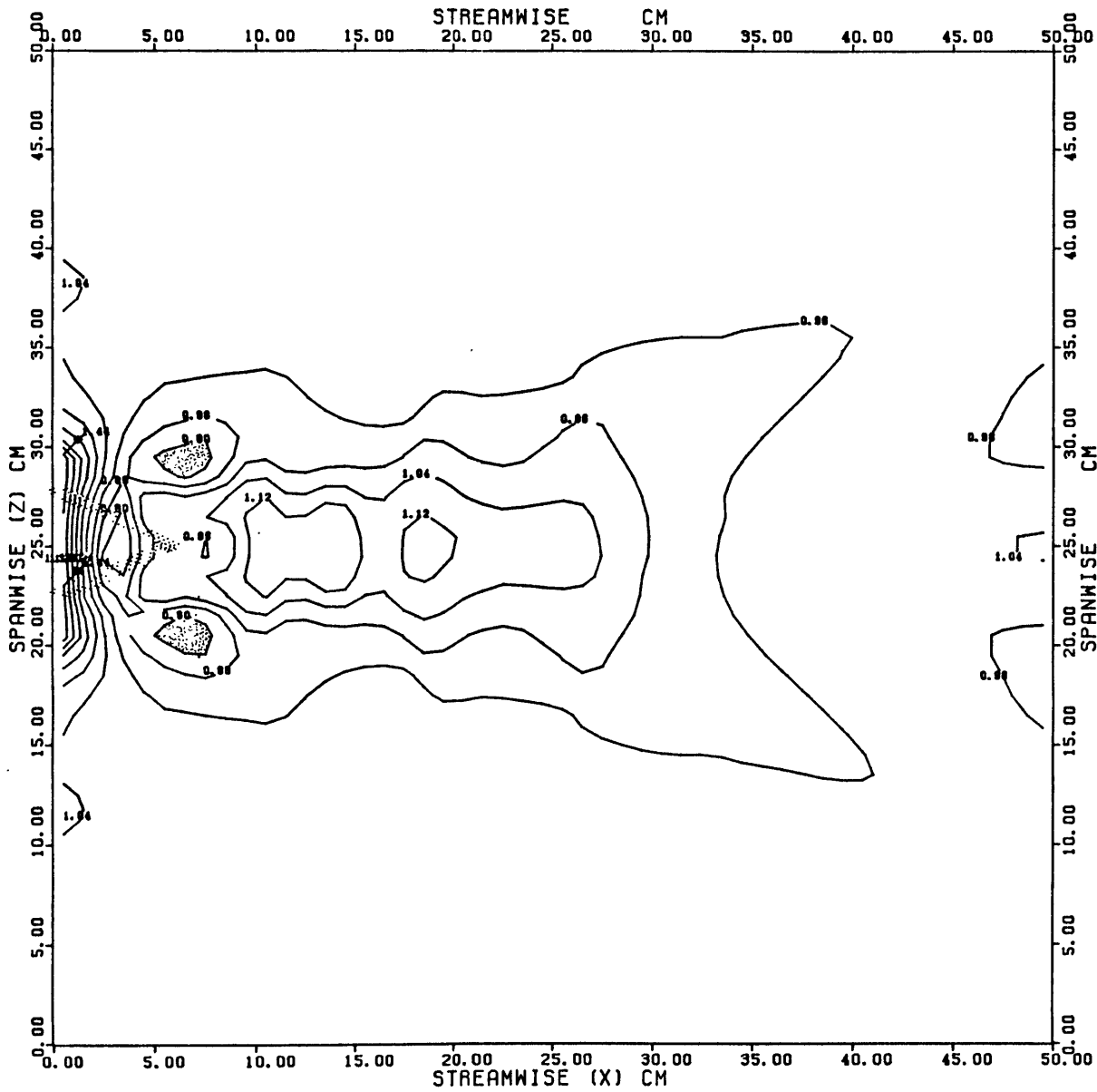
RUN 182



MEAN STRESS

REF = 0.808 DYNE/CM<sup>2</sup>

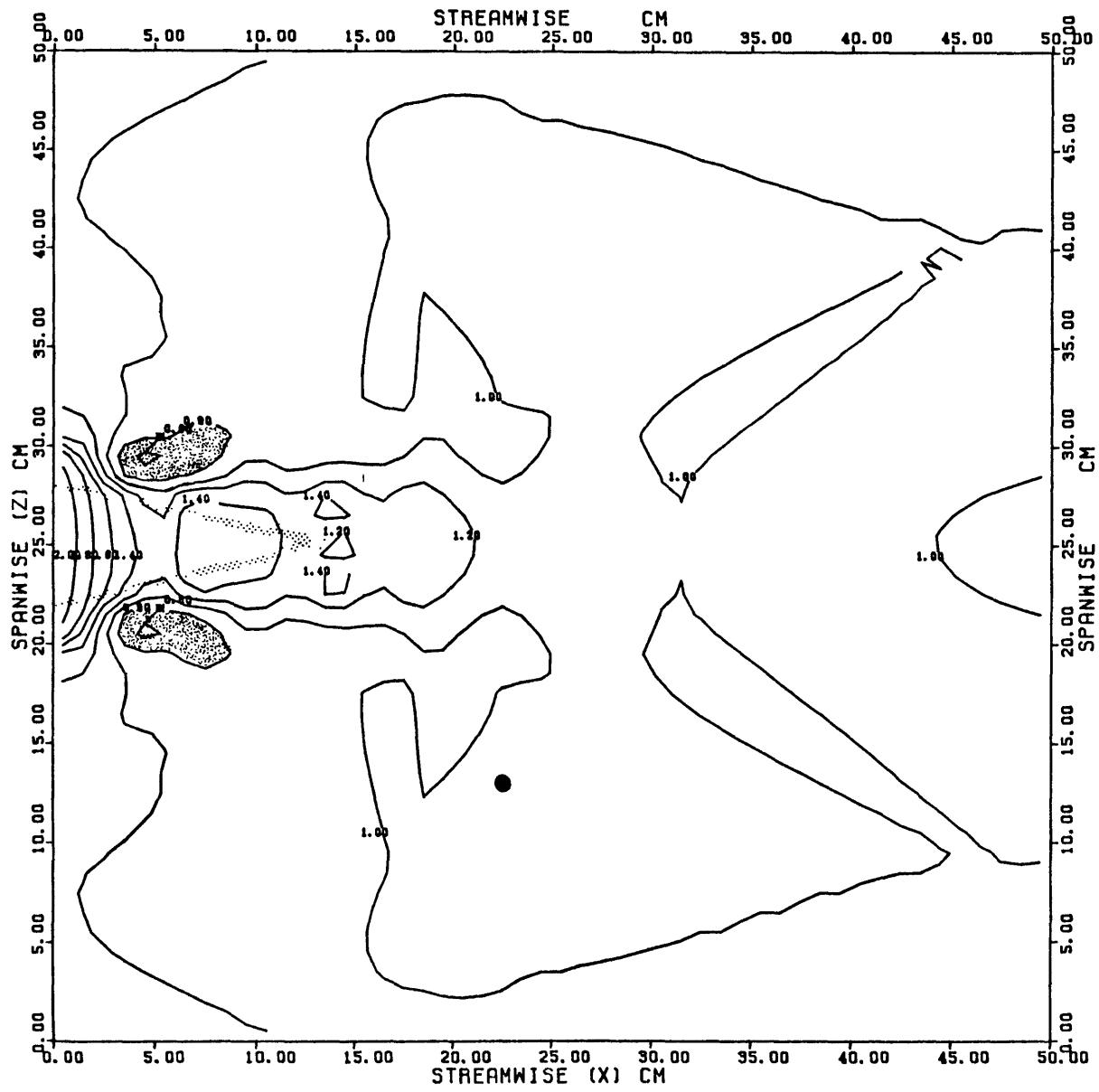
RUN 181



MEAN STRESS

REF = 1.476 DYNE/CM<sup>2</sup>

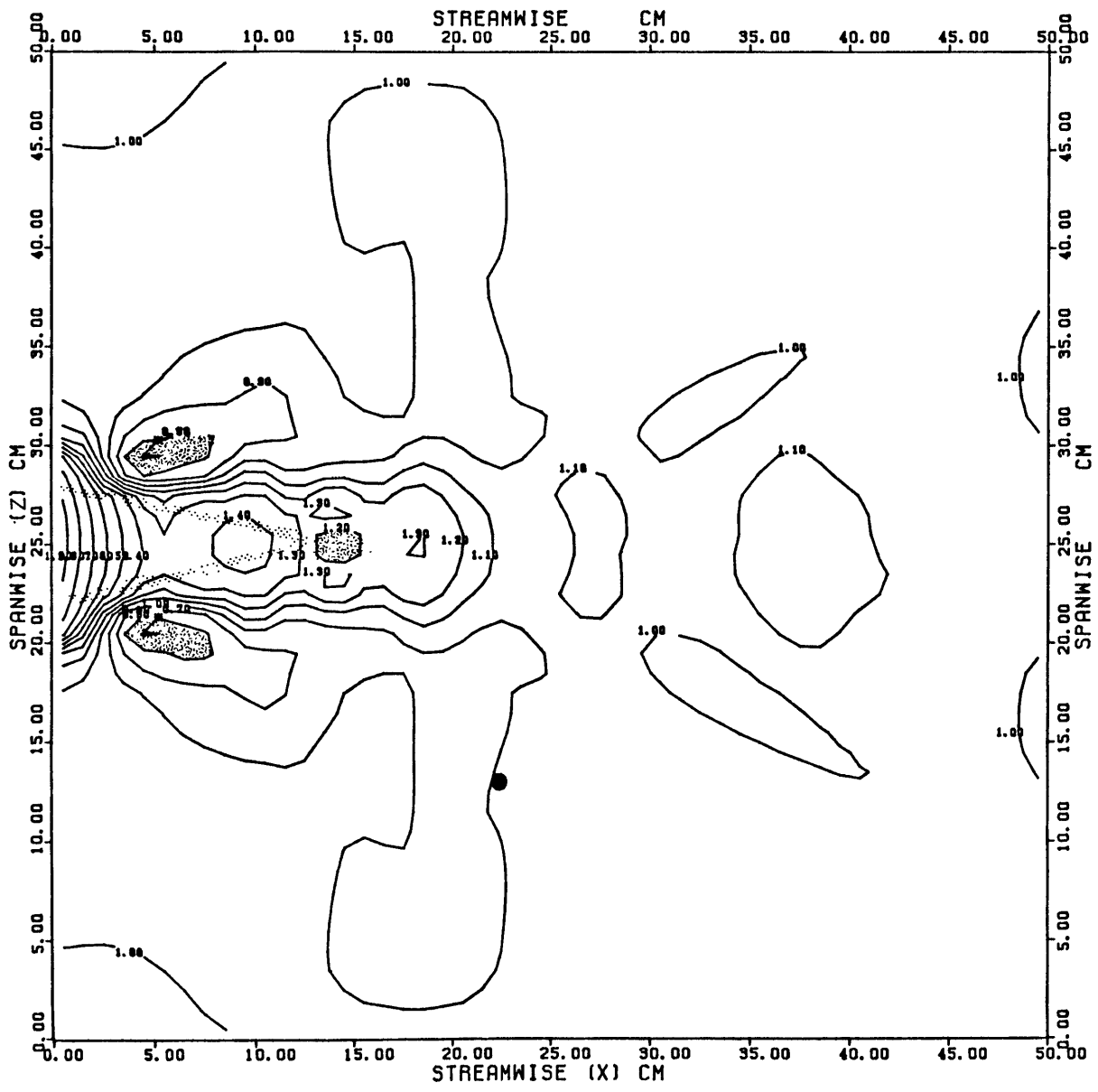
RUN 185



MEAN STRESS

REF = 0.401 DYNE/CM<sup>2</sup>

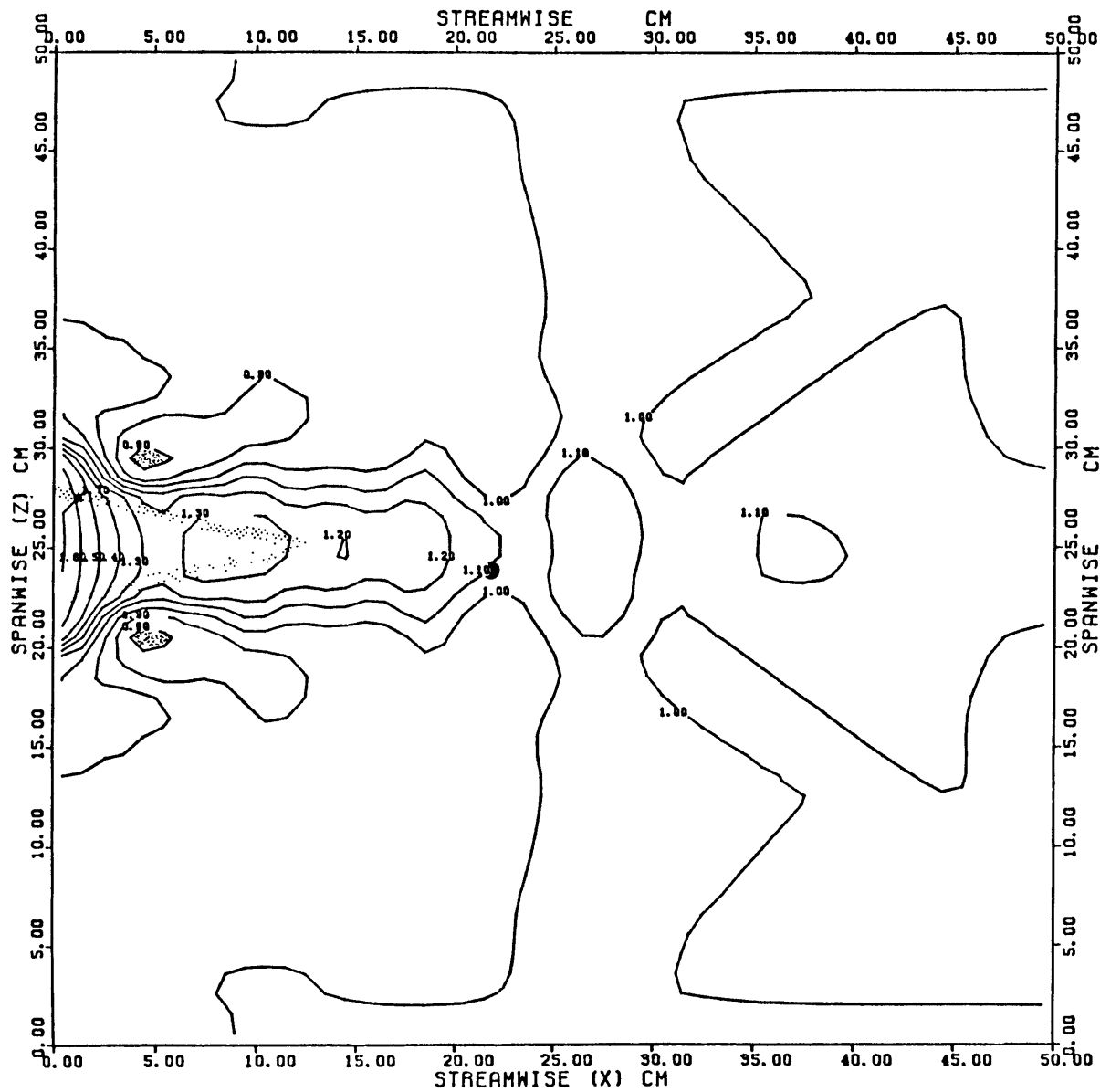
RUN 189



MEAN STRESS

REF = 0.910 DYNE/CM<sup>2</sup>

RUN 188



MEAN STRESS

REF = 1.460 DYNE/CM<sup>2</sup>

RUN 186

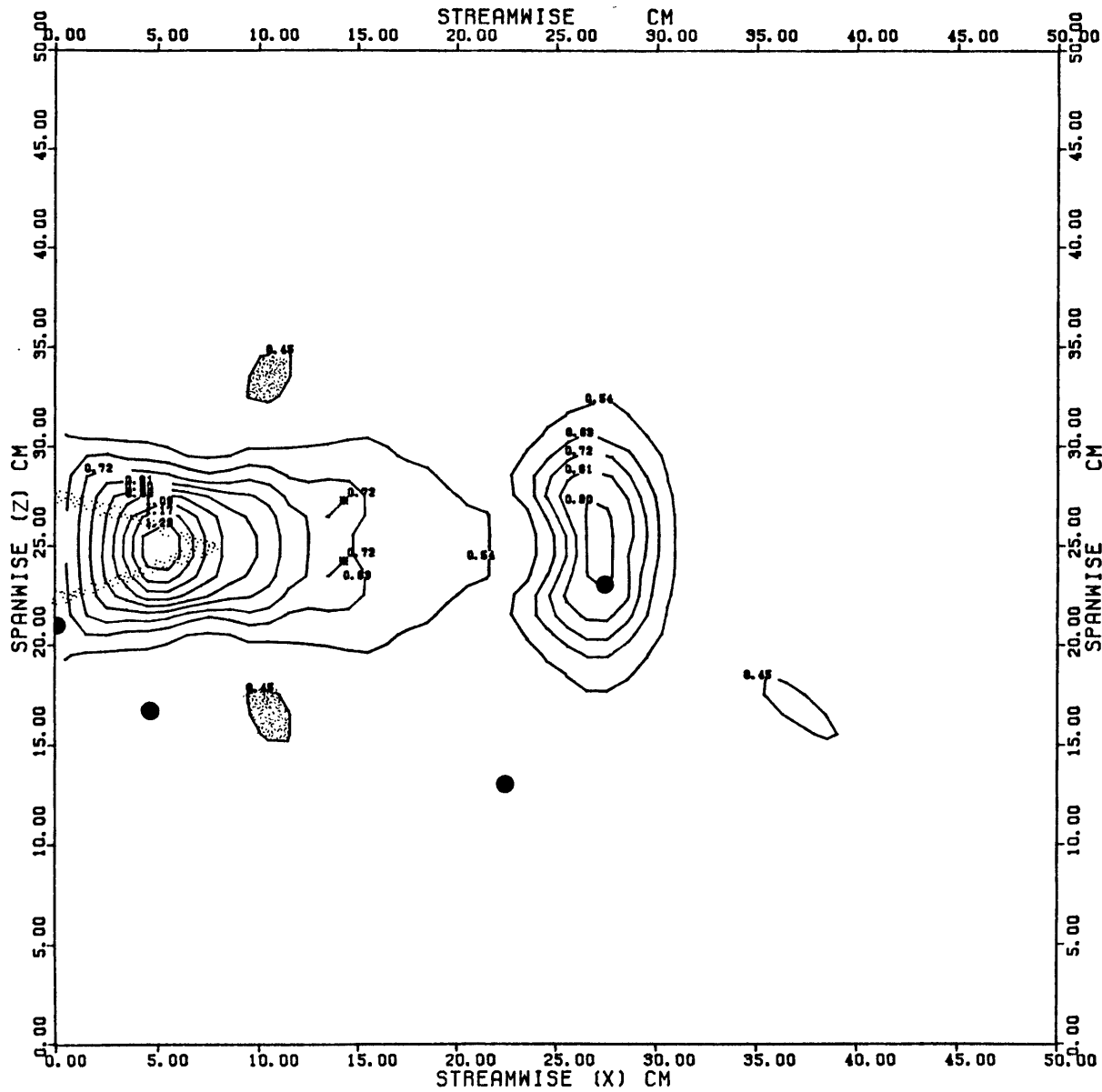


3.33. RMS skin friction. Contour maps of the root-mean-square value of the fluctuating skin friction nondimensionalized with the free-stream skin friction are shown in figure 3.15. This field shows the simplest structure of the three measured. There are maxima on either side of the hemisphere and where the flow reattaches at  $x \approx 9$  cm. The field relaxes monotonically downstream from reattachment. The rms value near reattachment is typically 50-70% of that of the mean magnitude at the same point. The nondimensional values generally decrease with Reynolds number, by 30-50%, as was found in smooth flow (section 2.41). Very weak minima can sometimes be associated with the magnitude lows discussed in the preceding section.

There is no systematic difference between the rms field with and without the short tail. The maximum nondimensional value occurs near reattachment, and its magnitude is not affected by the tail. Addition of the long tail, however, changes the rms field substantially. The reattachment maximum is moved to the end of the tail and is weakened to the extent that the maximum value overall is that attained alongside the element. This value is not affected significantly by the presence of the tail.

Figure 3.15. The root-mean-square skin-friction field interpolated from measurements behind isolated obstacles at the points shown in figure 3.4, nondimensionalized by the reference (free-stream) skin friction. Conditions for each run are given in Table 3.2; the graphs are arranged in order of increasing tail length and increasing Reynolds number. Stippled bands show the borders of areas covered by the obstacles or by separated flow. Shaded regions in the field are lows. The marked points are locations where data were not obtained, usually because of problems with the recorded digital cassette tapes. Contours more than about 10 cm off the centerline reflect mainly variation introduced by the interpolating program. Contour intervals for each graph are:

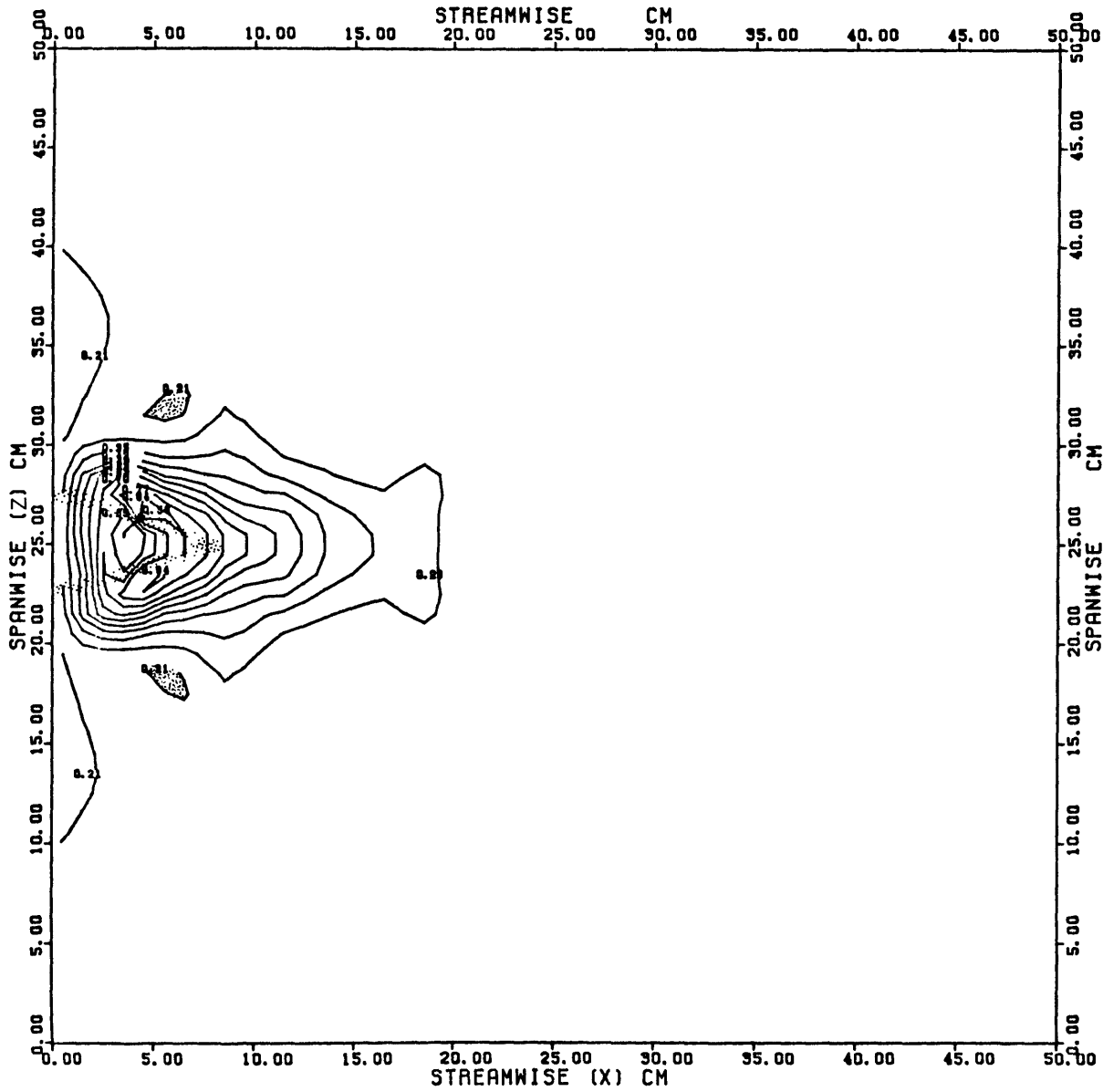
Run	Contour interval
178	0.09
176	0.07
179	0.07
182	0.09
181	0.08
185	0.03
189	0.04
188	0.02
186	0.02



RMS STRESS  
FLUCTUATION

REF = 0.385 DYNE/CM<sup>2</sup>

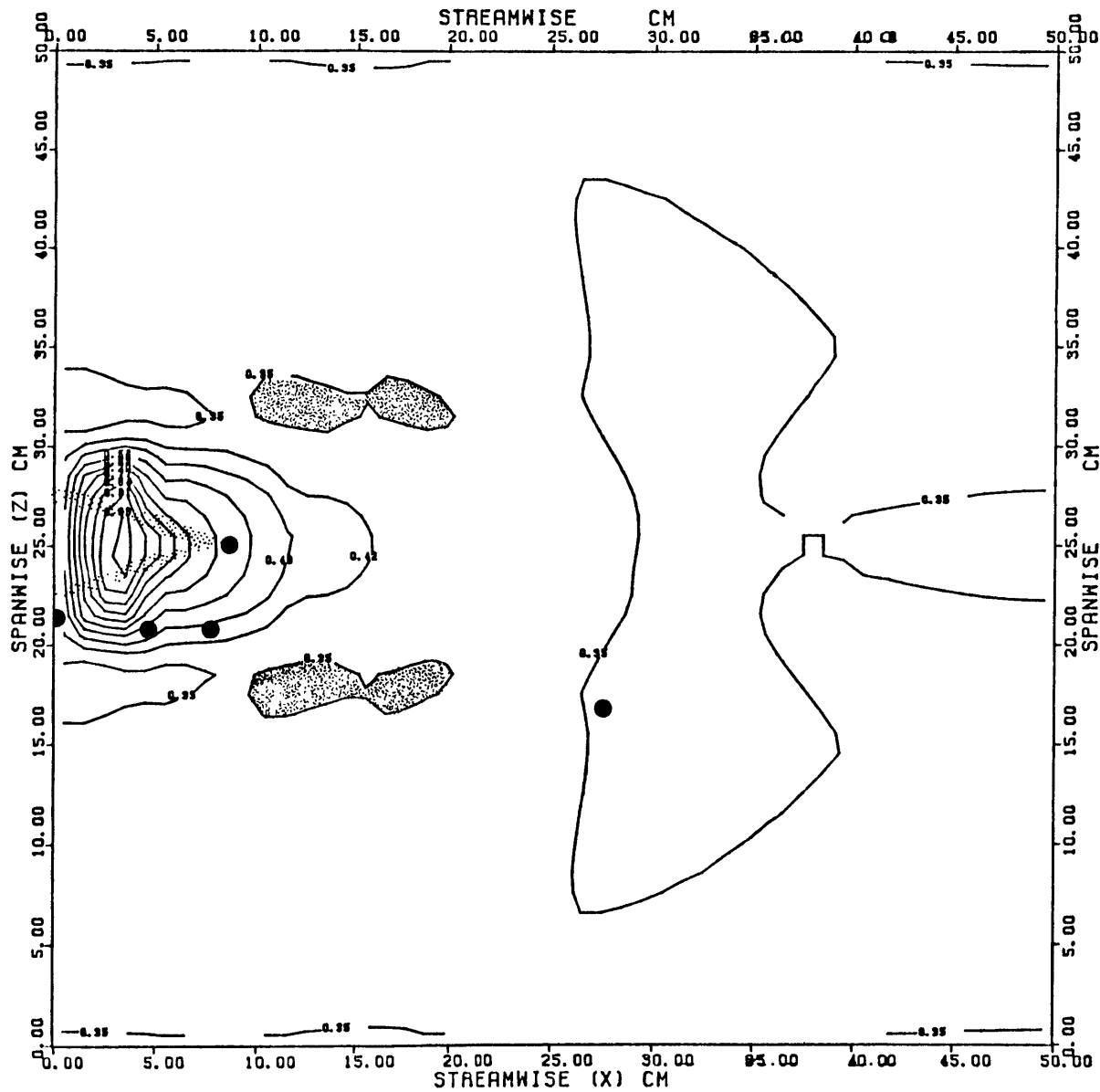
RUN 178



RMS STRESS  
FLUCTUATION

REF = 0.857 DYNE/CM<sup>2</sup>

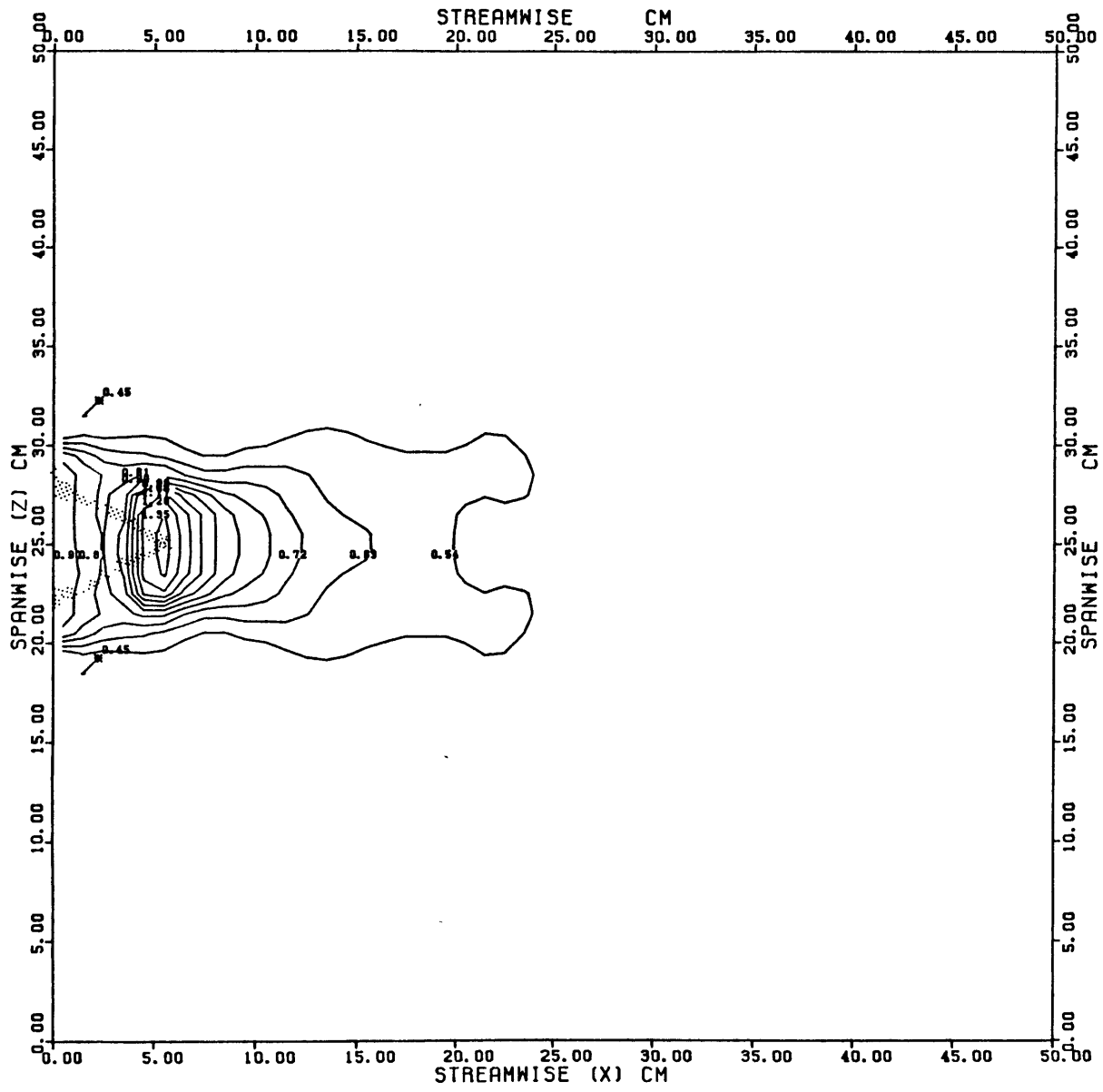
RUN 176



RMS STRESS  
FLUCTUATION

REF = 1.442 DYNE/CM<sup>2</sup>

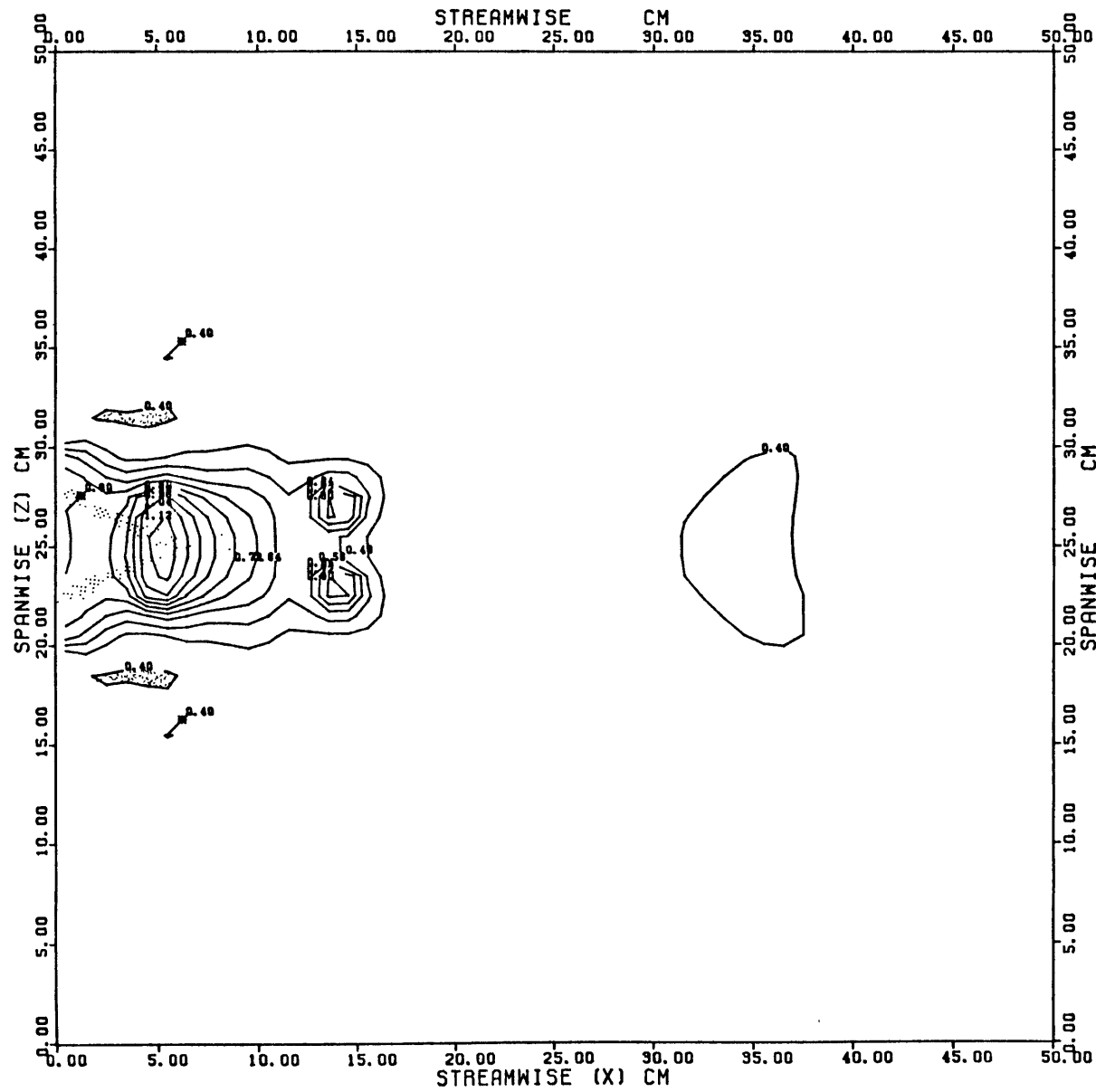
RUN 179



RMS STRESS  
FLUCTUATION

REF = 0.396 DYNE/CM<sup>2</sup>

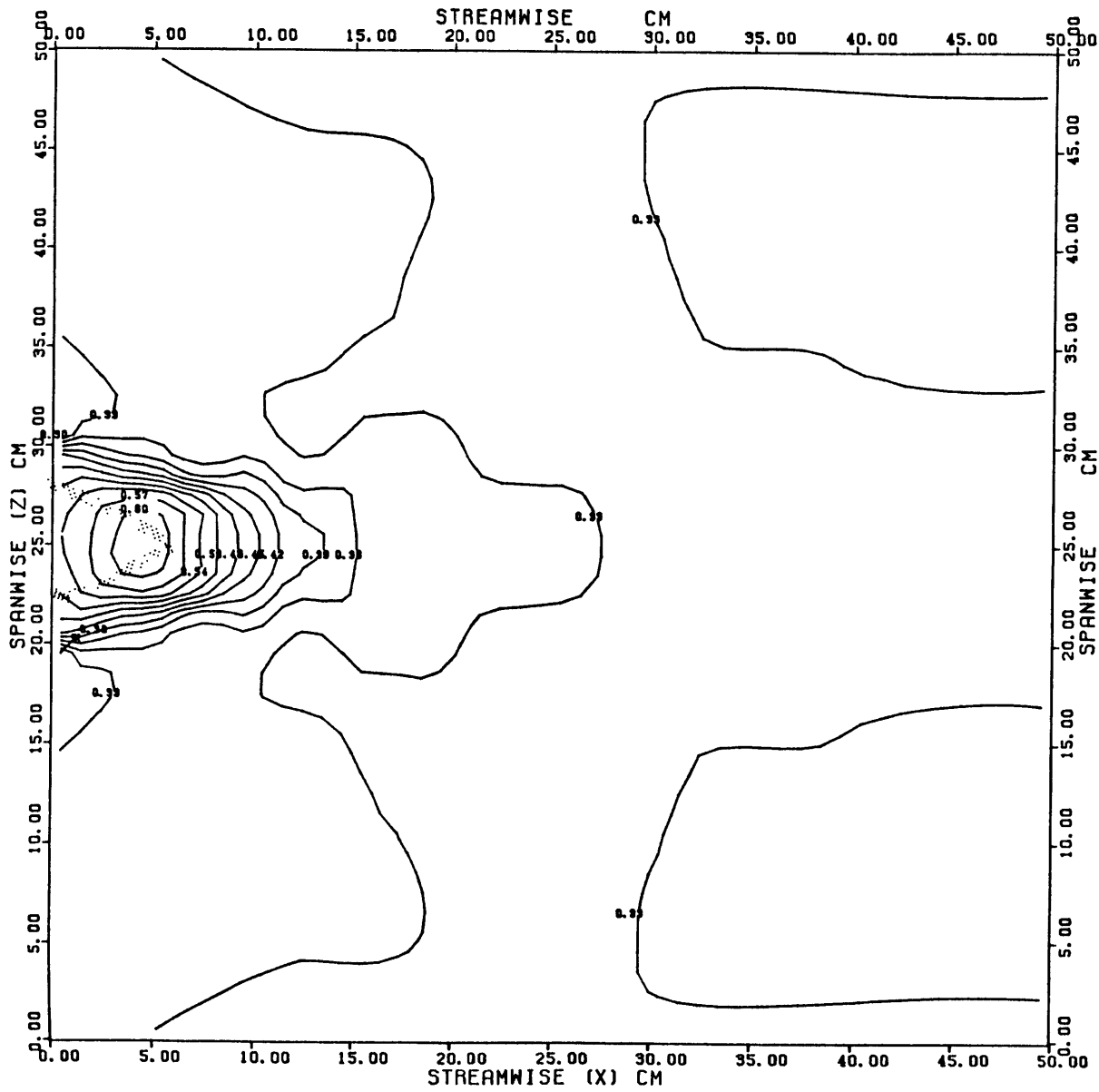
RUN 182



RMS STRESS  
FLUCTUATION

REF = 0.808 DYNE/CM<sup>2</sup>

RUN 181

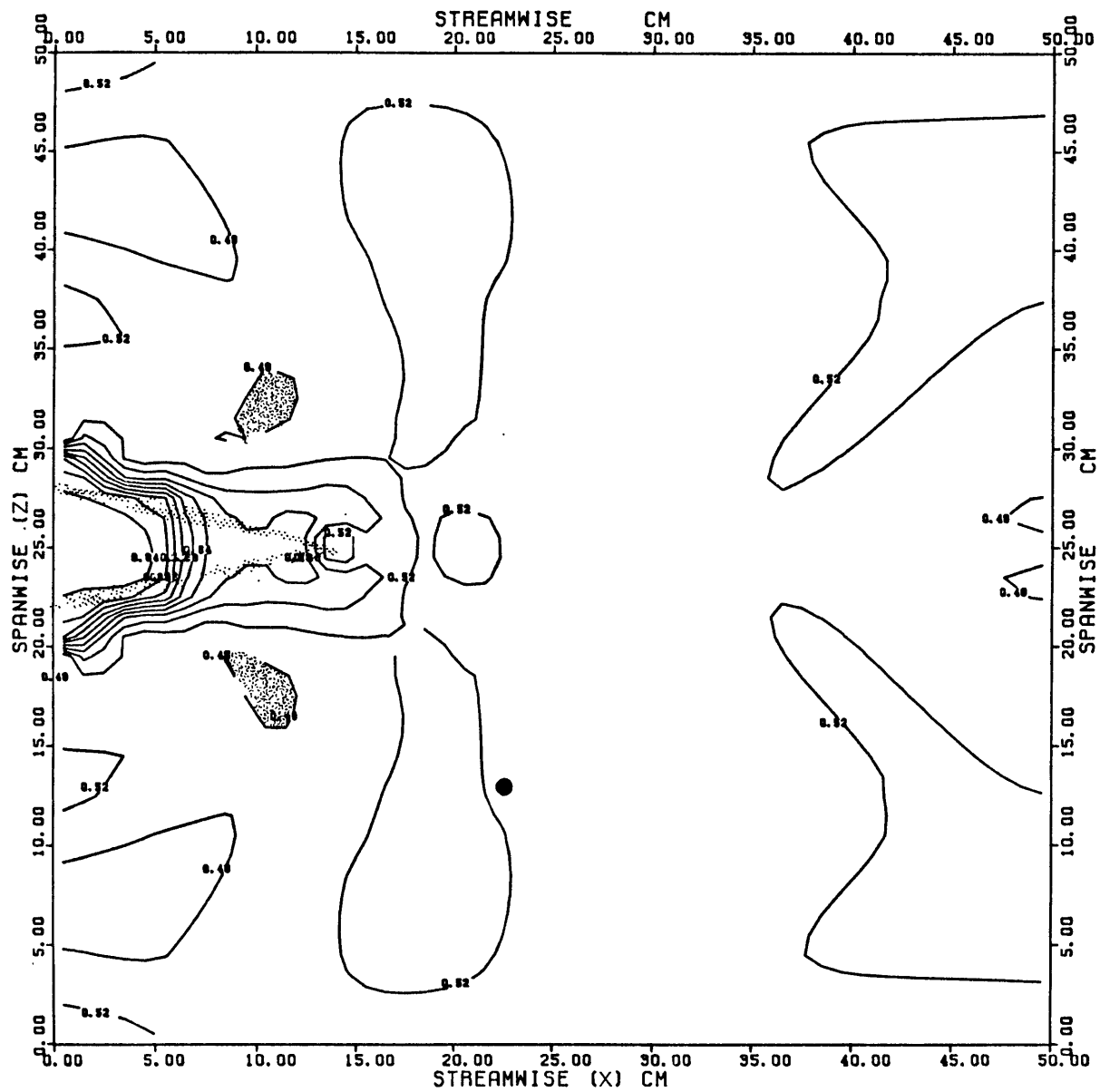


RMS STRESS  
FLUCTUATION

REF = 1.476 DYNE/CM<sup>2</sup>

RUN 185

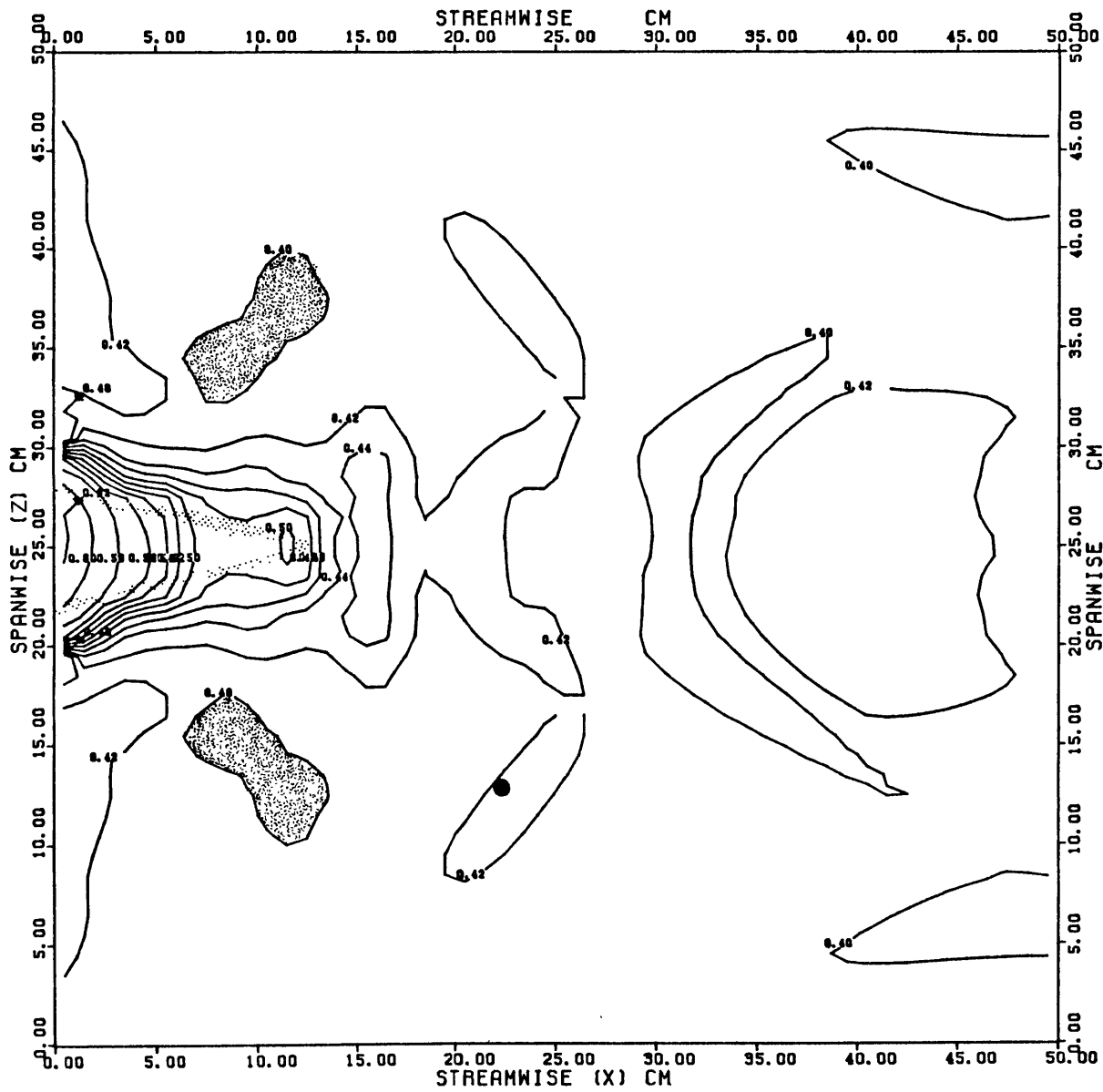




RMS STRESS  
FLUCTUATION

REF = 0.401 DYNE/CM<sup>2</sup>

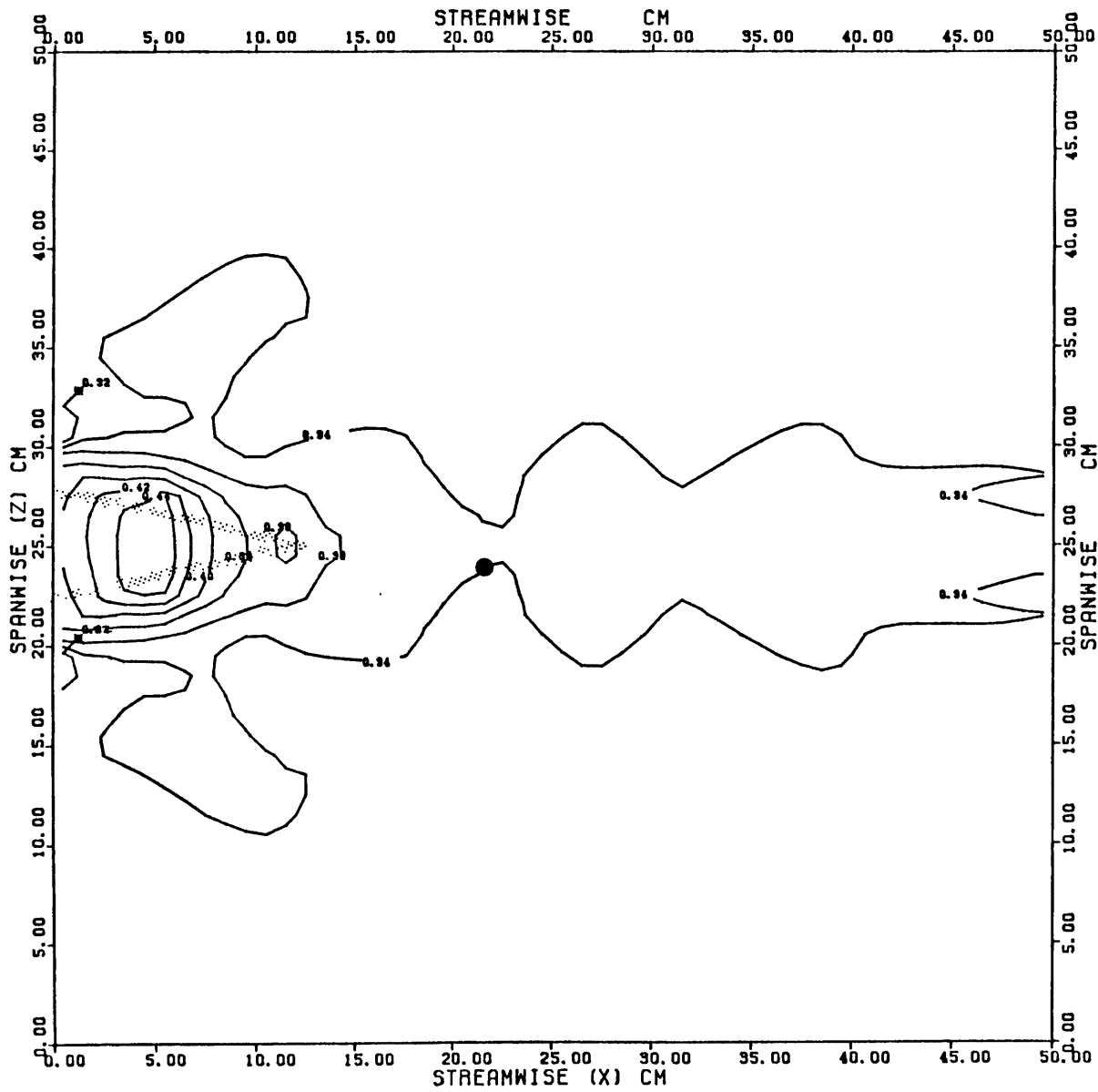
RUN 189



RMS STRESS  
FLUCTUATION

REF = 0.910 DYNE/CM<sup>2</sup>

RUN 188



RMS STRESS  
FLUCTUATION

REF = 1.460 DYNE/CM<sup>2</sup>

RUN 186

3.34 Horizontal divergence. The horizontal divergence of the mean skin friction field is presented in figure 3.16. Since the values have been divided through by the free-stream skin friction they have units of inverse length ( $\text{cm}^{-1}$ ). Positive values of the field are divergent (erosional) and negative values are convergent (depositional; section 3.1). The measured fields behave in general as follows. There is a strongly convergent region near reattachment; downstream of this point the field is divergent along the centerline and convergent to either side of it. This basic structure, which is what would be expected on the basis of the direction fields measured here and by Werner et al. (1980), is modified by streamwise variation that could not have been predicted on the basis of direction measurements alone. These streamwise variations arise because of streamwise changes in skin-friction magnitude as shown in figure 3.14. Where the magnitude increases downstream, its contribution to the divergence is positive and the divergent band is broadened; where it decreases downstream the reverse occurs. The adjacent convergent regions are similarly weakened by the increase in magnitude as the flow passes out of the flanking low-magnitude regions seen in figure 3.14. The balance of these competing effects is too fine to be resolved accurately and completely by the methods used here. It is clear, however, that in the far field ( $x > 10 \text{ cm}$ ) at least, neither direction nor magnitude completely controls the divergence field, so that small variations (or errors) in either affect

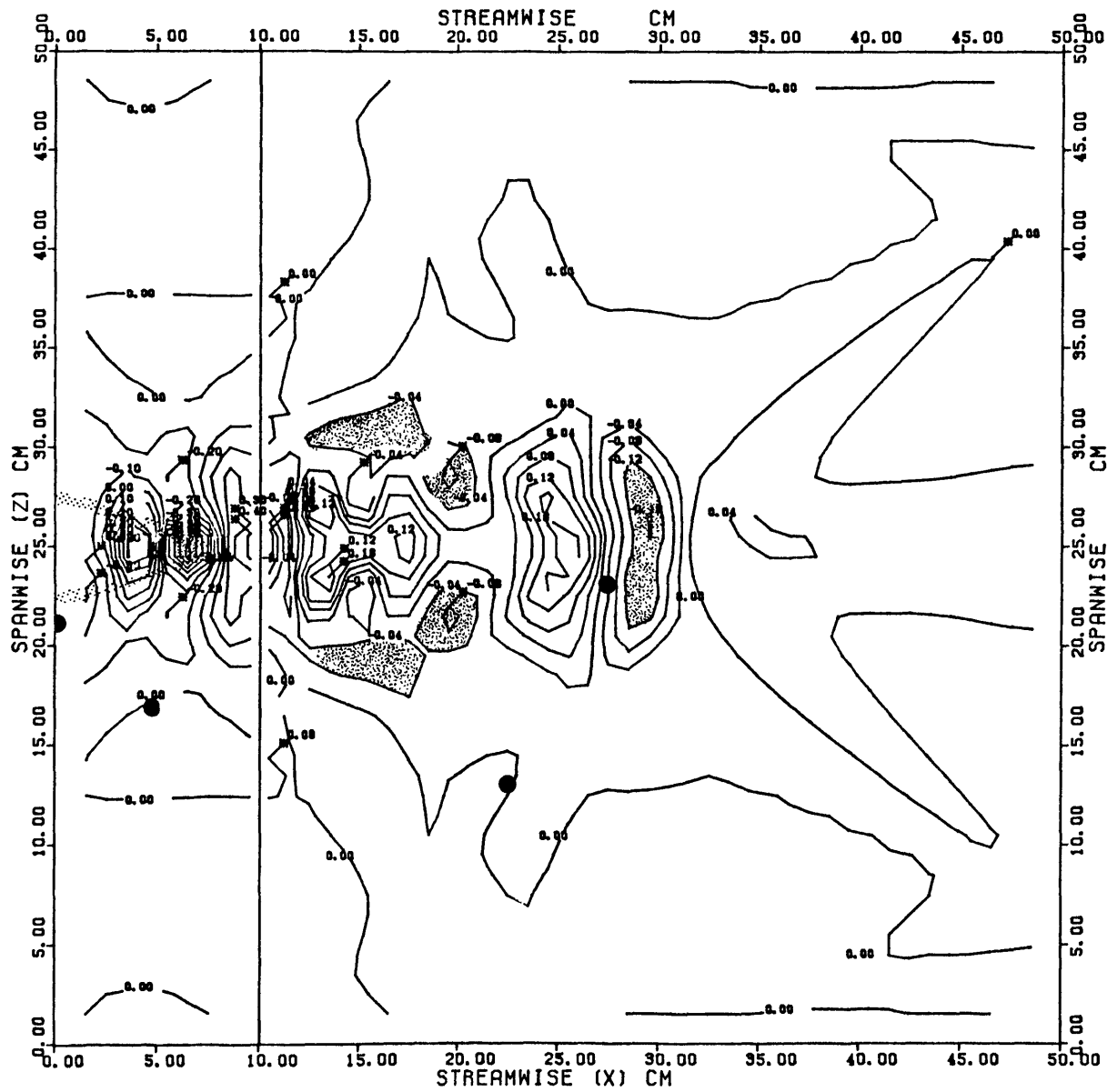
strongly the disposition of convergent and divergent regions.

The horizontal divergence fields show no qualitative changes with increasing Reynolds number, although as with the other fields the observed range of variability decreases by 20-30% going from low to high Reynolds number. The only effect of adding the short tail is to decrease the minimum value attained in the convergent region at reattachment by 50-70%. Addition of the long tail causes the convergent region to disappear; the divergence is positive at reattachment (that is, at the end of the tail).

Figure 3.16. The horizontal divergence of the time-averaged skin-friction field. The field has been interpolated from measurements behind isolated obstacles at the points shown in figure 3.4, and all the data have been divided through by the reference (free-stream) skin friction. Conditions for each run are given in Table 3.2; the graphs are arranged in order of increasing tail length and increasing Reynolds number. Stippled bands show the borders of areas covered by the obstacles or by separated flow. Shaded regions in the field are lows. The marked points are locations where data were not obtained, usually because of problems with the recorded digital cassette tapes. Contours more than about 10 cm off the centerline reflect mainly variation introduced by the interpolating program. Contour intervals for each graph are:

Contour interval:

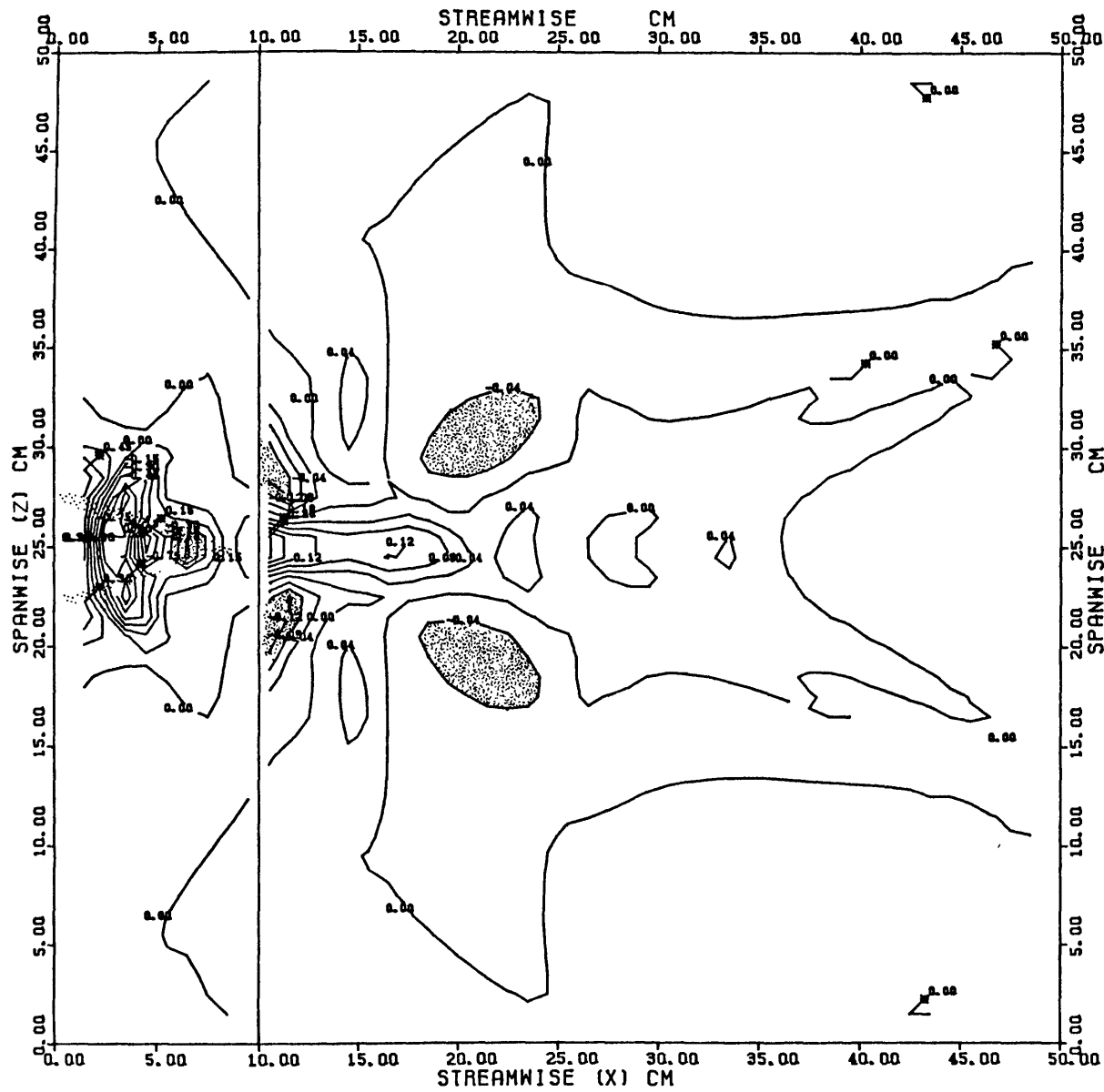
Run	near field	far field
178	0.10	0.04
176	0.15	0.04
179	0.08	0.04
182	0.10	0.02
181	0.09	0.02
185	0.07	0.02
189	0.09	0.03
188	0.08	0.03
186	0.06	0.02



HORIZONTAL  
DIVERGENCE (1/CM)

REF = 0.385 DYNE/CM<sup>2</sup>

RUN 178

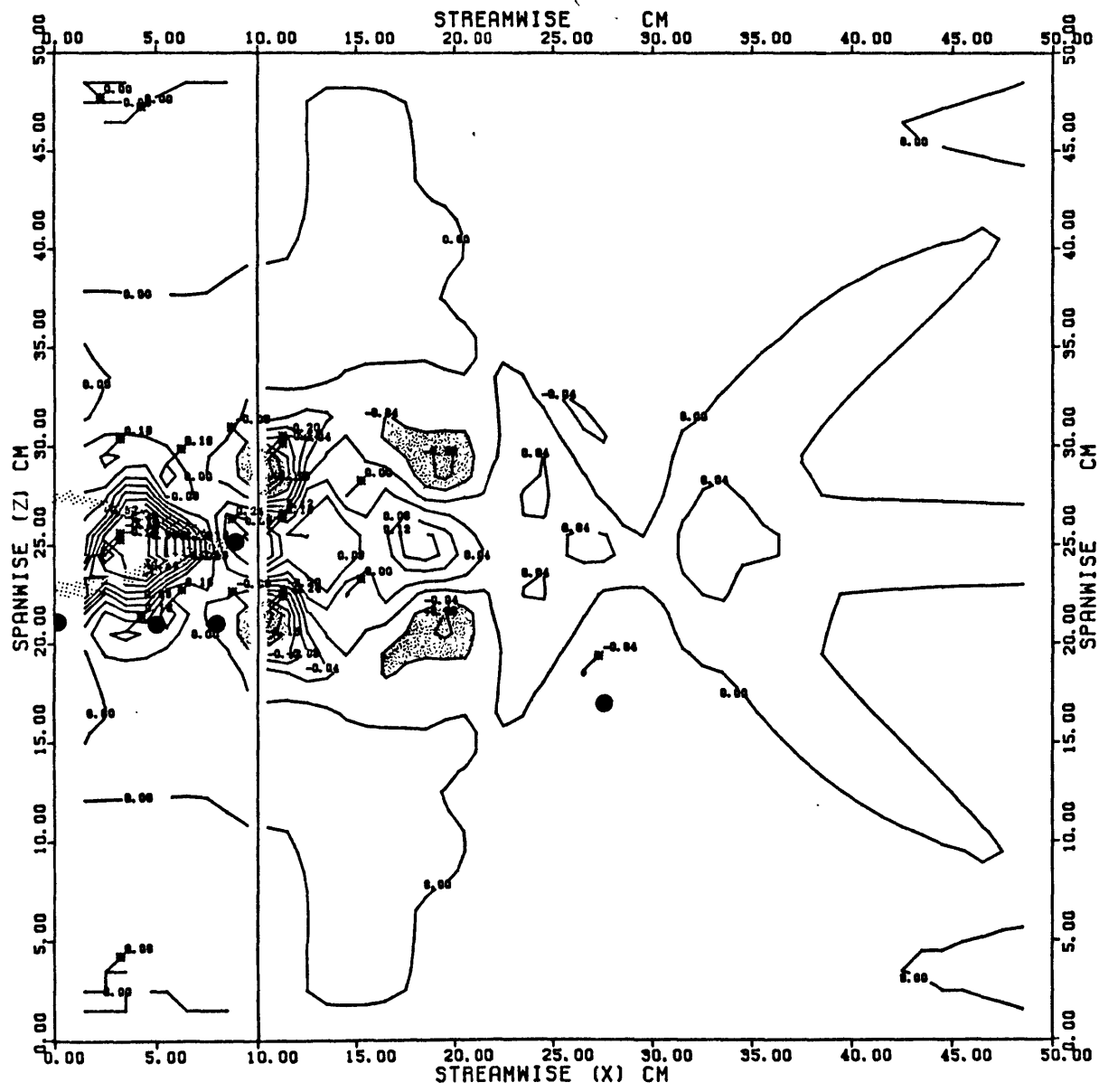


HORIZONTAL  
DIVERGENCE (1/CM)

REF = 0.857 DYNE/CM<sup>2</sup>

RUN 176

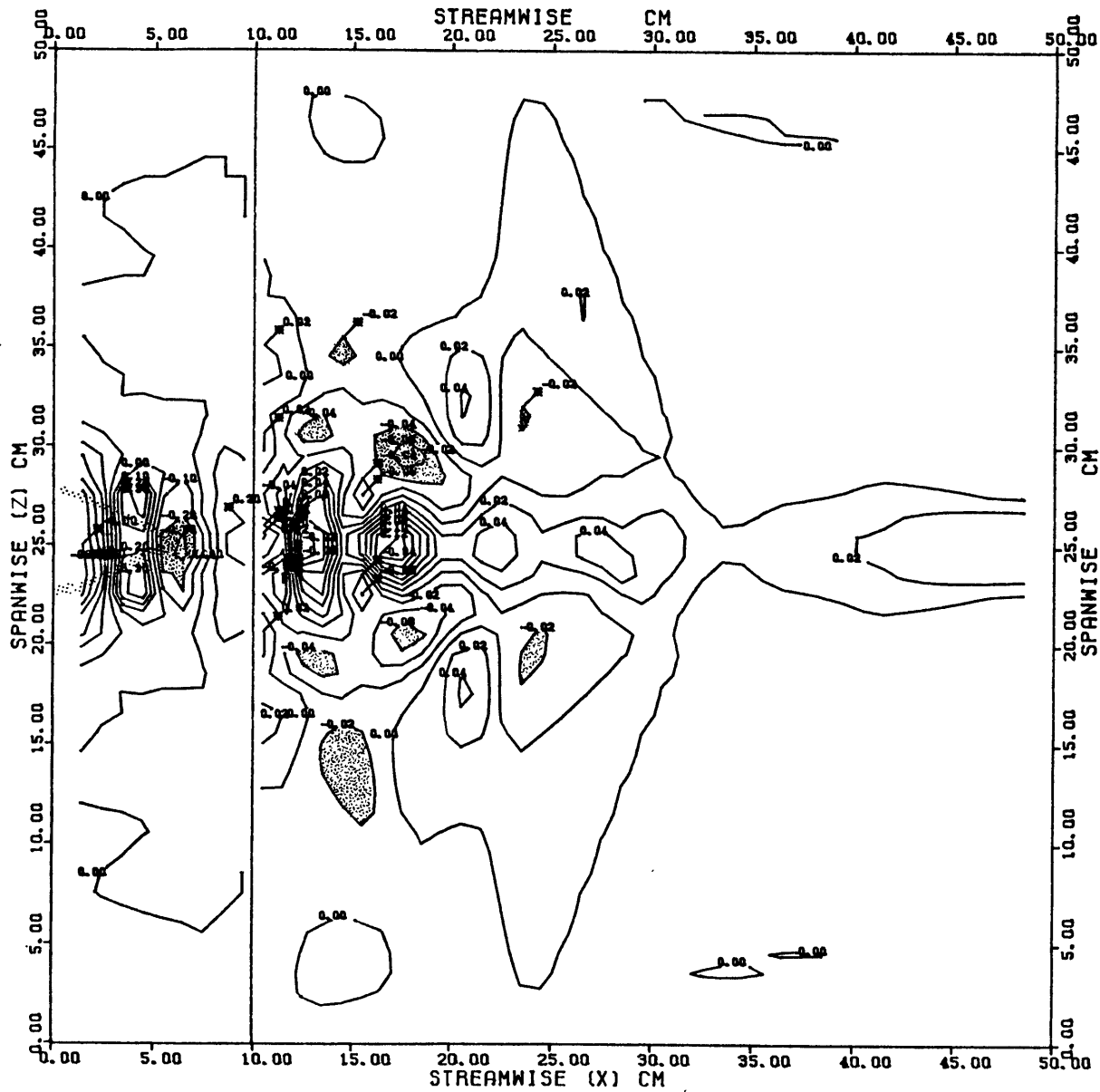




HORIZONTAL  
DIVERGENCE (1/CM)

REF = 1.442 DYNE/CM<sup>2</sup>

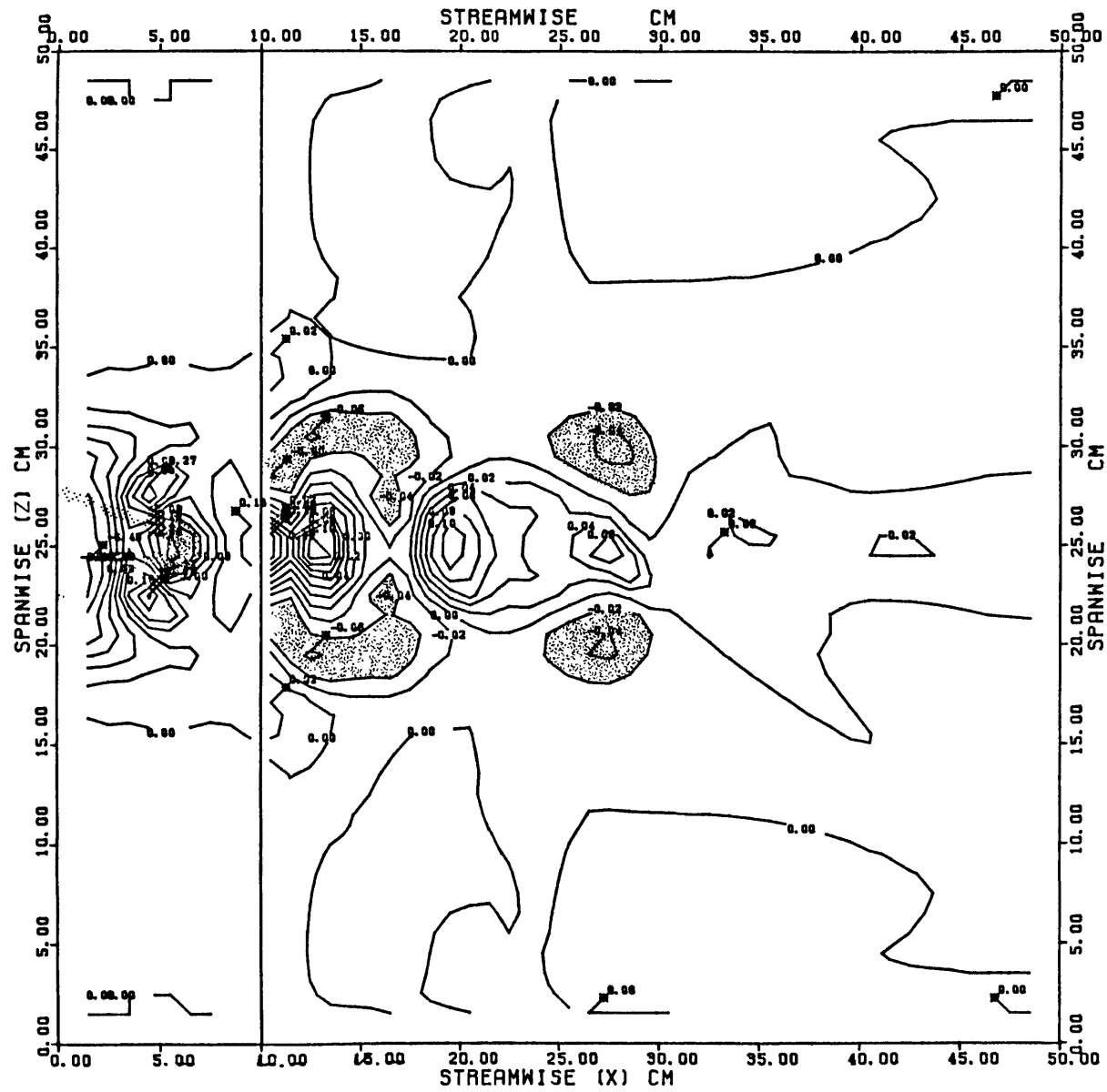
RUN 179



HORIZONTAL  
DIVERGENCE (1/CM)

REF = 0.396 DYNE/CM<sup>2</sup>

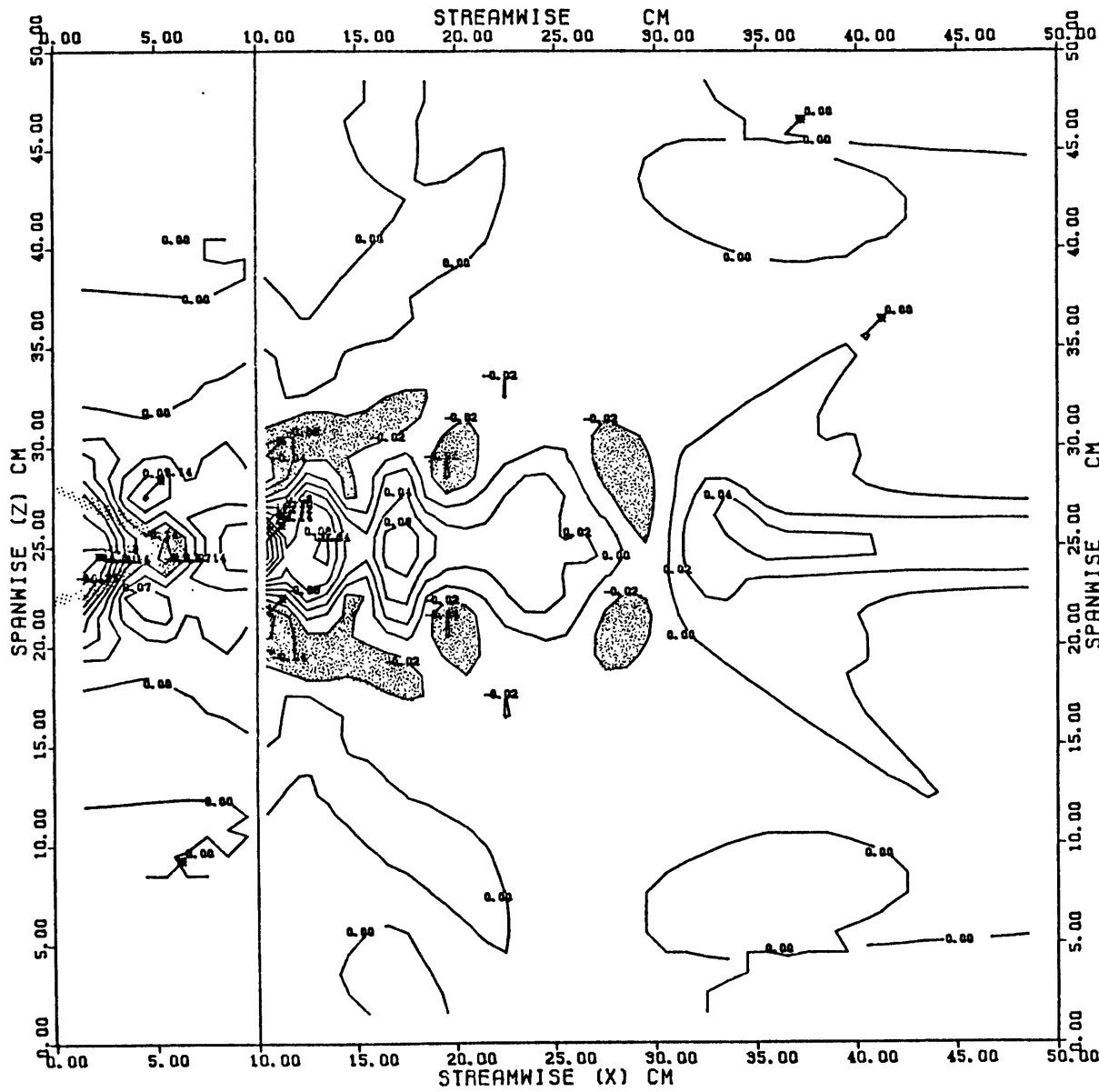
RUN 182



HORIZONTAL  
DIVERGENCE (1/CM)

REF = 0.808 DYNE/CM<sup>2</sup>

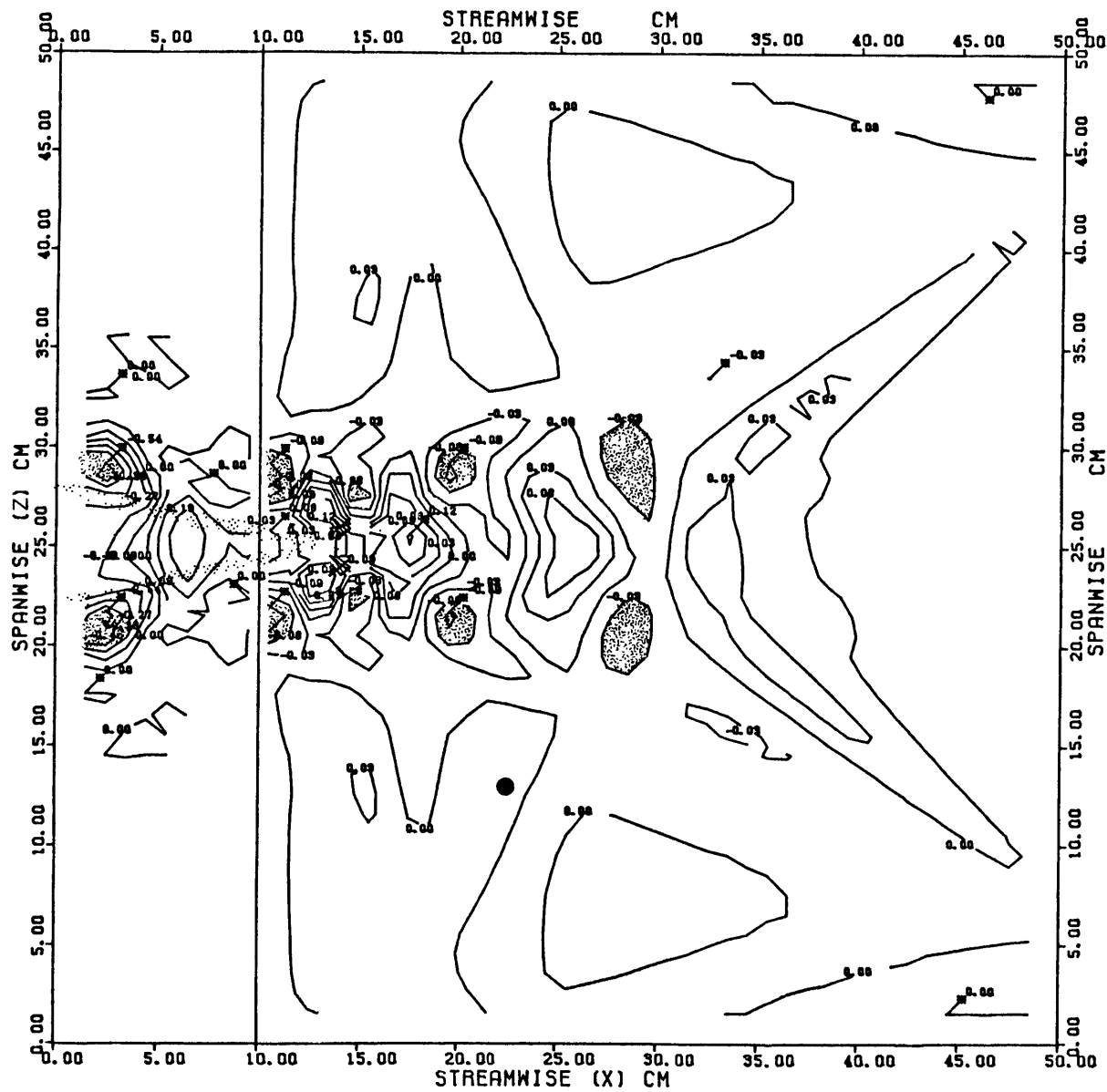
RUN 181



HORIZONTAL  
DIVERGENCE (1/CM)

REF = 1.476 DYNE/CM<sup>2</sup>

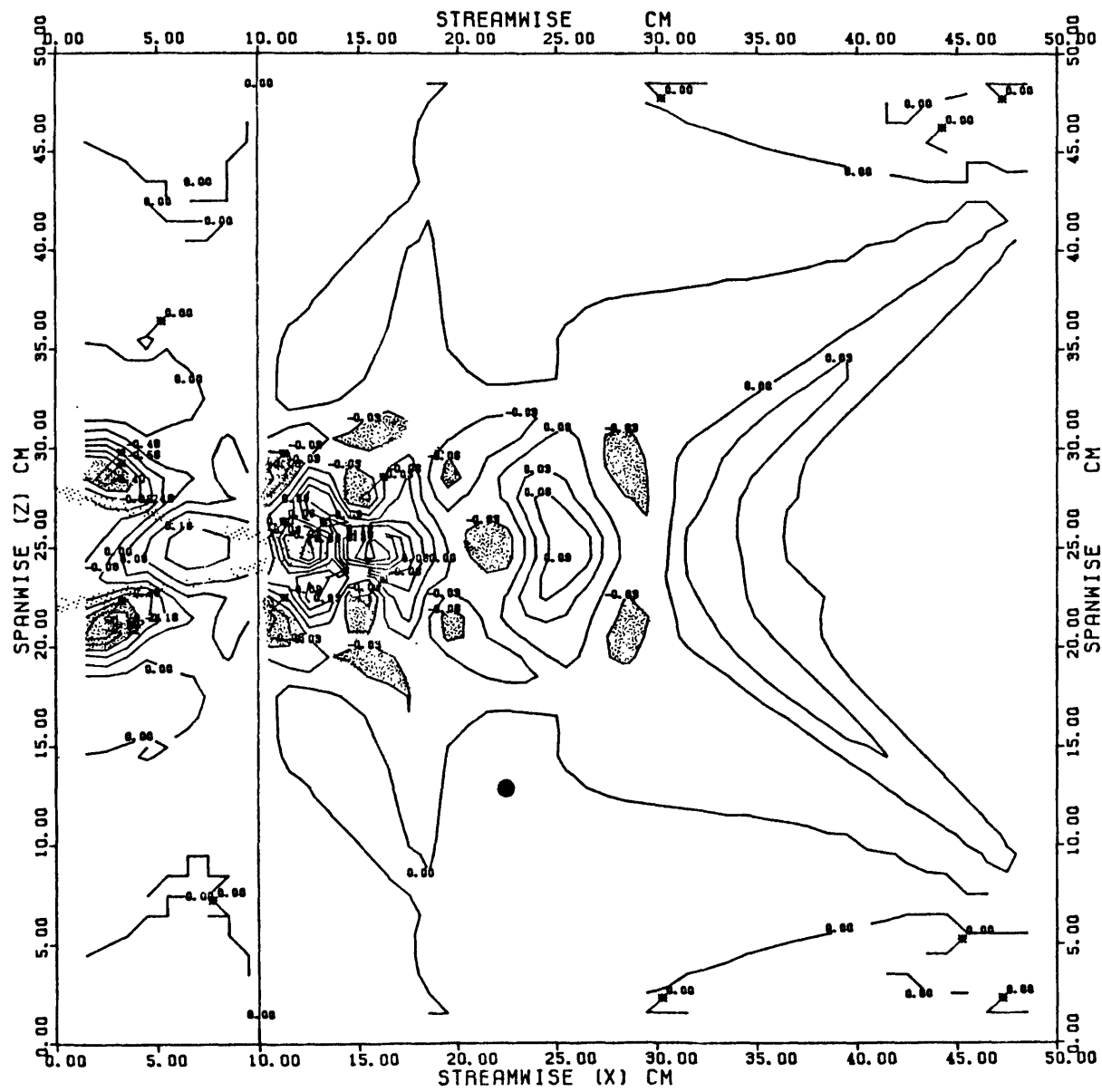
RUN 185



HORIZONTAL  
DIVERGENCE (1/CM)

REF = 0.401 DYNE/CM<sup>2</sup>

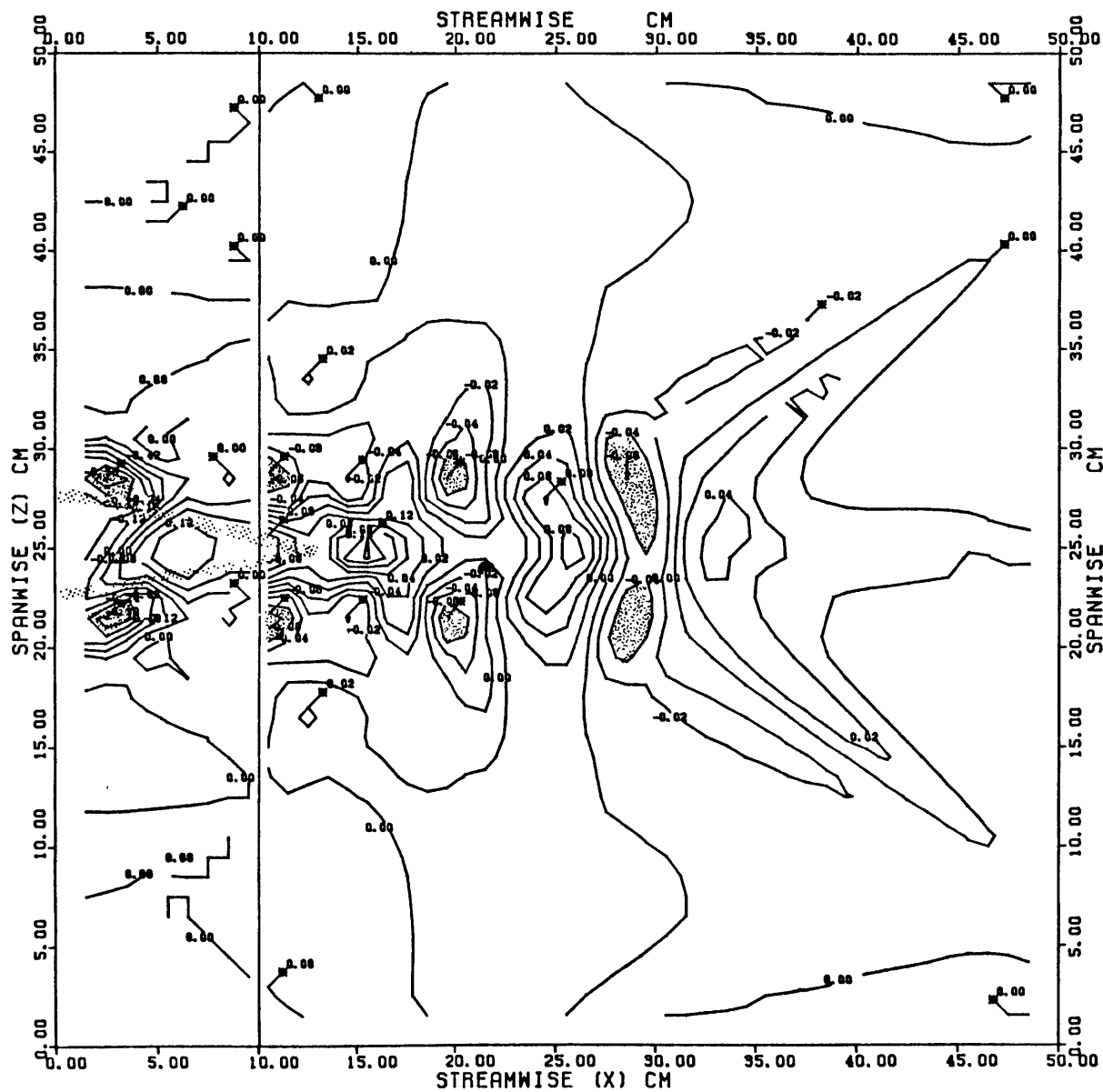
RUN 189



HORIZONTAL  
DIVERGENCE (1/CM)

REF = 0.910 DYNE/CM<sup>2</sup>

RUN 188



HORIZONTAL  
DIVERGENCE (1/CM)

REF = 1.460 DYNE/CM<sup>2</sup>

RUN 186

3.4. Results: full fields. For the reasons discussed in section 3.2, all the full-field runs were made at a water depth of 20 cm. At this large depth, it was necessary to run the flume at its full discharge to get an accurately measurable total bottom stress (about  $0.8 \text{ dynes/cm}^2$ ), so data were obtained for only one Reynolds number. There are four runs at two areal densities, with and without long tails. The experimental conditions are summarized in Table 3.3.

3.41. Skin friction. The main purpose of the skin-friction array shown in figure 3.6 was to determine whether or not the skin-friction field behind a test roughness element is affected by the presence of neighboring elements, and to provide a basis for estimating the spatially averaged skin-friction. Since there is no readily identifiable reference skin friction in the full-field case, interference has been operationally defined as relative distortion of the skin-friction field compared to that measured for an isolated element. To make this comparison, all the skin-friction values for each run have been normalized by that measured at Position 3 (figure 3.6) for that run. This somewhat arbitrary choice was made because (1) this position is well within the wake of the test roughness element so it is itself protected from interference, (2) in the isolated-element runs Position 3 was not affected strongly by variations in tail length, (3) data were obtained at this location for all the isolated-element runs, and (4) Sensor 3 showed especially good stability



Run	Tail	Areal Density $\lambda$	Bulk Velocity $\bar{u}$	Reynolds Number $\bar{u}D/\nu$	Total Bottom Stress $\tau_{ot}$
199	none	0.00845	16.5 cm/s	33,700	0.85 d/cm <sup>2</sup>
202	long	0.00845	16.4	32,500	0.84
203	long	0.0197	15.9	31,700	1.09
204	none	0.0197	16.1	31,800	1.07

Table 3.3. Experimental conditions for runs of the second (full-field) series.

during the full-field runs.

The results from the skin-friction array are given in Table 3.4 along with similarly treated data from the isolated-element runs. Based on the error considerations discussed in section 1.23, consistent differences of about 20% or more in the normalized data are considered significant. Position 1 shows a reduction in normalized magnitude in the full-field runs for Configuration 2 (the dense array) only, and Position 2 shows no significant variation. Position 4 is reduced in the sparse array and significantly reduced in the dense array, but only when the tail is absent. Position 5 is significantly reduced in the sparse array when the tail is present. Position 6 is significantly increased in the dense array (Configuration 2). Position 7 is reduced in the sparse array and reduced significantly in the dense array.

Taken as a whole, the data indicate that there is substantial skin-friction interference in the dense array and possible interference in the sparse array, although in the latter case most of the observed variation is within the error limits of the data. Some of the observed changes can be accounted for by incorporating in a very simple way the effects of the next roughness element upstream, as shown in the bottom panel of Table 3.4. The entries in this panel are the normalized isolated-element data from the top panel multiplied by normalized values of the isolated-element field referred to the nearest upstream roughness element. The

Table 3.4. Time-averaged skin-friction magnitudes at the seven positions shown in figure 3.6. The values on each line have been normalized by that at Position 3 for that line; the dimensional values for Position 3 (in dynes/cm<sup>2</sup>) are given in parentheses. The isolated-element values are those for the lowest of the three Reynolds numbers at which measurements were made. The simple interference model for the bottom panel is described in the text.

Tail	Sensor Position						
	1	2	3	4	5	6	7
	Isolated element						
none	0.78	0.72	1.00 (0.58 d/cm <sup>2</sup> )	0.74	0.40	0.64 <sup>1</sup>	1.52 <sup>2</sup>
long	0.71	0.68	1.00 (0.59)	1.00	0.50	0.66	1.44
	Configuration 1 (sparse array)						
none	0.77	0.83	1.00 (0.75)	0.63	0.41	0.59	1.39
long	0.75	0.75	1.00 (0.69)	1.04	0.39	0.70	1.30
	Configuration 2 (dense array)						
none	0.69	0.76	1.00 (0.69)	0.58	0.46	0.93	1.11
long	0.58	0.76	1.00 (0.71)	0.96	0.46	1.00	1.23
	Configuration 2 -- with simple interference correction						
none	0.78	0.72	1.00	0.73	0.43	0.82	1.76
long	0.75	0.67	1.00	0.98	0.50	0.84	1.51

---

<sup>1</sup> interpolated

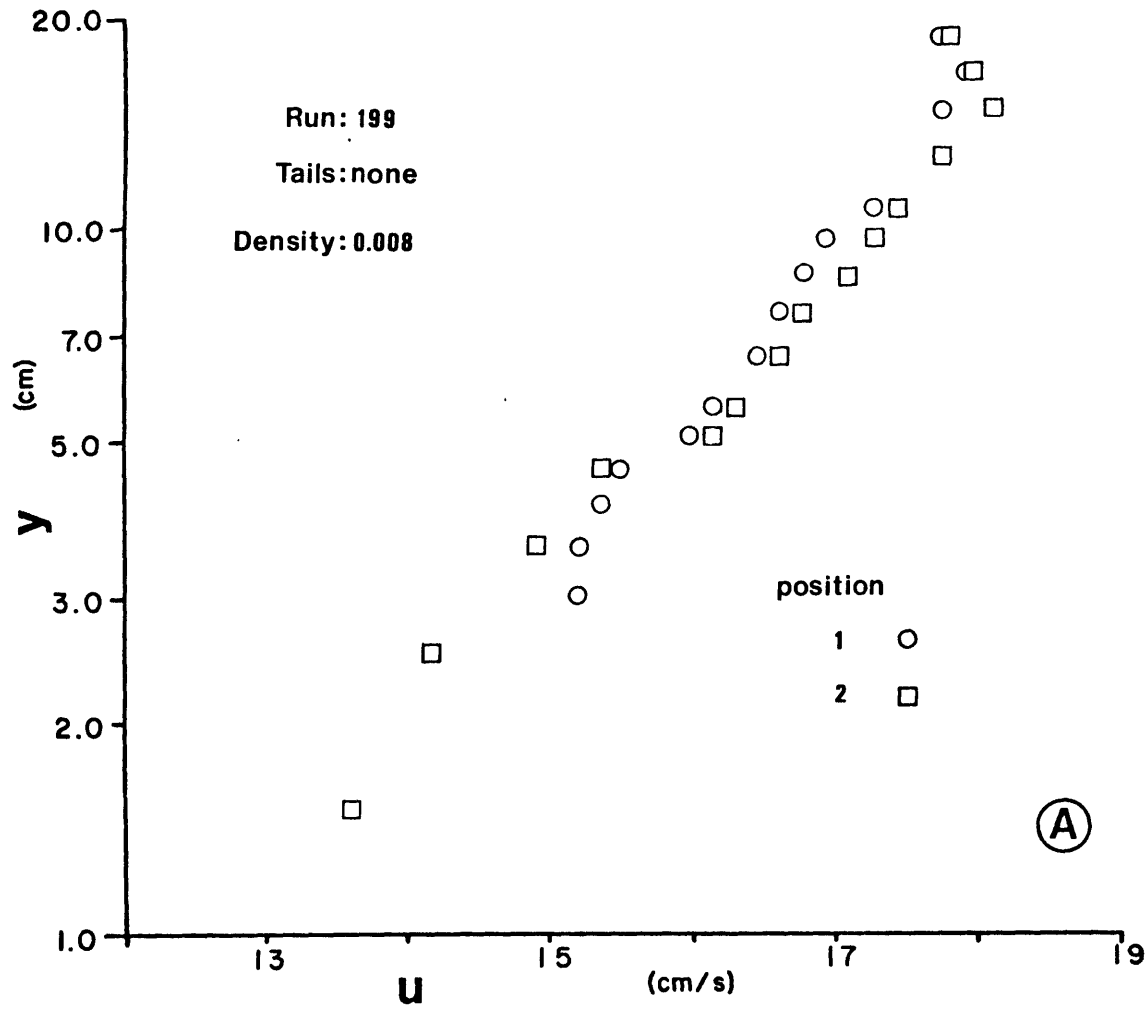
<sup>2</sup> with short tail

skin-friction field for the upstream element was estimated at each of the seven measuring positions, in a coordinate system centered on the upstream element, from interpolated data from the first series of runs (the output of program SKINFRIC). These estimates were then normalized by the upstream-element value at Position 3. As shown in Table 3.4, this simple interference correction accounts for much of the effect of the array on Position 6 but not Positions 1 and 4. The interference correction is in the wrong sense for Position 7.

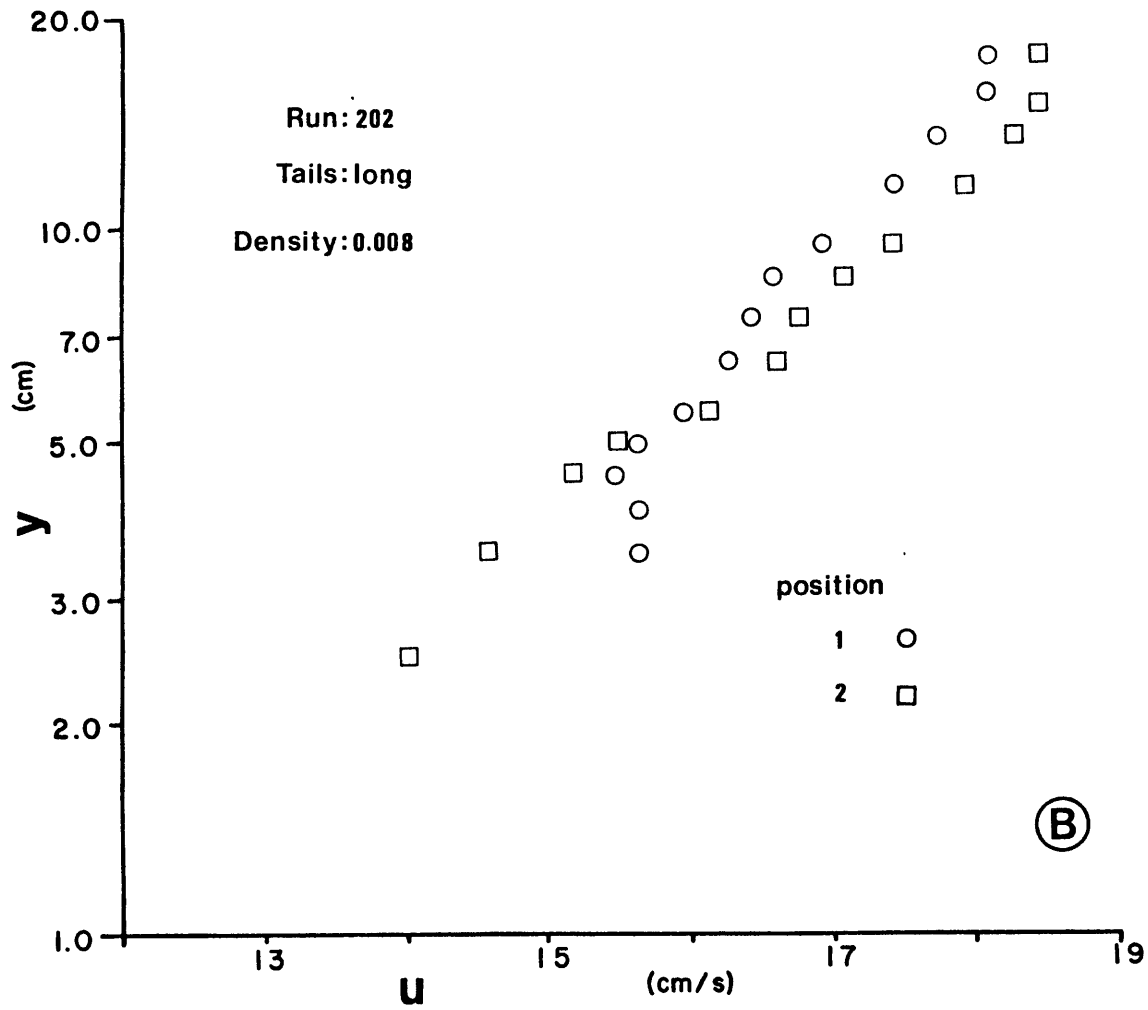
3.42. Velocity profiles. Mean-velocity profiles measured in each of the four runs are shown in figure 3.17; the two profiles shown for each run were measured at the two streamwise positions shown in figure 3.10. The profiles show good convergence above  $y \approx 5$  cm, that is, about one roughness height above the tops of the roughness elements.

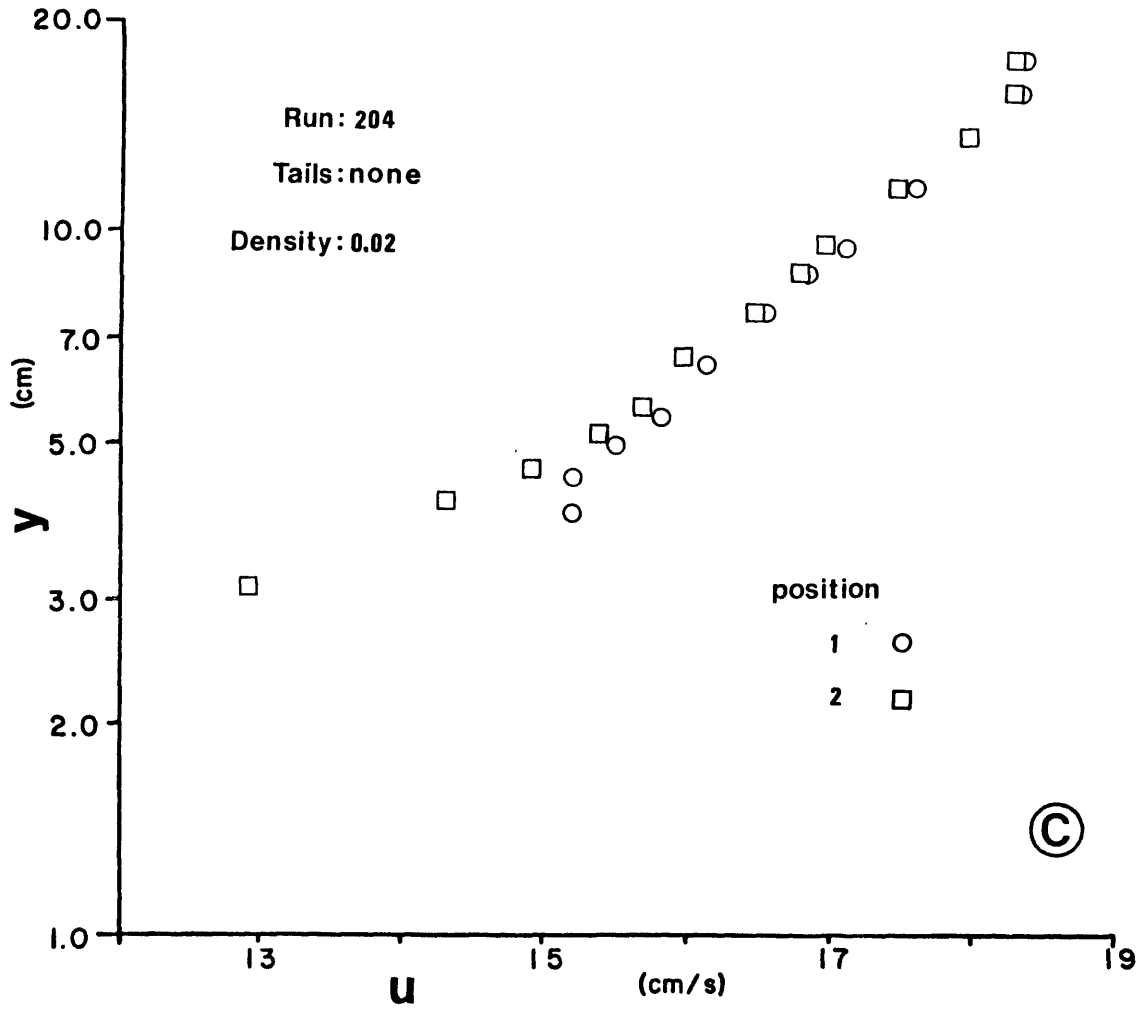
Before the profiles can be used to estimate the empirical constants in the law of the wall (1.6), the zero-plane displacement must be determined and the region of the profiles to be included in the least-squares fit to (1.6) must be defined. Based on the results of Counihan (1971), the displacement of the origin for both arrays is less than 1 mm; this is smaller than the scatter in Counihan's data and too small to be resolved accurately from the present data by maximizing  $r^2$ , so the origin was left at the bed (that is, the flat area between roughness elements). The extent of the profile to be fitted to (1.6) was determined as follows. The lower limit was fixed at  $y = 5.5$  cm to ensure that the profiles were spatially invariant. The upper limit was determined by taking the lowermost five points in the integrated region, determining the correlation coefficient  $r^2$ , and then adding points until it began to decline. An optimal upper limit of 13.5 cm was chosen on the basis of all the profiles, and then all the profiles were analyzed the same way. The mean value of von Karman's coefficient  $\kappa$  determined by combining the calculated least-squares fits to the eight measured profiles with the measured total bottom

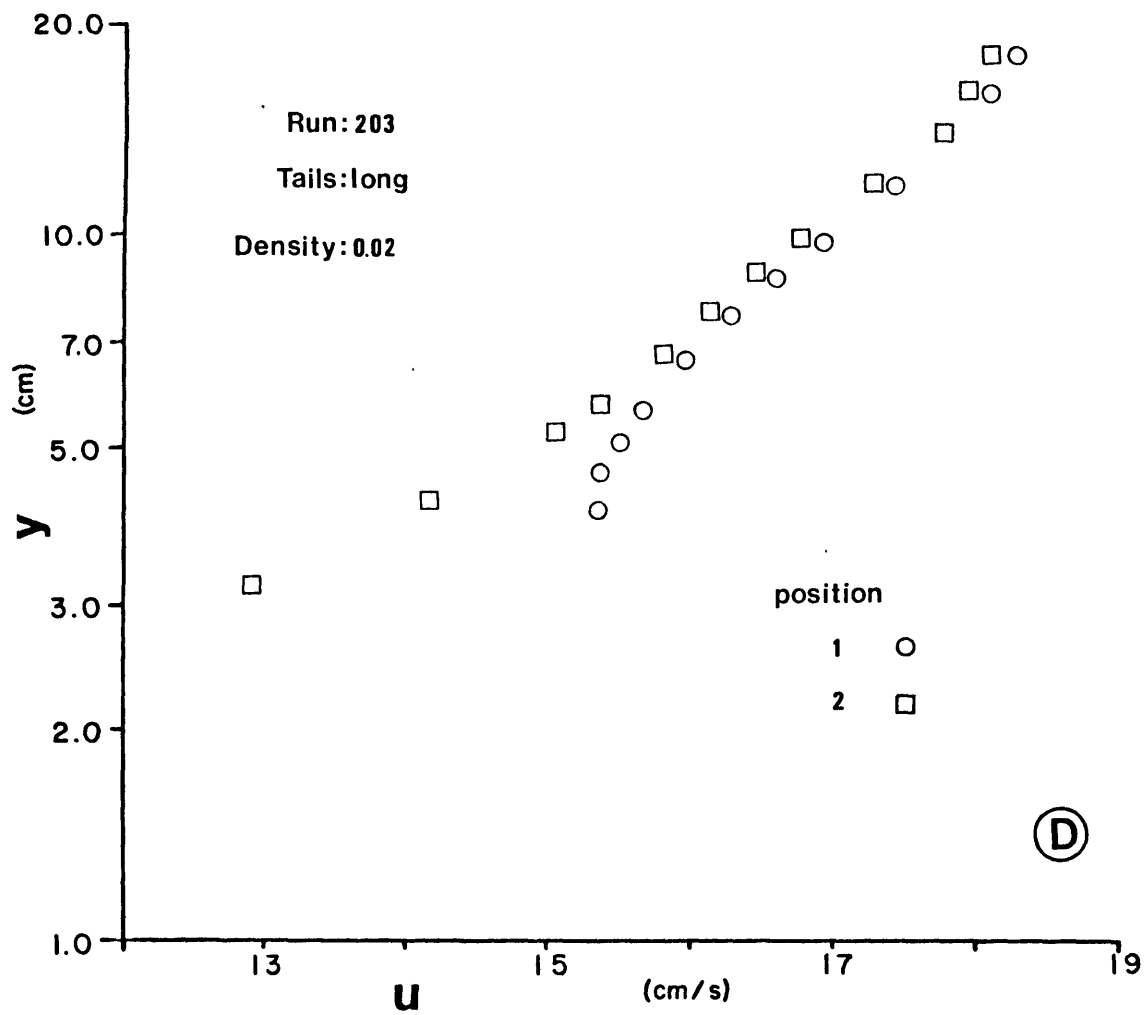
Figure 3.17. Mean-velocity profiles measured in the four full-field runs, conditions for which are given in Table 3.3. The locations of the two streamwise measuring stations are given in figure 3.10.











stress is 0.415, and the standard error of the mean is 0.017. The worst correlation coefficient,  $r^2 = 0.97$ , occurs in Run 199. These semilogarithmic correlation coefficients and the agreement between the calculated value of  $\kappa$  and the standard one of 0.4 are good enough to allow the data to be compared with some of the results reported by Wooding et al. (1973).

Figure 3.18 shows the data from the semilogarithmic region as defined above, nondimensionalized according to the scheme proposed by Wooding et al. For simplicity the velocities shown are the averages of the two measured values for each run. It is clear that this nondimensionalization does not collapse the data, and that the runs with and without the long tails fall into two groups. For comparison some velocity data measured over hemispheres similar to those used here are shown in figure 3.18; they have been taken from Figure 3a of Wooding et al. (1973) but are originally due to Marshall (1971). Their magnitudes are comparable to those of the data reported here, but they show a much smaller value for  $\kappa$ .

The segregation of the data based on tail size evident in figure 3.18 suggests that the function  $\phi$  used by Wooding et al. may not be appropriate for the present class of roughness elements. In figure 3.19, the same data are shown with the height  $y$  nondimensionalized by  $h\lambda$  only, and they are more closely grouped. The line shown has a correlation

Figure 3.18. Mean-velocity profiles for the four full-field runs nondimensionalized according to the scheme of Wooding et al. (1973).

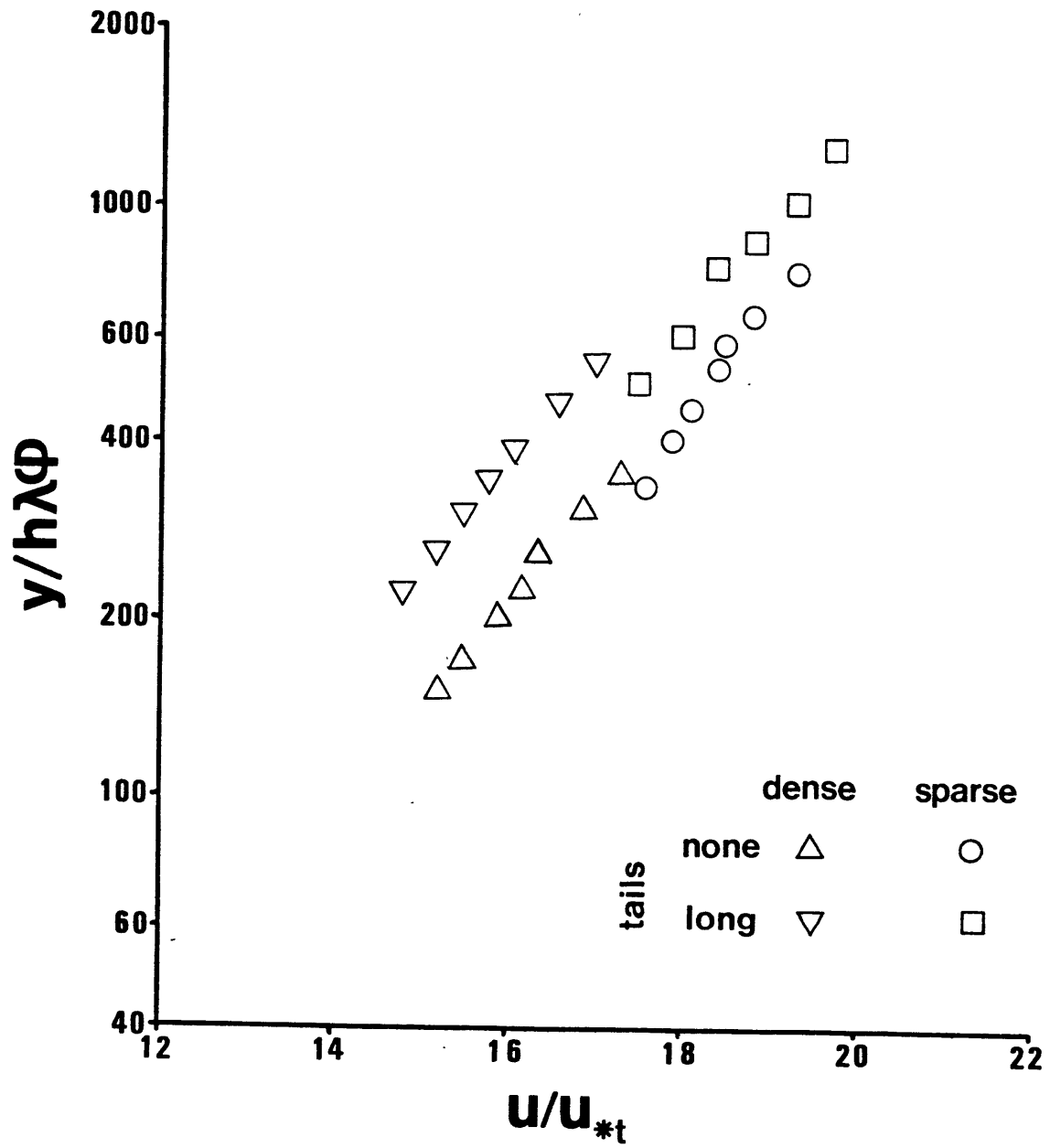
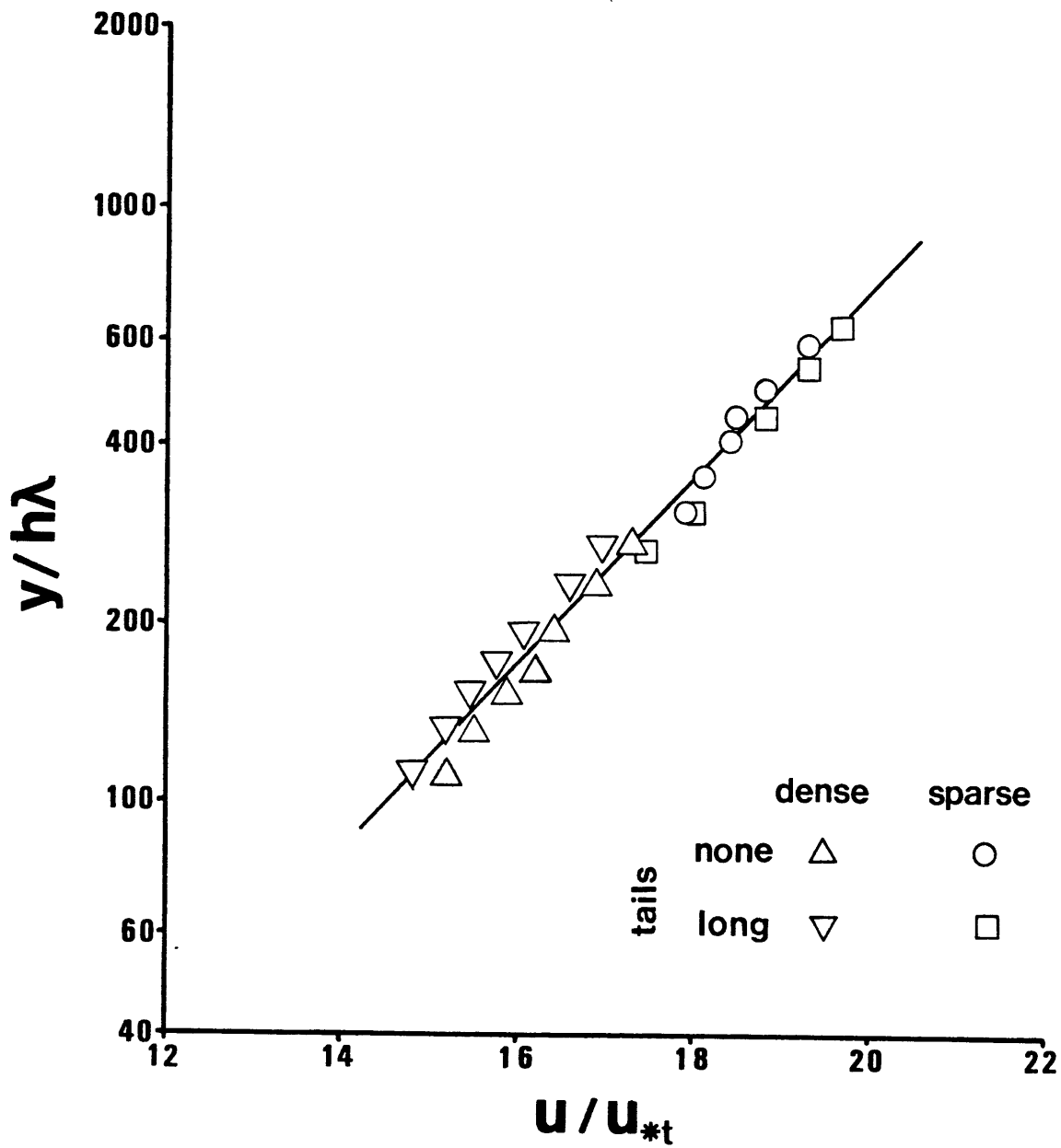


Figure 3.19. Mean-velocity profiles for the four full-field runs, nondimensionalized as in figure 3.18 but excluding the factor  $\phi$  introduced by Wooding et al. (1973) to account for the effect of the streamwise extent of roughness elements on the roughness length  $z_{ot}$ .





coefficient  $r^2$  of 0.98 and yields the following relation for the roughness length  $z_{ot}$ :

$$z_{ot} = 0.53(h\lambda) \quad 3.5$$

A relation identical to this one with a coefficient of 0.5 has been proposed by Lettau (1969, Equation 1), and a similar relation has been successfully applied to predicting the roughness of wave ripples by Grant and Madsen (1982).

### 3.5. Discussion.

3.5.1. Obstacle-trapped bedforms. Before attempting to apply the ideas developed in section 3.1 regarding the role of the skin-friction divergence in governing patterns of erosion and deposition, it is necessary to determine under what conditions sediment could be expected to respond to the measured spatial variations. One may immediately exclude suspended load, for the observations apply at the bed and cannot be used to infer the interior stresses responsible for suspending sediment (e.g. McTigue, 1981). The behavior of sediment moving as bed load may be determined by comparing its response distance under a change in shear stress with the spatial scale of the variability. Grant and Madsen (1982) derive an expression for the response time of a particle that may be used in this connection. For coarse sand ( $d = 0.1$  cm),  $t_{90}$ , the time required for the particle to attain 90% of its final velocity under a sudden change in fluid velocity near the bed, is  $t_{90} \approx 3.5\sqrt{d/g} = 0.035$  s. An upper limit for the particle velocity is found to be  $\sim 9u_{*s}$ . Taking a fairly high value for  $u_{*s}$ , 1.5 cm/s, the response distance is about 0.5 cm. Even for the unfavorable conditions assumed, then, such particles should respond to the spatial variability measured downstream of obstacles in this study.

If the above condition is satisfied the horizontal-divergence fields around isolated elements shown in figure 3.16 may be used to predict patterns of erosion and deposition, except near reattachment, where there are very

large temporal fluctuations in the skin-friction field (figure 3.15). The directions of these cannot be resolved by single-element sensors such as the ones used here; one would need probes with at least two elements for this (Kreplin and Eckelmann, 1978). As mentioned in section 3.2, plaster-of-paris flow visualization allows determination only of time-averaged direction, although the presence of strong directional variability can be inferred from flaring of the pits as opposed to creation of a distinct flute. Under such circumstances the time-averaged transport of sediment cannot reliably be inferred from the divergence of time-averaged skin friction. The fluctuations in the separated region upstream of reattachment are large enough that the direction cannot be measured; the computed divergence there is meaningless.

This point is stressed because examination of figure 3.16 shows clearly that the only place where sediment can accumulate directly behind a hemispherical obstacle is near or upstream of reattachment; everywhere else the field is divergent. Furthermore, the short-tail results show that the relative strength of the convergent region near reattachment is reduced by the presence of the tail; that is, to the extent that this region actually traps sediment that could extend the tail, tail growth is self-inhibiting. With the long tail, the convergent region is completely eliminated.

The above applies only to conditions of local bed-load erosion and deposition. The skin-friction measurements

reported here can also be used to predict the results of deflation (general erosion) of the bed without concomitant deposition, a condition that requires that the bed be cohesive. The pattern of topography that results reflects the local rate of erosion only, so the controlling factor is the skin-friction magnitude rather than the divergence. The large values of the rms magnitude relative to the mean magnitude near reattachment suggest that the former also plays an important role in determining the erosion rate, but for the reasons given in section 2.53 this cannot be evaluated precisely at present. Based on figure 3.14, lowering of the bed would be most rapid along the sides of the obstacle and directly behind it at reattachment. Going downstream along the centerline the skin friction remains large, so relative lowering of the bed would be expected throughout this region. On the other hand, the two areas of relatively small skin friction adjacent to the centerline would be expected to appear as low mounds upon general deflation of the bed.

The skin-friction field behind a hemisphere, then, is not consistent with deposition of a sedimentary tail more than about two element-heights long (the length of the separated region) under the flow conditions examined here; neither does the presence of either a long or a short tail change the field so as to cause its further extension. This applies both to conditions of bed-load erosion and deposition and of general erosion of a cohesive surface. Nonetheless,

sedimentary tails several obstacle heights long are known in both cohesive (Allen, 1965; Heezen and Hollister, 1971 ch.9) and cohesionless sediments (Karcz, 1968; Werner et al., 1980). How are they formed?

The following proposal is advanced as a hypothesis for tail formation on which further experiments might be based.

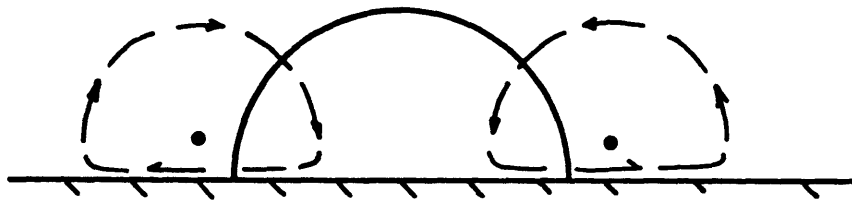
Fundamentally, the problem is that downstream of reattachment, the vortex system set up by the obstacle draws high-momentum fluid down along the centerline in the wake, increasing the skin friction there. Deposition along the centerline would be possible if the secondary flow moved up instead of down in this region.

Hawthorne and Martin (1955) carried out an extensive theoretical study of the vortex system behind a hemisphere in shear flow. They found a theoretical vorticity field well downstream of the obstacle that is qualitatively consistent with the vortex structure sketched in figure 3.1. They also investigated the effect of density stratification on the vorticity. Stable stratification induces vorticity in the same sense as the shear does, so it enhances the secondary flow. Unstable stratification has the opposite effect, causing the wake flow to break up into regions controlled either by shear (near the bed) or by stratification (around the upper part of the obstacle). Stratification in either sense also has the important effect of moving the axes of maximum vorticity up and away from the centerline. Moving the centers of the paired vortices apart might be expected to

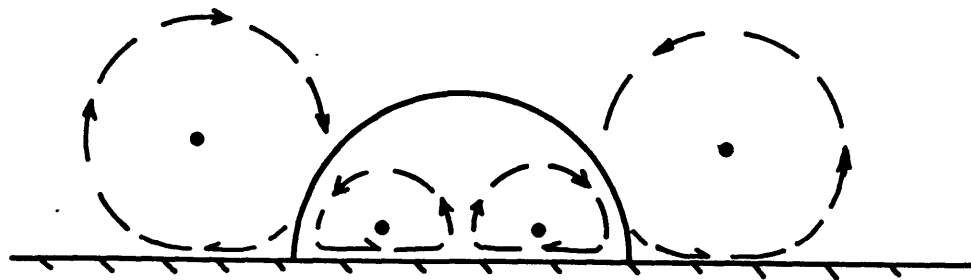
reduce the downward transport of high-momentum fluid at the centerline, thus making conditions there more favorable for deposition. More importantly, as Hawthorne and Martin point out, displacement of the vortex system can lead to formation of counter-rotating tertiary vortex pairs within the main (secondary) system. A configuration of tertiary vortices that would result in depositional conditions at the centerline is shown in figure 3.20.

In natural environments, salt, heat, and suspended sediment are all possible causes of flow stratification. The last seems a likely candidate, since bed-form development is naturally associated with sediment transport. Although recent calculations by Adams and Weatherly (1981) suggest that under natural conditions suspended sediment can induce strong stratification in the lower part of the boundary layer, in the region within one roughness height of the bed that would critically affect the vortex system, sediment transport involves rolling and saltation modes whose effects on the flow cannot be described accurately by existing stratification models. Nonetheless, a qualitative analogy may be drawn between the stratification effects evident in the experiments of Hawthorne and Martin (1955) and effects of near-bed sediment transport on the flow. Further experimental work on OTBs should focus on the effects of sediment in transport near the bed on the vortex structure behind obstacles.

Figure 3.20. Sketches of the vortex system behind an isolated hemisphere (A) with no stratification and (B) with stable stratification. The arrangement shown in (B) is speculative. The figure shows a section normal to flow, looking upstream, taken several element heights downstream of the trailing edge of the hemisphere.



**A - Without stratification**



**B - With stable stratification (speculative)**



3.52. Skin-friction patterns in relation to overall flow resistance. The general conclusion of section 3.3 is that addition of tapered forms representative of sedimentary tails to the lee of hemispherical obstacles has little effect on the pattern of skin friction downstream, except in the immediate vicinity of the tail. One would anticipate, then, that adding such tails to an array of these obstacles would not affect their overall resistance to flow either. That this is indeed the case is shown by comparison of figures 3.18 and 3.19, in which the overall scatter in the velocity profiles measured in the integrated logarithmic layer is considerably reduced by eliminating from the nondimensionalization the factor  $\phi$  introduced by Wooding et al. (1973) to account for the streamwise aspect ratio of macroroughness elements. The absence of a strong effect on either the skin-friction field or the overall flow resistance suggests that tapered sedimentary tails are passive features that do not interfere with the wake structure set up by the obstacle. This is consistent with the above discussion of tail formation. Conditions for the accumulation of sediment beyond the separated region must be set up by changes in the flow field imposed from outside; such an accumulation does not itself induce changes that allow it to grow.

It was hoped that the skin-friction fields for the four  $h, B$ -rough arrays examined would be substantially free from interference, so that the complete skin-friction field could be reconstructed by combining the isolated-element results

with the seven skin-friction measurements made in the arrays, but this did not prove to be the case. Although the skin friction cannot be accurately reconstructed, the drag-partition theory of Wooding et al. (1973), based largely on data obtained by Marshall (1971), may be evaluated for rough comparison with the spot measurements obtained here. The heart of the Wooding et al. scheme is the semi-empirical relation

$$(w_r/\rho A_p)^{1/2}/u_*t = a_5 \ln(1/\lambda\phi) + a_6 \quad 3.5$$

where  $w_r$  is the mean drag per roughness element and  $a_5$  and  $a_6$  are empirical constants found by Wooding et al. to be -0.179 and 1.63 respectively. The spatially averaged skin friction  $\langle u_*s^2 \rangle$  is then obtained from the definition

$$w_r/A_p = \rho u_*t^2 - \rho u_*s^2 (A_s/A_p) \quad 3.6$$

in which  $A_s$  is the fraction of  $A_p$  not covered by roughness elements; for hemispheres  $A_s/A_p = 1-2\lambda$ . Application of this method to the present data gives values of 0.40 dynes/cm<sup>2</sup> and 0.27 dynes/cm<sup>2</sup> for the sparse (Configuration 1) and dense (Configuration 2) arrays respectively, without tails. The mean measured values for all sensor points in the skin-friction array are 0.58 dynes/cm<sup>2</sup> and 0.56 dynes/cm<sup>2</sup> for the sparse and dense arrays (without tails) respectively. Although these values are not extremely accurate estimates of the spatially averaged skin-friction because the sampling grid is sparse and because the measurements are of

magnitudes and not streamwise components, it is nonetheless clear that the Wooding et al. estimates are much too low. For comparison, a simple estimate of the skin friction may be made using a smooth-flow law such as this semi-empirical one due to Blasius (Daily and Harleman, 1966, p. 271):

$$f = 0.316 R_h^{-1/4} \quad 3.8$$

in which  $f$  is the Darcy-Weisbach friction factor, equal to  $8u_*^2/\bar{u}^2$ ,  $\bar{u}$  is the vertically averaged velocity, and  $R_h \equiv 4r_h\bar{u}/\nu$  where  $r_h$  is the hydraulic radius of the channel. Equation (3.8) is only valid if  $R_h < 10^5$ . Application of (3.8) to the present case gives a mean skin friction of 0.64 dynes/cm<sup>2</sup> for the sparse array and 0.62 dynes/cm<sup>2</sup> for the dense one. These figures are comparable with the average measured values, and the absence of a sharp change in averaged skin friction with the change in areal density is also consistent with the observations. The data of Marshall (1971), on which (3.6) is based, were obtained by measurement of the force on a test roughness element using a drag balance. Future similar drag-partition studies should include skin-friction measurements as well, so that the internal consistency of the data can be checked. The Wooding et al. (1973) relation (3.6) should be used with caution until such data are available.

3.53. Application of the full-field results to natural conditions. There are a great many problems associated with comparing boundary layers in natural and laboratory settings. The overall Reynolds numbers characterizing marine and atmospheric (geophysical) boundary layers are generally much larger than can be attained in the laboratory. Furthermore, boundary layers in the field are often highly variable spatially and temporally, and may reflect the presence of a wide range of complicating influences, some of which will be enumerated below. It makes sense to approach such problems piecewise at first, remembering that the pieces may need to be modified when they are fitted together. The subproblem to be considered in this section is that of estimating the roughness length  $z_{ot}$  when the roughness field is spatially variable, as is usually the case in the field.

How does this problem fit into the larger one of understanding boundary layers in natural settings? The importance of estimating the roughness length stems from its connection with the general problem of estimating  $u_*t$  from mean-velocity measurements in the boundary layer, with the ultimate goal of allowing calculation of sediment-transport rates in the field in as straightforward a manner as possible. In section 1.1 it was mentioned that one of the great virtues of the velocity-profile laws (1.3) and (1.6) is that they allow determination of the boundary shear stress from velocity measurements in the logarithmic layer; over macrorough beds an analogous statement is that velocity measurements in the ILL

can be used to determine  $\tau_{ot}$ . The reader should be cautioned that the determination of the total boundary shear stress in most field settings involves a number of complications that cannot be discussed fully here. Some that relate specifically to  $z_{ot}$  will be given below; for general discussions from a variety of points of view of boundary layers and sediment transport in marine settings reference may be made to Smith (1977), McCave (1976), Bowden (1978), Hollister et al. (1980), Gust (1982b), and Grant and Glenn (in press).

The boundary-layer variable that ultimately governs sediment transport near the bed is not the total bottom stress but rather the skin friction. The level of detail to which the latter must be known (anywhere from the spatial average to the complete vector field along with one or more higher moments) depends on how accurately and at what spatial and temporal scales the sediment transport is to be calculated. These matters cannot be given justice here; what is important for present purposes is that the only access we have to the skin friction is through the total bottom stress unless measurements are made in or below the surface layer (Gust, 1982a,b), which is too difficult a procedure to be used routinely in the field.

It is possible in principle to determine  $u_*t$  by differentiating (1.6), thus bypassing the roughness length. At present, however, the empirical coefficients and limits of applicability for (1.6) in geophysical boundary layers cannot be considered to be fully established (Businger et al., 1971;

Hollister et al., 1980; Gust, 1982b; Nowell et al., 1982). As a result, considerable effort is being directed towards obtaining independent estimates of the variables  $u_*t$  and  $z_{ot}$  to constrain the empirical coefficients in models for natural boundary layers, of which (1.6) is a simple example. Comparing the results of well-controlled laboratory studies like this one and the ones compiled by Wooding et al. (1973) with boundary-layer data from the field is thus an important part of making models like (1.6) reliable tools for use in natural settings.

The apparent roughness length  $z_{otA}$  of natural boundary layers is affected by a variety of flow phenomena: stratification (Weatherly and Martin, 1978; Adams and Weatherly, 1981; Smith and McLean, 1977), bed-load sediment transport (Smith and McLean, 1977; Grant and Madsen, 1982; Gust and Southard, in press), and acceleration, either temporal (Grant and Madsen, 1979, 1982; Grant, 1982) or spatial (Zilker et al., 1977; Zilker and Hanratty, 1979; Yaglom, 1979). All of these are common in field settings. Evaluation of their importance requires that one be able to estimate the roughness length  $z_{ot}$  due only to physical bottom roughness; this "topographic roughness length" is that against which measured or calculated apparent values  $z_{otA}$  are compared. But the roughness distribution upstream of a measuring station in the field is generally not uniform, unlike the arrays used here and in other laboratory studies, in which a specific unit cell is repeated upstream. How can

the results of laboratory studies such as this one be used to estimate  $z_{ot}$  in field settings where the bottom roughness is spatially nonuniform?

The following analysis was made as part of the HEBBLE (High Energy Benthic Boundary Layer Experiment) sea-bed landing project (McCave et al., 1978; Hollister et al., 1980; Nowell et al., 1982). The project involves fluid-dynamical, biological and sediment-transport measurements at a range of scales, from those of the ILL to those of the interior flow, over a crag-and-tail field on the Nova Scotian continental rise. For present purposes, all that need be considered is a vertical stack of current meters a few meters high that is used to measure a time series of velocity profiles over a bed randomly strewn with small-scale (centimeters to decimeters) roughness elements but free of large-scale topography. The problem of roughness-length variability then boils down to two questions: (1) What areas of the sea floor affect each section of the vertical profile? (2) What spatial roughness scales are important in each such area?

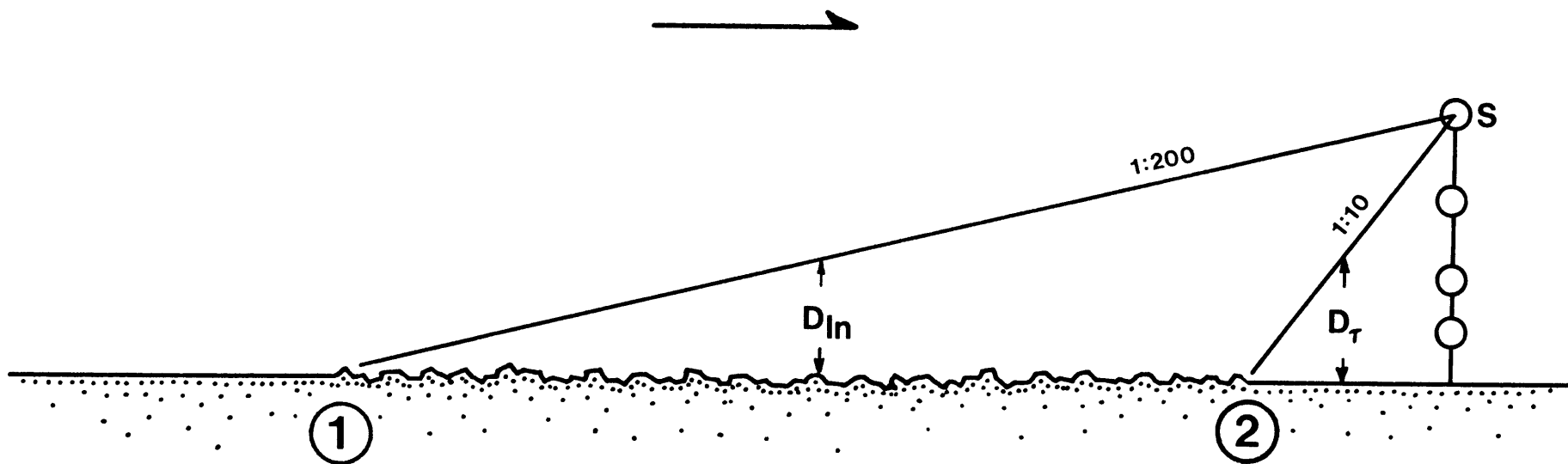
Before discussing these questions, it is helpful to extend the meaning of the roughness length somewhat. We may define the generalized roughness length as  $z_{ot}(x, z, L_a)$  where  $x$  and  $z$  are horizontal coordinates,  $L_a$  is a length and  $z_{ot}$  is the roughness length that would be obtained from measurements in the integrated logarithmic layer developed over a bed made by repeating infinitely far upstream the square patch of area  $L_a^2$

centered at  $(x, z)$ . Formally we may define the absolute roughness length at  $(x, z)$  as  $(z_{ot})_o = \lim(z_{ot}(x, z, L_a))$  as  $L_a$  approaches some value small compared with any averaging scale of interest (see below). For practical purposes, the value of  $z_{ot}$  at  $(x, z)$  means approximately  $z_{ot}(x, z, 50\text{cm})$  since 50 cm is about the length scale at which laboratory measurements of  $z_{ot}$  would be made.

Areas of influence. Intuition suggests that the area of the bed to which boundary-layer flow is sensitive must increase with height above the bed. This can be made more precise through the application of internal boundary layer (IBL) theory (section 2.11). The IBL notion gives us a connection between streamwise distance and height at a measuring station, because there are subregions within an IBL that grow at different rates as shown in figure 3.21 (based on the results of Rao et al., 1974). Two of these are of interest in estimating the area that influences each vertical position. The first is defined by  $D_{1n}$ , the height below which the Reynolds shear stress is within 10% of the local total bottom stress and the velocity profile displays a semilogarithmic form in accord with (1.6); this is the region that is completely in equilibrium with the new (downstream)  $z_{ot}$  after a change in roughness (figure 2.1). According to the numerical model of Rao et al. (1974), if  $x$  is the distance from the change in roughness (the fetch), then  $D_{1n}/x > 1/200$ . The second subregion we need is defined by  $D_\tau$ , the height above which the Reynolds shear stress is within 1% of its



Figure 3.21. The two-dimensional region of influence for a measuring station  $S$  in a boundary-layer profile. If a change in  $z_{0t}$  occurs upstream of 1, the boundary layer will have completely adjusted to the new roughness length at  $S$ . If a change in roughness occurs downstream of 2, the new boundary layer cannot grow quickly enough to affect  $S$ .



upstream (undisturbed) value. Since the Reynolds stress is more sensitive to disturbance than is the mean velocity,  $D_\tau$  is the height above which the boundary layer is completely unaffected by a change in  $z_{ot}$ . Again referring to Rao et al. (1974),  $D_\tau/x \approx 1/10$ . Now it is easy to see how the area of influence shown in figure 3.21 was arrived at: if a change in  $z_{ot}$  occurs upstream of the upstream limit, the boundary layer will have completely adjusted to the new  $z_{ot}$  at Station S; if a change occurs downstream of the downstream limit, the disturbance caused by it cannot grow quickly enough to affect Station S. Table 3.5 gives limits of the area of influence for each height in a vertical current-meter array based on these considerations.

A series of areas of influence are shown as sectors of a circle in figure 3.22. The angular dimension of the sector cannot be derived from the preceding theory, all of which is strictly two-dimensional. Rather, it was arrived at as follows. Suppose there were a patch of sea bed with a different value of  $z_{ot}$ , but off the axis defined by the measuring position and the mean current direction. How would the resulting flow disturbance spread itself laterally? In the small-disturbance limit, this is equivalent to determining the lateral diffusion of a passive contaminant introduced at the point of the disturbance. For distances larger than a few boundary-layer heights downstream of the disturbance, the

diffusion can be modelled as (Tennekes, 1977)

$$L_z^2 \cong t \epsilon_z \quad 3.9$$

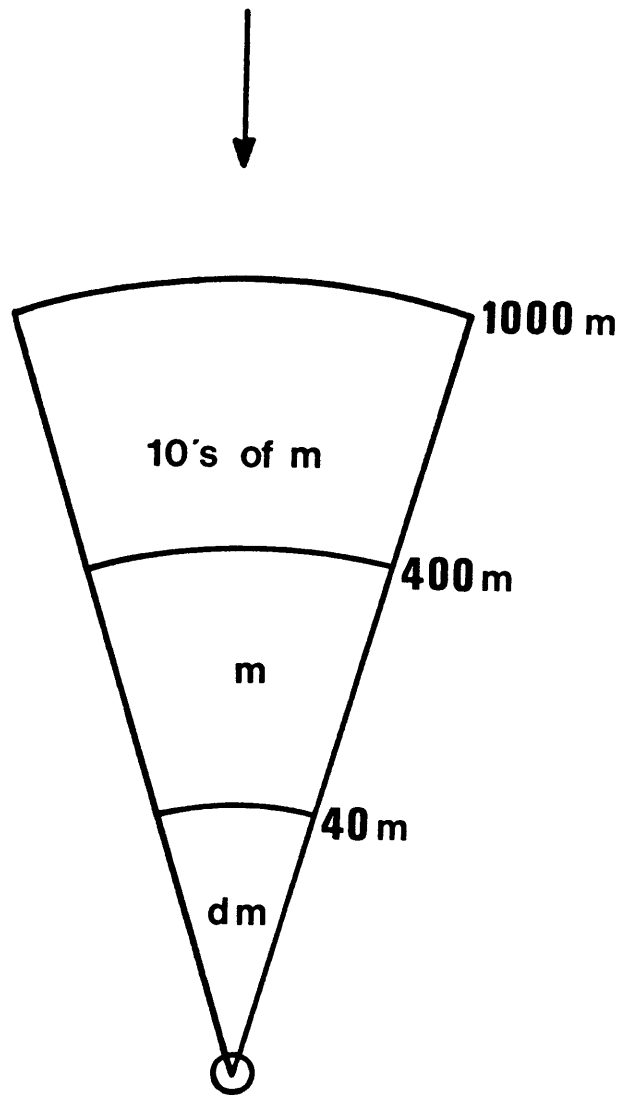
where  $L_z$  is the width of the disturbance,  $t$  is time and  $\epsilon_z$  is the lateral turbulent diffusivity. It is more straightforward to estimate the maximum growth rate for  $L_z$  than to estimate  $\epsilon_z$ . In the absence of a mean lateral strain rate, it is reasonable to assume  $\epsilon_z < \epsilon_y$ , the vertical eddy diffusivity, which can be estimated as  $\kappa u_* t$ . The disturbed region grows vertically as an internal boundary layer, so  $y$  is at most  $x/10$ . Replacing  $t$  by  $x/\bar{u}$ , where  $\bar{u}$  is some representative mean velocity in the boundary layer, we obtain

$$L_z^2 < \frac{\kappa u_* t x^2}{10 \bar{u}} \quad 3.10$$

As an upper limit, we may take  $u_* t / \bar{u} \approx 0.1$  to give  $L_z < 0.1x$ ; that is, the lateral spreading rate is at most equal to the greatest expected vertical (IBL) growth rate. On this basis, lateral variation of  $z_{ot}$  outside the sector in figure 3.22 should not disturb the boundary layer at the observation site.

Averaging areas. As discussed in section 1.1 and at the beginning of this section,  $z_{ot}$  is by its nature a spatially averaged quantity; its value at a given location depends in general on the area around that location over which it is averaged (although it could be constant when averaged over some range of areas). How do the dimensions of such averaging areas vary with height in a velocity profile? Intuitively, we might make an argument similar to one advanced in the

Figure 3.22. Roughness-averaging scales for a series of regions upstream of a hypothetical boundary-layer measuring station (circle), based on the data in Table 3.5.



preceding section: as the height increases, so does the area over which  $z_{ot}$  is averaged by the flow, because the turbulence is larger in scale and interacts with more of the bed. This can be made more precise using the following line of reasoning, adapted from Townsend (1965a).

To begin, let us rephrase the question slightly. Suppose the bed has roughness which is patchy on scales less than or equal to some length  $L_r$ ; that is, the value of  $z_{ot}$  is independent of averaging area when averaged over areas larger than  $L_r^2$ . Above what height (call it  $y_i$ ) does the boundary layer behave as if the roughness were spatially uniform; that is, what is the lower limit for the ILL? We know that for  $y > y_i$ , the rate of production or dissipation of turbulence is about  $u_*^3 / \kappa y$ , while the turbulent kinetic energy is about  $3u_*^2$ . Hence if the turbulence encounters a region where the strain rate changes, it cannot respond in a time less than about  $t_c = 3\kappa y / u_*^3$ . If we assume that the turbulence is advected at about the mean velocity, given by (1.6), we can convert  $t_c$  to a response distance  $x_c$  given by

$$x_c = ut_c = 3y \ln(y/z_{ot}) \quad 3.11$$

Evidently, the turbulence will be insensitive to changes in roughness on a scale  $L_r$  if  $x_c \gg L_r$ . Since the turbulence is known to be more sensitive to disturbance than the mean field (Rao et al., 1974), this should be a sufficient condition for both the mean field and the turbulence. If we choose  $x_c = 10L_r$

as a fairly conservative limit,  $y_i$  is defined implicitly by

$$10L_r = 3y_i \ln(y_i/z_{ot}) \quad 3.12$$

Table 3.5 shows values of  $L_r$  defined by (3.12) for various  $y_i$  and also values based on a weaker limit  $x_c=2L_r$  for comparison. The values of  $L_r$  are identified as averaging scales. They are the scales of roughness variation at and below which the flow at that height cannot respond to the variation. Figure 3.22 shows an approximate synthesis of the area of influence and averaging-area data given in Table 3.5. For example, the boundary layer will be sensitive to variability in  $z_{ot}$  when averaged over areas of the order of square decimeters in the region up to 40 m distant from a landing site, but will be sensitive only to the residual variability in  $z_{ot}$  when it is averaged over areas of the order of several square meters in the region from 40 m to 400 m from the site. These are fairly conservative estimates, and could be relaxed if one were willing to be more adventurous. It is worth emphasizing that the length scales in figure 3.22 and Table 3.5 are averaging scales, and are in no way related to roughness wavenumber. It is implicit in the foregoing that the dimensions of the roughness elements are small compared to any averaging scale of interest; otherwise the averaging itself loses meaning.

So far it has been assumed implicitly that the roughness length  $z_{ot}(x,y,L_a)$  can be obtained by averaging a set of smaller-scale estimates within  $L_a^2$ , which is equivalent to



assuming that a random array of roughness elements has the same drag behavior as a regular one of the same areal density. The experimental program of Marshall (1971) included an extensive comparison of random and regular arrays; he concluded that there is little dynamical difference between them. Random arrays show slightly smaller (15% or less) total bottom stresses than do regular ones under the same flow conditions, a difference that Marshall attributes to interference between closely spaced elements. Unfortunately, there is considerable scatter in the data. It seems reasonable to estimate  $z_{ot}$  by simple averaging until a better method has been demonstrated.

Height <u>Above Bottom</u>	Area of Influence: <u>Between</u>	Roughness <u>Averaging Scale</u>	
10 cm	1 - 20 m	14 cm	69 cm
20	2 - 40	32	159
50	5 - 100	93	470
100	10 - 200	210	1,040
200	20 - 400	460	2,280
500	50 - 1,000	1,280	6,400
1,000 cm	100 - 2,000 m	2,800 cm	13,800 cm
		$x_c=10L_r$	$x_c=2L_r$

Table 3.5. The limits of the upstream region that influences each height in a hypothetical current-meter array, and the roughness averaging scale  $L_r$  in each region, for a typical  $z_{ot}$  of 0.1 cm.

### 3.6. Conclusions.

Based on measurements of the skin-friction field downstream of an isolated hemisphere by itself and with model sedimentary tails one and four obstacle heights long:

1. The skin-friction field behind a hemisphere is not consistent with formation of sedimentary tails more than about two obstacle heights long (the length of the separated region). This is true under conditions of local erosion and deposition from bed load as well as of general deflation of the bed.

2. Adding tapered tails to a hemisphere does not produce substantial changes in either the magnitude or the horizontal divergence of the mean skin friction. The changes that are produced are such as to inhibit growth of the tail.

Based on the isolated-element results and on measurements of skin friction, ILL velocity profiles, and total bottom stress for  $h, B$ -rough arrays of hemispheres with and without model tails, at two areal densities (0.008 and 0.02):

3. The skin-friction field around roughness elements in an array of areal density 0.02 departs significantly from that of a single isolated element. The departure cannot be accounted for by introducing in a simple way effects of the next element upstream. At an areal density of 0.008 there are differences between the skin-friction fields in the array and around an isolated obstacle, but they may not be significant.

4. The roughness length of arrays of hemispheres is not reduced by the addition of tapered tails four roughness heights long. A significant reduction would be expected if the hemisphere-tail system obeyed a drag law proposed by Wooding et al. (1973) for h,B-rough beds.

5. A drag-partition formula proposed by Wooding et al. (1973) gives estimates of spatially averaged skin friction that are significantly lower than measured values.

4. References.

- Adams, C.E. Jr. and Weatherly, G.L. 1981. Some effects of suspended sediment stratification on an oceanic bottom boundary layer. J. geophys. Res. 86: 4161-4172
- Allen, J.R.L. 1965. Scour marks in snow. J. sedim. Petrol. 35: 331-338
- Allen, J.R.L. 1966. Note on the use of plaster of paris in flow visualization and some geological applications. J. fluid Mech. 25: 331-335
- Allen, J.R.L. 1969. On the geometry of current ripples in relation to stability of fluid flow. Geogr. Ann. 51A: 61-96
- Allen, J.R.L. 1977. The plan shape of current ripples in relation to flow conditions. Sedimentology 24: 53-61
- Arya, S.P.S. 1975. A drag partition theory for determining the large-scale roughness parameter and wind stress on Arctic pack ice. J. geophys. Res. 80: 3447-3454
- Banks, N.L. and Collinson, J.D. 1975. The size and shape of small-scale current ripples: an experimental study using medium sand. Sedimentology 22: 583-599
- Bayazit, M. 1976. Free surface flow in a channel of large relative roughness. J. hydraulic Res. 14: 115-126
- Bellhouse, B.J. and Schultz, D.L. 1966. Determination of mean and dynamic skin friction, separation and transition in low-speed flow with a thin-film heated element. J. fluid Mech. 24: 379-400
- Bendat, J.S. and Piersol, A.G. 1966. Measurement and Analysis of Random Data. New York: John Wiley and Sons, Inc., 381 p.
- Blackwelder, R.F. and Eckelmann, H. 1977. The spanwise structure of the bursting phenomenon. Göttingen: Max-Planck-Institut für Stromungsforschung, Bericht 121, 15 p.
- Blinco, P.H. and Simons, D.B. 1974. Characteristics of the turbulent boundary shear stress. J. engr. Mech. Div. amer. Soc. civ. Engrs. 100(EM2): 203-220
- Boothroyd, J.C. and Hubbard, D.K. 1975. Genesis of bedforms in mesotidal estuaries. In Cronin, L.E. (ed.) Estuarine Research, vol. 2. New York: Academic Press, Inc., p. 217-234.

- Bowden, K.E. 1978. Physical problems of the benthic boundary layer. Geophys. Surv. 3: 255-296
- Bradley, E.F. 1968. A micrometeorological study of velocity profiles and surface drag in the region modified by a change in surface roughness. Quat. J. roy. meteor. Soc. 94: 361-379
- Bradshaw, P. and Wong, F.Y.F. 1972. The reattachment and relaxation of a turbulent shear layer. J. fluid Mech. 52: 113-135
- Brown, G.L. 1967. Theory and application of heated films for skin friction measurement. Proc. 1967 Heat Transfer and Fluid Mech. Inst., p. 363-381
- Brown, G.L. and Roshko, A. 1974. On density effects and large structure in turbulent mixing layers. J. fluid Mech. 64: 775-816
- Businger, J.A., Wyngaard, J.C., Izumi, Y. and Bradley, E.F. 1971. Flux-profile relationships in the atmospheric surface layer. J. atmos. Sci. 28: 181-189
- Cantwell, B.J. 1981. Organized motion in turbulent flow. Ann. Rev. fluid Mech. 13: 457-515
- Castro, I.P. 1979. Relaxing wakes behind surface-mounted obstacles in rough-wall boundary layers. J. fluid Mech. 93: 631-659
- Chandrsuda, C. and Bradshaw, P. 1981. Turbulence structure of a reattaching mixing layer. J. fluid Mech. 110: 171-194
- Chriss, T.M. and Caldwell, D.R. 1982. Evidence for the influence of form drag on bottom boundary layer flow. J. geophys. Res. 87: 4148-4154
- Comte-Bellot, G. 1976. Hot-wire anemometry. Ann. Rev. fluid Mech. 8: 209-231
- Costello, W.R. 1974. Development of bed configurations in coarse sands. Ph.D. thesis, Mass. Inst. Tech., Cambridge, Mass., Dept. of Earth and Plan. Sci. Rept. 74-1.
- Counihan, J. 1971. Wind tunnel determination of the roughness length as a function of the fetch and the roughness density of three-dimensional roughness elements. Atmos. Environ. 5: 637-642
- Daily, J.W. and Harleman, D.R.F. 1966. Fluid Dynamics. Reading, Mass.: Addison-Wesley, 433 p.

- Dalrymple, R.W., Knight, R.J. and Lambiase, J.J. 1978. Bedforms and their hydrodynamic stability relationships in a tidal environment, Bay of Fundy, Canada. Nature 275: 100-104
- Dzulynski, S. and Sanders, J.E. 1962. Current marks from firm mud bottoms. Connecticut Acad. Arts Sci. Trans. 42: 57-96
- Eaton, J.K. and Johnston, J.P. 1981. A review of research on subsonic turbulent flow reattachment. Am. Inst. Aeronaut. Astronaut. J. 19: 1093-1100
- Eckman, J.E., Nowell, A.R.M. and Jumars, P.A. 1980. Bed-load transport about biogenous structures. EOS 61: 1017
- Elliot, W.P. 1958. The growth of the atmospheric internal boundary layer. Trans. am. geophys. Union 39: 1048-1054
- Engelund, F. 1966. Hydraulic resistance of alluvial streams. J. hydraulic Div. am. Soc. civ. Engrs. 92(HY2): 315-326
- Engelund, F. and Fredsoe, J. 1982. Sediment ripples and dunes. Ann. Rev. fluid Mech. 14: 13-37
- Etheridge, D.W. and Kemp, P.H. 1978. Measurements of turbulent flow downstream of a rearward-facing step. J. fluid Mech. 86: 545-566
- Freytmuth, P. 1967. Feedback control theory for constant-temperature hot-wire anemometers. Rev. sci. Instrum. 38: 677-681
- Grant, W.D. 1982. The influence of internal waves on near bottom velocity profiles measured on the continental shelf: stress and roughness estimates. EOS 63: 987
- Grant, W.D. and Glenn, S.M. in press, 1983. Continental shelf bottom boundary layer model. vol. 1. theoretical model development, 160 p., vol. 2. model/data comparison, 63 p. Woods Hole, Mass.: Woods Hole Oceanographic Institution Tech. Rept.
- Grant, W.D. and Madsen, O.S. 1979. Combined wave and current interaction with a rough bottom. J. geophys. Res. 84: 1797-1808
- Grant, W.D. and Madsen, O.S. 1982. Moveable bed roughness in unsteady oscillatory flow. J. geophys. Res. 87: 469-481
- Gust, G. 1982a. Tools for oceanic small-scale, high-frequency flows: metal-clad hot wires. J. geophys. Res. 87: 447-455

- Gust, G. 1982b. The benthic boundary layer. In: Sundermann, J. (ed.), Oceanography. Berlin: Springer-Verlag (preprint, 67 p.)
- Gust, G. and Southard, J.B. in press, 1983. Effects of weak bedload on the universal law of the wall. J. geophys. Res.
- Hanratty, T.J., Chorn, L.G. and Hatzivramidis, D.T. 1977. Turbulent fluctuations in the viscous wall region for Newtonian and drag reducing fluids. Phys. Fluids 20: 5112-5119
- Harms, J.C. 1969. Hydraulic significance of some sand ripples. Geol. Soc. Am. Bull. 80: 363-396
- Harms, J.C., Southard, J.B. and Walker, R.G. 1982. Structures and Sequences in Clastic Rocks. Soc. econ. Paleontol. Mineral. Short Course 9, 249 p.
- Hawthorne, W.R. 1954. The secondary flow about struts and airfoils. J. aeron. Sci. 21: 588-608
- Hawthorne, W.R. and Martin, M.E. 1955. The effect of density gradient and shear on the flow over a hemisphere. Proc. roy. Soc. Lond. A232: 184-195
- Heezen, B.C. and Hollister, C.D. 1971. The Face of the Deep. New York: Oxford University Press, 650 p.
- Hinze, J.O. 1975. Turbulence. New York: McGraw-Hill, 780p.
- Hollister, C.D., Nowell, A.R.M. and Smith, J.D. 1980. The third annual report of the High Energy Benthic Boundary Layer Experiment. Woods Hole, Mass.: Woods Hole Oceanogr. Inst. Tech. Rept. WHOI-80-32, 48 p.
- Jackson, P.S. 1981. On the displacement height in the logarithmic velocity profile. J. fluid Mech. 111: 15-25
- Jackson, P.S. and Hunt, J.C.R. 1975. Turbulent flow over a low hill. Quart. J. roy. meteor. Soc. 101: 929-955
- Karcz, I. 1968. Fluvial obstacle marks from the wadis of the Negev (southern Israel). J. sedim. Petrol. 38: 1000-1012
- Kim, J., Kline, S.J. and Johnston, J.P. 1980. Investigation of a reattaching turbulent shear layer: flow over a backward-facing step. J. fluids Engrg. 102: 302-308



- King, L.V. 1914. On the convection of heat from small cylinders in a stream of fluid: determination of the convection constants of small platinum wires with applications to hot-wire anemometry. Phil. Trans. roy. Soc. Lond. A214: 373-432
- Knight, D.W. and MacDonald, J.A. 1979b. Open channel flow with varying bed roughness. J. hydraulic Div. am. Soc. civ. Engrs. 105(HY9): 1167-1183
- Knight, D.W. and MacDonald, J.A. 1979b. Hydraulic resistance of artificial strip roughness. J. hydraulic Div. am. Soc. civ. Engrs. 105(HY6): 675-690
- Kondo, J. 1971. Relationship between the roughness coefficient and other aerodynamic parameters. J. meteor. Soc. Japan 49: 121-124
- Kreplin, H.-P. and Eckelmann, H. 1978. Propagation of perturbations in the viscous sublayer and adjacent wall region. Gottingen: Max-Planck-Institut fur Stromungsforschung, Bericht 119, 35 p.
- Kreplin, H.-P. and Eckelmann, H. 1979. Behavior of the three fluctuating velocity components in the wall region of a turbulent channel flow. Phys. Fluids 22: 1233-1239
- Lettau, H. 1969. Note on aerodynamic roughness-parameter estimation on the basis of roughness-element description. J. appl. Meteor. 8: 828-832
- Liepmann, H.W. and Skinner, G.T. 1954. Shearing-stress measurements by use of a heated element. NACA Tech. Note 3268, 27 p.
- Ludwig, H. 1950. Instrument for measuring the wall shearing stress of turbulent boundary layers. NACA Tech. Memo. 1284, 22 p.
- Madsen, O.S. 1975. Lecture Notes on Mechanics of Sediment Transport in Steady Flow. Cambridge, Mass.: Mass. Inst. Tech. Dept. of Civ. Engrg.
- Marshall, J.K. 1971. Drag measurements in roughness arrays of varying density and distribution. Agric. Meteor. 8: 269-292
- McCave, I.N. (ed.) 1976. The Benthic Boundary Layer. New York: Plenum Publishing Corp., 315 p.
- McCave, I.N., Hollister, C.D. and Pyle, T. 1978. The HEBBLE report. Woods Hole, Mass.: Woods Hole Oceanogr. Inst. Tech. Rept. WHOI-78-48, 79 p.

- McCorquodale, J.A. and Giratella, M.K. 1973. Flow over natural and artificial ripples. Proc. fifteenth Congr. intl. Assoc. for hydraulic Res., Istanbul, vol. 1: 167-172
- McLean, S.R. 1981. The role of nonuniform roughness in the formation of sand ribbons. Mar. Geol. 42: 49-74
- McTigue, D.F. 1981. Mixture theory for suspended sediment transport. J. hydr. Div. am. Soc. civ. Engrs. 107: 659-673
- Meyer-Peter, E. and Muller, R. 1948. Formulas for bed-load transport. Second Meeting, intl. Assoc. for hydraulic Structures Res., Stockholm, 7-9 June 1948, Appendix 2: 39-64
- Middleton, G.V. and Southard, J.B. 1977. Mechanics of Sediment Transport. Soc. econ. Paleontol. Mineral. Short Course 3,
- Miller, M.C., McCave, I.N. and Komar, P.D. 1977. Threshold of sediment motion under unidirectional currents. Sediementology. 24: 507-527
- Millikan, C.B. 1939. A critical discussion of turbulent flow in channels and circular tubes. Proc. fifth intl. Congr. of appl. Mech., Cambridge, Mass., 1938, p. 386-392
- Morris, H.M. 1955. Flow in rough conduits. Trans. am. Soc. civ. Engrs. 120: 373-398
- Nowell, A.R.M. and Church, M. 1979. Turbulent flow in a depth-limited boundary layer. J. geophys. Res. 84: 4816-4824
- Nowell, A.R.M., Hollister, C.D. and Jumars, P.A. 1982. High Energy Boundary Layer Experiment: HEBBLE. EOS 63: 594-595
- O'Loughlin, E.M. and Annambhotla, V.S.S. 1969. Flow phenomena near rough boundaries. J. hydraulic Res. 7: 231-250
- Otnes, R.K. and Enochson, L. 1972. Digital Time Series Analysis. New York: John Wiley and Sons, 460 p.
- Peabody, F.E. 1947. Current crescents in the Triassic Moenkopi Formation. J. sedim. Petrol. 17: 73-76
- Perry, A.E. and Abell, C.J. 1975. Scaling laws for pipe-flow turbulence. J. fluid Mech. 67: 257-271
- Perry, A.E. and Morrison, G.L. 1971. Static and dynamic calibrations of constant-temperature hot-wire systems. J. fluid Mech. 47: 765-777

- Perry, A.E., Schofield, W.H. and Joubert, P.N. 1969. Rough wall turbulent boundary layers. J. fluid Mech. 37: 383-413
- Rao, K.S., Wyngaard, J.C. and Cote, O.R. 1974. The structure of the two-dimensional internal boundary layer over a sudden change of surface roughness. J. atmos. Sci. 31: 738-746
- Raudkivi, A.J. 1963. Study of sediment ripple formation. Proc. hydraulic Div. am. Soc. civ. Engrs. 89(HY6): 15-33
- Raudkivi, A.J. 1966. Bed forms in alluvial channels J. fluid Mech. 26: 507-514
- Raupach, M.R., Thom, A.S. and Edwards, I. 1980. A wind-tunnel study of turbulent flow close to regularly arrayed rough surfaces. Boundary-layer Meteor. 18: 373-397
- Richardson, P.D. 1968. The generation of scour marks near obstacles. J. sedim. Petrol. 38: 965-970
- Sadeh, W.Z., Cermak, J.E. and Kawatani, T. 1971. Flow over high roughness elements. Boundary-layer Meteor. 1: 321-344
- Schlichting, H. 1979. Boundary Layer Theory. New York: McGraw-Hill, 796 p.
- Smith, J.D. 1970. Stability of a sand bed subjected to a shear flow of low Froude Number. J. geophys. Res. 75: 5928-5940
- Smith, J.D. 1977. Modelling of sediment transport on continental shelves. In Goldberg, E.D., McCave, I.N., O'Brien, J.J. and Steele, J.H. (eds.), The Sea. vol. 6. New York: John Wiley and Sons, p. 539-577
- Smith, J.D. and McLean, S.R. 1977. Spatially averaged flow over a wavy surface. J. geophys. Res. 82: 1735-1746
- Southard, J.B. 1971. Representation of bed configurations in depth-velocity-size diagrams. J. sedim. Petrol. 41: 903-915
- Sreenivasan, K.R. and Antonia, R.A. 1977. Properties of wall shear stress fluctuations in a turbulent duct flow. J. appl. Mech. 44: 389-395
- Swift, S.A., Hollister, C.D. and Chandler, R.S. 1983. Close-up stereo photogrammetry of abyssal bedforms on the Nova Scotian continental rise. Preprint, February 1983, 26 p.

- Tennekes, H. 1977. Turbulence: diffusion, statistics, spectral dynamics. In: Frost, W. and Moulden, T. (eds.), Handbook of Turbulence. New York: Plenum Press, p. 127-146
- Tennekes, H. and Lumley, J.L. 1972. A First Course in Turbulence. Cambridge, Mass.: MIT Press, 293 p.
- Townsend, A.A. 1965a. Self-preserving flow inside a turbulent boundary layer. J. fluid Mech. 22: 773-797
- Townsend, A.A. 1965b. The response of a turbulent boundary layer to abrupt changes in surface conditions. J. fluid Mech. 22: 799-822
- Townsend, A.A. 1976. The Structure of Turbulent Shear Flow. Cambridge, U.K.: Cambridge Univ. Press, 424 p.
- Tritton, D.J. 1977. Physical Fluid Dynamics. New York: Van Nostrand Reinhold, 353 p.
- Vanoni, V.A. and Brooks, N.H. 1957. Laboratory studies of the roughness and suspended load of alluvial streams. Pasadena, Calif.: Calif. Inst. Tech. Sedimentation Lab. Rept. E-68, 121 p.
- Vanoni, V.A. and Hwang, L.-S. 1967. Relation between bed forms and friction in streams. J. hydraulic Div. am. Soc. civ. Engrs. 93(HY3): 121-144
- Wallace, J.M., Brodkey, R.S. and Eckelmann, H. 1976. Pattern recognized structures in bounded turbulent shear flows. Gottingen: Max-Planck-Institut fur Stromungsforschung, Bericht 108, 32 p.
- Weatherly, G.L. and Martin, P.J. 1978. On the structure and dynamics of the oceanic bottom boundary layer. J. phys. Oceanogr. 8: 557-570
- Werner, F. Unsold, G., Koopmann, B. and Stefanon, A. 1980. Field observations and flume experiments on the nature of comet marks. Sedim. Geol. 26: 233-262.
- Wonnacott, T.H. and Wonnacott, R.J. 1972. Introductory Statistics. New York: John Wiley and Sons, Inc., 501 p.
- Wooding, R.A., Bradley, E.F. and Marshall, J.K. 1973. Drag due to regular arrays of roughness elements of varying geometry. Boundary-layer Meteor. 5: 285-308
- Wyganski, I. and Fiedler, H.E. 1970. The two-dimensional mixing region. J. fluid Mech. 41: 327-361

- Yaglom, A.M. 1979. Similarity laws for constant-pressure and pressure-gradient turbulent wall flows. Ann. Rev. fluid Mech. 11: 505-540
- Zilker, D.P. 1976. Flow over wavy surfaces. Ph.D. thesis, Dept. Chem. Engrg., Univ. Ill., Urbana-Champaign, Ill., 361 p.
- Zilker, D.P., Cook, G.W. and Hanratty, T.J. 1977. Influence of the amplitude of a solid wavy wall on a turbulent flow. Part 1. Non-separated flows. J. fluid Mech. 82: 29-51
- Zilker, D.P. and Hanratty, T.J. 1979. Influence of the amplitude of a solid wavy wall on a turbulent flow. Part 2. Separated flows. J. fluid Mech. 90: 257-271
- Znamenskaya, N.S. 1967. The analysis and estimating of energy losses by instantaneous velocity distribution of streams with movable bed. Proc. twelfth Congr. intl. Assoc. for hydraulic Res. 1: 27-31

Appendix A. Symbols

$a$  diffusivity of heat; bed-form amplitude

$a_{1...n}$  empirical constants

$A$  horizontal averaging area; endpoint of confidence interval

$A'$  true wetted surface area

$A_h$  frontal area of one roughness element

$A_p$  total horizontal area per roughness element

$A_r$  overheat ratio

$B$  bandwidth of a random signal; endpoint of a confidence interval

$C$  constant

$C_o$  volume concentration of sediment in the bed

$C_D$  drag coefficient

$d$  grain diameter

$D$  flow depth

$D_i$  thickness of internal boundary layer

$D_{ln}$  thickness of logarithmic region

$D_s$  thickness of sublayer controlled by skin friction

$D_{th}$  thickness of thermal boundary layer

$D_\tau$  maximum height of stress disturbance due to a change in roughness

$f$  Darcy-Weisbach friction factor

$g$  gravitational acceleration

$h$  roughness height

$I$  thermal-sensor current

$k$  bed-form wavenumber

$k_s$  equivalent sand roughness height; instantaneous sediment-transport function  
 $K_u$  kurtosis of a fluctuating signal  
 $L$  sensor length; bed-form spacing  
 $L_a$  horizontal length scale for  $z_{ot}$   
 $L_p$  pressure-gradient length scale  
 $L_r$  horizontal length scale of roughness variability  
 $L_z$  width of disturbance induced by upstream roughness change  
 $N$  number of degrees of freedom  
 $p$  pressure; significance level; probability density  
 $q_s$  time-averaged sediment transport  
 $r^2$  correlation coefficient  
 $r_h$  hydraulic radius: cross-sectional area divided by wetted perimeter  
 $R$  bulk Reynolds number:  $\bar{u}D/\nu$   
 $R_*$  roughness Reynolds number:  $u_*t_h/\nu$   
 $R_a$  resistance of a thermal sensor at fluid temperature  
 $R_h$  Reynolds number based on hydraulic radius:  $r_h\bar{u}/\nu$   
 $R_w$  resistance of a heated thermal sensor  
 $s$  streamwise length of roughness elements  
 $S$  energy slope  
 $Sk$  skewness of a fluctuating signal  
 $t_a$  averaging time  
 $t$  time  
 $t_c$  response time

$u$  time-averaged streamwise fluid velocity  
 $\bar{u}$  bulk velocity or vertically averaged velocity  
 $u_o$  scaling velocity for potential flow  
 $u_s$  free-surface velocity  
 $u^*$  friction velocity (time-averaged)  
 $u^*_{cs}$  skin-friction velocity at the initiation of sediment transport  
 $u^*_{cs\beta}$   $u^*_{cs}$  for a bed of slope  $\beta$   
 $u^*_{ss}$  representative skin-friction velocity  
 $U$  instantaneous streamwise fluid velocity  
 $v$  time-averaged, unlinearized bridge output voltage  
 $v_o$  bridge voltage in still water  
 $w_r$  form drag on one roughness element  
 $x$  streamwise coordinate  
 $x_c$  response distance  
 $y$  vertical coordinate  
 $y_i$  lower limit of the ILL  
 $z_o$  roughness length  
 $(z_{ot})_o$  absolute roughness length  
 $\alpha$  1-(significance level)  
 $\beta$  local bed slope  
 $\epsilon_{ijk}$  alternating tensor:  $\epsilon_{ijk} = 0$  if  $i=j$  or  $j=k$   
 $= 1$  if  $ijk = 123, 231$  or  $312$   
 $= -1$  if  $ijk = 321, 132$  or  $213$   
 $\epsilon_y$  vertical turbulent diffusivity  
 $\epsilon_z$  lateral turbulent diffusivity



$\zeta$  curvilinear vertical coordinate  
 $\eta$  height of the bed  
 $\kappa$  von Karman's coefficient  
 $\lambda$  areal density of roughness elements;  $\lambda = A_h/A_p$   
 $\mu$  dynamic viscosity  
 $\nu$  kinematic viscosity  
 $\rho$  fluid density  
 $\sigma$  bed-form propagation speed; (with one subscript)  
     root-mean-square value of fluctuating signal  
 $\sigma_{ij}$  stress tensor  
 $\tau_0$  time-averaged boundary shear stress  
 $T_0$  instantaneous boundary shear stress  
 $\phi$  velocity potential; aspect-ratio function for  $z_{ot}$   
 $\Phi$  power spectral density  
 $\chi^2$  point of chi-squared distribution  
 $\psi$  angle of repose  
 $\omega$  time-averaged vorticity  
 $\Omega$  instantaneous vorticity

Modifiers and subscripts

A apparent

f of form drag

$i, j, k, l$  tensor indices whose domain comprises all three  
coordinate directions

$m, n$  tensor indices whose domain comprises only the horizontal  
directions  $x$  and  $z$

$n$  locally normal to the bed

$p$  locally parallel to the bed

$s$  of skin friction or sediment transport

$t$  of the bed as a whole

$*$  of the boundary

$\circ$  of or at the bed, or a reference value

$\langle \rangle$  spatially averaged

$\bar{\quad}$  spatially averaged

" spatial fluctuation

' temporal fluctuation

$\Delta$  finite difference

Acronyms and abbreviations

ESL equilibrium surface layer

d dynes

HEBBLE High Energy Benthic Boundary Layer Experiment

IBL internal boundary layer

ILL integrated logarithmic layer

OTB obstacle-trapped bed form

PDF probability density function

Appendix B. Computer programs

FILE . YBL	FORTRAN A	VM/SP CONVERSATIONAL MONITOR SYSTEM	PAGE 001
C	PROGRAM YBL CONVERTS LOCAL HEIGHT ABOVE ABOVE A RIPPLED BED TO	YBL00010	
C	BOUNDARY LAYER HEIGHT BASED ON POTENTIAL FLOW STREAMLINES OVER A	YBL00020	
C	A SINUSOIDAL BED.	YBL00030	
C		YBL00040	
	AMP = 0.52	YBL00050	
	WAVENO = 0.612994	YBL00060	
	PHASE = 0.306497	YBL00070	
C		YBL00080	
C	INPUT VALUE OF X, THE STREAMWISE COORDINATE, AND CALCULATE BOUNDARY	YBL00090	
C	AMPLITUDE.	YBL00100	
C		YBL00110	
	WRITE(6,20)	YBL00120	
20	FORMAT(' VALUE OF X')	YBL00130	
	READ(5,+) X	YBL00140	
	ANGLE = (WAVENO*X)+PHASE	YBL00150	
	COSFN = AMP*COS(ANGLE)	YBL00160	
C		YBL00170	
C	ASK FOR A VALUE OF LOCAL HEIGHT AND CONVERT TO CARTESIAN HEIGHT	YBL00180	
C		YBL00190	
	WRITE(6,40)	YBL00200	
40	FORMAT(' INPUT VALUES OF LOCAL HEIGHT; 999 ENDS THE JOB')	YBL00210	
60	CONTINUE	YBL00220	
	READ(5,+) YLOC	YBL00230	
	IF (YLOC .EQ. 999.0) STOP	YBL00240	
	YCART = YLOC+COSFN	YBL00250	
	YP1 = YCART	YBL00260	
C		YBL00270	
C	CALCULATE THE BOUNDARY LAYER HEIGHT ITERATIVELY, STOPPING WHEN	YBL00280	
C	SUCCESSIVE VALUES AGREE WITHIN 0.0001.	YBL00290	
C		YBL00300	
	DO 80 I=1,500	YBL00310	
	ARG = -(WAVENO*YP1)	YBL00320	
	Z = COSFN*EXP(ARG)	YBL00330	
	YP2 = YCART-Z	YBL00340	
	IF (ABS(YP2-YP1) .LE. 0.0001) GO TO 120	YBL00350	
80	YP1 = YP2	YBL00360	
C		YBL00370	
C	IF THE LOOP EXITS NORMALLY CONVERGENCE HAS NOT OCCURRED	YBL00380	
C		YBL00390	
	WRITE(6,100)	YBL00400	
100	FORMAT(' FAILED TO CONVERGE')	YBL00410	
	GO TO 60	YBL00420	
C		YBL00430	
C	UPON CONVERGENCE WRITE OUT YBL AND GET ANOTHER HEIGHT	YBL00440	
C		YBL00450	
120	WRITE(6,140) YP2	YBL00460	
140	FORMAT(' YBL = ',F6.3)	YBL00470	
	GO TO 60	YBL00480	
	END	YBL00490	

FILE: SKINFRIC FORTRAN A

VM/SP CONVERSATIONAL MONITOR SYSTEM

PAGE 001

```

C SKI00010
C PROGRAM SKINFRIC SKI00020
C CONVERTS AN INPUT FIELD OF SKIN FRICTION MEANS, STANDARD DEVIATIONS SKI00030
C AND ANGLES AT IRREGULAR POSITIONS TO AN INTERPOLATED VECTOR FIELD ON SKI00040
C A 1 CM GRID AND COMPUTES THE VECTOR DIVERGENCE OF THE FIELD SKI00050
C ON THE GRID. THE TOTAL FIELD SIZE IS 50 CM BY 50 CM. X IS THE SKI00060
C STREAMWISE COORDINATE, Y IS THE SPANWISE COORDINATE AND THE SKI00070
C ORIGIN CAN BE IN ANY CORNER PROVIDED THE ANGLE IS GIVEN PROPERLY SKI00080
C (THE ANGLES ARE USED IN THE DO 100 LOOP) FOR EXAMPLE, WITH THE SKI00090
C ORIGIN IN THE UPSTREAM LEFT CORNER (LOOKING DOWNSTREAM) <ANGLE> IS SKI00100
C THE ANGLE FROM THE POSITIVE X-AXIS RECKONED POSITIVE CLOCKWISE. SKI00110
C IT IS ASSUMED THAT THE ORIGINAL Y DATA ARE GIVEN RELATIVE TO AN SKI00120
C ORIGIN IN THE CENTER OF THE X-AXIS; THEY ARE TRANSFORMED SO THAT SKI00130
C THE ORIGIN IS IN THE CORNER (THE INTERVAL (0,25) BECOMES (25,0)). SKI00140
C YOU WILL BE ASKED WHETHER YOU WANT TO REFLECT THE INPUT DATA SKI00150
C ABOUT THE LINE Y=25 CM. IF YOU DO, BE SURE ALL THE Y VALUES IN THE SKI00160
C INPUT MATRIX ARE LESS THAN OR EQUAL TO 25 THE DATA SHOULD BE IN A SKI00170
C DISK FILE IN FORMAT 5F10.0 ASSOCIATED WITH LOGICAL NUMBER 31, IN THE SKI00180
C FOLLOWING ORDER. Y X MEAN S.F. RMS S.F. DIRECTION SKI00190
C SKI00200
  CALL SKINSB SKI00210
  STOP SKI00220
  END SKI00230
@PROCESS SC(AXIS,SYMBOL) SKI00240
C SKI00250
  SUBROUTINE SKINSB SKI00260
  REAL XIN(200),YIN(200),TSD(200),ANGLE(200),TAUM(200), SKI00270
  1 TAUX(200),TAUY(200),TGRIDX(50,50),TGRIDY(50,50),XGRID(52), SKI00280
  2 YGRID(52),DIVHT(52,52),WK(1200),TGRIDM(52,52),TGRIDS(52,52), SKI00290
  3 DIVHN(11,52),DIVHF(41,52),XGRIDN(11),XGRIDF(41) SKI00300
  INTEGER IWK(9700) SKI00310
  LOGICAL REFLN,ANS SKI00320
  LOGICAL*1 LABEL(7) SKI00330
  DATA PI/3.141592654/ SKI00340
C SKI00350
  CALL PLOTS(IDUM,IDUM,11) SKI00360
  CALL FACTOR(0.77) SKI00370
C SKI00380
  WRITE(6,2) SKI00390
  2 FORMAT(' DO YOU WANT REFLECTION (T OR F)?') SKI00400
  READ(5,4) REFLN SKI00410
  4 FORMAT(L4) SKI00420
C SKI00430
  DO 10 I=1,1000 SKI00440
  READ(31,20,END=40)YIN(I),XIN(I),TAUM(I),TSD(I),ANGLE(I) SKI00450
  IF ((YIN(I).LE.25.0).OR.(.NOT. REFLN)) GO TO 10 SKI00460
  WRITE (6,5) SKI00470
  5 FORMAT(' FOR REFLECTION ALL Y'S MUST BE .LE. 25 - CORRECT THE '/ SKI00480
  1 ' INPUT FILE AND TRY AGAIN') SKI00490
  RETURN SKI00500
  10 CONTINUE SKI00510
C SKI00520
  20 FORMAT(5F10.0) SKI00530
  40 NPTS = I-1 SKI00540
C SKI00550

```

```

NDIM = 200
IPLUS = 0
DO 100 I=1,NPTS
YIN(I) = 25.0-YIN(I)
RAD = (ANGLE(I)/180.0)*PI
C
C DEFINITION OF COMPONENTS OF STRESS IN TERMS OF THE INPUT ANGLES
C
TAUX(I) = TAUM(I)*COS(RAD)
TAUY(I) = TAUM(I)*SIN(RAD)
C
IF((.NOT.REFLN).OR.(ABS(YIN(I)-25.0) .LE. 0.001)) GO TO 100
IPLUS = IPLUS+1
XIN(NPTS+IPLUS) = XIN(I)
YIN(NPTS+IPLUS) = 50.0-YIN(I)
TAUX(NPTS+IPLUS) = TAUX(I)
TAUY(NPTS+IPLUS) = -TAUY(I)
TSD(NPTS+IPLUS) = TSD(I)
C
100 CONTINUE
C
DO 120 I=1,50
XGRID(I) = 0.5+(FLOAT(I)-1.0)
YGRID(I) = 0.5+(FLOAT(I)-1.0)
C
NXGRID = 50
NYGRID = 50
ITGRID = 50
ISGRID = 52
NPTS = NPTS+IPLUS
C
IF (NPTS.LE.200) GO TO 130
WRITE(6,125) NPTS
125 FORMAT(' NPTS EQUALS ',I4,'. REDUCE THE NUMBER OF DATA POINTS'/
1' OR INCREASE THE DIMENSIONS OF THE INITIAL ARRAYS')
RETURN
C
130 CALL IOHSCV(XIN,YIN,TAUX,NPTS,XGRID,NXGRID,YGRID,NYGRID,
1 TGRIDX,ITGRID,IWK,WK,IER)
CALL IOHSCV(XIN,YIN,TAUY,NPTS,XGRID,NXGRID,YGRID,NYGRID,
1 TGRIDY,ITGRID,IWK,WK,IER)
CALL IOHSCV(XIN,YIN,TSD,NPTS,XGRID,NXGRID,YGRID,NYGRID,
1 TGRIDS,ISGRID,IWK,WK,IER)
C
DELTAX = 1.0
DELTAY = 1.0
C
DO 140 I=2,49
DO 140 J=2,49
IP = I+1
IM = I-1
JP = J+1
JM = J-1
DTXDX = (TGRIDX(IP,J)-TGRIDX(IM,J))/(2.0*DELTAX)
DTYDY = (TGRIDY(I,JP)-TGRIDY(I,JM))/(2.0*DELTAY)

```

```

SK100560
SK100570
SK100580
SK100590
SK100600
SK100610
SK100620
SK100630
SK100640
SK100650
SK100660
SK100670
SK100680
SK100690
SK100700
SK100710
SK100720
SK100730
SK100740
SK100750
SK100760
SK100770
SK100780
SK100790
SK100800
SK100810
SK100820
SK100830
SK100840
SK100850
SK100860
SK100870
SK100880
SK100890
SK100900
SK100910
SK100920
SK100930
SK100940
SK100950
SK100960
SK100970
SK100980
SK100990
SK101000
SK101010
SK101020
SK101030
SK101040
SK101050
SK101060
SK101070
SK101080
SK101090
SK101100

```

FILE: SKINFRIC FORTRAN A

VM/SP CONVERSATIONAL MONITOR SYSTEM

PAGE 003

```

140 DIVHT(I,J) = DTXXD+DTYDY          SKIO1110
C                                     SKIO1120
    TSUM = 0 0                        SKIO1130
    NSUM = 0                           SKIO1140
    DO 145 I=1,50                      SKIO1150
    DO 145 J=1,50                      SKIO1160
    TGRIDM(I,J) = SQRT(TGRIDX(I,J)**2+TGRIDY(I,J)**2) SKIO1170
    IF (.NOT.((J.EQ.1).OR.(J.EQ.50))) GO TO 145 SKIO1180
    TSUM = TSUM+TGRIDM(I,J)           SKIO1190
    NSUM = NSUM+1                     SKIO1200
145 CONTINUE                          SKIO1210
    TINF = TSUM/FLOAT(NSUM)          SKIO1220
C                                     SKIO1230
    DO 147 I=1,50                      SKIO1240
    DO 147 J=1,50                      SKIO1250
147 WRITE(33,148) TGRIDX(I,J),TGRIDY(I,J),TGRIDS(I,J) SKIO1260
148 FORMAT(3F10.6)                   SKIO1270
C                                     SKIO1280
    WRITE(6,150)                      SKIO1290
150 FORMAT(' DO YOU WANT A PRINT-OUT OF THE DATA (T OR F)?') SKIO1300
    READ(5,151) ANS                   SKIO1310
151 FORMAT(L4)                        SKIO1320
    IF (.NOT.ANS) GO TO 300           SKIO1330
C                                     SKIO1340
    WRITE(4,159)                      SKIO1350
159 FORMAT(1X,/' HORIZONTAL DIVERGENCE'/) SKIO1360
    WRITE(4,160)((DIVHT(I,J),J=2,49),I=2,49) SKIO1370
160 FORMAT(1X,8F8.3/1X,8F8.3/1X,8F8.3/1X,8F8.3/1X,8F8.3//) SKIO1380
C                                     SKIO1390
    WRITE(4,199)                      SKIO1400
199 FORMAT(1X,/' STRESS MAGNITUDE'/) SKIO1410
    WRITE(4,200)((TGRIDM(I,J),J=1,50),I=1,50) SKIO1420
200 FORMAT(1X,10F7.2/1X,10F7.2/1X,10F7.2/1X,10F7.2/1X,10F7.2//) SKIO1430
C                                     SKIO1440
    WRITE(4,205)                      SKIO1450
205 FORMAT(1X,/' STRESS-X'/)         SKIO1460
    WRITE(4,200)((TGRIDX(I,J),J=1,50),I=1,50) SKIO1470
C                                     SKIO1480
    WRITE(4,210)                      SKIO1490
210 FORMAT(1X,/' STRESS-Y'/)         SKIO1500
    WRITE(4,200)((TGRIDY(I,J),J=1,50),I=1,50) SKIO1510
C                                     SKIO1520
C PLOTTING SECTION                   SKIO1530
C                                     SKIO1540
300 CONTINUE                          SKIO1550
    WRITE(6,310)                      SKIO1560
310 FORMAT(' DO YOU WANT CONTOUR PLOTS (T OR F)?') SKIO1570
    READ(5,320) ANS                   SKIO1580
320 FORMAT(L4)                        SKIO1590
    IF (.NOT.ANS) RETURN              SKIO1600
    WRITE(6,340)                      SKIO1610
340 FORMAT(' ENTER A PLOT LABEL 7 CHARACTERS LONG') SKIO1620
    READ(5,360)(LABEL(I),I=1,7)       SKIO1630
360 FORMAT(7A1)                       SKIO1640
C                                     SKIO1650

```

	Z0 = 0.0	SKIO1660
	Z1 = 1.0	SKIO1670
	Z2 = 2.0	SKIO1680
	Z10 = 10.0	SKIO1690
	Z90 = 90.0	SKIO1700
	Z9 = 9.0	SKIO1710
	Z11 = 11.0	SKIO1720
	Z97 = 9.8	SKIO1730
	Z25 = 0.2	SKIO1740
	Z8 = 8.0	SKIO1750
	Z81 = 8.1	SKIO1760
	Z93 = 9.5	SKIO1770
	Z99 = 999.0	SKIO1780
	Z18 = 24.0	SKIO1790
	Z4 = 4.0	SKIO1800
	Z6 = 6.0	SKIO1810
	Z13 = 13.4	SKIO1820
	Z114 = 11.4	SKIO1830
C		SKIO1840
	DO 380 I=1,50	SKIO1850
	DO 380 J=1,50	SKIO1860
380	TGRIDM(I,J) = TGRIDM(I,J)/TINF	SKIO1870
C	TGRIDS(I,J) = TGRIDS(I,J)/TINF	SKIO1880
		SKIO1890
	DO 385 I=2,49	SKIO1900
	DO 385 J=2,49	SKIO1910
385	DIVHT(I,J) = DIVHT(I,J)/TINF	SKIO1920
C		SKIO1930
	CALL PLOT(Z0,Z2,-3)	SKIO1940
C		SKIO1950
	WRITE (6,390)	SKIO1960
390	FORMAT(' MAGNITUDE?')	SKIO1970
	READ(5,151)ANS	SKIO1980
	IF(.NOT. ANS) GO TO 392	SKIO1990
C		SKIO2000
	CALL SCALE(XGRID,Z10,50,1)	SKIO2010
	CALL SCALE(YGRID,Z10,50,1)	SKIO2020
	CALL AXIS(Z0,Z0,'STREAMWISE (X) CM',-17,Z10,Z0,	SKIO2030
	1 XGRID(51),XGRID(52))	SKIO2040
	CALL AXIS(Z0,Z0,'SPANWISE (Y) CM',15,Z10,Z90,	SKIO2050
	1 YGRID(51),YGRID(52))	SKIO2060
	CALL AXIS(Z0,Z10,'STREAMWISE (X) CM',17,Z10,Z0,	SKIO2070
	1 XGRID(51),XGRID(52))	SKIO2080
	CALL AXIS(Z10,Z0,'SPANWISE (Y) CM',-15,Z10,Z90,	SKIO2090
	1 YGRID(51),YGRID(52))	SKIO2100
	CALL PLOT(Z0,Z0,3)	SKIO2110
C		SKIO2120
	CALL FNCON1(TGRIDM,XGRID,YGRID,52.52,50,50,Z0,Z0,Z0,6,3)	SKIO2130
	CALL SYMBOL(Z11,Z97,Z25,'MEAN STRESS',Z0,11)	SKIO2140
	CALL SYMBOL(Z11,Z8,Z25,'REF = ',Z0,6)	SKIO2150
	CALL NUMBER(Z99,Z8,Z25,TINF,Z0,3)	SKIO2160
	CALL SYMBOL(Z13,Z8,Z25,'DYNE/CM',Z0,7)	SKIO2170
	CALL SYMBOL(Z99,Z81,Z25,'2',Z0,1)	SKIO2180
	CALL SYMBOL(Z11,Z6,Z25,LABEL,Z0,7)	SKIO2190
C		SKIO2200



FILE: SKINFRIC FORTRAN A

VM/SP CONVERSATIONAL MONITOR SYSTEM

PAGE 005

```

      CALL PLOT(Z18,ZO,-3)
C
392  WRITE (6,394)
394  FORMAT(' STANDARD DEVIATION?')
      READ(5,151)ANS
      IF(.NOT. ANS) GO TO 400
C
      CALL SCALE(XGRID,Z10,50,1)
      CALL SCALE(YGRID,Z10,50,1)
      CALL AXIS(ZO,ZO,'STREAMWISE (X) CM',-17,Z10,ZO,
1 XGRID(51),XGRID(52))
      CALL AXIS(ZO,ZO,'SPANWISE (Y) CM',15,Z10,Z90,
1 YGRID(51),YGRID(52))
      CALL AXIS(ZO,Z10,'STREAMWISE (X) CM',17,Z10,ZO,
1 XGRID(51),XGRID(52))
      CALL AXIS(Z10,ZO,'SPANWISE (Y) CM',-15,Z10,Z90,
1 YGRID(51),YGRID(52))
      CALL PLOT(ZO,ZO,3)
C
      CALL FNCON1(TGRIDS,XGRID,YGRID,52,52,50,50,ZO,ZO,ZO,6,3)
      CALL SYMBOL(Z11,Z97,Z25,'RMS STRESS',ZO,10)
      CALL SYMBOL(Z11,Z93,Z25,'FLUCTUATION',ZO,11)
      CALL SYMBOL(Z11,Z8,Z25,'REF = ',ZO,6)
      CALL NUMBER(Z99,Z8,Z25,TINF,ZO,3)
      CALL SYMBOL(Z13,Z8,Z25,'DYNE/CM',ZO,7)
      CALL SYMBOL(Z99,Z81,Z25,'2',ZO,1)
      CALL SYMBOL(Z11,Z6,Z25,LABEL,ZO,7)
C
      CALL PLOT(Z18,ZO,-3)
C
400  WRITE (6,405)
405  FORMAT(' HORIZONTAL DIVERGENCE?')
      READ(5,151)ANS
      IF(.NOT. ANS) GO TO 500
C
      DO 420 I=2,49
      DO 410 J=2,49
410  DIVHT(I-1,J-1) = DIVHT(I,J)
      XGRID(I-1) = XGRID(I)
420  YGRID(I-1) = YGRID(I)
C
      CALL SCALE(XGRID,Z10,48,1)
      CALL SCALE(YGRID,Z10,48,1)
C
      CALL AXIS(ZO,ZO,'STREAMWISE (X) CM',-17,Z10,ZO,
1 XGRID(49),XGRID(50))
      CALL AXIS(ZO,ZO,'SPANWISE (Y) CM',15,Z10,Z90,
1 YGRID(49),YGRID(50))
      CALL AXIS(ZO,Z10,'STREAMWISE (X) CM',17,Z10,ZO,
1 XGRID(49),XGRID(50))
      CALL AXIS(Z10,ZO,'SPANWISE (Y) CM',-15,Z10,Z90,
1 YGRID(49),YGRID(50))
C
C DEFINE THE NEAR FIELD...
C

```

```

SK102210
SK102220
SK102230
SK102240
SK102250
SK102260
SK102270
SK102280
SK102290
SK102300
SK102310
SK102320
SK102330
SK102340
SK102350
SK102360
SK102370
SK102380
SK102390
SK102400
SK102410
SK102420
SK102430
SK102440
SK102450
SK102460
SK102470
SK102480
SK102490
SK102500
SK102510
SK102520
SK102530
SK102540
SK102550
SK102560
SK102570
SK102580
SK102590
SK102600
SK102610
SK102620
SK102630
SK102640
SK102650
SK102660
SK102670
SK102680
SK102690
SK102700
SK102710
SK102720
SK102730
SK102740
SK102750

```

```

      DO 440 I=1,9                                SKI02760
      XGRIDN(I) = XGRID(I)                        SKI02770
      DO 440 J=1,48                                SKI02780
440   DIVHN(I,J) = DIVHT(I,J)                    SKI02790
      C                                            SKI02800
      CALL SCALE(XGRIDN,Z2,9,1)                   SKI02810
      CALL PLOT(Z0,Z0,3)                           SKI02820
      CALL FNCON1(DIVHN,XGRIDN,YGRID,11,52,9,48,Z0,Z0,Z0,6,3) SKI02830
      C                                            SKI02840
      C DEFINE THE FAR FIELD...                   SKI02850
      C                                            SKI02860
      DO 460 I=1,39                                SKI02870
      II = I+9                                     SKI02880
      XGRIDF(I) = XGRID(II)                       SKI02890
      DO 460 J=1,48                                SKI02900
460   DIVHF(I,J) = DIVHT(II,J)                   SKI02910
      C                                            SKI02920
      CALL SCALE(XGRIDF,Z8,39,1)                   SKI02930
      CALL PLOT(Z2,Z0,-3)                           SKI02940
      CALL PLOT(Z0,Z10,2)                           SKI02950
      CALL PLOT(Z0,Z0,3)                           SKI02960
      CALL FNCON1(DIVHF,XGRIDF,YGRID,41,52,39,48,Z0,Z0,Z0,6,3) SKI02970
      C                                            SKI02980
      CALL SYMBOL(Z9,Z97,Z25,'HORIZONTAL',Z0,10)   SKI02990
      CALL SYMBOL(Z9,Z93,Z25,'DIVERGENCE (1/CM)',Z0,17) SKI03000
      CALL SYMBOL(Z9,Z8,Z25,'REF = ',Z0,6)         SKI03010
      CALL NUMBER(Z99,Z8,Z25,TINF,Z0,3)           SKI03020
      CALL SYMBOL(Z114,Z8,Z25,'DYNE/CM',Z0,7)     SKI03030
      CALL SYMBOL(Z99,Z81,Z25,'2',Z0,1)           SKI03040
      CALL SYMBOL(Z9,Z6,Z25,LABEL,Z0,7)           SKI03050
500   CALL ENDPLT(Z18,Z0,999)                     SKI03060
      RETURN                                       SKI03070
      END                                         SKI03080

```

## BIOGRAPHICAL SKETCH

I was born on December 22, 1954 in Plainfield, New Jersey. I graduated from Roselle Park High School in Roselle Park, New Jersey, in 1972, and received my B.S. in environmental geology from Lehigh University, Bethlehem, Pennsylvania, in 1976. I then spent a year at the University of Reading (U.K.), receiving an M.Sc. in sedimentology in 1977. I have been in the MIT/WHOI Joint Program since I left Reading.